UNIVERSITEIT GENT

FACULTEIT WETENSCHAPPEN
VAKGROEP SUBATOMAIRE EN STRALINGSFYSICA
ACADEMIEJAAR 2006-2007

The HERMES recoil photon-detector and nuclear p_t-broadening at HERMES

De HERMES recoil photon-detector en nucleaire p_t-verbreding in HERMES

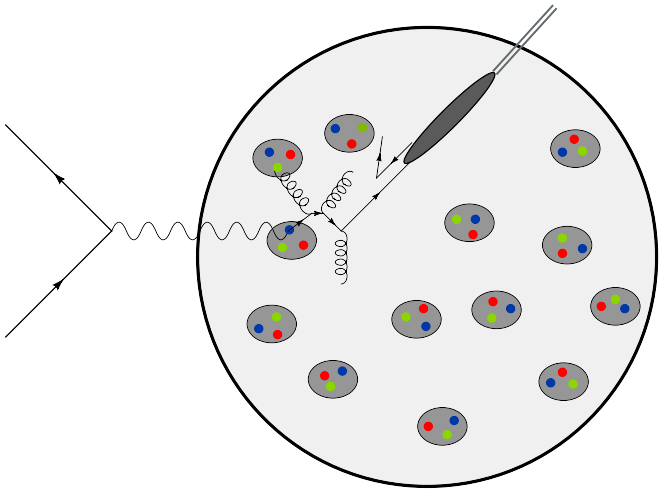

Yves Van Haarlem
Promotor: Prof. Dr. Dirk Ryckbosch

Proefschrift ingediend tot het verkrijgen van de graad van
Doctor in de Wetenschappen: Natuurkunde

”To one, science is an exalted goddess, to another it is a cow which provides him with butter.”

- Bertrand Russell

Contents

Chapter 1

Introduction

This thesis is situated in medium-energy physics performed at the HERa MEasurement of Spin (HERMES) experiment located at the Deutsches Elektronen-SYnchrotron (DESY) laboratory in Hamburg, Germany.

This work consists of two separate subjects. The first part is about construction and testing that was done for the HERMES recoil detector. More precisely for the HERMES recoil photon-detector and a test was done for the HERMES recoil scintillating fiber tracker. The second part is about the analysis of the transverse momentum broadening of hadrons produced in semi-inclusive deep-inelastic scattering on nuclear targets in order to study hadronization, which is a process that is still not completely understood.

The motivation for the HERMES recoil detector is given in the second part of chapter 2 where deeply virtual Compton scattering is introduced. To identify this process it is important to detect all final-state particles. This is the main motivation for building the HERMES recoil detector. Details on this detector are given in chapter 4 where the construction and testing of the recoil photon-detector are discussed in more detail.

Deep-inelastic and semi-inclusive deep-inelastic scattering are introduced in the first part of chapter 2. Concepts as parton distribution functions and hadronization are discussed. The last part describes nuclear effects in hadronization inside the nucleus and focusses on transverse momentum broadening that is analyzed later in this thesis.

In chapter 3 the HERA accelerator that accelerates and stores protons and leptons ($e^{\pm}$) is described. The accelerated leptons are used by the HERMES experiment to scatter off a "fixed" gaseous target. The HERMES forward spectrometer configuration, at the time data was taken for the analysis presented, is discussed as well.

The transverse momentum broadening analysis is described in chapters 6. In this chapter the event selection and kinematic cuts are described, and the analysis with all the applied corrections is covered. The results are presented in chapter 7 and some interpretations are given. The Monte Carlo simulations that are used in this analysis are described in chapter 5.

This work ends with a summary and outlook plus a summary in Dutch.

Chapter 2

Nuclear semi-inclusive deep-inelastic scattering and deeply virtual Compton scattering

The first part of this chapter provides an introduction in the underlying theories of the transverse momentum broadening analysis performed in this thesis. Semi-inclusive deep-inelastic scattering (SIDIS), nuclear SIDIS, and p_t-broadening are introduced. At the moment this thesis was written there were several models available to describe nuclear effects like p_t-broadening. The second part of this chapter introduces deeply virtual Compton scattering (DVCS) as the main motivation for building the HERMES recoil detector.

2.1 Nuclear semi-inclusive deep-inelastic scattering

This section starts by introducing several kinematic variables that are important for semi-inclusive deep-inelastic scattering. The cross section is calculated and interpreted using the quark-parton model. The nucleus as a laboratory to study hadronization is introduced.

2.1.1 Semi-inclusive deep-inelastic scattering: kinematics

In deep-inelastic scattering (DIS) a lepton (electron or positron) scatters off a nucleon; in the interaction the target breaks up and hadrons are formed:

$$l + N \rightarrow l' + X. \tag{2.1}$$

In inclusive events only the scattered lepton is detected, while in semi-inclusive events at least one final-state hadron is detected together with the scattered lepton. A schematic drawing of a DIS event can be seen in figure 2.1. In first order quantum electrodynamics (QED), i.e., in the one-photon-exchange approximation, the nucleon is probed by a virtual photon (γ^*) that has 4-momentum q:

$$q = k - k', \tag{2.2}$$

with k and k' the 4-momenta of the lepton before and after the interaction, respectively (cf. figure 2.1). In principle, the interaction between the lepton and the target can also be mediated

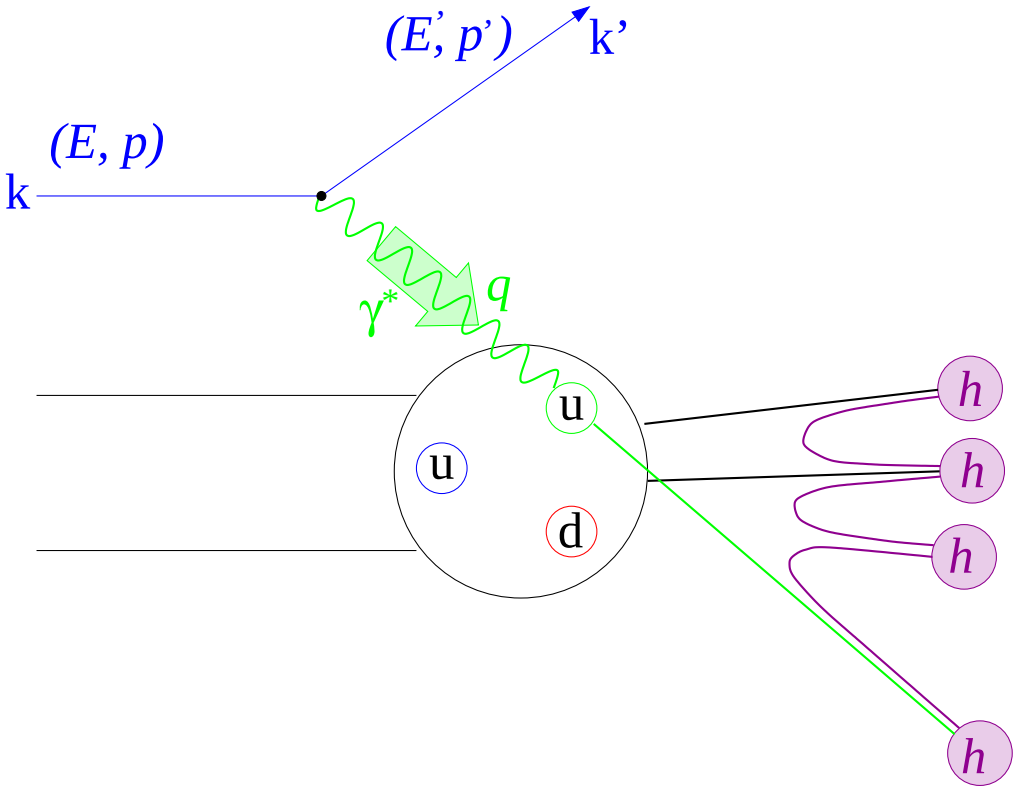

Figure 2.1: Schematic drawing of a deep-inelastic event. An incoming lepton with 4-vector $k(E,p)$ scatters off a nucleon.

by a virtual Z-boson. However, at HERMES, the energy of the lepton beam (27.6 GeV) is well below the Z-mass, so the weak interaction can be neglected. The *spatial resolution* (Q^2) of the probe is defined as:

$$Q^2 = -q^2 \overset{lab}{\approx} 4EE' \sin^2\left(\frac{\theta}{2}\right), \tag{2.3}$$

with θ the polar scattering angle of the lepton, and E and E' are the energy of the incoming and scattered lepton, respectively. Q^2 is called the spatial resolution because in the Breit frame (see section 2.1.3) it sets the spatial resolution with which structures can be studied, this is illustrated in figure 2.2. Q^2 above 1 GeV^2 provides a the resolution that is able to probe substructures the target. The squared center-of-mass energy (s) is:

$$s = (P + k)^2, \tag{2.4}$$

where P is the 4-momentum of the target before the interaction. The energy transfer to the target ν is defined as:

$$\nu = \frac{P \cdot q}{M} \overset{lab}{=} E - E'. \tag{2.5}$$

The squared invariant mass of the photon-nucleon system (W^2) is a Lorentz-invariant variable (also ν, s, and Q^2 are):

$$W^2 = (P + q)^2 \overset{lab}{=} M^2 + 2M\nu - Q^2, \tag{2.6}$$

where M is the mass of the target. If the scattering is elastic then $W^2 = M^2$ or

$$2M\nu - Q^2 = 0. \tag{2.7}$$

This leads to the definition of a variable that measures the inelasticity of the process. This variable is called the x-Bjorken variable:

$$x = \frac{Q^2}{2M\nu}, \tag{2.8}$$

x-Bjorken is 1 for elastic processes and between 0 and 1 for inelastic processes. In the impulse approximation, the interaction of the lepton with the nucleon can be seen as the incoherent sum of the interactions with the individual partons. In this approximation, and assuming that the parton masses can be neglected, the Bjorken variable has the interpretation of the 4-momentum fraction of the nucleon that is carried by the struck parton (see section 2.1.3). Another kinematic variable is y:

$$y = \frac{P \cdot q}{P \cdot k} \overset{lab}{=} \frac{\nu}{E}, \tag{2.9}$$

the fractional energy of the virtual photon. A SIDIS variable or a variable that applies to detected hadrons in a SIDIS event is z, the fraction of the available energy carried by the produced hadron:

$$z = \frac{P \cdot p_h}{P \cdot q} \overset{lab}{=} \frac{E_h}{\nu}, \tag{2.10}$$

with p_h the 4-momentum of the final-state hadron and E_h the energy of the final-state hadron. Finally, $\vec{p_h}$ is the momentum of the final-state hadron and $\vec{p_t}$ is the transverse momentum of the final-state hadron with respect to the virtual photon. A SIDIS event is illustrated in figure 2.3.

2.1.2 The DIS cross section

To calculate the DIS cross section two tensors have to be introduced: a leptonic one, $L_{\mu\nu}$, to describe the leptonic interaction ($l \rightarrow l' + \gamma^*$) and a hadronic one, $W^{\mu\nu}$, to describe the hadronic part ($P + \gamma^* \rightarrow P'$). The expression for the differential cross section for a scattered lepton in the one-photon-exchange approximation, inside solid angle $d\Omega$ in the laboratory frame, with an energy between E' and $E + dE'$, is [1]:

$$\frac{d^2\sigma}{dE'd\Omega} = \frac{\alpha^2}{2MQ^4} \cdot \frac{E'}{E} \cdot L_{\mu\nu}W^{\mu\nu}, \tag{2.11}$$

with $\alpha = \frac{e^2}{4\pi}$ the electromagnetic coupling constant. In quantum electrodynamics (QED) $L_{\mu\nu}$ can be calculated and for pointlike unpolarized leptons:

$$L_{\mu\nu} = 2 \cdot \left[k_\mu k'_\nu + k'_\mu k_\nu - g_{\mu\nu}(k \cdot k')\right], \tag{2.12}$$

with $g_{\mu\nu}$ the Minkowski metric. The hadronic tensor contains information about the inner structure of the target nucleon. This structure is very complex and prevents an exact calculation of the hadronic tensor. Therefore a parametrization is used where two structure functions

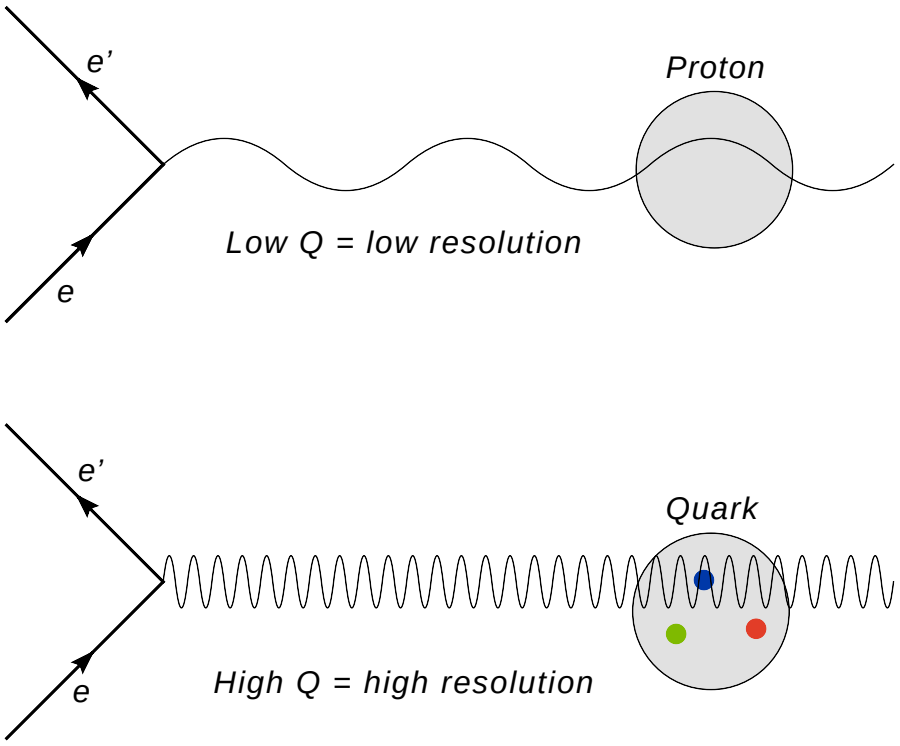

Figure 2.2: Illustration of Q as the spatial resolution.

W_1 and W_2 are introcuced:

$$W_{\mu\nu}(x,q^2) = W_1(x,q^2)\cdot\left(\frac{q_\mu q_\nu}{q^2} - g_{\mu\nu}\right) + W_2(x,q^2)\cdot\frac{1}{M^2}\left(P_\mu - \frac{P\cdot q\, q_\mu}{q^2}\right)\left(P_\nu - \frac{P\cdot q\, q_\nu}{q^2}\right). \tag{2.13}$$

Contraction with the leptonic tensor yields following DIS cross section:

$$\frac{d^2\sigma}{dE'd\Omega} = \frac{\alpha^2}{4E^2\sin^4\frac{\theta}{2}}\left(W_2(x,Q^2)\cos^2\left(\frac{\theta}{2}\right) + 2W_1(x,Q^2)\sin^2\left(\frac{\theta}{2}\right)\right). \tag{2.14}$$

There is a relation between W_1 and W_2, and the more widely used F_1 and F_2 structure functions:

$$F_1 = MW_1 \tag{2.15}$$

$$F_2 = \nu W_2. \tag{2.16}$$

The first DIS measurements were performed at Stanford Linear Accelerator Center (SLAC).

2.1.3 The quark-parton model

To simplify the interpretation of DIS an appropriate reference frame is chosen. The physics of the process should be independent of this choice.

If one uses a frame in which the nucleon has a large momentum, then the rest masses and transverse momenta of the proton constituents, or partons, are much smaller than their

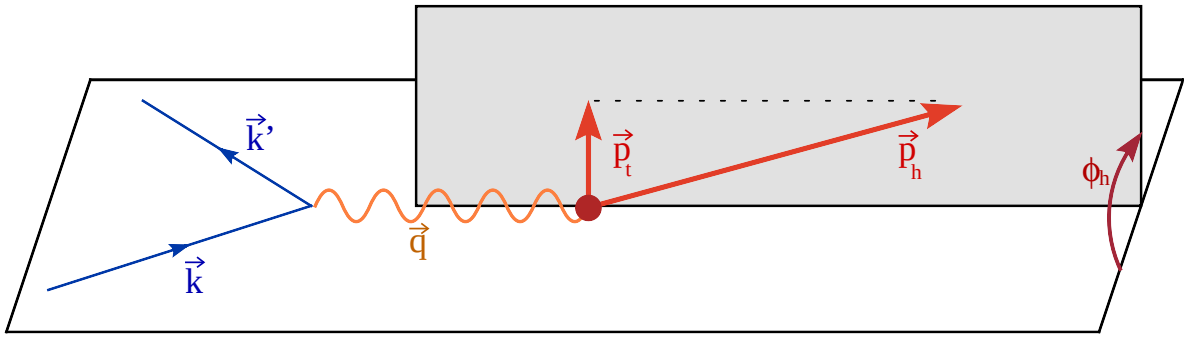

Figure 2.3: Kinematics of semi-inclusive $e + N \rightarrow e' + h + X$ scattering. The scattering plane (the white plane) is defined by the lepton momenta $\vec{k}$ and $\vec{k}'$. The hadron production plane (the gray plane) is defined by $\vec{q}$ and $\vec{p_h}$, $\vec{p_t}$ is the transverse momentum of the produced hadron, and ϕ_h is the angle between the scattering and the hadron production plane.

longitudinal momenta. In this frame the structure of the nucleon is given by the longitudinal momenta of the partons. If the interaction of the virtual photon with the parton is short enough that the interactions between the partons can be neglected, then DIS can be seen as an elastic scattering off the partons. A reference frame that satisfies these conditions and is often used is called the Breit frame. In this frame the energy component of q is zero and the struck parton has the same momentum before and after the interaction, with only its sign changed.

In this reference frame quarks are considered free and one can try to reduce the differential DIS cross section to the cross section describing elastic electron interaction off a point-like spin-$\frac{1}{2}$-particle (an electron off a Dirac particle) given by:

$$\frac{d\sigma}{d\Omega} = \frac{4\alpha E'^2}{Q^4}\cos^2\left(\frac{\theta}{2}\right)\frac{E'}{E}\left(1 - 2\frac{q^2}{4M^2}\tan^2\left(\frac{\theta}{2}\right)\right). \tag{2.17}$$

By doing so the structure functions become:

$$W_1(x) = \frac{1}{2M}\sum_i e_f^2\left(q_f(x) + \overline{q}_f(x)\right) \tag{2.18}$$

$$W_2(x) = -\frac{2x^2M}{q^2}\sum_i e_f^2\left(q_f(x) + \overline{q}_f(x)\right) \tag{2.19}$$

or

$$F_1(x) \equiv MW_1 = \frac{1}{2}\sum_i e_f^2\left(q_f(x) + \overline{q}_f(x)\right) \tag{2.20}$$

$$F_2(x) \equiv \nu W_2 = \frac{p\cdot q}{M}W_2 \overset{x=\frac{Q^2}{2(p\cdot q)}}{=} x\sum_i e_f^2\left(q_f(x) + \overline{q}_f(x)\right), \tag{2.21}$$

with $q_f(x)$ and $\overline{q}_f(x)$ the parton (number) density functions that are associated with quarks and anti-quarks with flavor f, respectively and e_f is the fractional charge of quarks with flavor f. The quark flavors relevant in the HERMES kinematics are up (u), down (d), and strange

(s) and their respective anti-quarks. The quarks responsible for the quantum numbers of the nucleon are called the valence quarks. It can happen that quark anti-quark pairs are created in the strong color field that binds the valence quarks. These quarks are called sea quarks. For example: a proton consists of three valence quarks (uud). The u quark has fractional charge 2/3 and the d, s quark -1/3.

In the quark-parton model there is a relation between F_1 and F_2 that can be calculated by combining 2.20 and 2.21:

$$F_2(x) = 2xF_1(x). \tag{2.22}$$

This relation is called the Callan-Gross relation [3]. This was confirmed by measurements at SLAC and elsewhere, implying that the nucleon consists of point-like particles with spin 1/2. A measurement of $\frac{2xF_2}{F_1}$ is shown in figure 2.4. This is the reason that one often refers to F_2 as the structure function of the nucleon. The world data on F_2 measurement is shown in figure 2.5 and 2.6 versus Q^2 and x-Bjorken, respectively.

2.1.4 Quark-parton model and perturbative QCD

As can be seen in figure 2.5, F_2 is basically independent of Q^2 for intermediate x-Bjorken. For low and high x a Q^2 dependence can be observed. This is called *scaling violation*. When Q^2 (the resolution of the probe) increases, a finer structure of the nucleon can be observed, as illustrated in figure 2.7. Measurements also showed that the individual quarks contribute only about half of the nucleon's momentum. This means that the other half has to be carried by the gluons [7], the particles that mediate the strong interaction.

In the framework of quantum chromodynamics (QCD) scaling violation is explained by the existence of the quantum field gauge bosons of the strong force, the gluons. Unlike the gauge bosons for the electromagnetic interactions, gluons carry the charge of the field they mediate, color, and can therefore interact with each other as well as with quarks. The strong coupling constant α_s is given by (in first order QCD):

$$\alpha_s(\mu^2) = \frac{12\pi}{(33 - 2N_f)\ln\left(\mu^2/\Lambda^2\right)}, \tag{2.23}$$

with μ the renormalization scale, that imposes a cut on the time scale in which virtual fluctuations are taken into account. In DIS this is set to Q. The number of quark flavors is N_f. Usually only the quark flavors with a mass smaller than μ are taken into account. The scale where perturbative QCD can be applied is Λ (≈ 200 MeV). The application of the perturbative expansion procedure in QCD is only valid if $\alpha_s \ll 1$. It is satisfied when $\mu^2 \gg \Lambda^2 \approx 0.04$ GeV^2. The world data of α_s measurements can be seen in figure 2.8. For μ (Q^2) $\rightarrow \infty$ the coupling constant becomes zero and the quarks behave as free unbound states. This is called *asymptotic freedom* and this regime is described in the quark-parton model in section 2.1.3. For a decreasing μ, the strong coupling increases and gives rise to *confinement*. This explains why quarks are strongly bound together in colorneutral objects at "low" energy.

The evolution of the parton density functions in QCD are described by the Dokshitzer-Gribov-Lipatov-Altarelli-Parisi (DGLAP) equations [9]-[12]:

$$\frac{\partial q_f(x,Q^2)}{\partial \ln Q^2} = \frac{\alpha_s(Q^2)}{2\pi}\int_x^1 \frac{dx'}{x'}\left[q_f(x',Q^2)\cdot \mathcal{P}_{qq}\left(\frac{x}{x'}\right) + g(x',Q^2)\cdot \mathcal{P}_{qg}\left(\frac{x}{x'}\right)\right] \tag{2.24}$$

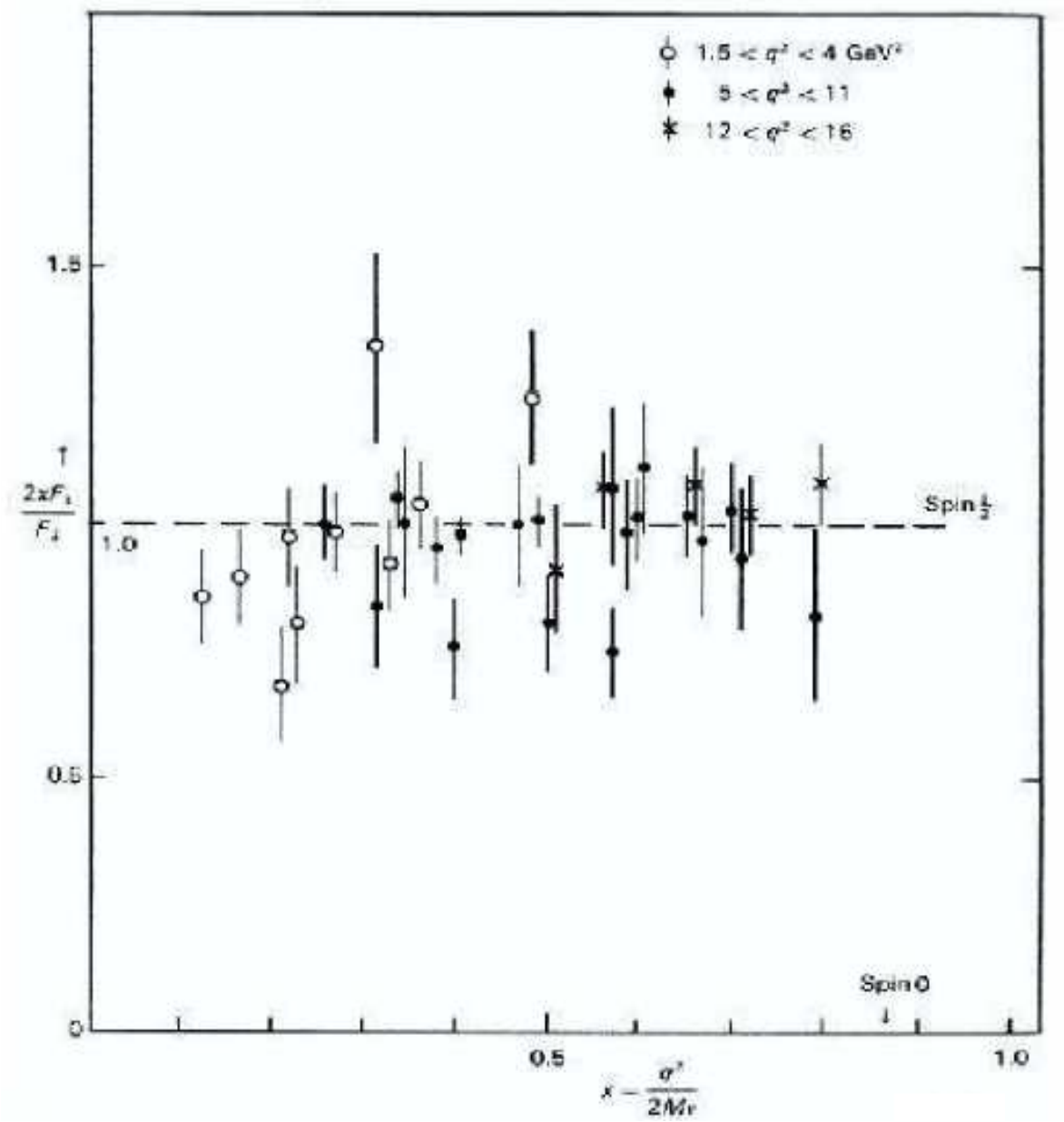

Figure 2.4: SLAC measurement of the Callan-Gross relation: $\frac{2xF_2}{F_1}$ is plotted versus $x = \frac{Q^2}{2M\nu}$. This plot was taken from [4].

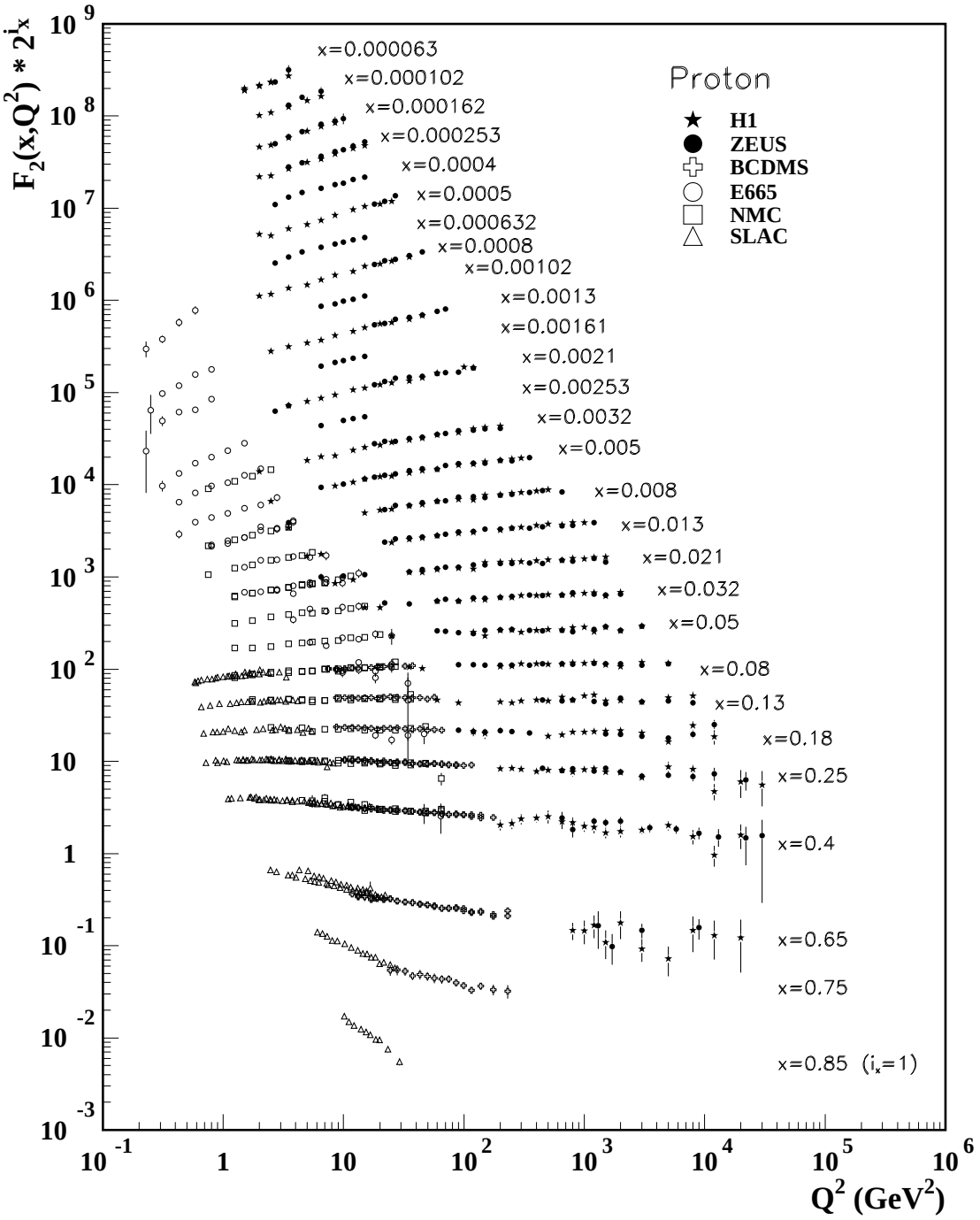

Figure 2.5: World data on the structure function F_2 of the proton versus Q^2 for various x-Bjorken. This plot was taken from [5].

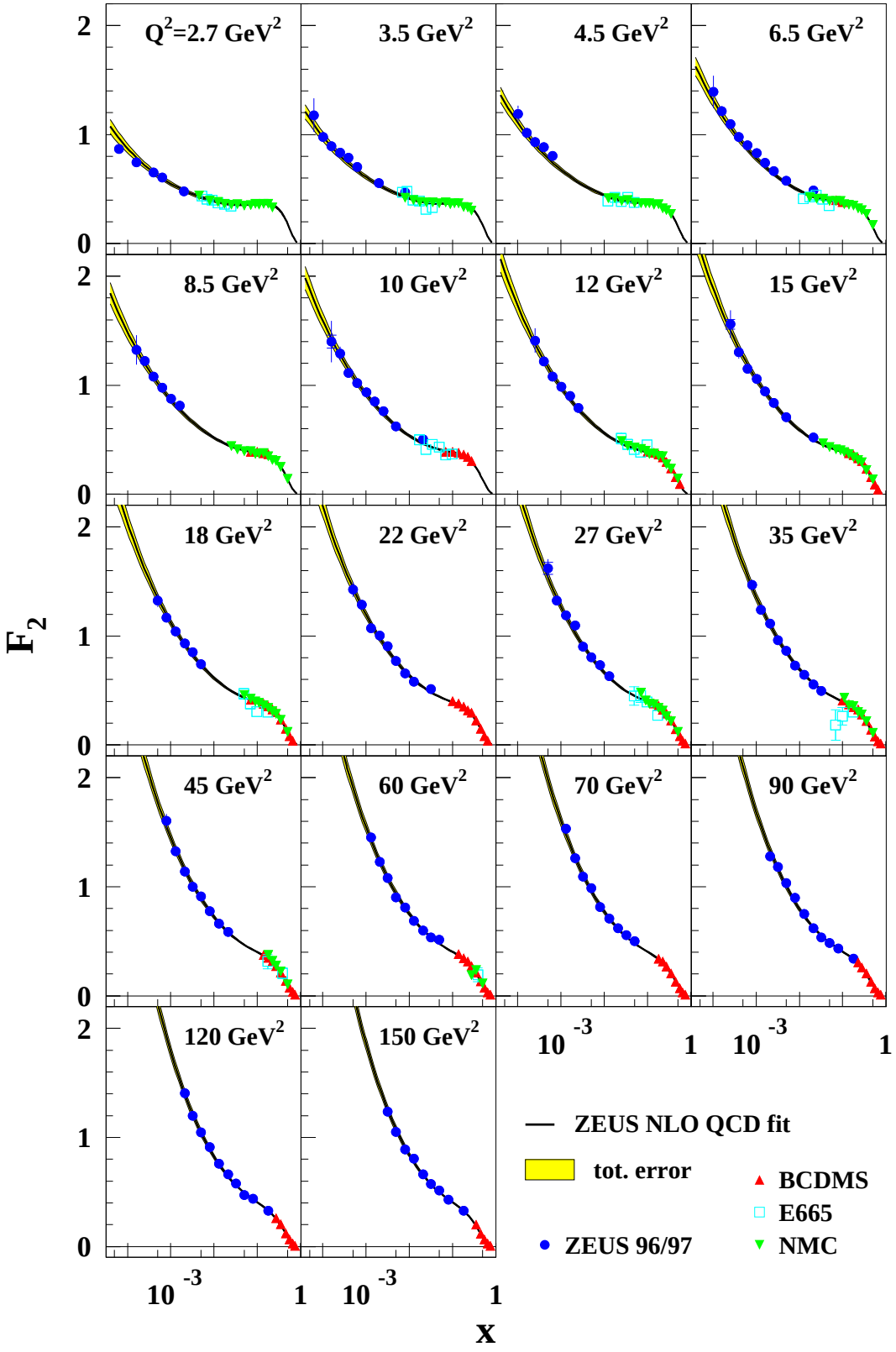

Figure 2.6: World data on the structure function F_2 of the proton versus x-Bjorken for various Q^2. This plot was taken from [6].

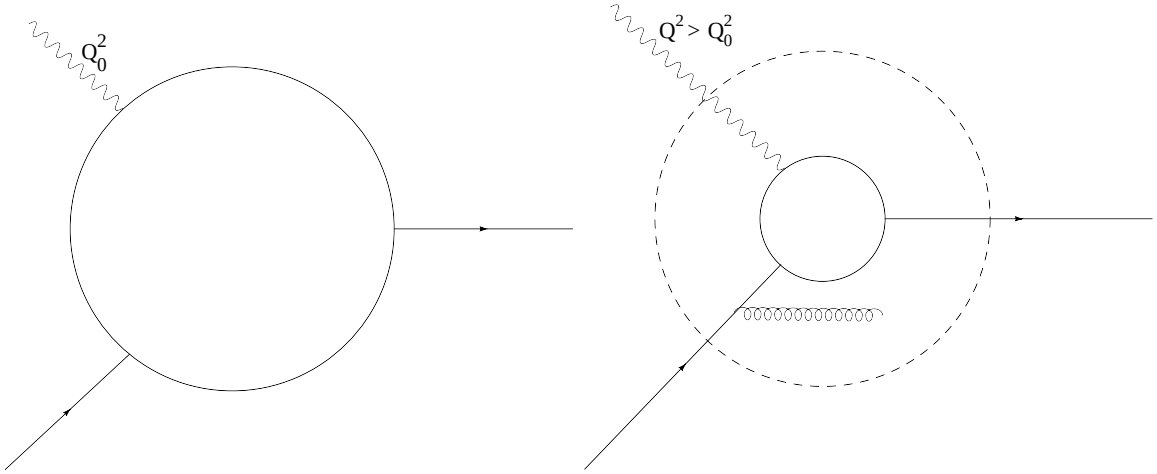

Figure 2.7: Illustration of scaling violation. At low resolution of the probe ($Q = Q_0$) a parton radiating another parton is seen as a unit and there total x-Bjorken is measured. When the resolution increases the two partons can be seen separately and one measures the x-Bjorken of one of them.

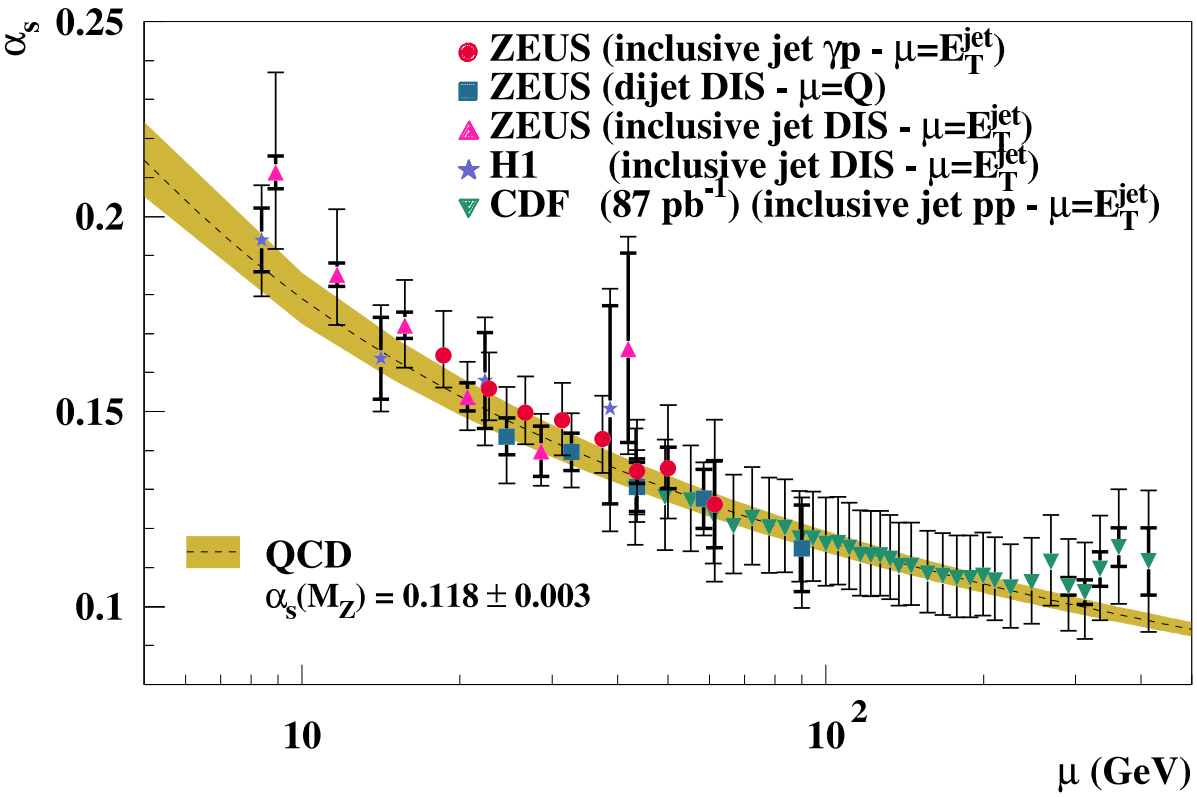

Figure 2.8: Experimental measurement of the running strong-coupling constant α_s versus μ measured at ZEUS, CDF, and H1 [8].

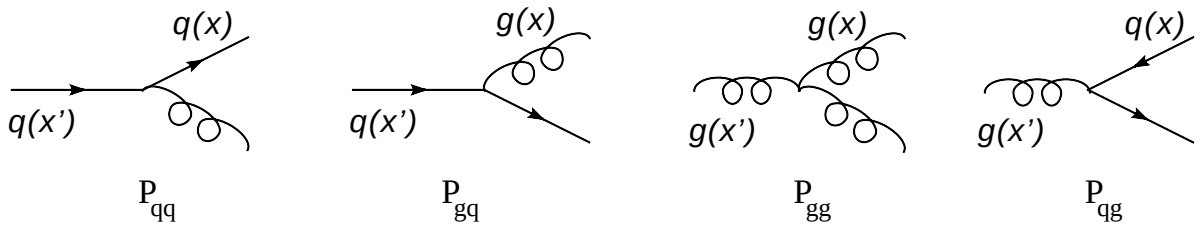

Figure 2.9: The four splitting functions.

$$\frac{\partial g(x,Q^2)}{\partial \ln Q^2} = \frac{\alpha_s(Q^2)}{2\pi} \int_x^1 \frac{dx'}{x'} \left[g(x',Q^2) \cdot \mathcal{P}_{gg}\left(\frac{x}{x'}\right) + \sum_f q_f(x',Q^2) \cdot \mathcal{P}_{qg}\left(\frac{x}{x'}\right) \right]. \quad (2.25)$$

The splitting functions $\mathcal{P}_{ij}\left(\frac{x}{x'}\right)$ give the probability that a parton i with momentum fraction x was radiated from a parton j with momentum fraction x'. Alternatively, they can be interpreted as the probability to find a parton i inside a parton j with a momentum fraction $\frac{x}{x'}$. The splitting functions are illustrated in figure 2.9. The DGLAP equations predict the evolution of the parton distribution functions with Q^2 (that can be used to calculate $F_2(x,Q^2)$ showed in figures 2.5 and 2.6).

2.1.5 Hadronization

In DIS hadrons are formed; the virtual photon kicks a quark out of the nucleon. However, as mentioned before, quarks are confined and they form color neutral states (called hadrons). This process is called hadronization or fragmentation. It is very fascinating because it cannot be calculated in perturbative QCD, as α_s is too large at the time hadronization takes place. As of today, this process, forming hadrons out of quarks, is not completely understood. In the DIS cross section calculated in section 2.1.2 one integrates over all final-states. However, in the SIDIS cross section one can no longer do this, thus the calculation is further complicated. Figure 2.10 illustrates the different steps between the interaction and the final-state (decay) hadrons in SIDIS. The leptonic part of the interaction can be described using QED (emission of a virtual γ^* and radiative effects). Then the hard scattering on a parton and the evolution of the struck parton can be described using perturbative QCD, until a certain energy is reached where the strong coupling constant becomes too large and perturbative QCD no longer converges. In this regime hadronization happens and final-state hadrons are formed. If these hadrons are unstable they will decay.

Factorization theory

In factorization theory one calculates the SIDIS cross section by assuming that hadronization effects and quark distribution functions factorize. Hadronization is described by introducing fragmentation functions $D_f^h(z)$ that are interpreted as the probability density that a struck quark with flavor f and a $z \in [z, z+dz]$ hadronizes in a hadron of type h. Factorization means that the quark distribution functions and the fragmentation function are functionally

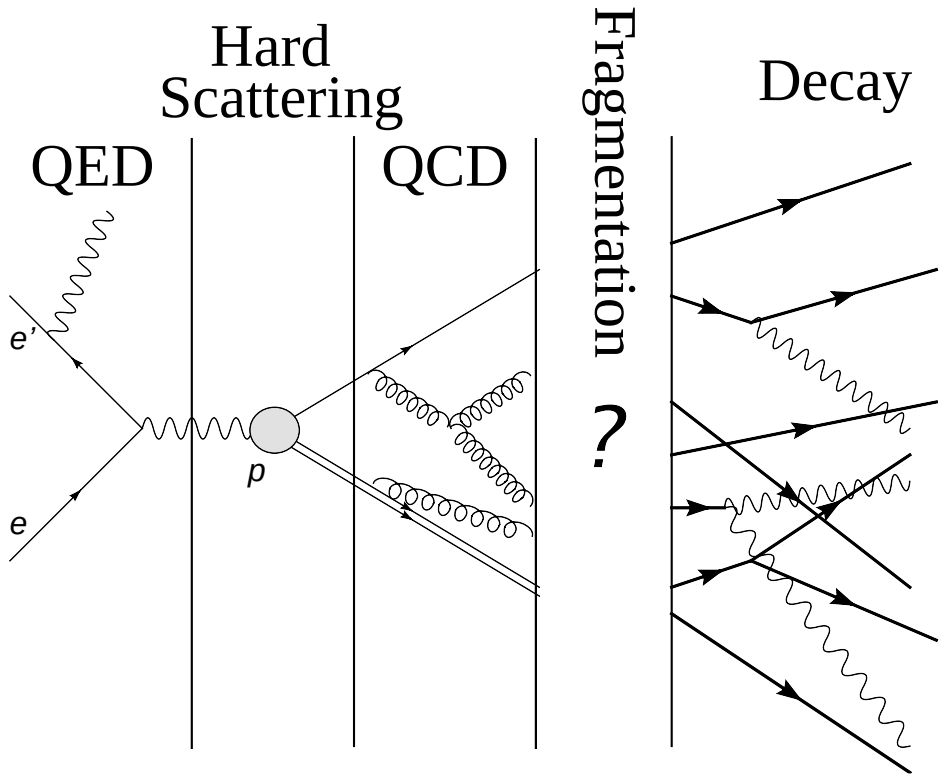

Figure 2.10: Illustration of the different steps between interaction and the final-state (decay) hadrons in SIDIS. Picture taken from [13].

independent. Scaling violation causes the fragmentation functions to become Q^2 dependent, i.e., it can happen that a parton of type f emits a parton of type j that then hadronizes in hadron type h (analogous to the splitting functions in section 2.1.4). There exist DGLAP evolution equations for the fragmentation functions. The obtained cross section for hadron (h) production integrated over the transverse momentum of the hadron is given by:

$$\frac{d^3\sigma^h}{dxdQ^2dz} = \frac{\sum_f e_f^2 q_f(x,Q^2)\cdot D_f^h(z,Q^2)}{\sum_f e_f^2 q_f(x,Q^2)} \cdot \frac{d^2\sigma_{\mathrm{DIS}}}{dxdQ^2}. \tag{2.26}$$

Factorization was proven at leading twist and all orders of α_s [14] but is not proven at higher twist.

2.1.6 Studying hadronization at HERMES

Studying hadronization in the HERMES kinematics is very interesting because at HERMES hadronization happens on the edge of the regime where perturbative QCD holds. There are several ways to study hadronization; one of them is looking at hadron multiplicities ($\frac{\#hadrons}{\#\mathrm{DIS}}$) that are very sensitive to the fragmentation functions. This was done at HERMES in [13] and [15].

Another way of studying hadronization is to introduce a nuclear target instead of a nucleon one to perturb the hadronization process. This works extremely well in the HERMES kinematics because the size (5-10 fm) of the nuclear targets is of the same order as the *yo-yo length* (l_y, the length the struck quark needs to form the final-state hadron) of the hadrons that in most models ranges in the order of 1 to 10 fm. Using lepton scattering makes the process "clean", i.e., there cannot be any initial-state interactions (ISI) as the lepton does not have a substructure. In contrast with, for example, proton-proton scattering, quarks can interact with each other before the scattering takes place. Studying hadronization at HERMES using nuclear SIDIS also provides precious information for the interpretation of relativistic heavy ion collisions ([16] and [17], in the latter a translation is made between SIDIS kinematic variables and the variables used in heavy ion collisions).

2.1.7 Nuclear effects in SIDIS

To study nuclear effects one usually compares measurements done on a D target with measurements performed on a nuclear target. D is used because it contains a proton and a neutron and so minimizes the effects that would be caused by the different structure function F_2 of the proton and the neutron. Several effects are observed, some of them are listed below.

The EMC effect

The EMC (European Muon Collaboration) effect, named for the collaboration that first observed it, is the effect that the nuclear DIS structure function is not equal to the D one [18]. This means that the structure function of a nucleon inside a nucleus is different then the one from the "bare" nucleon. A plot combining different data sets on the EMC effect is shown in figure 2.11.

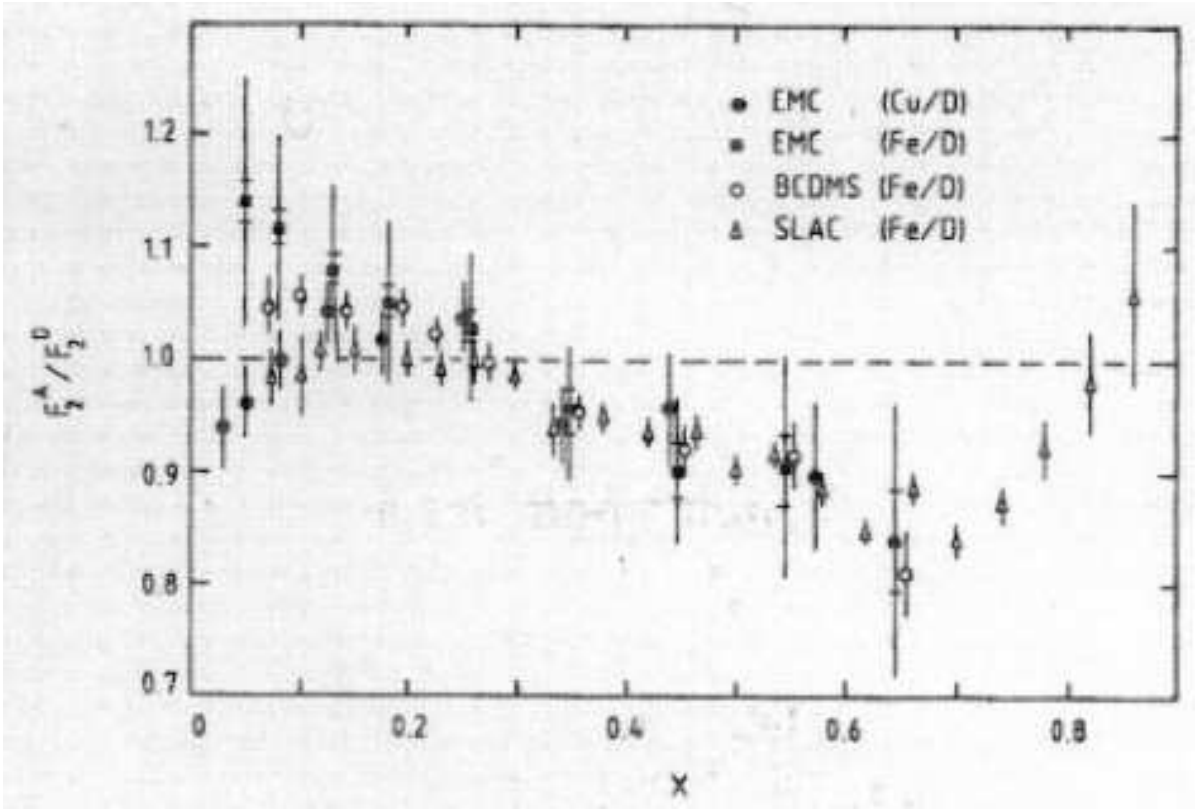

Figure 2.11: The EMC effect. EMC, SLAC, and BCDMS data is shown versus x, averaged over Q^2.

Nuclear attenuation

Nuclear attenuation is the reduction of the number of produced hadrons per DIS event on nuclear targets compared to the number produced on D. The observable used to study this is called the multiplicity ratio:

$$R^h(z,\nu,Q^2,p_t^2,\phi_h) = \frac{\left[\frac{N_h(z,\nu,Q^2,p_t^2,\phi_h)}{N_{\mathrm{DIS}}(\nu,Q^2)}\right]_{\mathrm{A}}}{\left[\frac{N_h(z,\nu,Q^2,p_t^2,\phi_h)}{N_{\mathrm{DIS}}(\nu,Q^2)}\right]_{\mathrm{D}}}, \tag{2.27}$$

with N_h the yield of semi-inclusive hadrons in a certain (z,ν,Q^2,p_t^2,ϕ_h)-bin and N_{DIS} the yield of inclusive deep-inelastic scattering events in the same (ν,Q^2)-bin. Some results of the nuclear attenuation at HERMES (integrated over p_t) can be seen in figure 2.12 [19]. A clear deviation from 1 is observed, which means that there is an effect. An increase of the multiplicity ratio is observed as a function of ν. This might be due to the Lorentz-boost that increases the probability that the hadron is formed outside the nucleus. The multiplicity ratio decreases as z increases. When z becomes larger and reaches 1 the produced hadron caries a large energy fraction and could not have undergone interactions. The probability for that is small which might explain the z behavior. The multiplicity ratio is constant versus Q^2 in the HERMES kinematics. A dependence of the attenuation on the atomic number and on the hadron type is also observed.

p_t-broadening

The effect analyzed in this work is called p_t-broadening. It is defined as:

$$\Delta\langle p_t^2\rangle_{\mathrm{A}}^h = \langle p_t^2\rangle_{\mathrm{A}}^h - \langle p_t^2\rangle_{\mathrm{D}}^h, \tag{2.28}$$

p_t-broadening of hadrons of type h produced on a nuclear target with atomic mass number A is the difference between the average transverse momentum (squared) of hadrons of type h produced on a nuclear target (A) and the ones produced on D. The p_t-broadening can be an absolute measurement of the production time (t_p) of the pre-hadron (also called a virtual hadron or off-shell hadron). The concept of production and formation time is illustrated in figure 2.13. First a quark is struck by the virtual photon. It takes a time/length called the *production time/length* t_p/l_p to produce a colorless state called a pre-hadron. In this stage one speaks of partonic effects. The struck quark loses energy by e.g., gluon radiation. The pre-hadron can be seen as a quark-dipole that is not yet a final-state hadron. It has therefore different elastic and inelastic cross sections as those of final-state hadrons. The time/length needed to form this final-state hadron out of the pre-hadron is called the formation time/length t_f/l_f. Note that these times/lengths are not to be confused with the *constituent formation length* l_c, defined in string models as the length between the interaction and the formation point of the first constituent quark of the final hadron h. Some models also define l_y (also referred to as l_f, as in [34]), the yo-yo length that is the length between the interaction point and the point where the final-state hadron is formed. The lengths l_c and l_y are illustrated in figure 2.14, l_y is equal to $l_p + l_f$. After the (pre-)hadron is formed one speaks of hadronic effects where the (pre-)hadron undergoes interactions with the medium if present. Models that try to describe nuclear effects on hadronization take only partonic or hadronic effects into account or a combination of both.

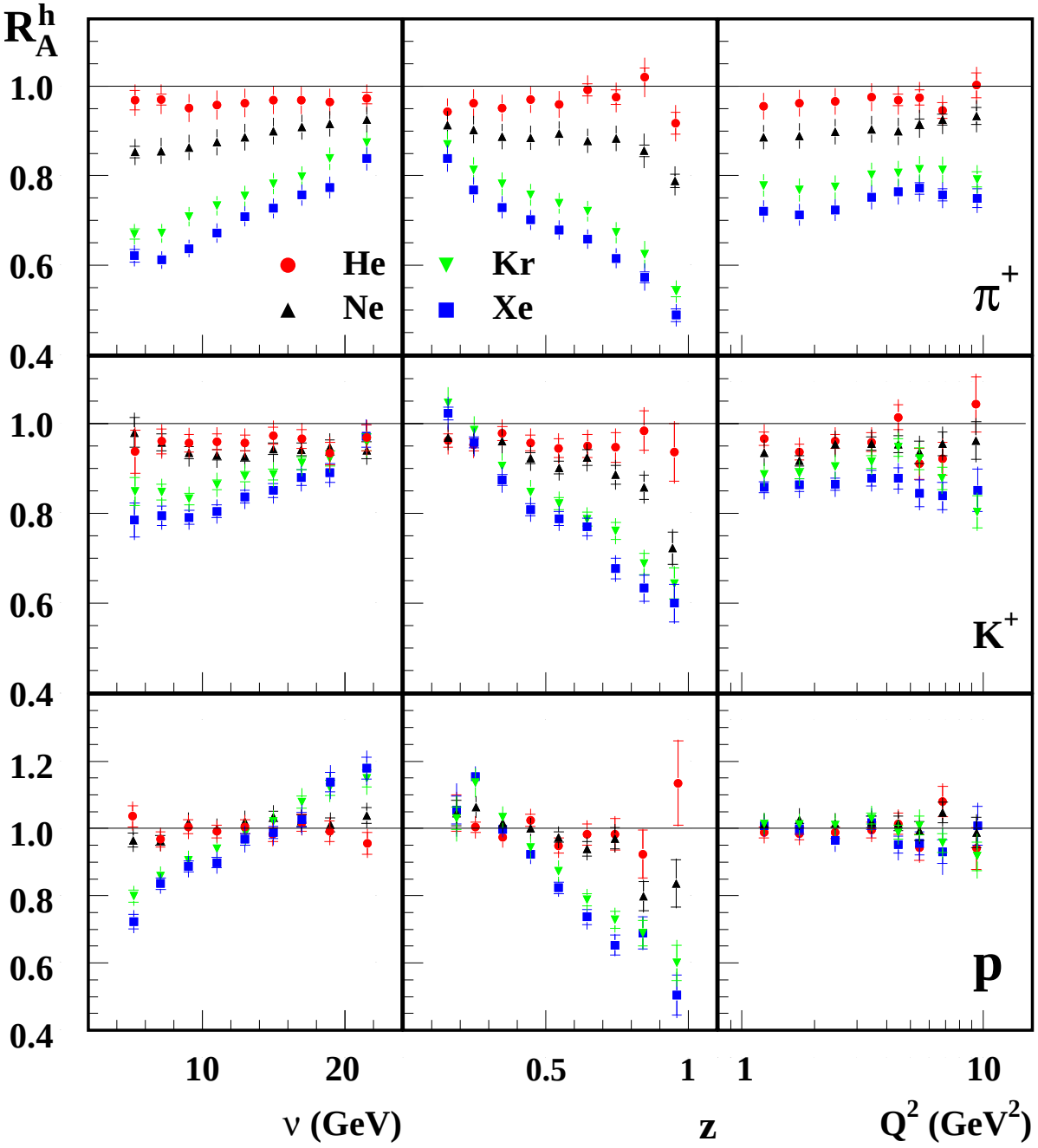

Figure 2.12: Nuclear attenuation for different nuclei versus ν, z, and Q^2 for positive charged pions, koans, and protons. A clear deviation from 1 can be seen [19].

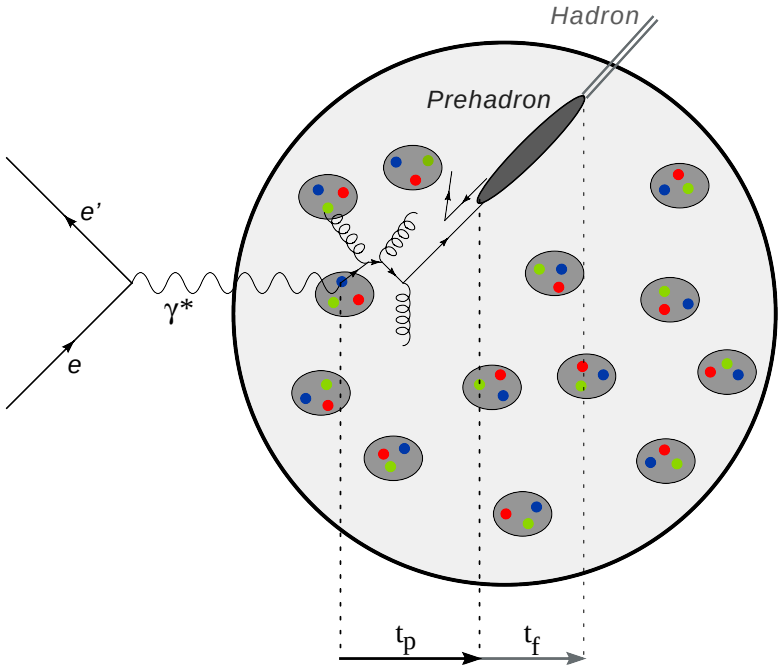

Figure 2.13: Illustration of the production (t_p) and formation time (t_f). The colored dots (red, yellow, and blue) represent quarks. The large circle is a nucleus and the small circles (containing quarks) represent nucleons. The struck quark forms a pre-hadron (gray ellipse) after the production time. Then it takes time t_f to form the final state hadron.

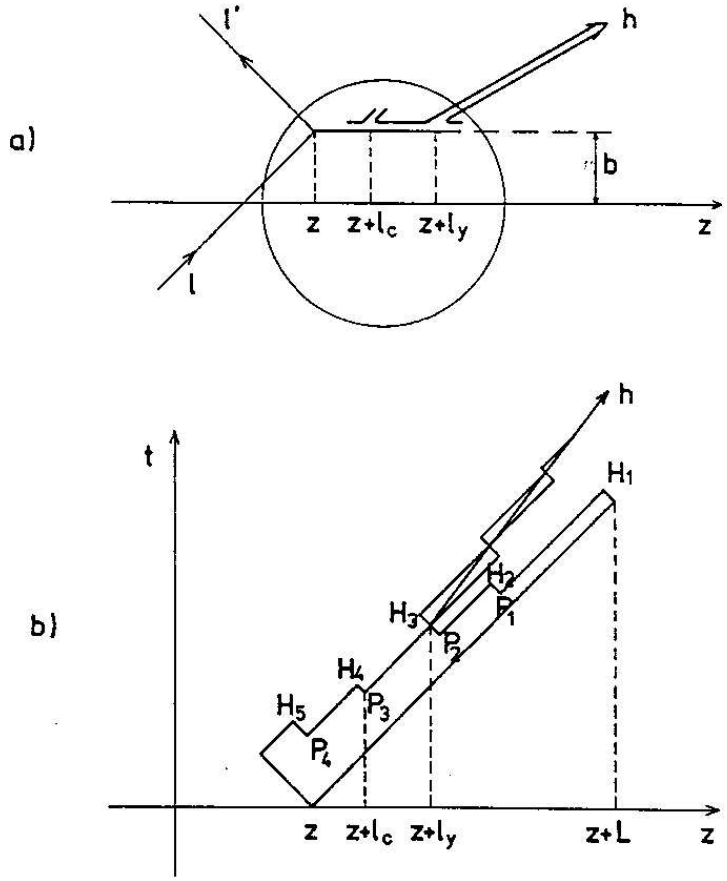

Figure 2.14: Illustration of the constituent (l_c) and yo-yo length (l_y). The DIS interaction takes place at z. At point $z + l_c$ the first constituent quark of final hadron h is formed, at point $z + l_y$ the final "yo-yo"-hadron is formed. Part (b) is the same as (a) but a time axis is added.

2.1.8 Hadronization in nuclear environment: models

Today there are a lot of models available that attempt to describe hadronization in nuclear environment. Traditionally, hadronization in the nuclear environment is described in the framework of phenomenological string models [20]-[23] and final-state interactions of the produced hadrons with the surrounding medium [24]. Alternatively, in-medium modifications of the quark fragmentation functions have been proposed. Fragmentation functions are expressed in terms of nuclear rescaling in [25] and [26]. In [27] only parton energy loss is considered and in [29] parton energy loss is calculated as higher-twist (twist-4) contributions to the fragmentation functions. In [30] a gluon-bremsstrahlung model for leading hadron attenuation is used. The models of references [26] and [30] also incorporate hadronic final-state interactions. These QCD-inspired models provide a theoretical description of the hadronization process in deep-inelastic scattering and are linked to heavy-ion collisions in [16], [17], and [29], and Drell-Yann reactions on nuclear targets [27], [31]. In the following subsections some models are discussed in more detail.

Models based on the string model

The DIS interaction takes place in one of the nucleons in the nucleus at a point described by a certain longitudinal coordinate and an impact vector. Between the knocked out (anti-)quark and the nucleon remnant a color string is stretched. Confinement between quarks gives rise to a (confining) potential; assumed to be

$$V(r) = \kappa r, \tag{2.29}$$

with κ the string tension, usually taken as 1 GeV/fm, and r the distance between the quarks. The maximal length of a string is

$$L_{\max} \approx \frac{2m_q}{\kappa}, \tag{2.30}$$

with m_q the mass of the quark. At this length string breaking, illustrated in figure 2.15, takes place by means of quark-antiquark pair production in the color field. In reality it is expected that string breaking takes place earlier due to spontaneous quark/anti-quark production out of the vacuum (called the Schwinger phenomenon) that breaks the string into shorter pieces. Two lengths are often used in string models: the constituent length (l_c) and the yo-yo-length (l_y), these lengths were defined in section 2.1.7. A string model that is often used is the LUND string model [32]. Some models add extensions, e.g., taking into account the flavor content of particles, to the string model.

In one model [24] the PYTHIA Monte Carlo (cf. section 5.2) is used in order to describe the lepton-nucleon interaction and the FRITIOF Monte Carlo [33] to model the hadronic interactions. Then the Boltzmann-Uehling-Uhlenbeck (BUU) transport model Monte Carlo described in [34] is used to transport the (pre-)hadron through the nucleus. In this way the so-called final-state interactions (FSI) are described. This model is able to give a good description of the HERMES nuclear attenuation data if the production length is set to zero, l_y is set to 0.5 fm, and the pre-hadron interaction cross section ($\sigma_{pre-hadron}$) is set to 1/3 of the hadron interaction cross section (σ_h) as shown in figure 2.16.

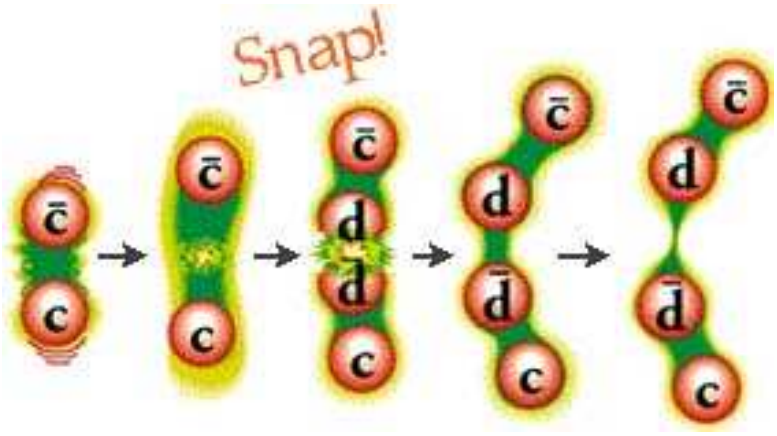

Figure 2.15: Illustration of string breaking. Picture taken from [43]

Rescaling of fragmentation functions in nuclei

The argument for modified fragmentation functions for in-medium hadronization is based on the EMC-effect. If parton distribution functions are affected by the nuclear environment it seems natural to expect changes in the way partons produce hadrons when the fragmentation takes place inside nuclear matter.

One way of modifying the fragmentation functions is based on the so-called deconfinement models. These models are based on the hypothesis that hadrons in nuclei are larger than in vacuum. This hypothesis was needed to obtain a good description of nuclear structure functions in [35]-[37]. Larger hadrons in nuclei point towards a weaker confinement force or a smaller string tension. As a consequence, hadronization in nuclei compared to hadronization in nucleons starts earlier and fragmentation functions are more evolved. This is called rescaling and a rescaling factor $\xi_A(Q^2)$ is calculated. The nuclear fragmentation function can then be written as:

$$D_f^{h|A}(z, Q^2) = D_f^h(z, \xi_A(Q^2)Q^2). \tag{2.31}$$

In [26], rescaling, together with 2 models that describe nuclear absorption ([38] and [39]), were applied in order to describe nuclear attenuation. In practice a nuclear absorption factor $\mathcal{N}_A(\nu, z)$ is calculated, which is the probability that neither the quark, the pre-hadron, nor the hadron interacted with a nucleon from the target. Results are shown in figure 2.17. In this figure it can be seen that in order to describe the HERMES nuclear attenuation data with rescaling, nuclear absorption is needed in addition.

Parton energy loss

In parton energy loss only the energy loss of the struck quark in the nuclear medium is considered to explain nuclear effects like attenuation. The energy loss is a combination of multiple scattering and medium-induced gluon radiation. In [27] the induced gluon spectrum radiated by a high energy quark propagating through a medium of length L is characterized by the energy scale, $\omega_c = \frac{1}{2}\hat{q}L^2$, with $\hat{q}$ the so-called transport coefficient that is proportional to the number of scattering centers in the medium. Analysis of the Drell-Yan (illustrated in figure

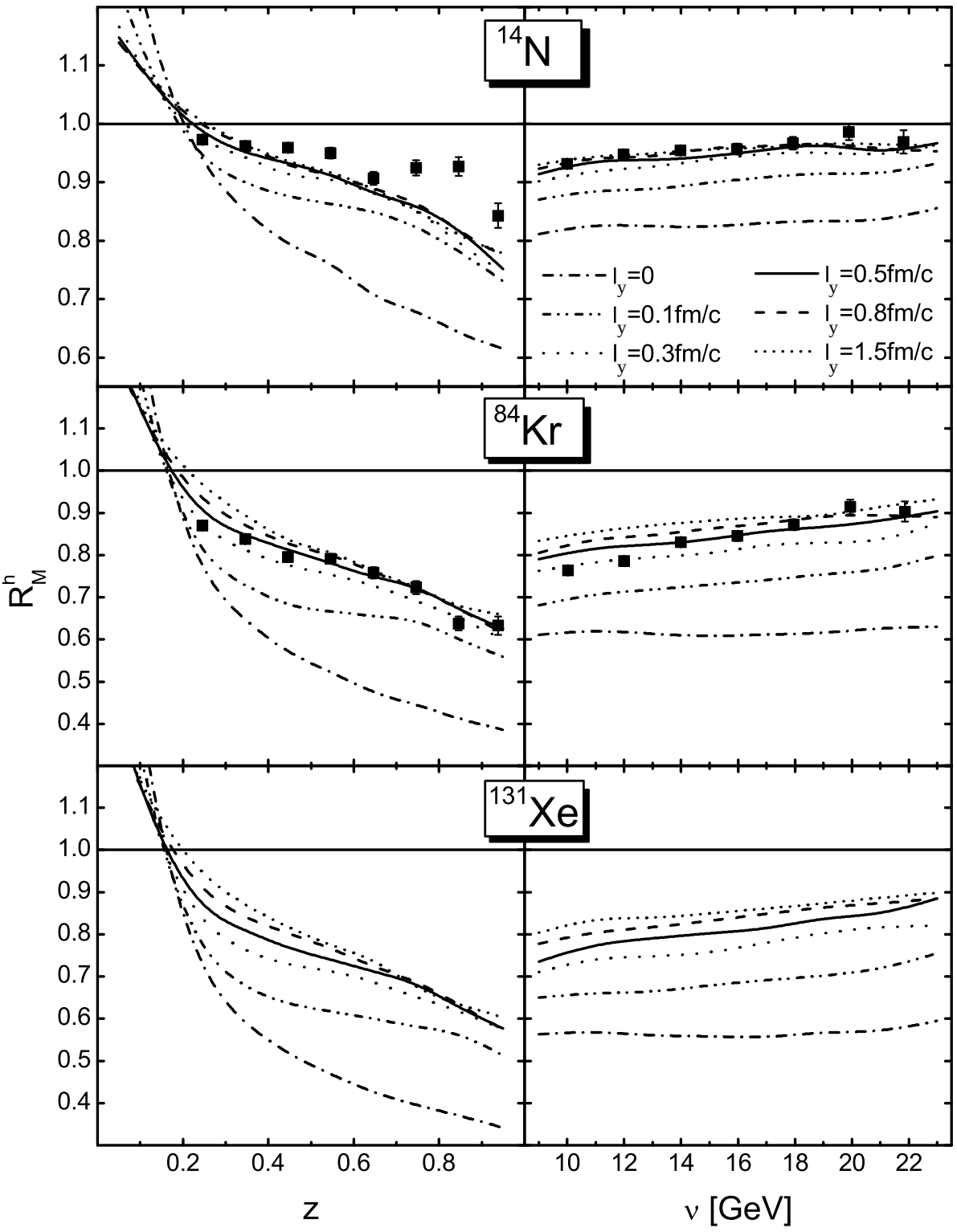

Figure 2.16: Calculated multiplicity ratios of charged hadrons for N, Kr, and Xe targets for different values of the yo-yo length $l_y = 0 - 1.5$ fm, using the PYTHIA Monte Carlo together with the FRITIOF one, and the BUU transport model described in [34]. The pre-hadron cross-section is set to $\frac{\sigma_h}{3}$. These calculations are compared with HERMES data (squares). In [34] no HERMES data with Xe target is shown.

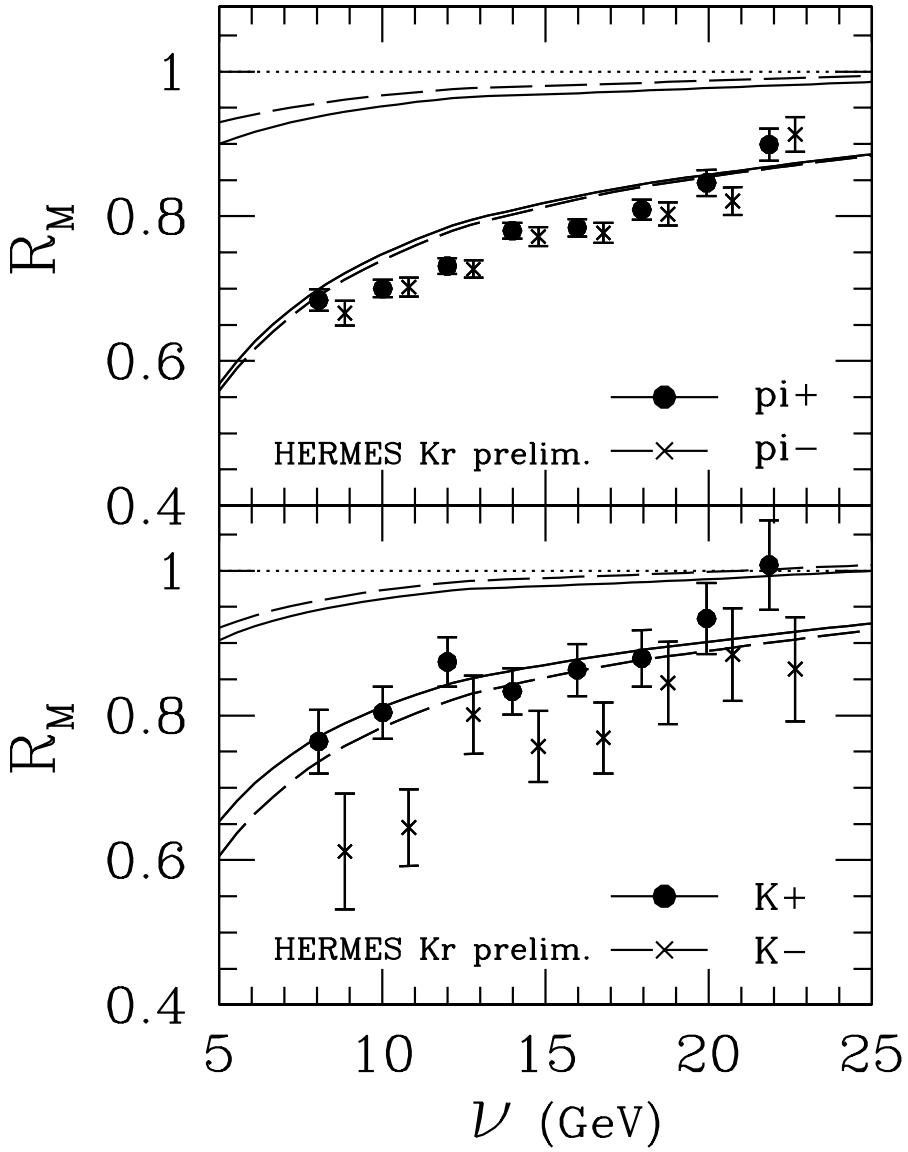

Figure 2.17: Charge and flavor separated theoretical multiplicity ratios $R_M(\nu)$ calculated in the rescaling model (cf. [26]), compared with preliminary HERMES data on Kr. The data of negative charged hadrons was slightly shifted to the right to improve readability. The upper pair of curves includes rescaling without absorption for positive and negative charged particles, and the lower pair rescaling plus absorption for positive and negative charged particles. Plot taken from [26].

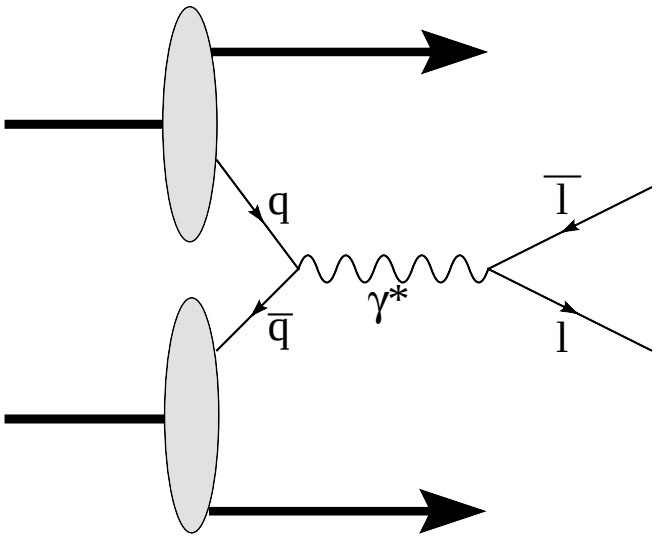

Figure 2.18: Diagram of the Drell-Yan process. The gray blobs represent objects containing quarks and $l\bar{l}$ is a lepton pair.

2.18) process is used to obtain this coefficient [28]. In this process a quark anti-quark annihilates in a virtual photon that decays in a lepton anti-lepton pair. The Drell-Yan mechanism is a process particularly suited for the study of quark energy loss in nuclei as the lepton pair does not strongly interact with the surrounding medium but the incoming quarks do. This coefficient is used to calculate the nuclear dependence of fragmentation functions in order to predict HERMES nuclear attenuation data. The result is shown in figure 2.19. A reasonable description of the data can be observed although for identified hadrons the calculation overshoots the data.

In [29] the effect of multiple scattering of a quark and the induced parton energy loss in a nuclear medium is expressed in terms of modified quark fragmentation functions. These modified quark fragmentation functions and their QCD evolution in DIS are derived using the generalized factorization of higher twist (twist-4) parton distributions.

Gluon-bremsstrahlung model

In this model only leading hadrons are considered. These hadrons most likely contain the quark that was struck by the virtual photon and have a $z \gtrsim 0.5$. More details about this model are provided, using references [30] and [40].

In this model the space-time evolution of hadronization that ends with the formation of the leading hadron happens in two steps, as illustrated in figure 2.13. After the quark is hit by the virtual photon it experiences multiple interactions that broaden its transverse momentum and extra energy loss is induced. After time t_p or length l_p it picks up an anti-quark and its color is neutralized. The produced color-dipole (also called pre-hadron or virtual hadron) is attenuated in the medium and develops a hadron wave function after a time t_f or a length l_f.

At times before t_p the struck quark loses energy by radiation of gluons and by interacting with the medium. The energy loss can be written as the sum of vacuum energy loss and

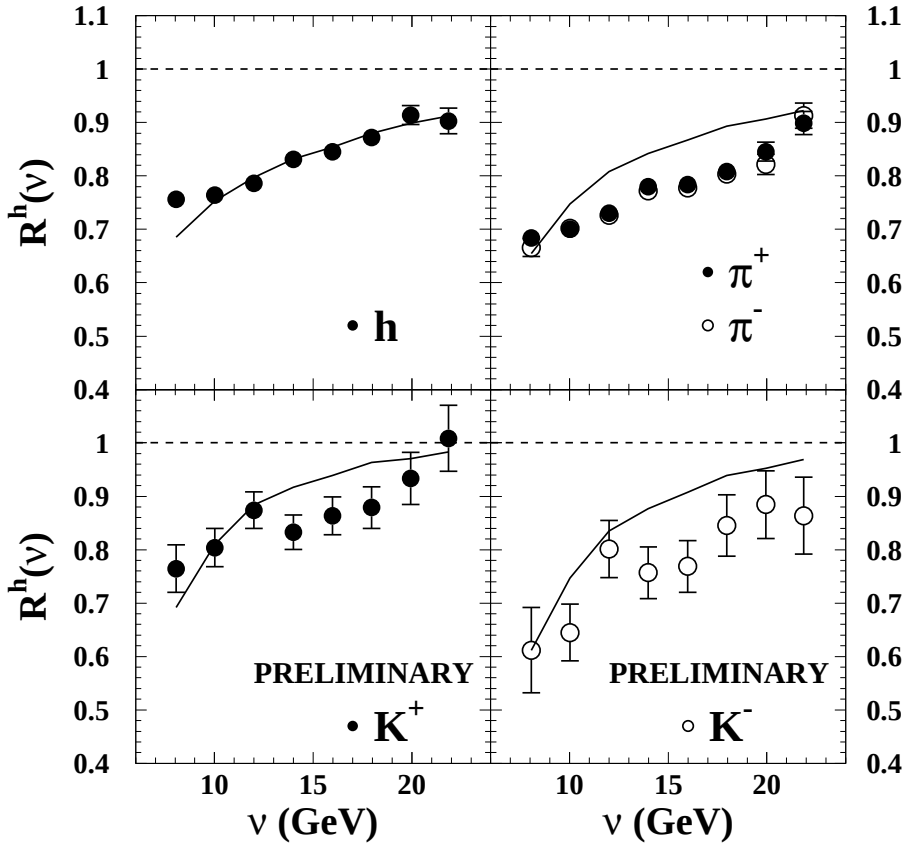

Figure 2.19: Multiplicity ratio for various hadron types produced on a Kr target calculated using parton energy loss in [27] and compared with preliminary HERMES data.

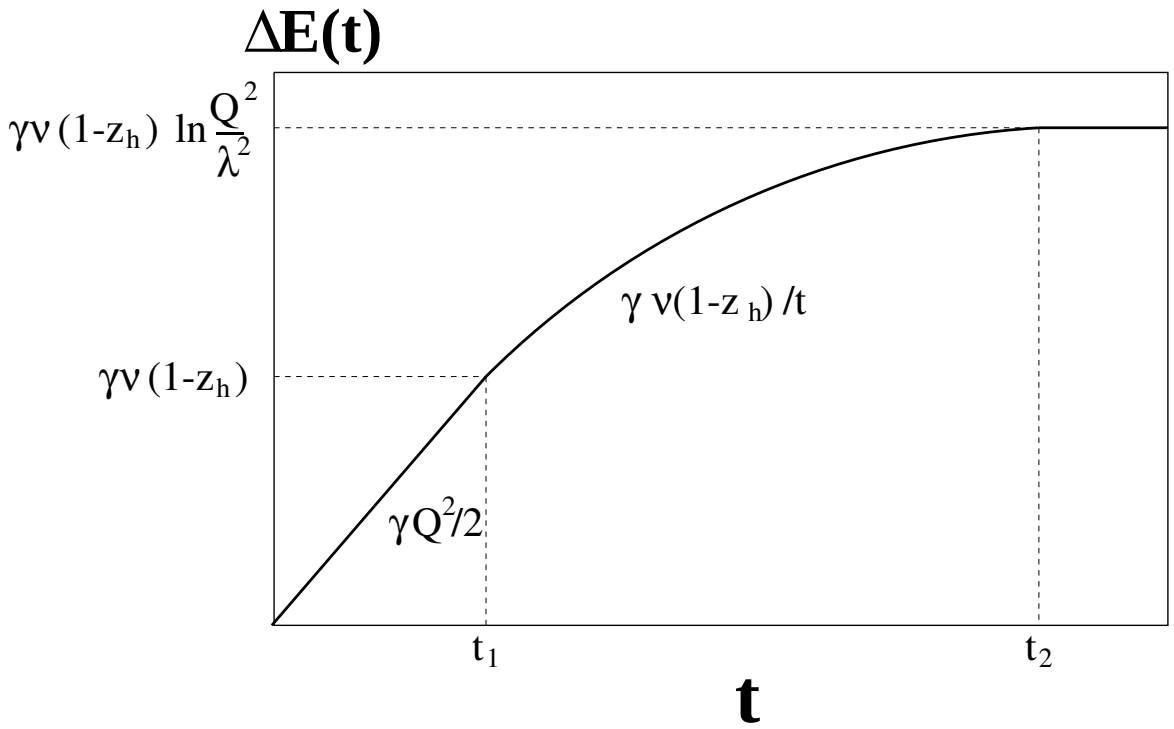

Figure 2.20: Time dependent vacuum energy loss $\Delta E_{vac}(t)$ during production of the leading pre-hadron (containing the leading quark). Figure was taken from [30].

medium-induced energy loss:

$$\Delta E(t) = \Delta E_{vac}(t) + \Delta E_{ind}(t). \tag{2.32}$$

The vacuum energy loss versus time for a leading hadron (containing the struck quark), assuming that $Q^2 \gg \Lambda$, is calculated in [30] and shown in figure 2.20. In the picture $\gamma = \frac{1}{\sqrt{1-\frac{v^2}{c^2}}}$, $\lambda = \Lambda$, $z_h = z$, $t_1 = \frac{1-z}{xM_{\text{nucleon}}}$, and $t_2 = \frac{Q^2}{\Lambda^2}t_1$. In the time interval $t < t_1$ the rate of energy loss is constant:

$$-\frac{dE}{dt} = \frac{\gamma Q^2}{2}, \tag{2.33}$$

with no restriction on the radiated energy. At larger times more energetic gluons can be radiated because it takes time, called the coherence time (t_c), to radiate a gluon with energy αE that becomes incoherent with the source [41]:

$$t_c \approx \frac{2E\alpha(1-\alpha)}{k_T^2}, \tag{2.34}$$

with E the energy of the quark before it radiates, α the energy fraction taken away by the radiated gluon, and k_T the transverse momentum of the radiated gluon. This transverse momentum has to be larger than a cut-off, set to Λ [30], for integrals in the calculation to converge. At this point the restriction $\alpha < 1 - z$ is effective because a leading hadron with a high z is detected. This results in an energy loss that has a $\frac{1}{t}$-dependence and becomes constant for $t > t_2$. This effect is called Sudakov suppression.

In the case of hadronization in a nuclear medium there is an additional source of energy loss caused by the interaction of the struck quark with the medium. Due to multiple collisions the parton increases its transverse momentum (squared) linearly with the path length because it undergoes a Brownian motion in the transverse momentum plane. This induced energy loss is calculated in [42]:

$$\Delta E_{ind}(L) = \frac{3}{8}\alpha_s \Delta\langle p_t^2\rangle L, \tag{2.35}$$

with L the distance that the quark travels through the nuclear medium. The induced energy loss is small compared to the vacuum energy loss. However, this effect has to be taken into account to describe the HERMES nuclear attenuation data better as can be seen in figure 2.21.

In [30] the production time distribution function ($W(t_p, z, Q^2, \nu)$) of a leading pre-meson is calculated. This function is shown in figure 2.22 versus production time t_p for different z ($0.5 < z < 0.9$). It can be seen that at high z the production time goes to zero. This is expected because of energy conservation. If a hadron with z close to 1 is detected, it means that the pre-hadron had to be formed immediately, because otherwise it would have had time to lose energy by radiating gluons or interactions with the medium that would cause z to go down. There is a relation between the fragmentation function of the struck quark and the leading hadron (the ν-dependence is considered weak):

$$\tilde{D}_q^h(z, Q^2) = \int_0^\infty dt_p \, W(t_p, z, Q^2). \tag{2.36}$$

At time t_p, color-neutralization takes place and a pre-hadron is formed. The pre-hadron is a colorless $q\overline{q}$ dipole. The pre-hadron attenuates on its way out of the nucleus with an absorptive cross section that is controlled by the varying dipole size. This process is calculated using a light-cone Green function approach [30]. The formation time t_f is similar to $\frac{E_h}{\Lambda}$. This is due to time dilation and the formation time reaches a maximum for high z. For leading hadron production one has to suppress inelastic (color-exchange) interactions at this point because they would cause a small z ($z < 0.5$). Elastic interactions of the pre-hadron are possible but rarely happen. This is closely related to a phenomenon called color-transparency. Color-transparency is an effect that exhibits a reduced elastic cross section of the pre-hadron due to a reduced dipole size. For pions it was calculated that the mean free path inside the nucleus is longer than 20 fm (the calculated diameter of Xe is 12 fm). For pre-hadrons this is even longer. This would mean that p_t-broadening is a measurement of the production time t_p.

As mentioned before, energy conservation imposes a restriction on the production length:

$$l_p \leq \frac{\nu}{\langle \frac{dE}{dl} \rangle}(1 - z). \tag{2.37}$$

Combined with equation 2.33:

$$\langle l_p \rangle \propto \frac{\nu}{Q^2}(1 - z), \tag{2.38}$$

see also reference [40]. These equations contain predictions for p_t-broadening: it has to rise with ν, until it exceeds the nuclear size, then it should stay constant. Broadening should reach 0 for z going to 1 and it should decrease with increasing Q^2 (for hadrons with $\langle z \rangle > 0.5$).

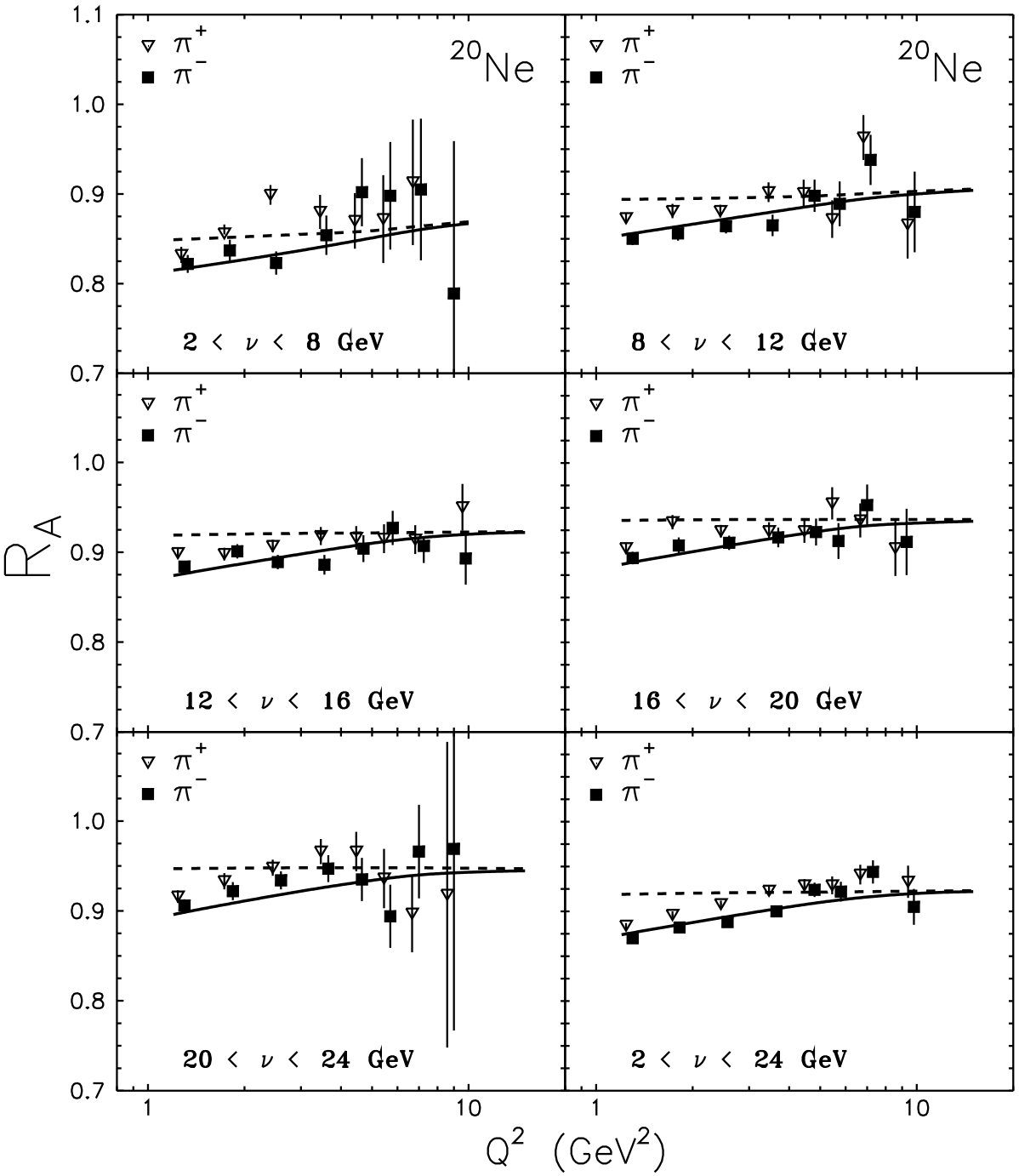

Figure 2.21: Comparison of calculations of nuclear attenuation versus Q^2 in ν-bins in the gluon bremsstrahlung model with HERMES preliminary data. The solid and dashed curve are the model predictions with and without corrections for induced energy loss. Picture taken from [30].

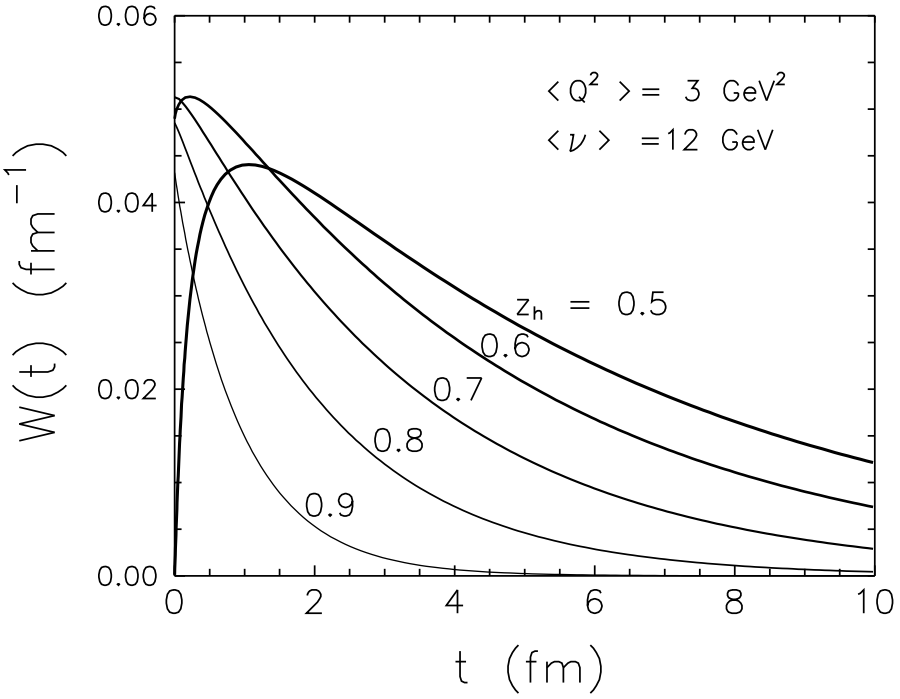

Figure 2.22: Distribution of the leading pre-hadron production time t_p, denoted t here. Picture taken from [30].

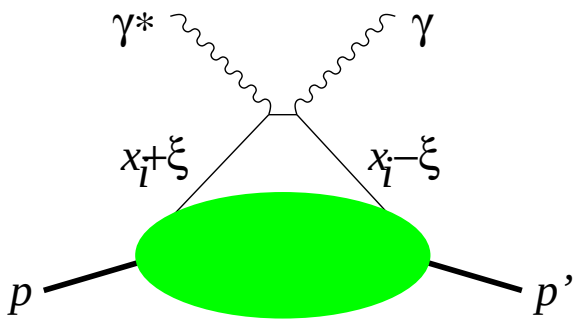

Figure 2.23: Feynman diagram of deeply virtual Compton scattering (non-forward Compton scattering). The shadow blob represents a generalized parton distribution.

2.2 Deeply virtual Compton scattering

In this section generalized parton distribution functions are introduced together with Deeply Virtual Compton Scattering (DVCS) as a process to access them. A first motivation to build a recoil detector for HERMES is to improve DVCS measurements. A more complete motivation can be found in [44].

2.2.1 Generalized parton distributions

The usual parton distributions are expectation values to find a parton in a hadron. They can be probed by forward Compton scattering and in inclusive DIS. In forward Compton scattering the momentum of the target is the same before and after the interaction. Generalized Parton Distributions (GPDs) are their natural extension and can be probed by non-forward Compton scattering. A diagram of non-forward Compton scattering, deeply virtual Compton scattering (DVCS), is shown in figure 2.23. In this diagram a virtual photon turns into a real photon. This means that the proton momentum changes in the interaction. Δ is defined as the momentum transfer to the proton, $p' - p$. It is related to Mandelstam variable $t = \Delta^2$. The average 4-momentum of the initial (p) and final (p') state nucleon is $\overline{p} = \frac{1}{2}(p + p')$. Before giving more kinematic variables useful for describing DVCS, light-cone coordinates are introduced.

Light-cone coordinates

It is often useful to transform to a different reference frame where the calculation and interpretation of the cross section becomes easier. In this case, first a Lorentz transformation is applied such that the virtual photon and the nucleon only move along one axis (the z-axis). The nucleon moves in positive z direction while the photon moves in negative z direction. An example of such a frame is the center-of-mass frame. To be precise, in the calculation of exclusive cross sections, it is usually required that $\overline{p}$ is collinear with the virtual photon.

The transformation to the light-cone coordinate system for an arbitrary 4-vector a is de-

fined by:

$$a^+ = \frac{1}{\sqrt{2}}\left(a^0 + a^3\right), \tag{2.39}$$

$$a^- = \frac{1}{\sqrt{2}}\left(a^0 - a^3\right), \tag{2.40}$$

$$\vec{a}_\perp = (a^1, a^2). \tag{2.41}$$

For a position vector y, y^+ is called *light-cone time* and y^- *light-cone distance*. The k^+ component of a 4-momentum vector k is called *light-cone momentum*. For fast moving particles in positive z direction, k^+ is large while k^- is small. All transverse components are assumed to be small, which results into light-cone momentum vectors that are dominated by one component.

The following definitions are required for consistency:

$$v \cdot w = v^+ w^- + v^- w^+ - \vec{v}_\perp \vec{w}_\perp, \tag{2.42}$$

$$\int d^4y = \int dy^- dy^+ d^2\vec{y}_\perp, \tag{2.43}$$

$$\partial^+ = \frac{\partial}{\partial^-}. \tag{2.44}$$

2.2.2 Deeply virtual Compton scattering: kinematics

A useful set of variables describing the DVCS kinematics are x_i and ξ (cf. figure 2.23), where x_i is defined as the ratio between the average longitudinal momentum of the outgoing (l') and incoming parton (l) and $\overline{p}$ ($x_i = \frac{l+l'}{p+p'}$), not to be confused with x-Bjorken. The values of x_i are defined between -1 and 1, negative values correspond to anti-quarks and positive ones to quarks (cf. section 2.2.3). The skewness ξ is defined as:

$$\xi = -\frac{1}{2}\frac{\Delta^+}{\overline{p}^+}, \tag{2.45}$$

and is invariant under Lorentz boosts along the z axis. In the limit of $|t| \ll Q^2$:

$$\xi \approx \frac{x}{2-x}. \tag{2.46}$$

Since x-Bjorken can only have a value between 0 and 1, the values of ξ have to be between 0 and 1.

2.2.3 GPDs: interpretation

Like the usual parton distributions, GPDs are subject to QCD evolution (as discussed in section 2.1.4) that makes them depend on Q^2. The scale-dependence of GPDs is well understood and can be calculated perturbatively to next-to leading order in α_s [45].

In the forward limit, i.e., at vanishing t (this means that ξ is also zero), the GPDs reduce to the parton distributions as introduced in the quark-parton model (cf. section 2.1.3). It is shown

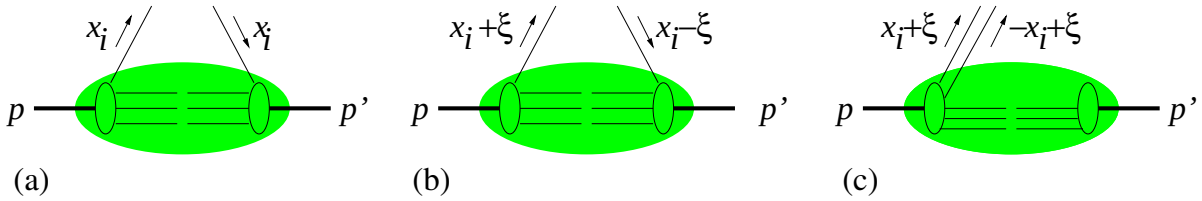

Figure 2.24: (a) Usual parton distribution (green blob), representing the probability to find a parton with longitudinal momentum fraction x_i in the nucleon. (b) GPD (green blob) in the region where it represents the emission of a parton with longitudinal momentum fraction $x_i+\xi$ and re-absorption with momentum fraction $x_i - \xi$. (c) GPD (green blob) in the region where it represents the emission of a parton anti-parton pair ($x_i + \xi > 0$ and $x_i - \xi < 0$).

in [46] that for GPDs at $\xi = 0$ a density interpretation is obtained by performing a Fourier transformation from $(p' - p)_\perp$ to the impact parameter that measures the transverse distance of the struck quark from the proton center of longitudinal momentum. GPDs at $\xi = 0$ thus describe the transverse distribution of partons with a given longitudinal momentum fraction x_i. At non-zero ξ this density interpretation no longer exists. GPDs probe the transverse and longitudinal structure of the proton simultaneously [47]. The GPDs can be interpreted as the probability amplitude to find a parton with longitudinal momentum fraction $x_i + \xi$ before the interaction and $x_i - \xi$ after the interaction.

The meaning of Generalized Parton Distributions at non-zero ξ, can also be explained in terms of light-cone wave functions [46]. At ξ= 0 the usual parton densities can be written as squared wave functions, summed over all configurations containing a parton with given longitudinal momentum fraction x_i (cf. figure 2.24(a)). Non-zero ξ opens up the kinematic regime and does not only describe emission and re-absorption of one parton (cf. figure 2.24(b)) but also the emission of two partons (cf. figure 2.24(c)). In this case $q\overline{q}$ or gluon pairs in the target wave function are probed. Sum rules (equations 2.51-2.54) show that the two regimes are intimately connected: both contribute to the integral of the distribution over x_i that is equal to the proton form factors as shown in equations 2.51-2.54.

At leading twist (twist-2) level, there are four different types of quark-helicity conserving quark GPDs: the unpolarized distributions $H^q(x_i, \xi, t)$ and $E^q(x_i, \xi, t)$ and the polarized distributions $\tilde{H}^q(x_i, \xi, t)$ and $\tilde{E}^q(x_i, \xi, t)$. The GPDs H^q and $\tilde{H}^q$ conserve nucleon helicity while E^q and $\tilde{E}^q$ are associated with a helicity-flip of the nucleon. In the limit of $t \to 0$, $\xi \to 0$ for positive x_i:

$$H^q(x_i, 0, 0) = q(x_i), \tag{2.47}$$

$$\tilde{H}^q(x_i, 0, 0) = \Delta q(x_i), \tag{2.48}$$

and for negative x_i:

$$H^q(x_i, 0, 0) = -\overline{q}(-x_i), \tag{2.49}$$

$$\tilde{H}^q(x_i, 0, 0) = \Delta\overline{q}(-x_i), \tag{2.50}$$

the ordinary quark and quark-helicity distributions $q(x)$ and $\Delta q(x)$ are obtained.

The first moment of the twist-two GPDs are equal to the corresponding parton form factors in the nucleon [49]:

$$\int_{-1}^{1} dx_i H^q(x_i,\xi,t) = F_1^q(t), \tag{2.51}$$

$$\int_{-1}^{1} dx_i E^q(x_i,\xi,t) = F_2^q(t), \tag{2.52}$$

$$\int_{-1}^{1} dx_i \tilde{H}^q(x_i,\xi,t) = g_A^q(t), \tag{2.53}$$

$$\int_{-1}^{1} dx_i \tilde{E}^q(x_i,\xi,t) = h_A^q(t), \tag{2.54}$$

where $F_1(t)$ and $F_2(t)$ are the Dirac and Pauli form factors, not to confuse with the structure functions introduced in section 2.1.2; $g_A(t)$ and $h_A(t)$ are the axial-vector and pseudo-scalar form factors. There is a very interesting relation between the second moment of a combination of GPDs and the total angular momentum J, i.e., the sum of intrinsic and orbital angular momenta carried by quarks in the proton:

$$J^q = \lim_{t\to 0} \frac{1}{2} \int_{-1}^{1} dx_i \; x_i \; \left[H^q(x_i,\xi,t) + E^q(x_i,\xi,t)\right], \tag{2.55}$$

called Ji's sum rule [49]. The total angular momentum J^q decomposes as

$$J^q = \frac{1}{2}\Delta\Sigma + L_q, \tag{2.56}$$

where $\Delta\Sigma/2$ and L_q are the quark spin and the orbital angular momentum contributions to the proton spin, respectively. Using the information on $\Delta\Sigma$ available from inclusive and semi-inclusive polarized DIS, this relation may be used to derive the contribution of the quark orbital angular momentum L_q to the nucleon spin. It should be noted that this requires access to both unpolarized GPDs, H^q and E^q, and that it is necessary to be able to extrapolate to $t \to 0$.

In electro-production processes GPDs can be accessed by studying hard exclusive reactions like DVCS and exclusive electro-production of mesons. The Feynman diagrams of these processes are shown in figure 2.25. The factorization theorems for these reactions have been proven [50]-[53] thus allowing a clear separation between the perturbative and the non-perturbative stages of the interactions. Therefore both types of processes (DVCS and exclusive meson production) can be described by the same GPDs.

Exclusive electro-production of mesons provides many channels in which GPDs can be accessed. In the large-Q^2 limit, the amplitude factorizes into a perturbatively calculable partonic subprocess, GPDs describing the target nucleon, and a distribution amplitude Φ that is the probability amplitude that a quark anti-quark pair form a meson [50]. An example diagram is shown in figure 2.25 (right panel). In contrast, the process of real photon production

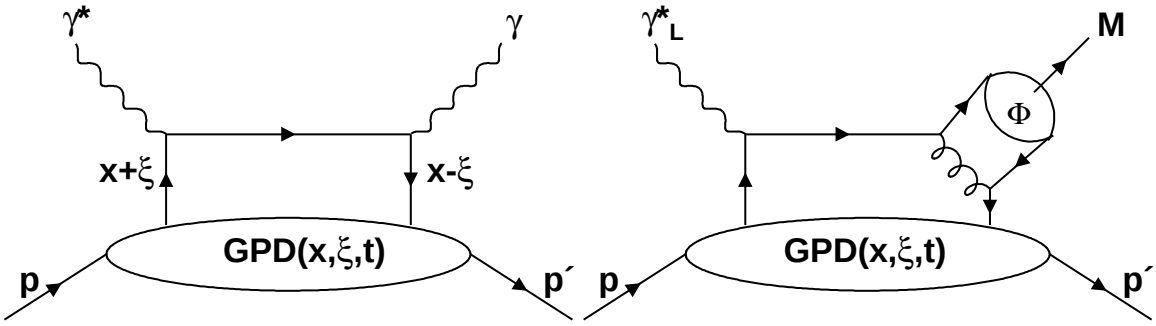

Figure 2.25: Handbag diagram for DVCS (left), and a diagram for meson production (right) is shown. Only a longitudinal polarized virtual photon is drawn because it is proven that the transversely polarized photons are suppressed by $\mathcal{O}(\frac{1}{Q^2})$ [50].

($\gamma^* + p \rightarrow \gamma + p$), DVCS, shown in figure 2.25 (left panel), is particularly simple for theoretical analysis because it can be described with one type of soft object, i.e., the GPDs only.

2.2.4 Probing GPDs at HERMES

In lepton (e^+ or e^-) scattering experiments there exists another process that leads to the same final-state as DVCS, namely the Bethe-Heitler process (BH), in which the incoming or outgoing electron radiates a Bremsstrahlung photon in the Coulomb field of the proton (for the Feynman diagram of BH see figure 2.26(b)). Hence, in the process $e + p \rightarrow e' + p' + \gamma$ the amplitudes of DVCS and BH interfere, thus prohibiting the measurement of the pure DVCS process. The relative contributions of BH and DVCS to the total BH/DVCS cross section depend strongly on the lepton energy. At HERMES energies, the BH contribution is dominant, except at large values of the Bjorken variable x and Q^2. This situation is used as an opportunity [54], since the interference of the two amplitudes offers a way to access both the real and the imaginary part of the DVCS amplitude (see below). At higher energies, where the DVCS amplitude dominates over the BH amplitude, only the square of the DVCS amplitude can be accessed [54].

The process amplitudes describing DVCS, BH, and their interference can be expanded into a power series in $\frac{1}{Q}$. They exhibit different characteristics as functions of the azimuthal angle ϕ between the scattering plane and the production plane (cf. figure 2.3 but the produced hadron has to be replaced with the produced photon), and can be expressed using moments $\langle\cos(n\phi)\rangle$ and $\langle\sin(n\phi)\rangle$. These cosine and sine moments are sensitive to the real and imaginary parts of the DVCS helicity amplitudes, respectively. In order to project out the various moments, measurements have to be done with different beam helicity and charge. Under the assumption of the validity of the handbag diagram (figure 2.25, left panel), each moment has its own characteristic fall-off with $\frac{1}{Q^n}$ at fixed x and t. The first cosine moment is then dominant with a $\frac{1}{Q}$ fall-off, while higher moments fall off with powers of 2 or higher [54].

A theoretical picture of the DVCS process has been developed in a number of papers like [49] and [54]. Explicit expressions for the amplitudes of DVCS, Bethe-Heitler, and interference terms including the first sub-leading correction in $\frac{1}{Q}$ for different kinds of polarized and

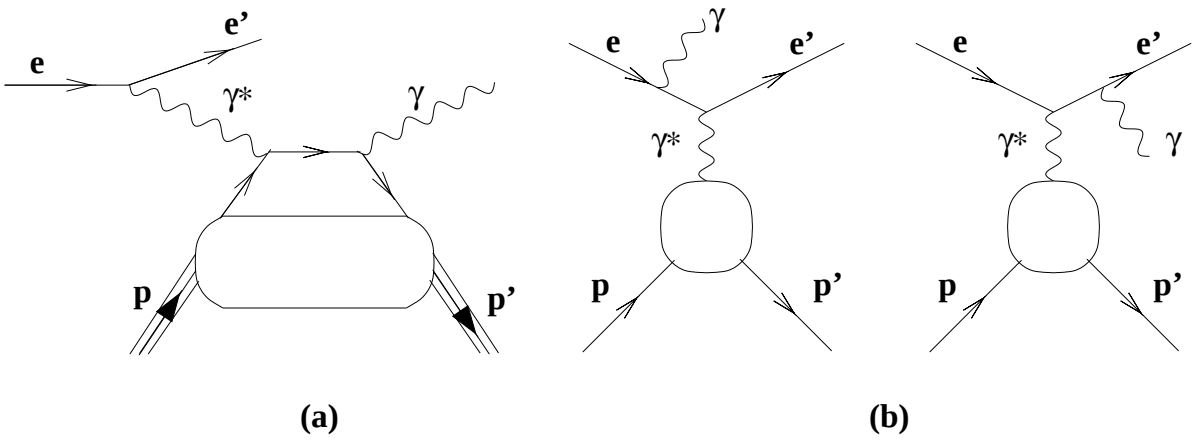

Figure 2.26: Feynman diagrams for the DVCS process (a) and the Bethe-Heitler process (b).

unpolarized initial particles have been calculated in [55]. The total photo-production amplitude ($\mathcal{T}$) squared can be written as [55]:

$$\mathcal{T}^2 = |\mathcal{T}_{\rm BH}|^2 + |\mathcal{T}_{\rm Dvcs}|^2 + \mathcal{I}, \tag{2.57}$$

with the interference term

$$\mathcal{I} = \mathcal{T}_{Dvcs}\mathcal{T}^*_{BH} + \mathcal{T}^*_{Dvcs}\mathcal{T}_{BH}. \tag{2.58}$$

The three terms from equation 2.57 (expanded in Fourier series) read [55]:

$$|\mathcal{T}_{\rm BH}|^2 = \frac{e^6}{x^2y^2(1-\epsilon^2)^2\Delta^2\mathcal{P}_1(\phi)\mathcal{P}_2(\phi)}\left\{c_0^{\rm BH} + \sum_{n=1}^{2} c_n^{\rm BH}\cos(n\phi) + s_1^{\rm BH}\sin\phi\right\}, \tag{2.59}$$

$$|\mathcal{T}_{\rm Dvcs}|^2 = \frac{e^6}{y^2Q^2}\left\{c_0^{\rm Dvcs} + \sum_{n=1}^{2}\left[c_n^{\rm Dvcs}\cos(n\phi) + \lambda s_n^{\rm Dvcs}\sin(n\phi)\right]\right\}, \tag{2.60}$$

$$|\mathcal{I}| = \frac{\pm e^6}{xy^3\Delta^2\mathcal{P}_1(\phi)\mathcal{P}_2(\phi)}\left\{c_0^{\mathcal{I}} + \sum_{n=1}^{3}\left[c_n^{\mathcal{I}}\cos(n\phi) + \lambda s_n^{\mathcal{I}}\sin(n\phi)\right]\right\}, \tag{2.61}$$

where the + (-) sign in the interference stands for negatively (positively) charged lepton beam, λ is the beam polarization, and $\mathcal{P}(\phi)$ are BH propagators [55]:

$$Q^2\mathcal{P}_1 \equiv Q^2 + 2k\cdot\Delta, \tag{2.62}$$

$$Q^2\mathcal{P}_2 \equiv -2k\cdot\Delta + \Delta^2, \tag{2.63}$$

with k the 4-moment of the incoming lepton. Also important are the leading twist (twist-2) coefficients in the interference term: $c_0^{\mathcal{I}}$, $c_1^{\mathcal{I}}$, and $s_1^{\mathcal{I}}$.

The measurement of the beam-spin asymmetry ($\mathcal{A}_{LU}$, where the L indicates a longitudinally polarized beam and U an unpolarized target) and the beam-charge asymmetry ($\mathcal{A}_C$) are approximately equal to [55]:

$$\mathcal{A}_{LU} = \frac{d\sigma(\overrightarrow{e^{\pm}}p) - d\sigma(\overleftarrow{e^{\pm}}p)}{d\sigma(\overrightarrow{e^{\pm}}p) + d\sigma(\overleftarrow{e^{\pm}}p)} \sim \mp\frac{x}{y}\frac{s_1^{\mathcal{I}}}{c_0^{\rm BH}}\sin\phi$$

$$\propto Im\left\{M^{11}\right\}\sin(\phi) \tag{2.64}$$

$$\mathcal{A}_C = \frac{d\sigma(e^+p) - d\sigma(e^-p)}{d\sigma(e^+p) + d\sigma(e^-p)} \sim \frac{x}{y}\frac{c_1^{\mathcal{I}}}{c_0^{\mathrm{BH}}}\cos\phi$$

$$\propto Re\left\{M^{11}\right\}\cos(\phi), \tag{2.65}$$

with M^{11} the photon helicity conserving DVCS amplitude:

$$M^{11} = F_1\mathcal{H}_1 + \xi(F_1+F_2)\tilde{\mathcal{H}}_1 - \frac{t}{4M_p^2}F_2\mathcal{E}_1, \tag{2.66}$$

where $\mathcal{H}_1$, $\tilde{\mathcal{H}}_1$, and $\mathcal{E}_1$ are the so-called Compton Form Factors (CFFs). The involved CFFs appear at twist-2 and are in fact convolutions of the hard scattering amplitude and the twist-2 GPDs H, $\tilde{H}$, and E.

At small values of x (t) the contribution of the CFFs $\tilde{\mathcal{H}}_1$ ($\mathcal{E}_1$) is suppressed in equations 2.64 and 2.65. Therefore, at low x and t the main contribution in these asymmetries is coming from CFF $\mathcal{H}_1$, and

$$Im\,\mathcal{H}_1(\xi,t) = -\pi\sum_q e_q^2\left(H^q(\xi,\xi,t) - H^q(-\xi,\xi,t)\right), \tag{2.67}$$

$$Re\,\mathcal{H}_1(\xi,t) = \sum_q e_q^2\left[P\int_{-1}^{1} H^q(x_i,\xi,t)\left(\frac{1}{x_i-\xi}+\frac{1}{x_i+\xi}\right)dx_i\right], \tag{2.68}$$

where P denotes Cauchy principal value because the integral is improper. This allows access to the GPD $H^q(x_i,\xi,t)$. Analogous expressions exist for transverse target spin asymmetry and GPD $E^q(x_i,\xi,t)$.

2.2.5 The HERMES recoil detector

The HERMES recoil detector that is designed to detect recoil particles is described in chapter 4. The detection of these recoil particles in the measurement of DVCS at HERMES will reject more efficiently the background caused by the associated Bethe-Heitler process and DIS events where a real photon is detected. In the associated Bethe-Heitler process the incoming or outgoing lepton radiates a real photon that is detected and leaves the nucleon in an excited state. The lightest nucleon resonance is a Δ-resonance and this is difficult background to cut away. Without the recoil detector the final-state of such an event is the same as a DVCS event. With the recoil detector one can detect the Δ-decay particles and then one knows that this event was not a DVCS event. It could happen that only a Δ-decay proton is detected. In that case the momentum of this decay-proton will not be coplanar anymore with the reaction plane determined by the momenta of the virtual and the real photon. The heavier nucleon resonances are cut away by using a missing mass cut. Background coming from DIS events can also be cut away using a coplanar and a missing mass cut. By applying all this cuts a very clean DVCS sample can be obtained. This is illustrated in figure 2.27. Furthermore, the distribution of the otherwise rejected resonant events can be studied.

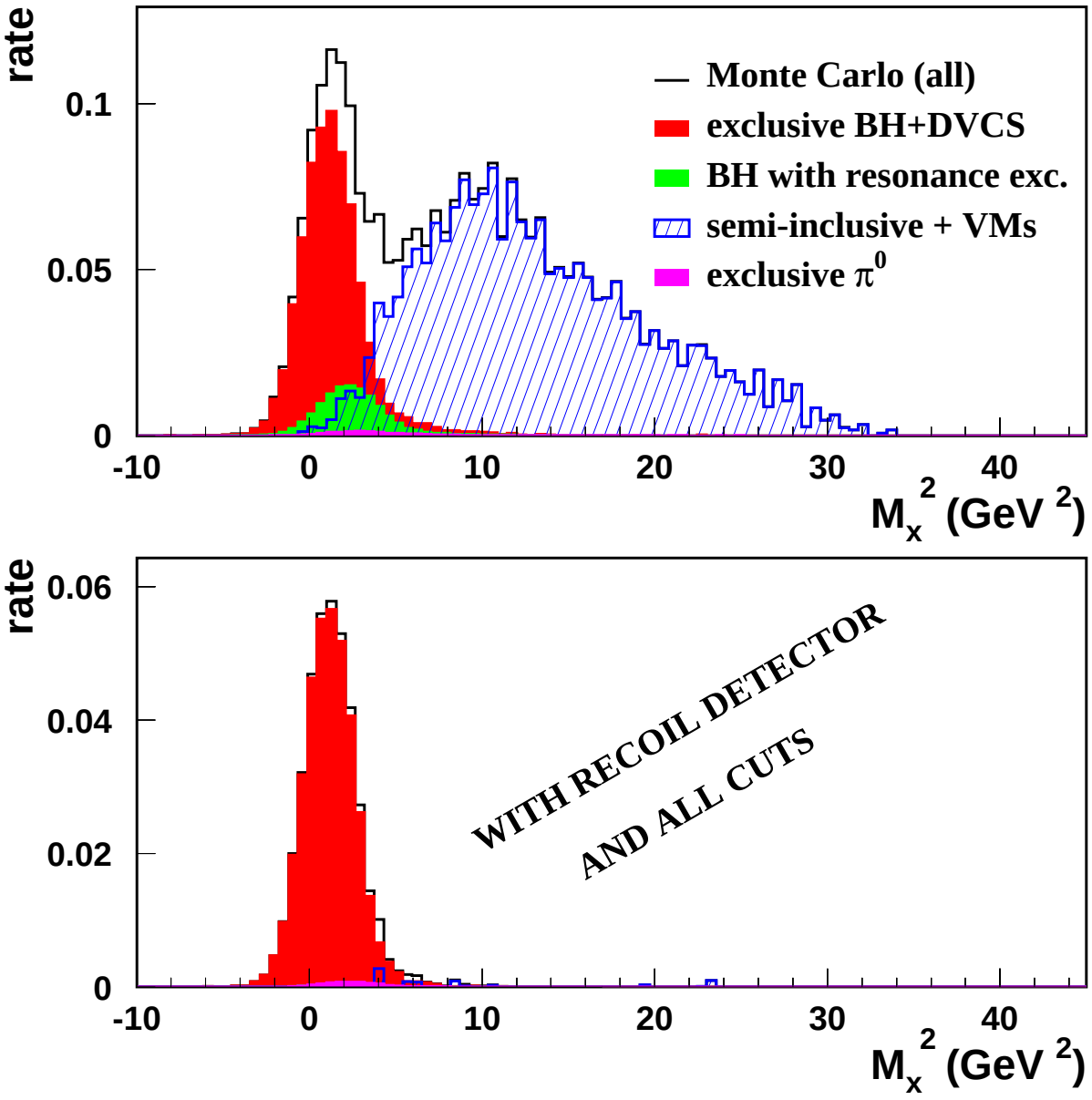

Figure 2.27: Missing mass squared spectrum without (top) and with (bottom) the HERMES recoil detector. Monte Carlo study [56].

Chapter 3

The HERMES experiment

In this chapter an overview of the HERMES experimental setup is given, starting from the HERA accelerator and ending with the data handling. Over data taking years the setup of the HERMES spectrometer changed; detectors were removed, upgrated, replaced, and/or installed. The setup described in this chapter is the one that is valid for the data taken in the analysis presented. This chapter ends with a section on reconstruction and tracking software used in almost every analysis of HERMES data.

3.1 DESY and HERMES

The HERa MEasurement of Spin (HERMES) experiment was one of the three high-energy experiments carried out at the Deutsches Elektronen-SYnchrotron (DESY) in Hamburg, Germany. This laboratory was founded in 1959 and the first synchrotron (DESY) was built between 1960 to 1964. In the period from 1976 to 1978, the Positron-Electron Tandem Ring Accelerator (PETRA) was constructed. One year later (1979) the gluon was discovered there. In 1990 the construction of the Hadron Elektron Ring Anlage (HERA) with a circumference of 6.3 km was finished. The HERA machine consists of two accelerators: one for protons and one for leptons (electrons or positrons). The proton accelerator delivered protons with an energy of 880 GeV until 1998. After the upgrade in 1998 this became 920 GeV. The electron accelerator delivers leptons with an energy of 27.6 GeV. The two accelerations take place in opposite direction and the two beams collide at two points: HERA-North and HERA-South (cf. figure 3.1). Two collider experiments, H1 and ZEUS, are located at these points, respectively. These experiments have been taking data since 1992 and the main goal is to investigate unpolarized nucleon structure functions by studying lepton-proton collisions. At HERA-West, the HERA-B experiment is located, which took data from 2000 to 2003 and used the accelerated protons on a fixed target, mainly to study charm and bottom meson production.

The HERMES experiment is located at HERA-East (cf. figure 3.1) and has been taking data since 1995. HERMES was proposed in 1990, approved in 1993, and installed in 1994/1995. In the HERMES experiment the accelerated leptons are used in collision with an internal "fixed" gaseous polarized proton and D target, although heavier (unpolarized) gas targets are also used. The main physics program of HERMES is to study the polarized structure functions of the nucleon using the polarized lepton beam on a polarized proton and D target.

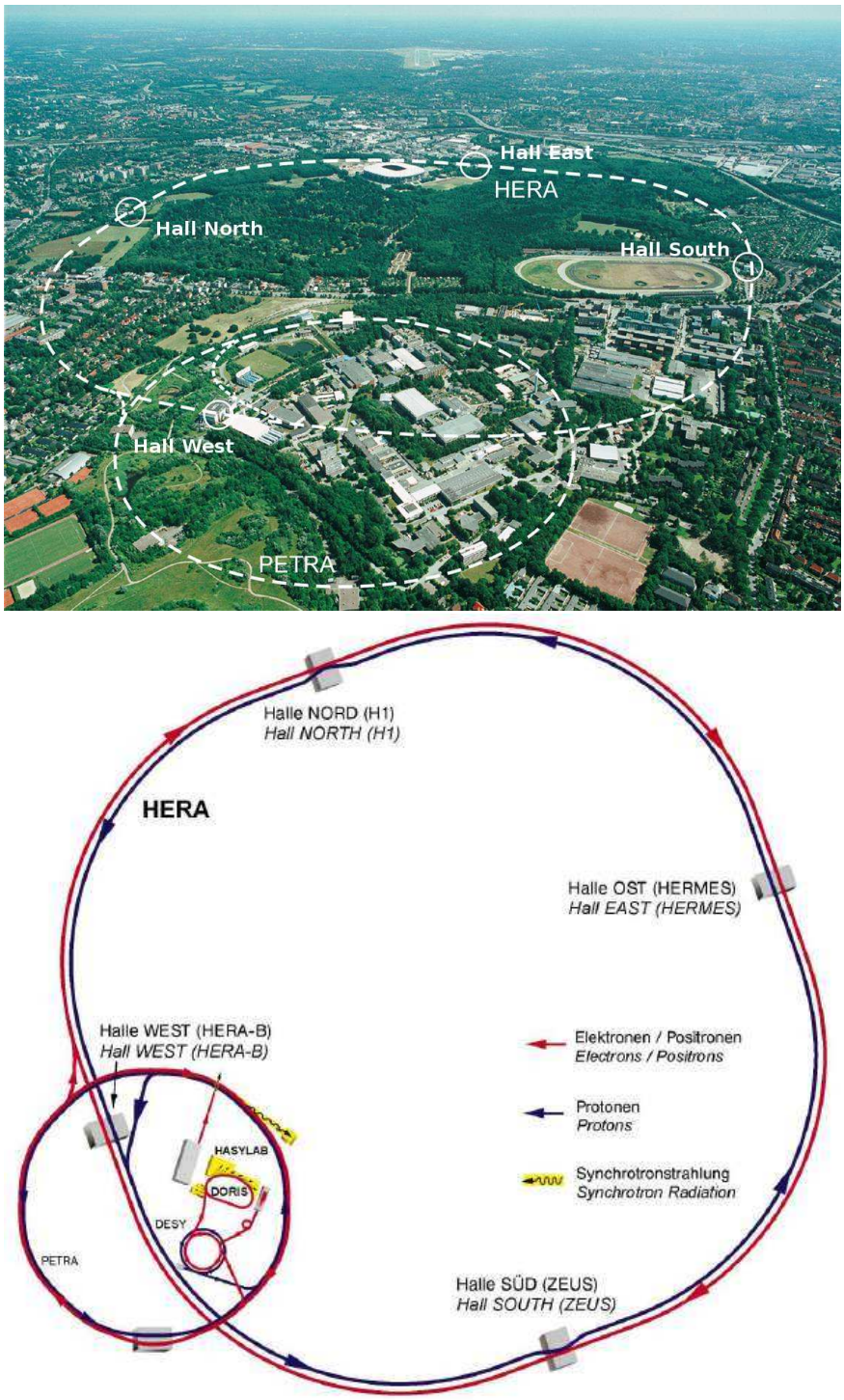

Figure 3.1: The upper part shows a photograph of the DESY site. The white lines show the underground location of the PETRA and HERA accelerators. The experiments are conducted in the four halls, currently there is no experiment running in Hall West. The lower part is a drawing of the HERA accelerator with its pre-accelerators: PETRA, DESY and two linear accelerators. The arrows point in the direction of acceleration. The lepton and proton beams collide in Hall North and Hall South were the two collider experiments H1 and ZEUS are located, respectively.

3.2 The HERA polarized lepton beam

The HERA lepton storage ring provides a lepton beam (positrons or electrons) with a momentum of 27.6 GeV. The lepton beam is arranged in bunches that are 27 ps long and there is an interval of 96 ns between these bunches. There are 220 positions for bunches in the storage ring. During a lepton fill only 189 positions are filled and organized in three trains of 63 bunches each. In two trains the last 7 positions are left empty and in the last train the last 17 positions are empty. In every train the 11^{th} bunch is not brought into collision with the proton beam: these bunches are called pilot bunches. The pilot bunches are monitored in order to tune the lepton beam.

3.2.1 Lepton beam polarization

When the leptons are injected they are unpolarized. After a certain time the lepton beam becomes polarized due to the Solokov-Ternov [57] mechanism. This involves a small asymmetry in the spin-flip probability of a lepton emitting synchrotron radiation in the aligned and anti-aligned spin state with respect to the magnetic field. The polarization of the lepton beam is given by:

$$P_B = \frac{N_- - N_+}{N_- + N_+}, \tag{3.1}$$

where $N_{+(-)}$ is the number of leptons (anti) aligned with the magnetic field of the bending magnets. The time dependent lepton beam polarization can be written as:

$$P_B(t) = P_{max}\left(1 - e^{-\frac{t}{\tau}}\right), \tag{3.2}$$

where τ is the characteristic polarization time and P_{max} (that also depends on τ) the maximum polarization achievable. At HERA the maximal polarization achieved is around 60% with a τ around 22 minutes.

In front of and behind the HERMES experiment are special magnets installed that are called Spin Rotators (cf. figure 3.2). These magnets change the transverse polarization of the lepton beam into a longitudinal polarization in front of the HERMES experiment and behind the HERMES experiment the transverse polarization orientation is restored.

3.2.2 Beam polarimetry

The lepton beam polarization is measured by two polarimeters. One is called the TPOL [58] and is located in the west straight section in the HERA ring. It uses a spatial asymmetry in the polarized Compton scattering cross section to measure the transverse beam polarization. The other detector is called the LPOL [59] and is located downstream of the HERMES experiment, but before the Spin Rotator. It uses an energy asymmetry in the Compton scattering cross section of circularly polarized laser light off the longitudinally polarized leptons to measure the longitudinal beam polarization. These two detectors provide independent measurements of the beam polarization.

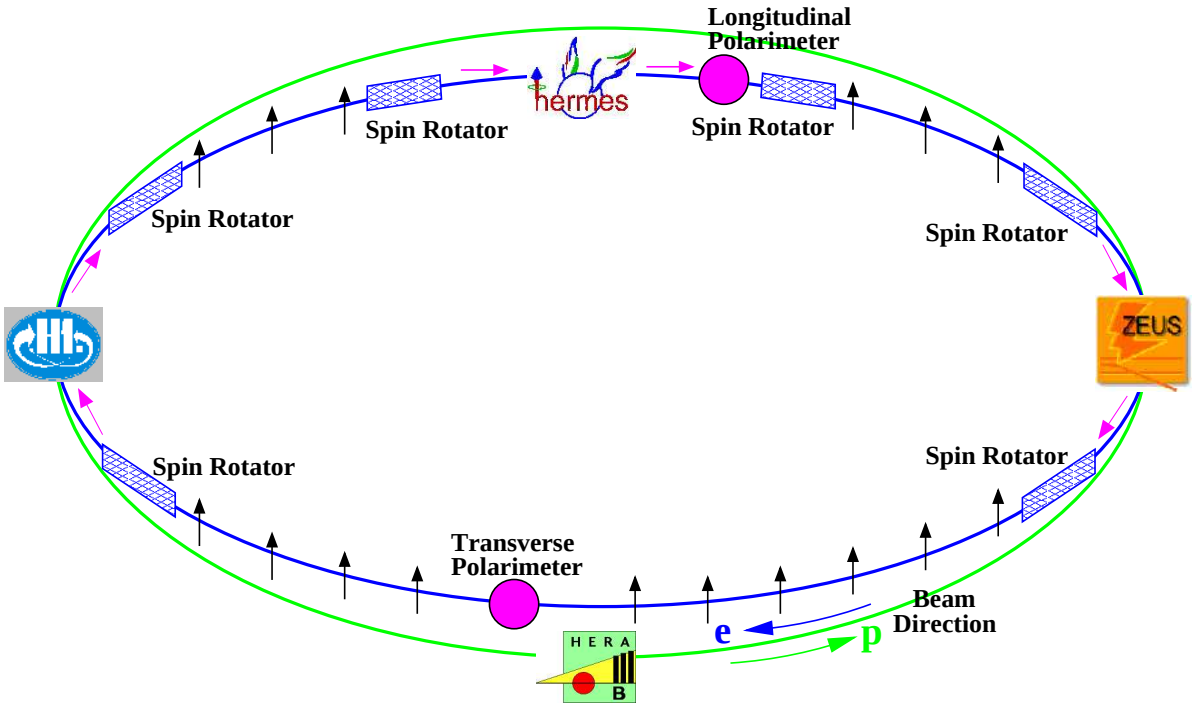

Figure 3.2: Schematic drawing of the two HERA storage rings, the locations of the experiments as of fall 2001 are also drawn. The arrows indicate the spin orientation of the lepton beam.

In the analysis described in this thesis, the beam polarization is of no importance. Because it is of crucial importance for other analyses done at HERMES it is mentioned here for the sake of completeness.

3.3 The HERMES internal gas target

HERMES has a "fixed" (not accelerated) gaseous target inside the lepton beam pipe. Data was taken with a longitudinally polarized ^{3}He target in 1995, H during 1996-1997, and D during 1998-2000. After 2000, HERMES switched to transversely polarized H until the end of 2005. In addition, unpolarized data was taken with H_2, D_2, N_2, ^{3,4}He, Ne, Kr, and Xe. Most of the "unpolarized" data was taken at the end of a HERA fill when the luminosity for the two collider experiments is too low to continue data taking. In that case HERMES is allowed to increase the target density such that most of the remaining lepton beam is used in about one hour (see also section 3.3.2).

The advantages of a polarized gaseous target over a solid target are that a much higher target polarization (P_T) can be reached ($P_T > 80\%$ compared to a typical $P_T < 50\%$ for solid targets). In addition, the dilutions of a gaseous target are much smaller than for a solid target, i.e., a gaseous target is purer and there is less rescattering in a gaseous target that might result in a better resolution. Finally, the polarization of a gaseous target can be flipped in milliseconds, instead of hours for a solid target. A disadvantage of a gaseous target is the low areal density: a solid polarized target has a typical areal density of 10^{25} atoms/cm^2 against

2.10^{11} atoms/cm^2 for a polarized atomic jet.

3.3.1 The storage Cell

The HERMES storage cell [60] confines the target atoms in a small volume to increase the target density. With the target cell HERMES reaches typical areal densities of $7.6{\cdot}10^{13}$ atoms/cm^2 for hydrogen and $2.1.10^{14}$ atoms/cm^2 for D that is two orders of magnitude better than the aerial density reached by using atomic jets.

A sketch of the HERMES target cell can be seen in figure 3.3. The cell walls are 75 μm thick and are made of 99.5% pure Aluminium. The profile is elliptic so that it fits the lepton beam shape. The spectrometer acceptance limits the usable target length to 400 mm. The cell tube is 147 mm longer in the downstream direction. This extension, ensures that all scattered particles inside the spectrometer acceptance pass through the same amount of Aluminium. The cell walls are coated with Drifilm [61], chosen for its radiation hardness, to minimize recombination of atoms in the target gas and so to reduce depolarization in the target. After a few weeks of operation an ice layer was formed (H_2O and D_2O) as the Drifilm became damaged. The ice layer was observed to improve the polarization of the target (by reducing the recombination of target atoms).

During operation, the target cell is cooled to 100 K (with liquid helium) to reduce the gas flow, increase the target areal density, and decrease the number of gas atom collisions.

Until the year 2000 a longitudinal magnetic field (0.335 T) was applied to maintain the target polarization, from 2001 until the end of 2005 a transverse magnetic field (0.297 T) was applied. The gas is injected in the middle of the cell (cf. figure 3.3) and is removed by turbo-molecular pumps at the edges of the cell volume.

The target cell is protected from synchrotron radiation by two collimators (called C1 and C2). C1 is located 2 meter upstream of the target cell. It actually consists of two collimators: one with two halves separated horizontally and one with two halves separated vertically. One can open C1 during injection and tuning of the beam. C1 is closed during data taking. C2 is located just upstream of the target cell and is designed to stop synchrotron radiation scattered by C1.

The bunched lepton beam induces mirror currents in the walls of the beam pipe. This causes the emission of strong radio-frequency (RF) fields or wake fields at discontinuities in the impedance of the beam pipe. These wake fields can deposit a sizable amount of energy in the target area. This heats up the target cell and, with feedback to the lepton beam, destabilizes the beam orbit. Therefore wake-field suppressors are installed upstream and downstream of the target cell (cf. figure 3.3) to minimize RF fields that are present in the target area and to provide a smooth transition between the cross section of the target cell and the HERA lepton beam pipe.

3.3.2 The unpolarized target

The HERMES experiment can run with a polarized or an unpolarized target. When running in unpolarized mode the following targets are used: H_2, D_2, ^{3,4}He, N_2, Ne, Kr, and Xe. The unpolarized gases are fed directly into the target in a way (using valves) such that the density stays constant. This system is called the Unpolarized Gas Feed System (UGFS). There are

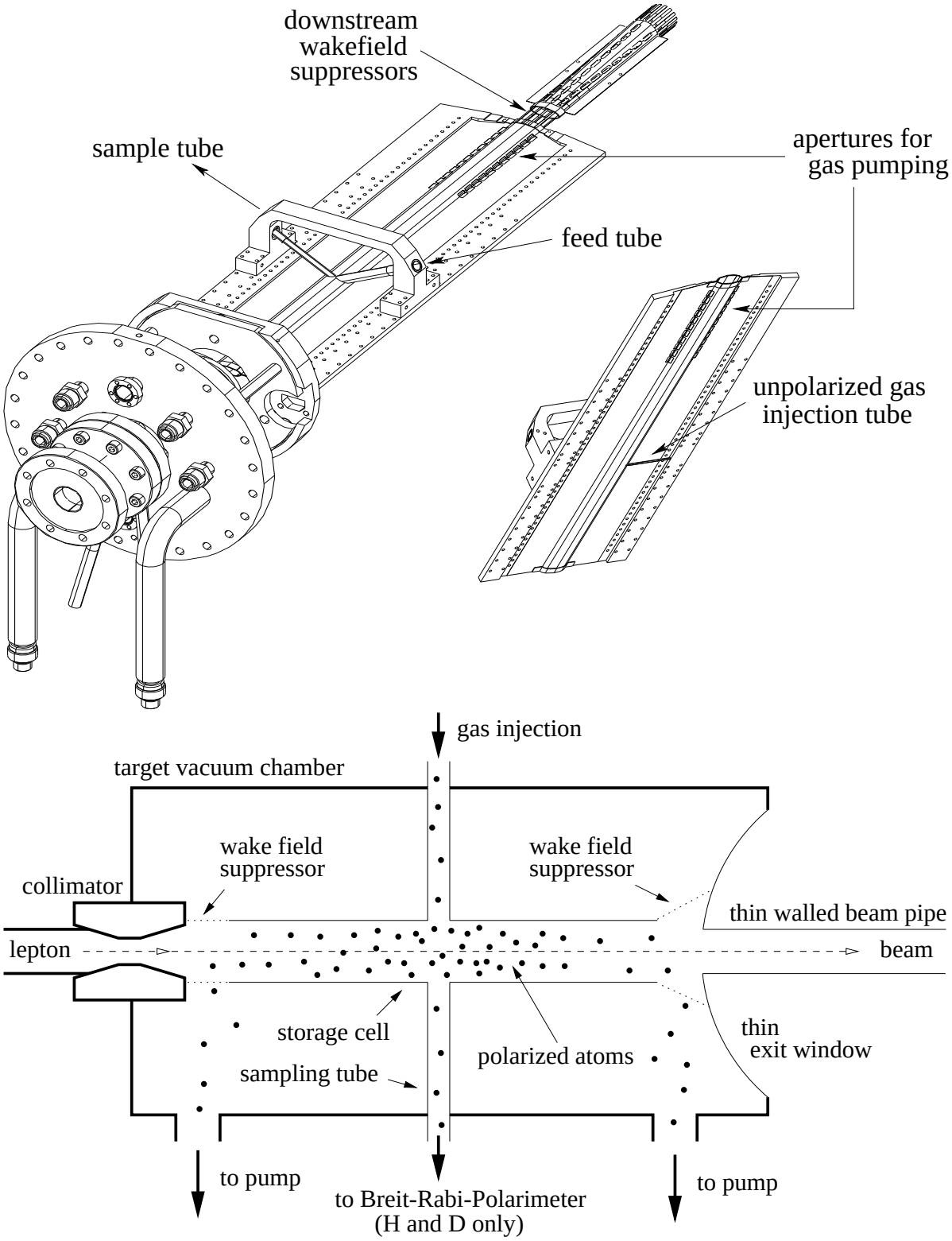

Figure 3.3: Schematic drawing of the HERMES target cell and chamber. The lower drawing is horizantaly and verticaly not to scale.

two modes of unpolarized data taking: one called "normal unpolarized mode" and one called "high density end-of-fill mode". In the first mode a target areal density around 10^{15} atoms/cm^2 is applied. The second mode is used at the end of a HERA fill when the beam current is too low to be used by the other experiments. Then the HERMES experiment is allowed to use target areal densities higher than 10^{16} atoms/cm^2 (depending on the target) for one hour. Switching to this mode takes a relatively short amount of time (about 15 minutes). The high density unpolarized target mode allows HERMES to take a lot of unpolarized target data in a relative short amount of time. Most of the HERMES unpolarized data comes from the end of fill running. This mode is also used to perform target and spectrometer calibration measurements.

3.3.3 The polarized target

Because the target polarization is irrelevant for the analysis presented in this thesis, only a short description of the polarized target is given.

Until the end of 2005 HERMES used polarized H and D. The polarized atoms are prepared in the Atomic Beam Source (ABS) [62] and then injected in the target cell. A small fraction of the target gas is analyzed by the Target Gas Analyzer (TGA) [63] and the Breit-Rabi Polarimeter (BRP) [64] (cf. figure 3.4).

The ABS uses radio frequency discharges to dissociate molecular gas in atomic gas. Then the atoms traverse a sextupole magnet system. This system consists of two sextupole magnets followed by a set of high frequency transitions and uses the Stern-Gerlach mechanism to select only one polarization of the nucleus [62].

The TGA is used to measure the amount of recombined molecular gas.

The BRP measures the polarization of the target gas using the same (but inverse) principle as the ABS.

3.4 The luminosity monitor

The luminosity monitor [65] was built to measure the luminosity. The luminosity ($\mathcal{L}$) can be determined by measuring the scattering rate of a certain well-known process, normalizing this to the cross section integrated over the acceptance (of the luminosity monitor) and correcting for the efficiency of the luminosity monitor. The processes used are Bhabha scattering ($e^+e^- \to e^+e^-$) and pair annihilation ($e^+e^- \to \gamma\gamma$) for a positron beam, and Møller scattering ($e^-e^- \to e^-e^-$) in the case of an electron beam. The cross sections of all three processes are known to a high degree of accuracy in quantum electrodynamics (QED).

The luminosity monitor is located close to the beam pipe, 7.2 m downstream of the target cell at the same z position as the calorimeter, as shown in figure 3.5. It consists of two calorimeters positioned left and right of the lepton storage ring. Each calorimeter is made from a matrix of 3×4 radiation hard $NaBi(WO_4)_2$ crystals with a total size of $66 \times 88 \times 200$ mm^3. The crystals are read out by individual Photo Multiplier Tubes (PMTs).

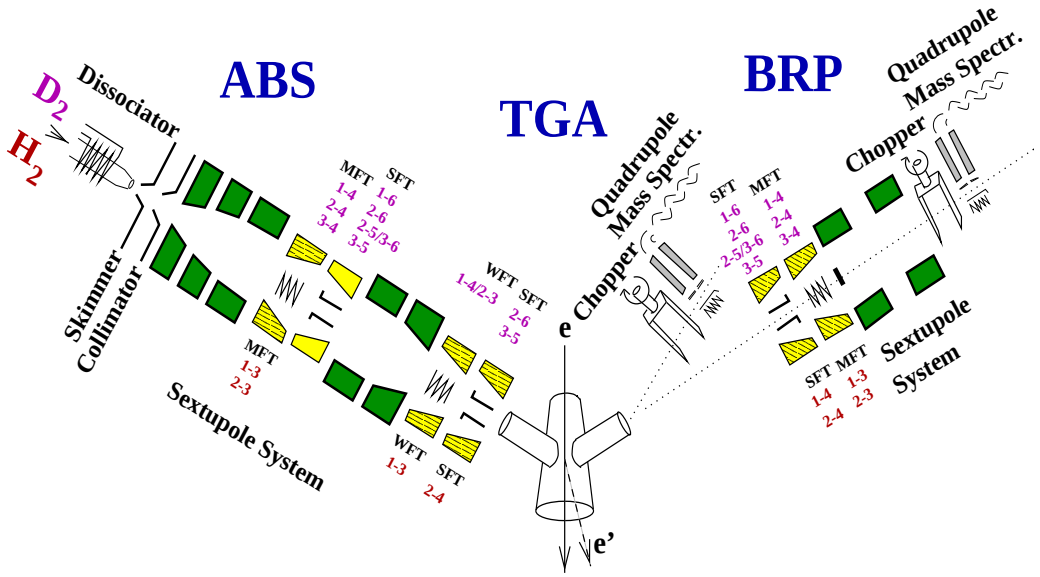

Figure 3.4: Schematic drawing of the HERMES polarized target. The atomic beam source (ABS) that provides polarized H or D is shown together with the target gas analyzer (TGA) and the Breit-Rabi-Polarimeter (BRP). SFT, MFT, and WFT are strong, medium, and weak field transitions in the ABS and the BRP.

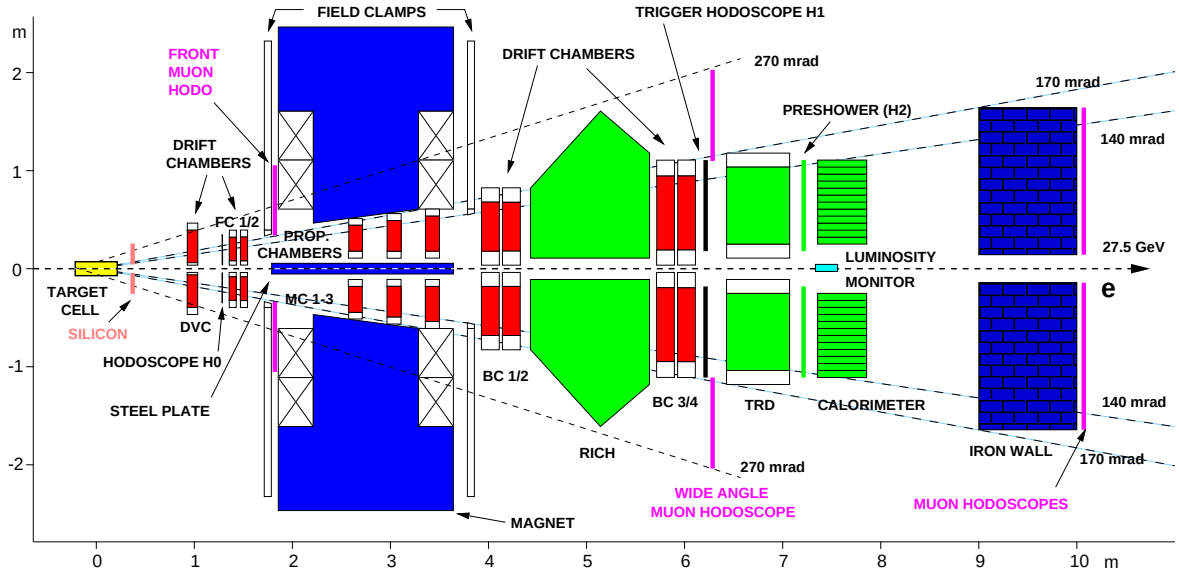

Figure 3.5: Drawing of the HERMES spectrometer. Detectors colored red are used for tracking of charged particles and the ones that are green colored are used for particle identification.

3.5 The HERMES spectrometer

The HERMES spectrometer [66] is a typical forward spectrometer, symmetric above and below a central, horizontal shielding plate in the magnet (see figure 3.5). The HERMES coordinate system satisfies the right-hand rule and has its origin at the center of the target, the z-axis along the beam direction, and the y-axis is perpendicular to the horizontal shielding plate in the magnet and points to the zenith.

A schematic side view drawing (y-z plane) of the HERMES spectrometer is drawn in figure 3.5. This spectrometer was designed for a study of deep-inelastic and semi-inclusive deep-inelastic scattering and has therefore an optimized acceptance for the detection of the scattered lepton and (a part of) the final state that are in case of semi-inclusive deep-inelastic scattering (some of) the hadrons produced off the target.

The spectrometer consists of three kinds of detectors: tracking detectors to determine charged particle tracks, detectors that enable Particle IDentification (PID), and detectors that are involved in the triggering on events of interest. These detectors are described in following paragraphs.

The horizontal shielding plate in the magnet that can be seen in figure 3.5 limits the acceptance for scattered particles to a minimum vertical scattering angle of $|\theta_y| > 40$ mrad. The maximum vertical scattering angle $|\theta_y|$ is 140 mrad and the horizontal scattering angel has to be smaller then 170 mrad ($|\theta_x| < 170$ mrad) in order to be inside the spectrometer acceptance.

The configuration shown is the one that was valid for the data used in the presented analysis.

In 2006 the target described in section 3.3 was removed and a new (unpolarized) target was installed with a HERMES recoil detector (cf. chapter 4).

3.5.1 The HERMES tracking system

In this section the HERMES tracking system is described. All tracking detectors (except the Lambda wheels "silicon") are colored red in figure 3.5.

Front tracking

The front tracking system is used to determine the event vertex and the angles of the emerging charged tracks with respect to the beam. This tracking system contains two sets of drift chambers: the Front Chambers (FCs, installed in 1995) [68] and the Drift Vertex Chambers (DVCs, installed in 1997). The DVCs were installed for redundancy in case an FC breaks and to replace the earlier installed vertex chambers. All the drift chambers are of the conventional horizontal drift type. Each layer of drift cells consists of a plane of alternating anode and cathode wires between a pair of cathode foils. The cathode wires and foils are at negative high voltage with the anode sense wires at ground potential. The chambers are assembled as modules consisting of six such drift cell layers in three coordinate doublets (XX', UU', and VV'). The wires are vertical for the X planes and at an angle of $\pm 30^\circ$ to the vertical for the U and the V planes. The X', U', and V' planes are staggered with respect to their partners by half the cell size in order to resolve left-right ambiguities. The DVCs are located at z = 1.1 m, have a cell size of 6 mm, and have a spatial resolution of 220 μm in each plane. The FCs are

mounted at z = 1.6 m on the front face of the spectrometer magnet. With a drift cell size of 7 mm, they provide a resolution of 225 μm in each plane. Both the FCs and the DVCs are arranged in the $XX'UU'VV'$ configuration.

The spectrometer magnet and tracking inside the magnet

The HERMES spectrometer magnet (shown in blue in figure 3.5) provides a deflecting power of $\int B \cdot dl$ = 1.3 Tm. It deflects charged scattered leptons and produced hadrons horizontally because the applied field is vertical. Together with the tracking detectors it is possible to measure the bending of these tracks and so to determine the momentum of the charged particles. A massive iron plate in the symmetry plane shields the lepton and proton beam pipes as they pass through the magnetic field. The magnetic field map was determined with model calculations and measured with a 3D-Hall-probe. The calculations agree with the measurement within a few percent. The field map was incorporated into the tracking algorithm.

The Multi-wire proportional Chambers or Magnet Chambers (MCs) [69] are installed in the gap inside the magnet. They are mostly used for momentum determination of low-energy particles that are bent outside of the acceptance of the back tracking detectors by the magnetic field. The three chambers have a XUV configuration. The chambers have a cell size of 2 mm that provides a resolution of 700 μm.

Back tracking

The back tracking system is used to reconstruct the tracks of charged particles that passed through the magnet. The reconstructed back tracks are matched with front tracks to determine the particle momentum. In addition, the position information of the Back Chambers (BCs) is used to associate signals in the particle identification detectors with particle tracks.

Two pairs of drift chambers (BC 1/2 and BC 3/4) [70, 71] are installed in front of and behind the Ring Imaging Čerenkov (RICH) detector. Each of the chambers has six planes in the $UU'XX'VV'$ configuration. The drift cell size of 15 mm provides a resolution of 250 and 275 μm per plane for BC 1/2 and BC 3/4, respectively. The differenece in resolution (all BCs have the same drift cell size) is due to the use of a higher threshold in BC 3/4 to reduce the cross-talk (BC 3/4 have more channels than BC 1/2).

3.5.2 Particle identification

The HERMES Particle IDentification (PID) is described in this section. First a description of all the detectors involved in PID is given in the same order as a particle passes through them. Detectors involved in PID are colored green in figure 3.5.

The Ring Imaging Čerenkov detector

The Ring Imaging Čerenkov detector (RICH) [101] was installed in spring 1998, replacing a threshold Čerenkov detector. This detector can identify pions, kaons, and protons using Čerenkov radiation. It also contributes to the separation of leptons and hadrons.

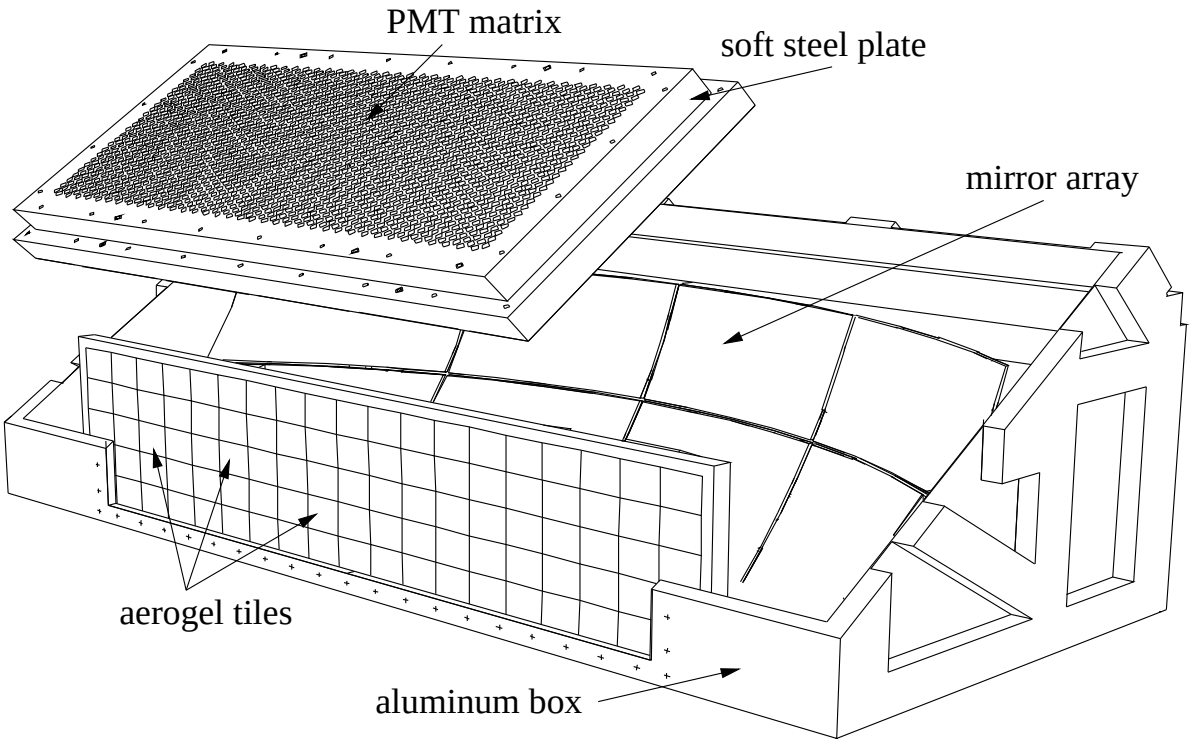

Figure 3.6: Drawing of the upper half of the RICH detector.

Čerenkov radiation is electromagnetic radiation emitted when a charged particle passes through an insulator at a speed greater then that of light in the medium (e.g., the characteristic "blue glow" of nuclear reactors is due to Čerenkov radiation). This radiation is emitted at a characteristic angle θ_c,

$$\cos\theta_c = \frac{1}{\beta n}, \tag{3.3}$$

where $\beta = \frac{v}{c}$, v is the speed of the particle, c is the speed of light in vacuum, and n is the refractive index of the medium. No light is emitted, if

$$\beta < \beta_{thresh} = 1/n \tag{3.4}$$

or

$$p < p_{thresh} = \frac{mc}{\sqrt{n^2-1}}, \tag{3.5}$$

with p the momentum of the particle and m its mass. By measuring the characteristic angle of the radiated photons and knowing the momentum of the particle, one can determine its mass (that means its type).

A schematic cut-away view of the upper half of the RICH detector can be seen in figure 3.6. The RICH detector uses two radiators: first, the particles enter through a wall of aerogel tiles [74], and then passes a space filled with C_4F_{10} gas. Properties of both radiators can be found in table 3.1. The aerogel radiator is used for hadron identification at low momentum, whereas the C_4F_{10} radiator is used for identification at high momenta. In this way the momentum range 2 - 15 GeV is covered as can be seen in figure 3.7.

	n	p^{π}_{thresh}	p^{K}_{thresh}	p^{p}_{thresh}
Aerogel	1.0304	0.6 GeV	2.0 GeV	3.8 GeV
C_4F_{10}	1.00137	2.7 GeV	9.4 GeV	17.9 GeV

Table 3.1: Refraction indices and Čerenkov light thresholds of the RICH detector for different charged hadron types (pions, kaons, and protons).

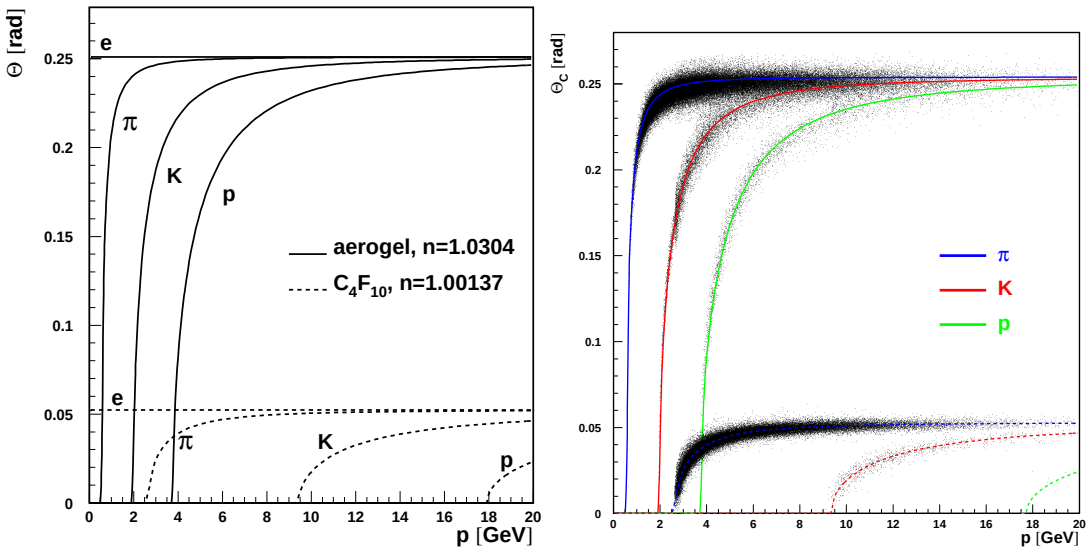

Figure 3.7: The Čerenkov angle versus particle momentum for the aerogel and the C_4F_{10} radiators used in the RICH detector. One can see that within the momentum range of 2 - 15 GeV, good hadron identification is possible. On the right plot data points are added (black points).

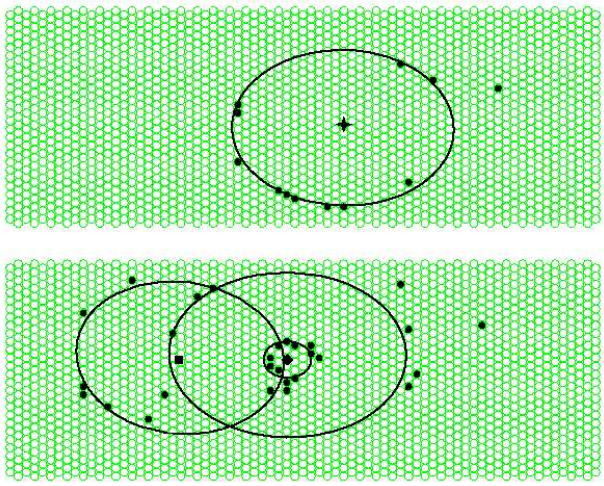

Figure 3.8: The RICH detector event display for an event with a 5.5 GeV kaon in the upper half and a 14.6 GeV electron (right) and a 1.5 GeV pion (left) in the lower half. The pion only radiates in the aerogel, whereas the electron radiates in both materials and generates two Čerenkov rings, the smaller ring being the gas ring. The solid rings were reconstructed using the inverse ray tracing method described in section 3.5.2. The black points in the middle of the reconstructed Čerenkov rings are virtual hits that would be caused by the particle track as if it was a photon.

The Čerenkov photons are emitted in a cone around the track, reflected by a mirror and then projected on an array of 1934 Photo-Multiplier Tubes (PMTs) per detector half. The cone projection on the PMT array is elliptical around a virtual point determined by the projection of the particle track reflected by the mirror. An example event can be seen in figure 3.8.

The RICH detector is subject to misidentification and a non-perfect efficiency. An unfolding method is applied to deal with these effects. This is explained in section 6.6.

RICH **particle identification** Two different algorithms [75] are used to reconstruct the Čerenkov angle from the hit pattern in the PMT array. They are called Indirect Ray Tracing (IRT) and Direct Ray Tracing DRT. In IRT, one starts from the particle track information and a hit in the PMT array and then tries to calculate the θ_c. In DRT, one also starts with the track information and calculates hit patterns in the PMT array for each particle type. The particle type that fits best is then taken.

The RICH detector assigns to each track a particle type (using IRT or DRT). This can be an electron, pion, kaon, or proton (or their anti particles). To this identification a quality factor rQp is assigned:

$$rQp = \log_{10} \frac{L_1}{L_2}, \tag{3.6}$$

with L_1 and L_2 the probabilities of the most likely and the second most likely hadron. If L_1 equals L_2 the RICH detector leaves the particle as unidentified. One has an rQp value for both the IRT and the DRT method. Both methods have their strengths and weaknesses, therefore a mechanism was developed to select the best method based on track information and event

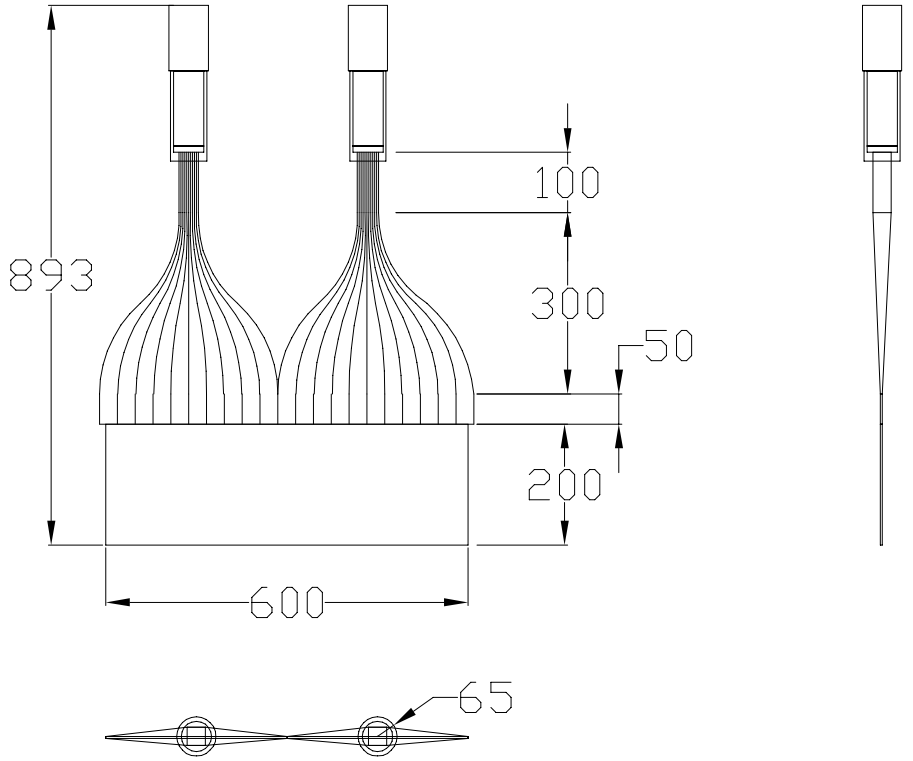

Figure 3.9: Technical drawing of the H0 detector. A 600 $\times$ 200 mm^2 scintillator is read out by 2 PMTs.

topology. This RICH PID Scheduler or RPS is described in [76].

The hodoscopes

The hodoscopes (H0, H1, and H2 in figure 3.5) are mainly responsible for generating a trigger for the spectrometer. In second order they also play a role as a PID detector. A hodoscope is basically scintillator material read out by a PMT. In the acceptance used in this analysis, there are 3 hodoscopes: H0, H1, and H2. A technical drawing of H0 can be seen in figure 3.9. H0 consists of a 3.2 mm thick, 60 $\times$ 20 cm^2 scintillator panel that is read out by two PMTs using twisted light guides [77]. Two such hodoscopes are used, one for the top detector half and one for the bottom half. The scintillator material used is BC-400 (from Bicron) and the PMTs used for readout are Thorn/EMI 2" 9954SB07 PMTs.

Per detector half H1 and H2 [78] consist of 42 paddles containing scintillator strips that are 1 cm thick, measure 9.3 $\times$ 91 cm^2, and are each read out by one PMT. Two neighboring paddles have an overlap of 3 mm. In figure 3.10 one can find a sketch of H1 and H2 (H2 can also be seen in figure 3.12). The scintillator material used is BC-412 (from Bicron) and the PMTs used to read out the paddles are the same ones that are used for H0: the Thorn/EMI 2" 9954SB07 PMTs.

In front of H2 a lead preshower is mounted in which electrons will initiate an electromagnetic shower, thus causing a larger signal in the H2 detector. Without the preshower, minimum

ionizing particles will deposit about 2 MeV in 1 cm of scintillator material. For electrons that have showered in the lead radiator, the deposited energy can be up to 100 MeV.

The transition radiation detector

The Transition Radiation Detector (TRD) [66] plays an important role in PID. It measures radiation caused when a relativistic charged particle passes through two media that have different dielectric constants. In each medium the particle induces a different Coulomb field. These fields do not match at the boundary. The required continuity at the boundary gives rise to an additional field: the transition radiation [79]. The total energy emitted as radiation is given by:

$$E = \frac{2}{3}\,\alpha\,\omega_p\,\gamma, \tag{3.7}$$

with α the fine structure constant, ω_p the plasma frequency of the medium, and γ the Lorentz factor. Transition radiation is emitted in a cone around the particle track with an opening angle $\theta = \frac{1}{\gamma}$. At high energies radiation (that is in the X-ray region) is emitted almost collinear with the particle track. Because the radiation has a small probability many material interfaces are needed.

The HERMES TRD is built from six consecutive modules that can be seen in figure 3.11. Each module has an active area of 72.4×325 mm^2 and is essentially an independent detector. The modules consist of a radiator that initiates the transition radiation and a Multi-Wire Proportional Chamber (MWPC) to measure the transition radiation and to provide a position measurement. The radiator material is predominantly a 2D matrix of fibers with 17-20 μm diameter. Each radiator is 6.35 cm thick and thus has approximately 267 dielectric layers.

Each MWPC is 2.54 cm thick and has 256 vertical wires with a separation of 1.27 cm. The chamber gas is a mix of 90 % Xe and 10 % CH_4 that was chosen because it efficiently absorbs X-rays.

At HERMES energies only leptons emit a significant amount of transition radiation photons because of the linear energy dependence of the total energy emitted on the Lorentz factor. For example the Lorentz factor of a 10 GeV electron is 19569, the Lorentz factor of a 10 GeV pion is 72. In addition, every charged particle deposits ionization energy in the chamber gas. At high energies, it is impossible to distinguish transition radiation from the ionization energy because of the small opening angle of the transition radiation photons. Leptons are therefore distinguished from hadrons simply by the larger amount of energy deposition in the MWPCs.

The calorimeter

The HERMES calorimeter [80] has four tasks to fulfill: (i) to provide (part of) a first-level trigger for scattered leptons, based on their energy deposition; (ii) to help separate leptons from hadrons; (iii) to measure the energy of the scattered leptons and of photons from radiative processes and DVCS or from π^0 and η decays; and (iv) to give a coarse position measurement of scattered leptons and photons.

The calorimeter consists of 840 radiation resistant F101 lead-glass blocks [81] arranged in a configuration with one wall above and one below the beam, with PMTs viewing from the rear, as shown in figure 3.12. Each wall is composed of 420 identical blocks, stacked in a

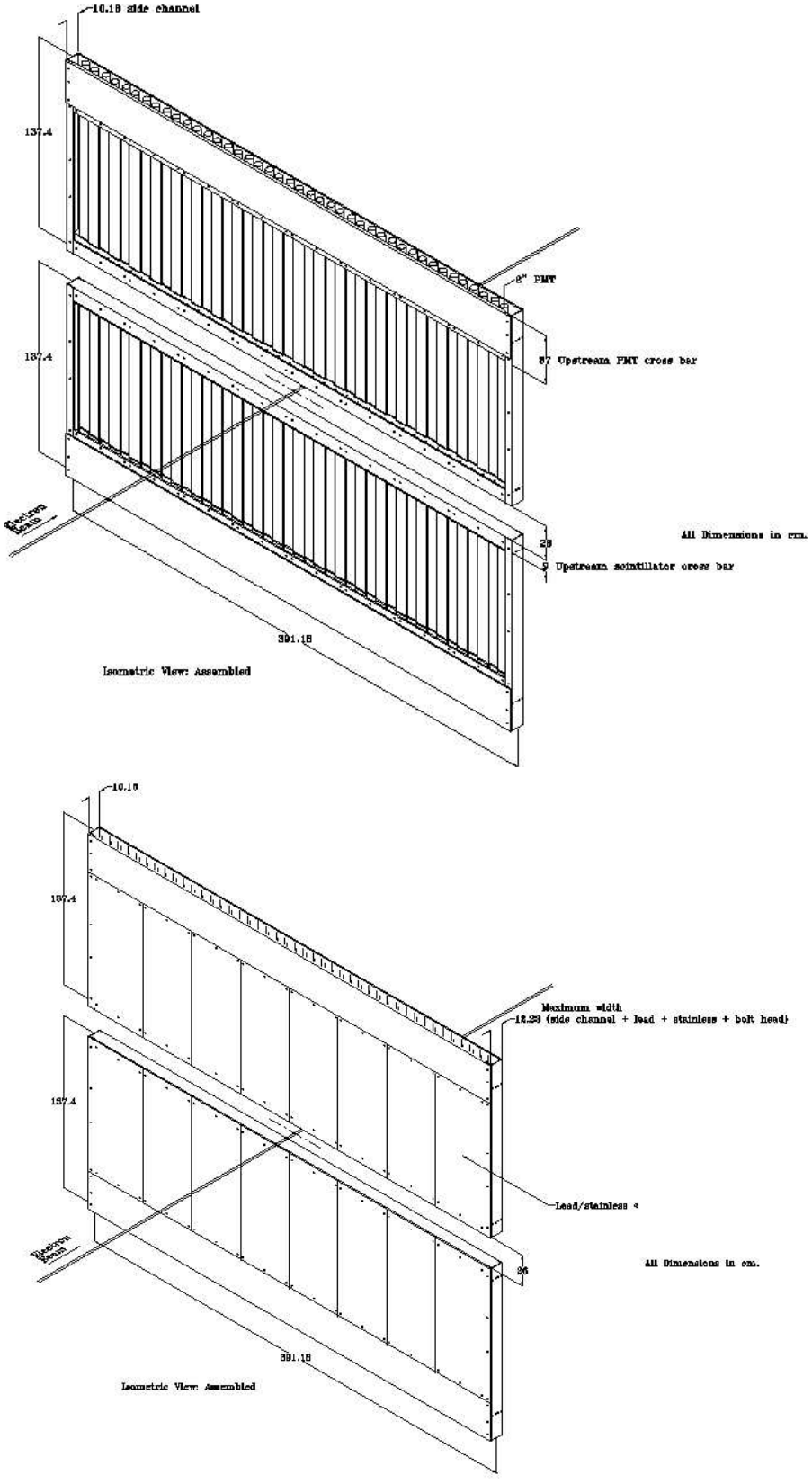

Figure 3.10: Drawing of the H1 and H2 detector. Note the lead preshower material placed in the front part of H2.

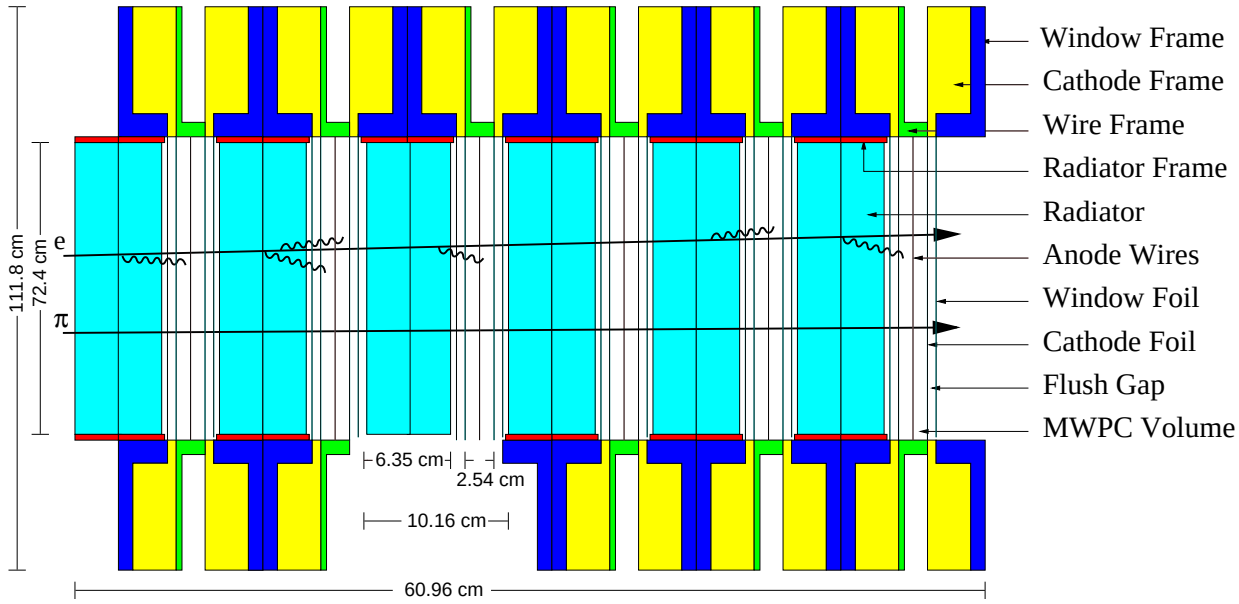

Figure 3.11: Drawing of the upper half of the TRD. The opening angles of the transition radiation are exaggerated.

42 $\times$ 10 array. Each block has a surface area of 9 $\times$ 9 cm^2 and a length of 50 cm (about 18 radiation lengths). Both top and bottom detectors are mounted on a movable frame that can be moved away from the beam pipe in the vertical direction during injection, beam tuning, and (controlled) beam dumps. This is done to prevent too much radiation damage to the lead glass blocks during these times.

The energy resolution for scattered leptons is well described by the following parametrization:

$$\frac{\sigma(E)}{E}[\%] = \frac{(5.1 \pm 1.1)}{\sqrt{E(\mathrm{GeV})}} + (2.0 \pm 0.5) + \frac{(10.0 \pm 2.0)}{E(\mathrm{GeV})}. \tag{3.8}$$

This parametrization is slightly worse than expected from test beam results [80] because of pre-showering of leptons in the lead material in the preshower, that improves the discrimination between leptons and hadrons, but causes the E^{-1} term in 3.8. Imperfections in the gain matching among modules cause an increase of the second term in 3.8.

The PID formalism

In figure 3.13 one can see the detector responses for leptons and hadrons. The threshold Čerenkov detector is also shown although not used in this analysis. For the calorimeter, one can see that leptons lose all their energy in an electromagnetic shower that results in an $\frac{E}{p}$ (the momentum in this ratio is the reconstructed momentum) distribution that is peaked around 1. Hadrons only lose a fraction of their energy through ionization that leads to an $\frac{E}{p}$ ratio that is lower than 1. Without preshower material in H2, one expects an energy deposition of passing leptons of 2 MeV in 1 cm of scintillator material because they are minimum ionizing

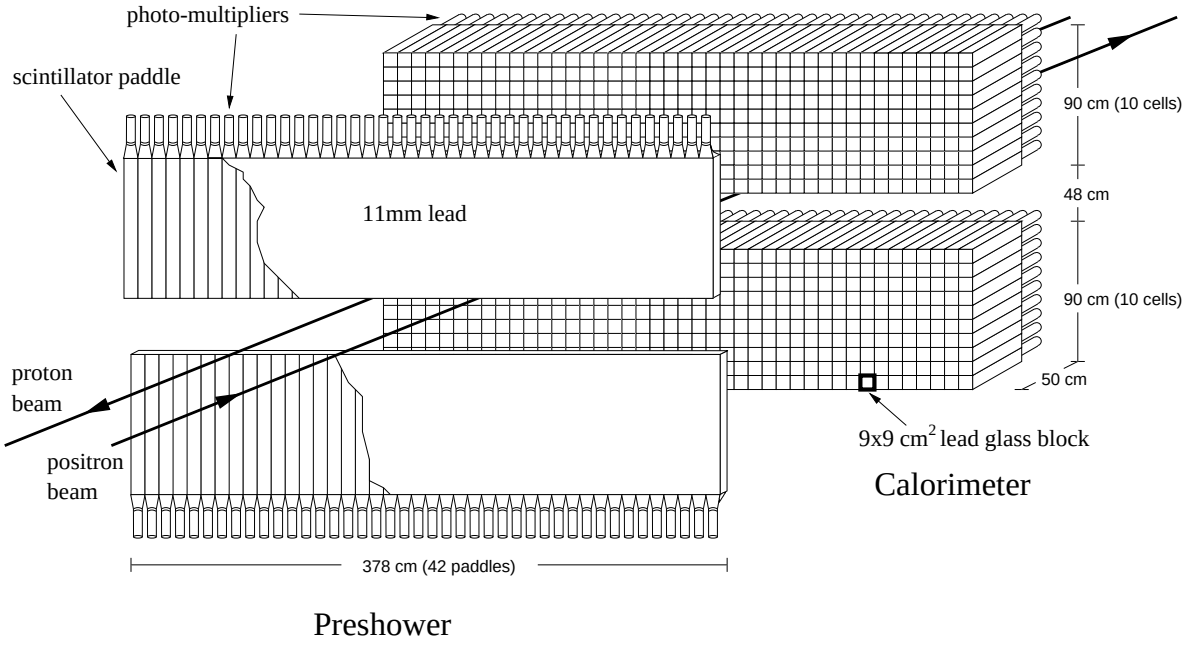

Figure 3.12: The preshower and the calorimeter.

particles. As one can see in figure 3.13, the preshower material, where the leptons shower, causes energy depositions up to 100 MeV in the scintillator material. Typical TRD responses for hadrons and leptons are also shown in figure 3.13. The truncated mean of the six modules is shown instead of the response of a single module. The truncated mean is the average of the five smallest signals. In this average the high energy tail of the hadronic response caused by δ-electrons (energetic electrons ejected from atoms in matter by the passage of ionizing particles) is significantly reduced, while the mean of the lepton signals remains virtually unchanged. The lepton distribution is broad and located at higher values than the hadron peak centered near the minimum ionizing energy of 11 keV for a 5 GeV pion.

The HERMES PID formalism is described in detail in [82] and is based on Bayes theorem. Conditional probabilities for a given track being a lepton or a hadron when the track momentum p, the polar angle θ, and the energy E deposited in a given detector are known, are given by:

$$P(H_{l(h)}|E,p,\theta) = \frac{P(H_{l(h)}|p,\theta)P(E|H_{l(h)},p,\theta)}{\sum_{i=l,h} P(H_i|p,\theta)P(E|H_i,p,\theta)}. \tag{3.9}$$

The hadron and lepton probabilities can then be acquired from: (i) $P(E|H_{l(h)},p,\theta)$ that are called "parent distributions"; these are the probabilities that a lepton (hadron) with momentum p and angular angle θ will deposit energy E in a given detector; and (ii) from $P(H_{l(h)}|p,\theta)$ that are called "particle fluxes" and are the probabilities that a track with momentum p and polar angle θ is a lepton (hadron). All the detector responses are assumed to be independent of θ, i.e., $P(E|H_{l(h)},p,\theta) = P(E|H_{l(h)},p)$ and

$$P(H_{l(h)}|E,p,\theta) = \frac{P(H_{l(h)}|p,\theta)P(E|H_{l(h)},p)}{\sum_{i=l,h} P(H_i|p,\theta)P(E|H_i,p)}. \tag{3.10}$$

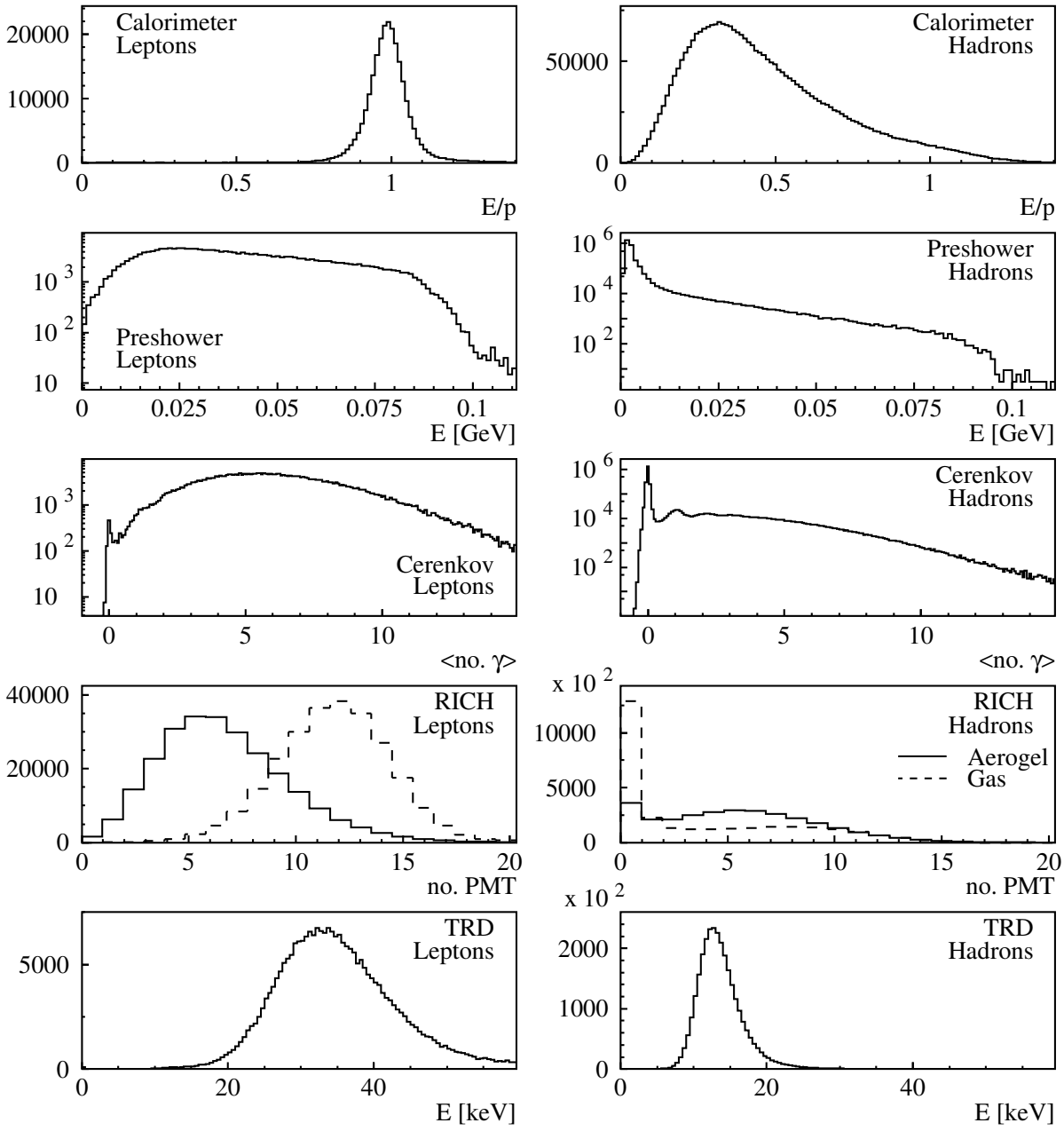

Figure 3.13: The PID detector responses for leptons and hadrons. To identify the hadrons and leptons in a certain detector, hard cuts were made on the other PID detectors. Although not used in this analysis, the threshold Čerenkov counter detector is also shown.

The probabilities $P(H|E,p,\theta)$ are combined into a logarithmic ratio called PID:

$$\mathrm{PID} \equiv \log \frac{P(H_l|E,p,\theta)}{P(H_h|E,p,\theta)}. \tag{3.11}$$

In terms of parent distributions and particle fluxes, the PID quantity becomes:

$$\mathrm{PID} = \log \frac{P(E|H_l,p)P(H_l|p,\theta)}{P(E|H_h,p)P(H_h|p,\theta)} = \mathrm{PID}_{det} - \log\Phi, \tag{3.12}$$

with

$$\mathrm{PID}_{det} \equiv \log \frac{P(E|H_l,p)}{P(E|H_h,p)}, \tag{3.13}$$

and

$$\Phi \equiv \frac{P(H_h|p,\theta)}{P(H_l|p,\theta)}. \tag{3.14}$$

This enables the possibility to combine the information of all PID detectors in one PID value:

$$\mathrm{PID}_{cal} + \mathrm{PID}_{pre} + \mathrm{PID}_{\mathrm{Rich}} + \mathrm{PID}_{trd}. \tag{3.15}$$

In HERMES the following PID values are commonly used:

$$\mathrm{PID2} \equiv \mathrm{PID}_{cal} + \mathrm{PID}_{pre} \tag{3.16}$$
$$\mathrm{PID3} \equiv \mathrm{PID}_{cal} + \mathrm{PID}_{pre} + \mathrm{PID}_{Rich} \tag{3.17}$$
$$\mathrm{PID5} \equiv \mathrm{PID}_{trd}, \tag{3.18}$$

that means that the full HERMES PID capabilities are in the combination:

$$\mathrm{PID} = \mathrm{PID3} + \mathrm{PID5} - \log\Phi. \tag{3.19}$$

The PID capabilities are illustrated in figure 3.14 and the impact of $\log\Phi$ in figure 3.15.

3.5.3 Triggering

The main detectors used for trigger generation at HERMES are H0, H1, H2, and the calorimeter. After delay and discrimination these (logical) signals are delivered to Programmable Logic Units (PLUs) that are used to make logical combinations between single detector triggers in order to generate first-level triggers, e.g., a DIS trigger, a photo-production trigger, and triggers for calibration and monitoring of the detectors. The first-level DIS trigger fires when there is a signal in H0, H1, and H2 above threshold, and an energy deposition in the calorimeter above 1.4 GeV when a normal target density is used, or 3.5 GeV when a high density target is used. All of this has to be in coincidence with a HERA beam-bunch signal. These first-level triggers are then delivered to (programmable) prescalers and scaler units. These (programmable units) ensure that a mix of useful (physics) events is dominating the total trigger rate. Finally, the triggers are passed to gate generators that generate the right triggers/gates for all detector readout modules.

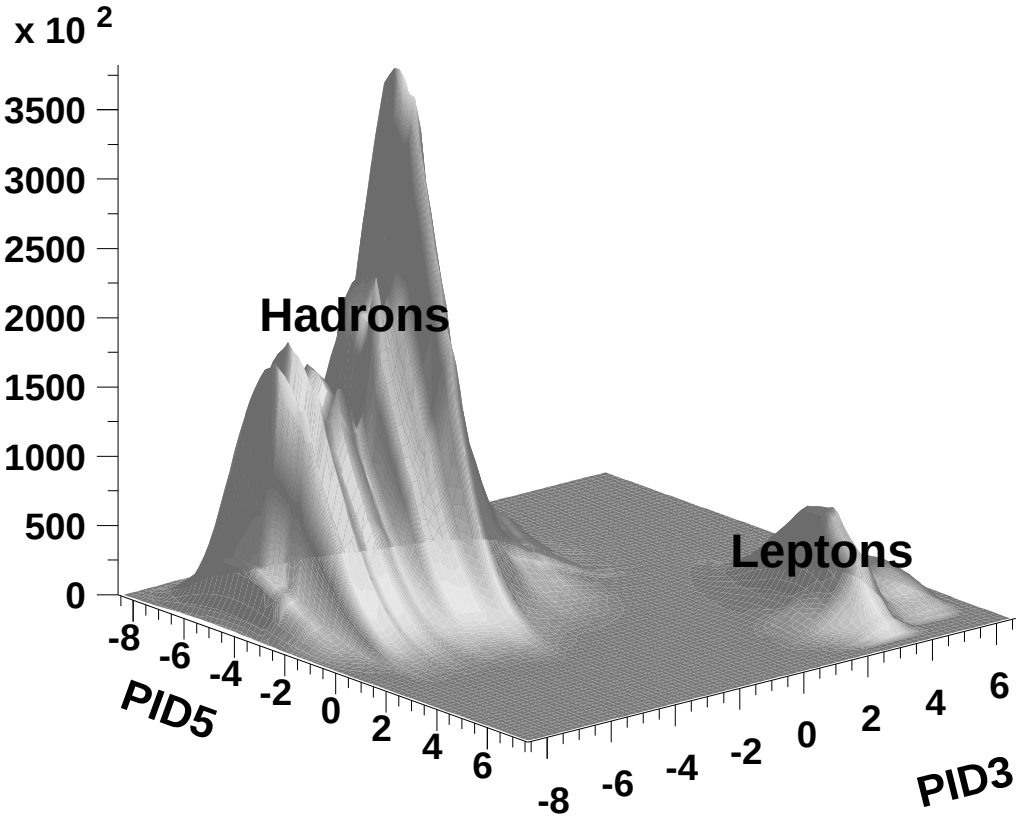

Figure 3.14: The correlation between PID3 and PID5 is shown. One can see that there is a clear separation between leptons and hadrons. Leptons have PID3 + PID5 > 0 while hadrons have PID3 + PID5 < 0.

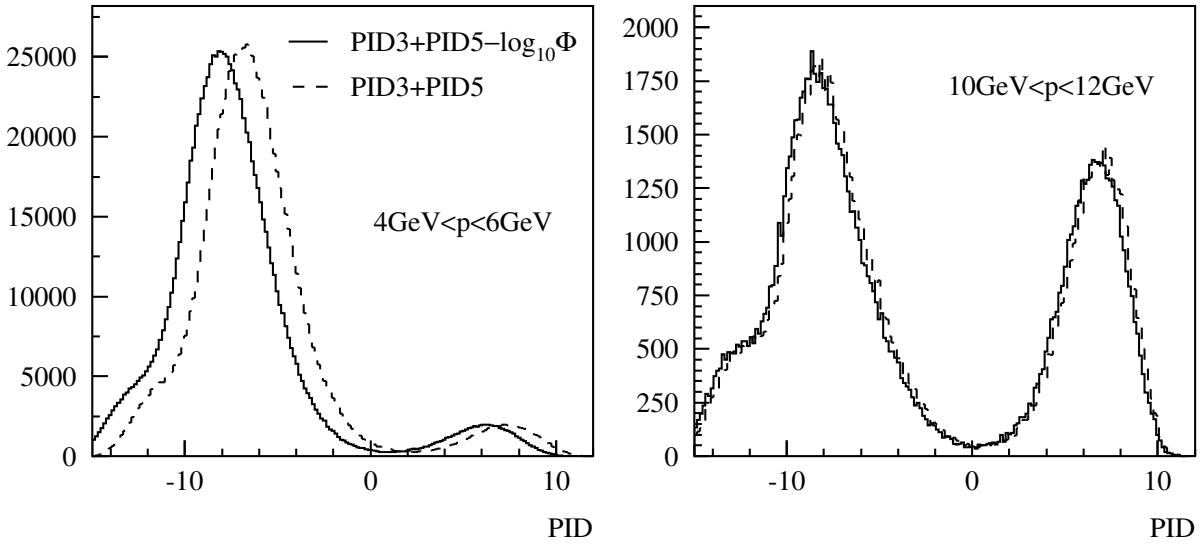

Figure 3.15: PID distribution for tracks with and without flux correction. Negative PID values identify hadrons, positive values leptons.

3.5.4 Data acquisition

The readout of the HERMES spectrometer consists basically of Time to Digital Converter (TDC) and Analog to Digital Converter (ADC) modules located in Fast Bus crates that are located in the Electronic Trailer (ET). A TDC module converts a time difference (e.g., between a bunch crossing and a detector hit) to a binary number, an ADC converts a signal maximum or the total charge of an analog signal to a binary number. All this raw information is bundled by the event builder in the Experimental Physics Input Output (EPIO) format and stored on hard disks and on tapes. In addition, so called "slow control" data is recorded, e.g., detector temperatures, detector high voltages, polarization measurements, scaler info, luminosity measurements, etc. This data is recorded every $\sim$10 seconds and defines a so called "burst". During data taking all data is written to a file every $\sim$500 MBytes: this is called a "run". At the end of each HERA fill slow control data and EPIO raw data are transferred to a taping robot using a Fast Distributed Data Interface (FDDI) link. A fill is determined by the storage time of the HERA lepton beam. A schematic overview of these steps is shown in figure 3.17 (top).

3.5.5 Tracking and μDSTs production

The geometry, mapping, and calibration information of each detector is made available for the HERMES DeCoder (HDC) by Distributed Adamo Database (DAD) servers. Using this information together with detector ADC/TDC information (stored in EPIO format) HDC determines detector hit positions and energy depositions. From this point on all information is stored in an ADAMO (Aleph DAta MOdel) [84] database. The output of HDC is used by the HERMES ReConstruction software (HRC) that reconstructs the particle tracks, the particle momenta, and particle types (cf. section 3.5.2). The track finding is based on a tree search pattern recognition algorithm. It uses a data bank, where 126 million tracks are stored, to compare to data with artificially reduced detector resolution. Each step the detector resolution is doubled, as illustrated in figure 3.16. First the tracks in each detector projection are reconstructed (X, U, and V) in front (FCs) and back part (BCs), then a 3D track is reconstructed (in front and back part). Finally these partial tracks are then combined with tracks reconstructed using hits in the MCs (track inside the magnet) using several methods described in [72] but usually these partial tracks are combined using the "forced bridge" method. In this method two tracks are combined (one track in the front part and one track in the back part) if they meet in the center of the magnet. Plots showing the resolution of the track reconstruction are in figure 3.18. After reconstruction this data is merged/synchronized with the slow control data using time stamps to the so called μDSTs (Data Summary Tape). These μDSTs are used by the analyzer to do her/his analysis. A schematic overview of all the steps from decoding until μDSTs can be seen in figure 3.17 (bottom).

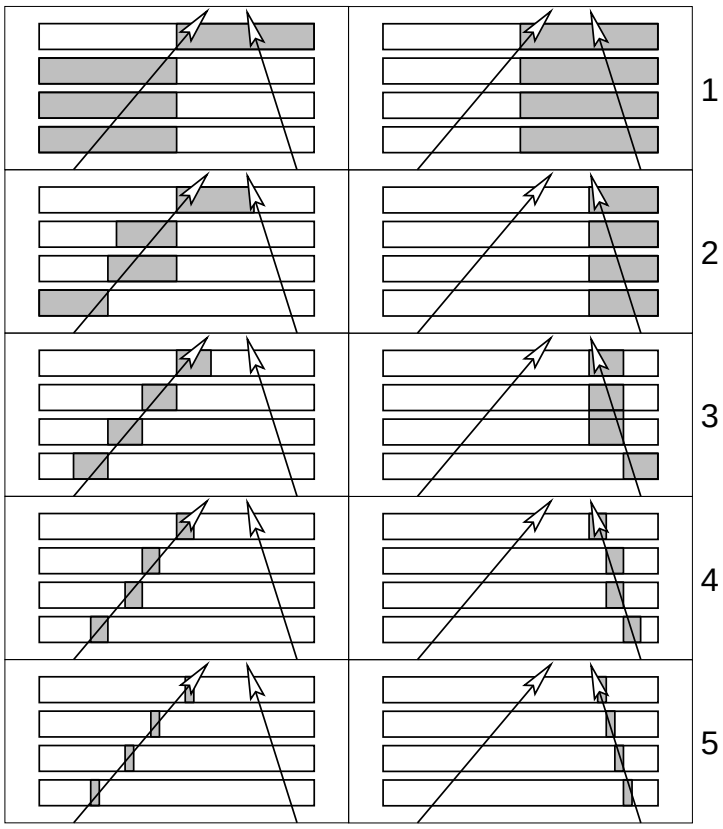

Figure 3.16: Treesearch for two tracks. The detector pattern is matched against the pattern data bank with increasing resolution (from top to bottom).

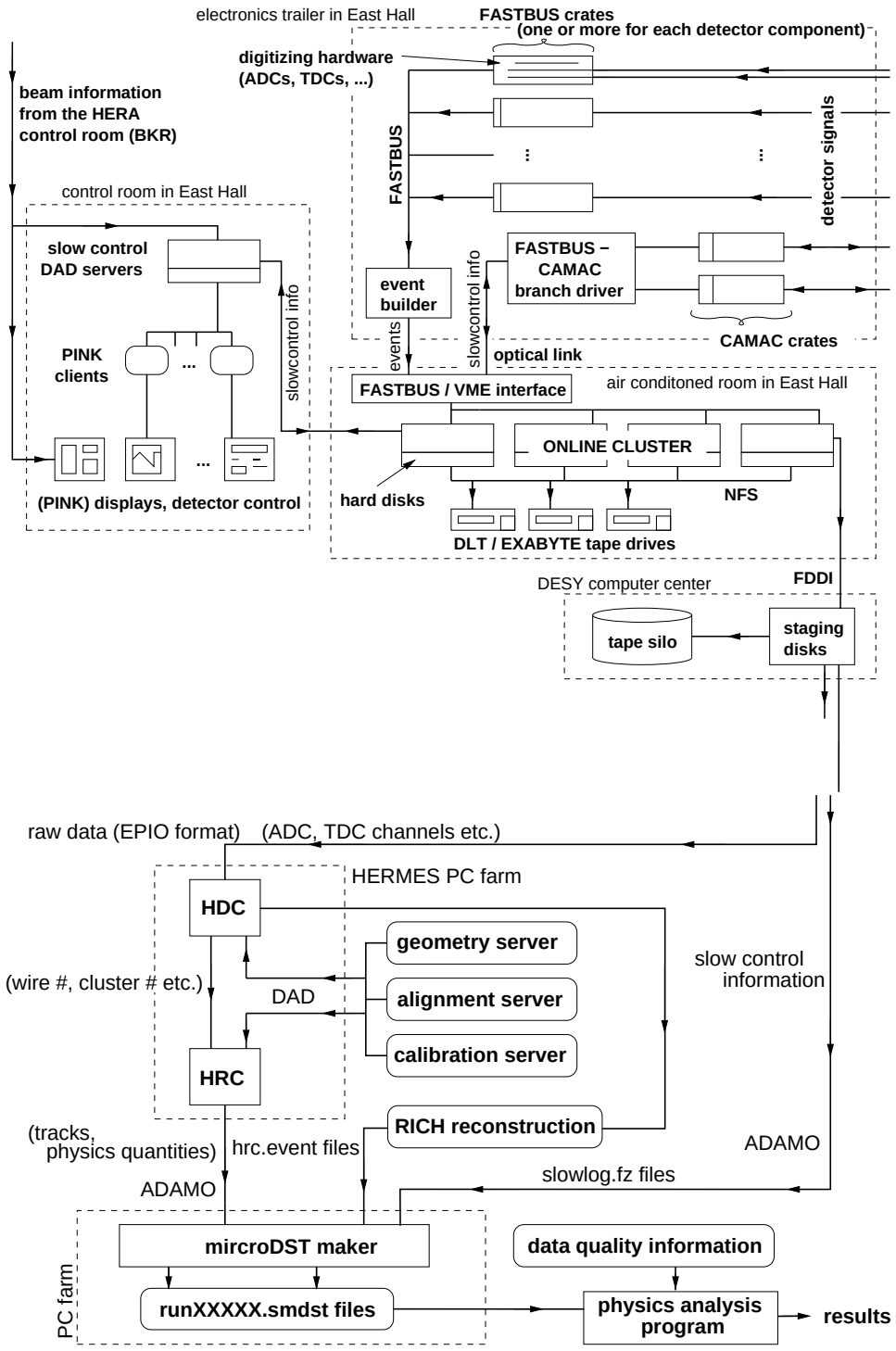

Figure 3.17: Diagram of the data acquisition flow (top) and of the offline μDST production (bottom) [83].

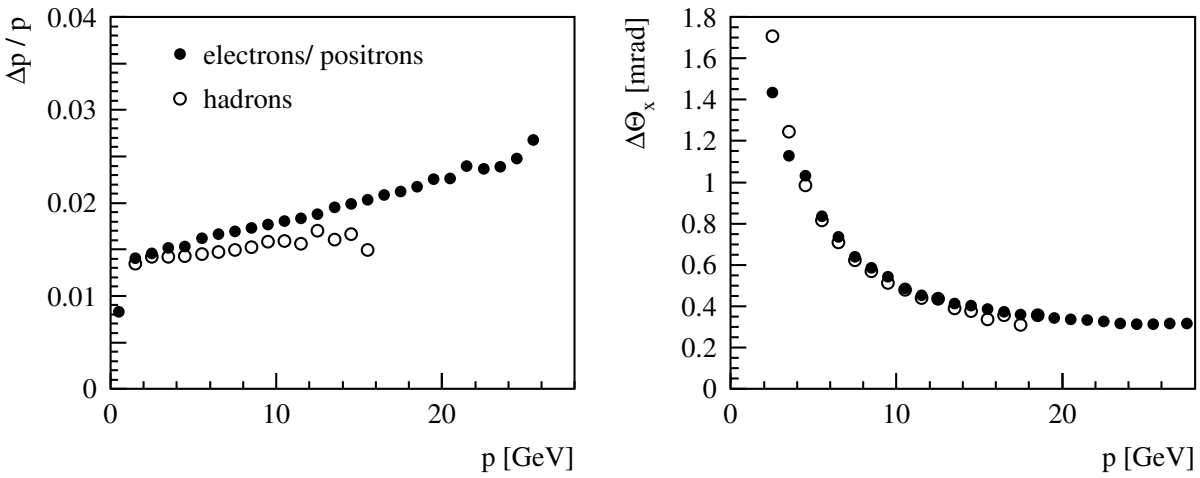

Figure 3.18: Momentum and angular θ_x resolution as a function of the momentum of the reconstructed particle.

Chapter 4

The HERMES recoil detector

In 2001 the HERMES collaboration decided to build the HERMES recoil detector around the target in order to detect recoiling protons and make event identification more exclusive. The physics prospects and motivation of this detector are described in chapter 2.2 and in more detail in [85]. The recoil detector is designed to study exclusive deeply virtual Compton scattering. Without the detection of the recoil proton one had to establish exclusivity by using constraints on the missing mass; with the recoil detector one can detect the recoil proton and establish exclusivity at the event level. Therefore, the recoil detector has to be able to veto background coming from the lowest excited state of the proton: the Δ-resonance, by detecting its decay particles. The higher resonances can be excluded by a cut on the invariant mass. In order to fulfill these requirements the recoil detector must be able to detect recoil protons with a momentum between 50 and 1400 MeV. In order to veto protons coming from Δ-resonance decays one should be able to detect decay protons with a momentum up to 1.4 GeV, charged pions with a momentum up to 800 MeV, and photons (from π^0 decays). According to a Monte Carlo study more statistics are contained in these kinematic regions.

The HERMES recoil detector consists of five parts (from the beam pipe out): the target, the silicon strip detector, the scintillating fiber tracker, the photon-detector, and the magnet. A detailed drawing of the recoil detector (the magnet not included) can be seen in figure 4.1.

After 3 years of research and development, the recoil detector was installed at the end of 2005 and the first data were taken in February 2006. A technical drawing of the HERMES spectrometer with the recoil detector included is shown in figure 4.2.

In this chapter the hardware components of the HERMES recoil detector are described from inside out, starting with the new (unpolarized) target. More attention will be spent on the recoil photon-detector because research and development work for this detector was done within the scope of this thesis.

4.1 The HERMES recoil target

The Hermes recoil target has the same dimensions as the target described in section 3.3, except that the volume containing the gas is 15 cm long instead of 40 cm. This was done to match the length of the Silicon detector. Due to the geometry of the recoil detector, there was no more space for the ABS and the BRP. Therefore, the target gas could no longer be polarized.

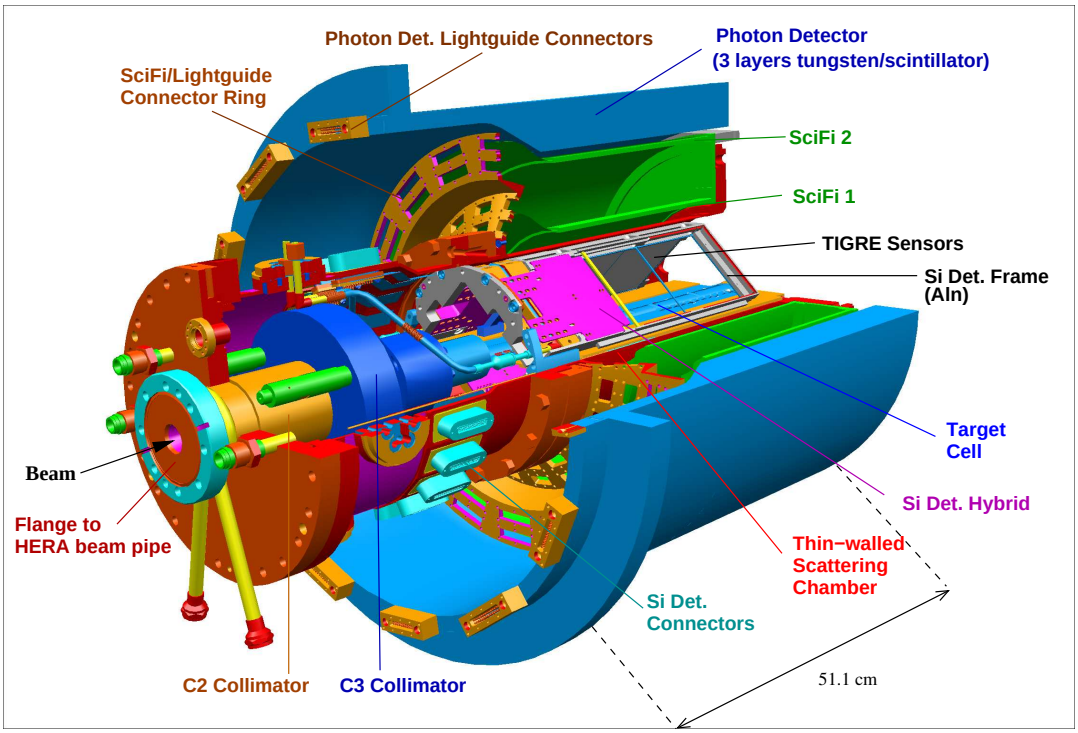

Figure 4.1: Detailed drawing of the HERMES recoil detector.

This means that it is no longer necessary to cool the target with liquid helium to improve the polarization. The target cell is still cooled with water. This cooling reduces mechanical stress caused by temperature gradients and in second order it keeps the cell temperature as constant as possible in order to have a target gas density that is better controllable. The UGFS described in section 3.3.2 is still used to inject target gas. A picture of the target is shown in figure 4.3.

4.2 The recoil silicon-strip detector

The recoil silicon-strip detector [86], also called silicon detector, is designed to detect recoil protons with very low momentum (between 135 MeV and 0.5 GeV). This detector is placed inside the beam vacuum (10^{-9} mbar) because the lower momentum cut-off is determined by the amount of material between the interaction point and the detector. In this momentum range the energy deposited in the silicon by a proton is a steep function of the momentum ($1/\beta^2$ term of the Bethe formula, cf. figure 4.4). Therefore, the proton momentum can be computed from the energy deposition in the two silicon layers.

The detector consists of 16 silicon sensors (TIGRE sensors from Micron Semiconductor Ltd.) that are organized in a double-layered diamond shape around the target, illustrated in figure 4.5. They cover a polar angular acceptance between 0.1 and 1.35 rad. Each silicon sensor measures 99 $\times$ 99 mm^2 and is double-sided. There is an n and a p side (an n-type material is doped so that the electrons can move freely and a p-type material is doped so that the holes can move freely). On each side there are 128 silicon strips. The strips on one side are

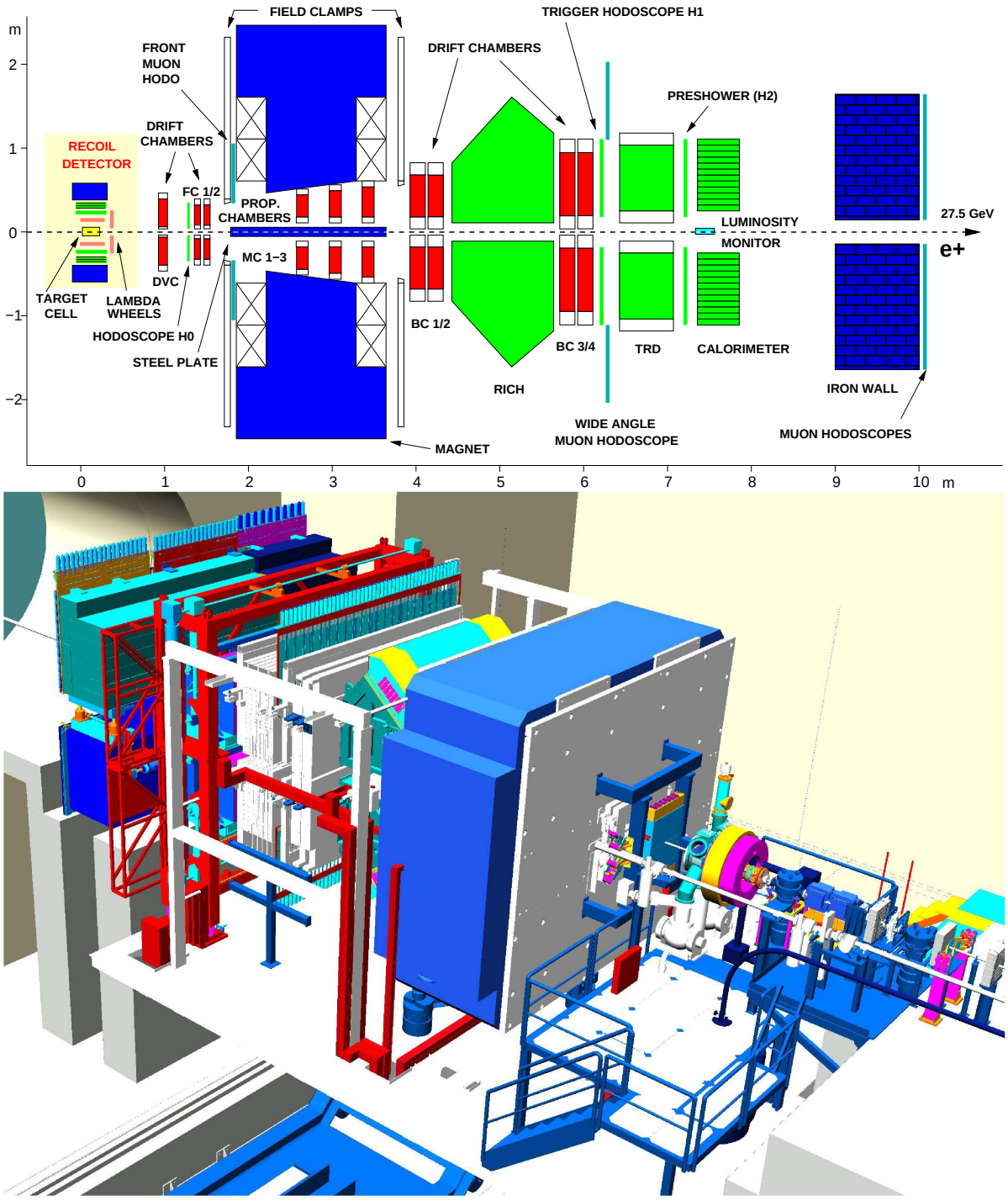

Figure 4.2: Drawings of the HERMES spectrometer with the recoil detector. In the lower drawing the recoil detector is inside the magenta cylinder that represents the cooling vessel of the magnet. Inside the magnet are the photon-detector, the scintillating fiber tracker, and the silicon detector. These detectors are not visible. The left-right direction in the upper drawing corresponds with direction lower-right to upper-left direction in the lower drawing.

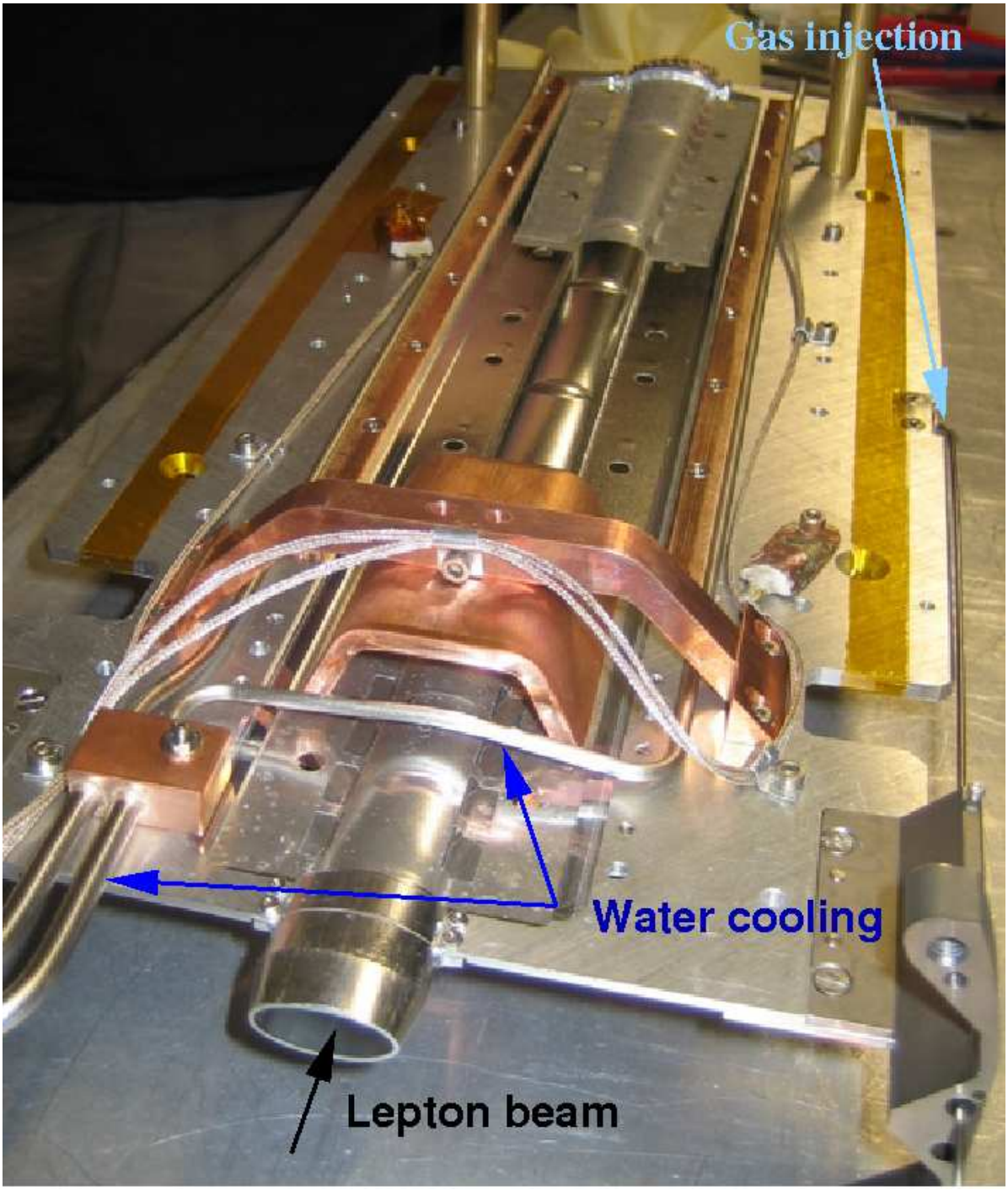

Figure 4.3: A picture of the HERMES recoil target.

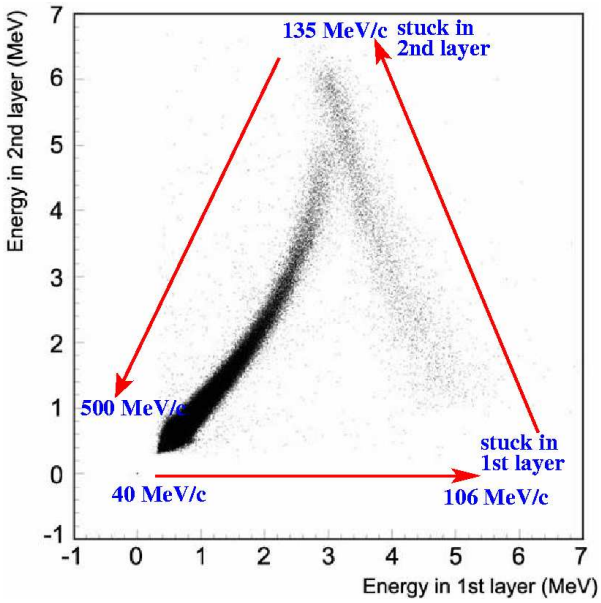

Figure 4.4: Deposited energy in both silicon detector layers as a function of proton momentum. A proton with a momentum between 40 and 106 MeV will be stopped in the first layer. There are no data points of these protons in the plot because a signal was required in both layers. A proton with momentum between 106 and 136 MeV will be stopped in the second layer. Protons with higher momentum will pass both layers.

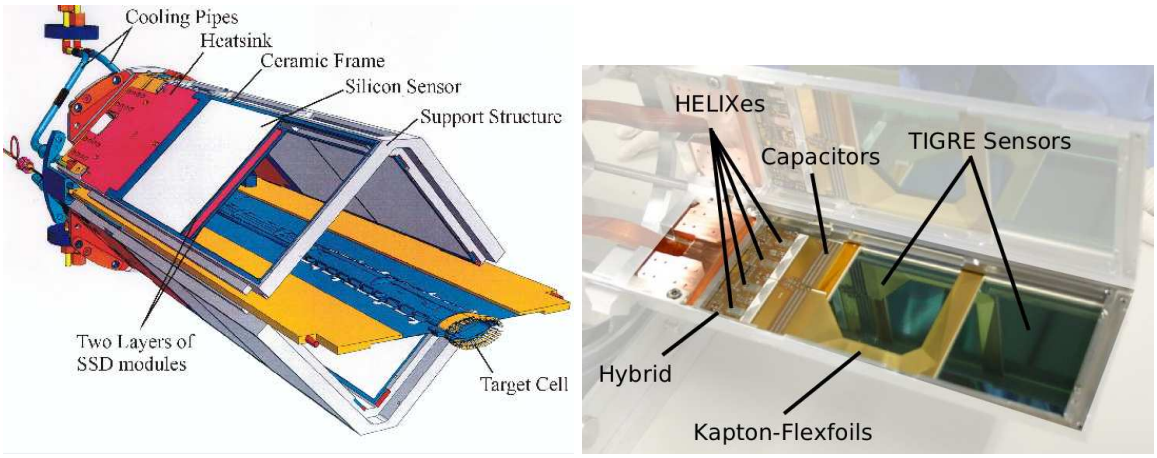

Figure 4.5: On the left side a drawing of the target plus the diamond shaped silicon detector and on the right side one silicon detector module is shown.

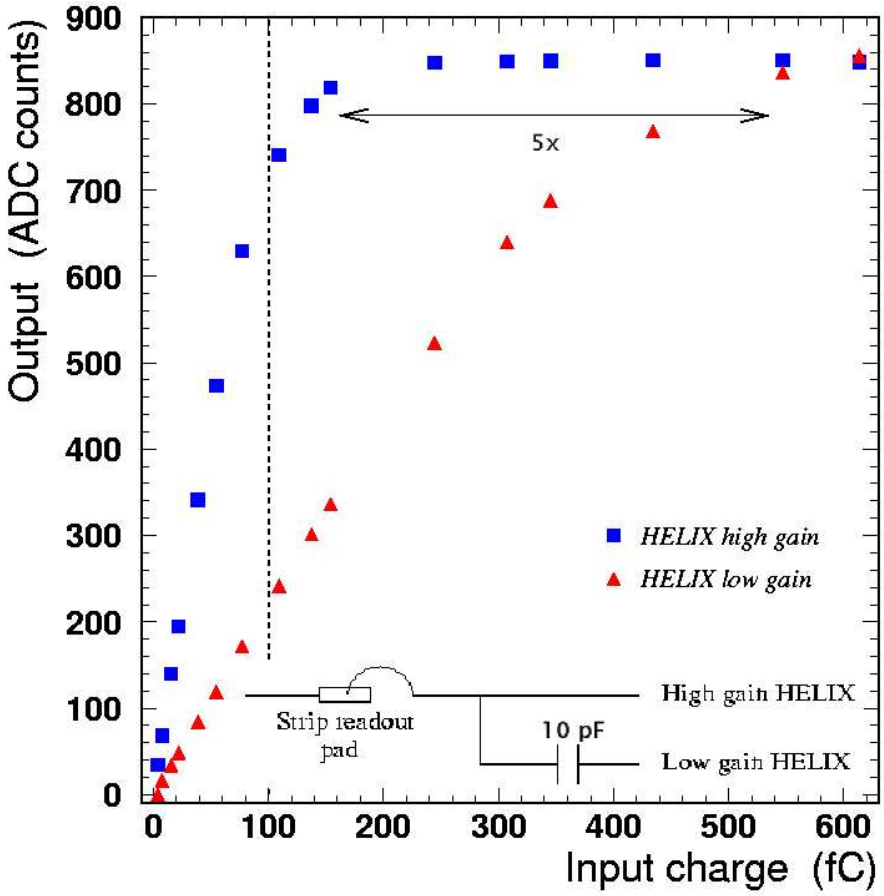

Figure 4.6: Illustration of the increase of dynamic range of the silicon detector. Every silicon strip is connected with two readout channels, one high gain channel and one low gain channel through a capacitor. The capacitor can be changed to adjust the dynamic range.

oriented perpendicularly to the strips on the other side. The strip pitch is 758 μm and the strip separation is 56 μm. The double-layered structure allows a maximum of two space points per track, with a resolution of 222 μm.

The dynamic range of the analog readout was drastically increased by connecting every silicon strip to two readout channels of a HELIX chip where one connection happens via a serial coupling capacitor [86] that causes a charge division between the two readout channels. There is a low-gain channel and a high-gain channel. The capacitor can be changed to adjust the dynamic range. As long as the high-gain channel is not saturated its signal is used. If the high-gain channel is saturated, the low gain channel is used. The principle of this increase in dynamic range is illustrated in figure 4.6. In this way the silicon detector is able to cover the range of $\sim 0 - 7$ MeV energy deposition.

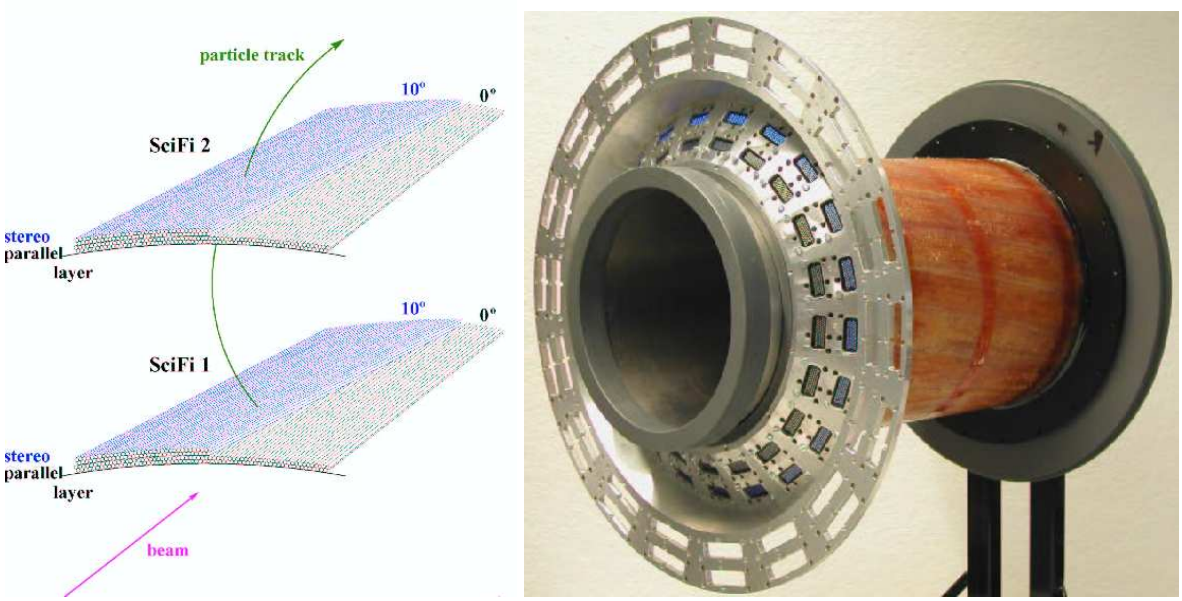

Figure 4.7: A drawing of the two SciFi barrels of the scintillating fiber tracker is shown on the left side. The right side shows a picture of the SciFi detector with only the inner barrel in place.

4.3 The recoil scintillating fiber tracker

The HERMES recoil Scintillating Fiber Tracker, also called SciFi and SFT, is located outside the beam vacuum and inside the recoil photon-detector as can be seen in figure 4.1. It consists of two "barrels" (SciFi1 and SciFi2 in figure 4.1 and 4.7). Each barrel is built out of four layers of scintillating fibers (1 mm diameter), two layers with the fibers oriented parallel to the lepton beam, and two stereo layers where the fibers have a 10° angle with respect to the parallel layer. The SciFi detector has a polar angular acceptance between 0.7 and 1.35 rad.

The scintillating fibers are read out by multi-anode PMTs (see section 4.4.4). In the inner barrel every fiber is read out by one read-out channel, in the outer barrel two adjacent fibers are read out by one read-out channel. This results in a ϕ-resolution of 0.008 rad. This detector is able to detect recoil protons with a momentum between 0.25 and 1.6 GeV and has particle identification capabilities for momenta from 0.25 to 0.40 GeV. This is illustrated in figure 4.8. Protons with lower momenta are only detected by the silicon detector while pions with a lower momentum are detected by both the silicon and the SciFi detector. For momenta higher than 0.4 GeV the photon-detector improves the PID (cf. section 4.4.9). In figure 4.9 the kinematic coverage of the Silicon and the SciFi detector for recoil protons based on a Monte Carlo simulation is shown. For exclusive ρ^0 production, deeply virtual Compton scattering, and Bethe-Heitler scattering the coverage is good, while for Δ-resonance decays the coverage is around 50%.

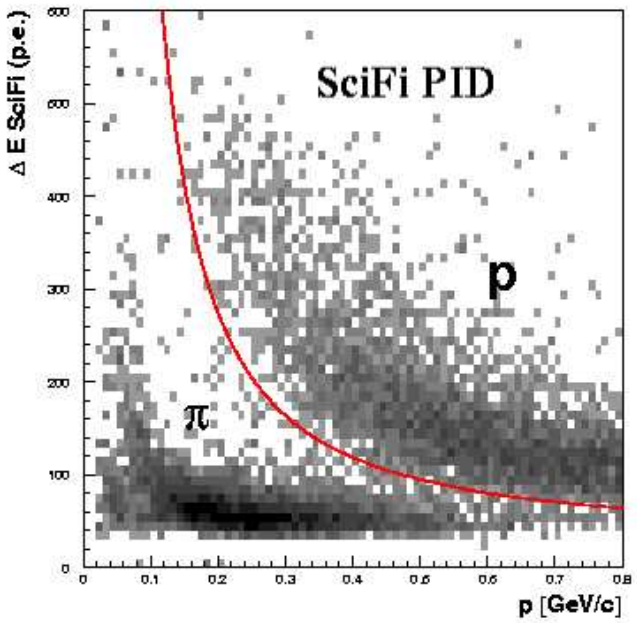

Figure 4.8: Monte Carlo simulation of the energy deposition versus momentum for pions and protons from Δ-decay. The line indicates a possible hyperbolic PID cut. The energy deposition is given in photo-electrons, the momentum measurement is provided by the SciFi detector.

4.4 The recoil photon-detector

Test calibrations and test-beam data are shown in this section. This was one of the main activities during this thesis.

The recoil Photon-Detector's (PD) main objectives are to detect photons coming from Δ^+ decays ($\Delta^+ \rightarrow p\pi^0 \rightarrow p\gamma\gamma$). To reconstruct the π^0 in case both decay photons are detected and to enhance proton/pion PID for momenta higher than 600 MeV. The photon-detector is also able to generate a trigger for cosmic rays.

The actual detector is 288 mm long (acceptance: $0.78 < \theta < 1.90$ rad) and consists of six layers. From inside out, there is 6.3 mm of tungsten (one radiation length corresponds to 3.5 mm of tungsten) showering material, a layer of 60 scintillator strips oriented parallel with the lepton-beam direction, a layer of 3.5 mm of tungsten, a layer of 44 scintillator strips that make an angle of 44.58° with the lepton-beam direction, again a layer of 3.5 mm of tungsten, and finally there is a layer of 44 scintillator strips that make an angle of -46.55° with the lepton beam direction. The inner scintillator layer is also called the A-layer, the middle one the B-layer, and the outer one the C-layer. Every scintillator is connected to two wave-length shifters that end in a connector ring on the edge of the detector (cf. figure 4.10). These connectors connect the wave-length shifters to light guides that are connected to PMTs. The PMTs are then read out by charge sensitive ADCs. In the next sections the different components are discussed in more detail.

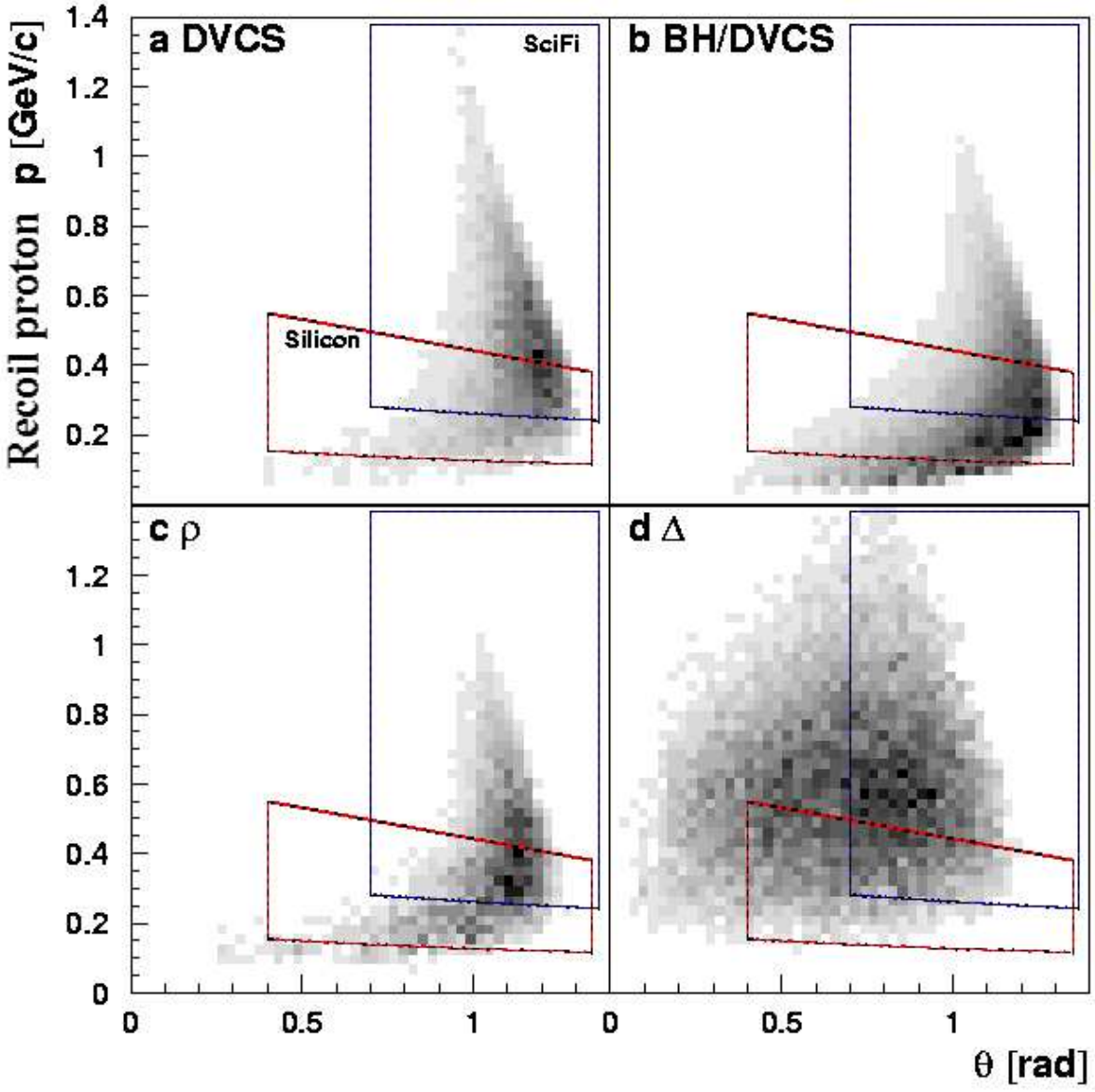

Figure 4.9: Recoil proton momentum versus polar angle with respect to the beam for (a) deeply virtual Compton scattering only, (b) Bethe-Heitler and deeply virtual Compton scattering, (c) exclusive ρ^0 production, and (d) Δ decays. The lines indicate the kinematic coverage by the Silicon detector (red) and the SciFi detector (blue).

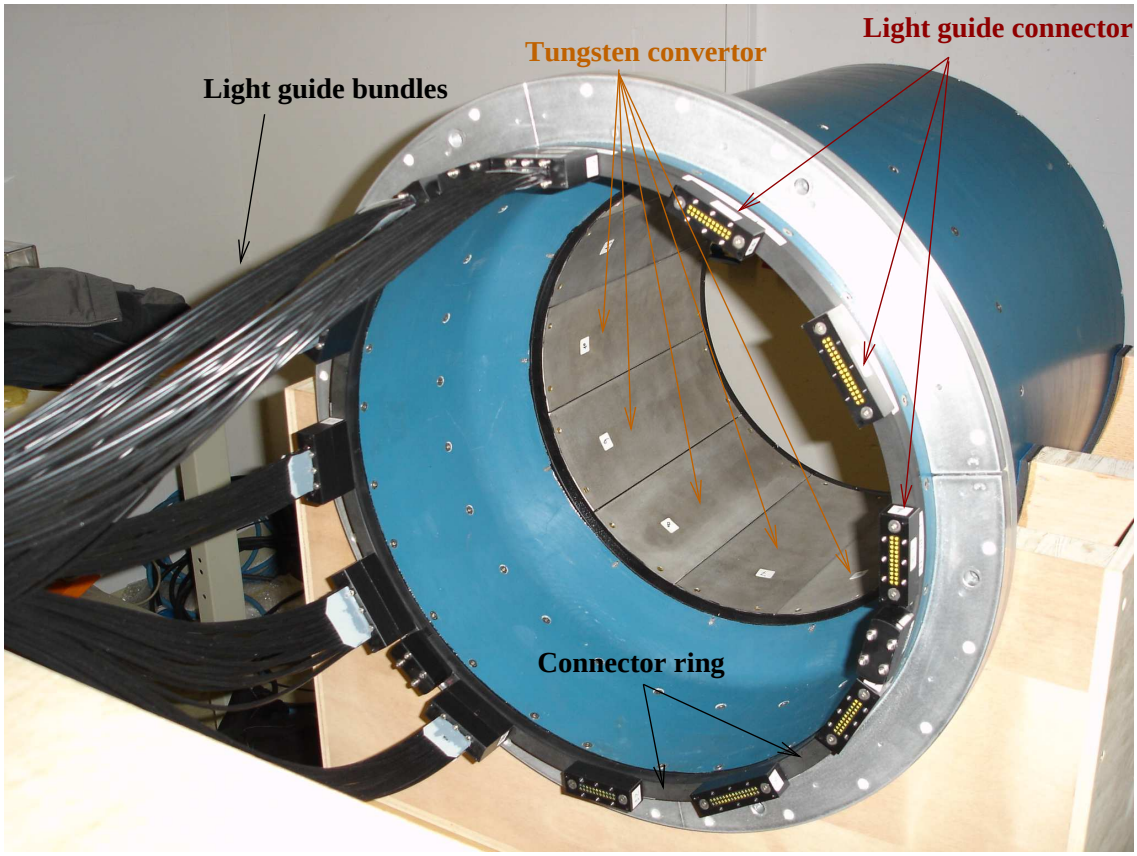

Figure 4.10: The recoil photon-detector with 6 light-guide bundles connected.

4.4.1 The converter

Pure industrial tungsten is used as a preshower converter. Each of the three converters is segmented in 12 pieces (some segments of the A-layer converter can be seen in fig. 4.10). This is done to protect the photon-detector from too large electromagnetic forces induced during a possible magnet quench. The thickness of the converter layers was chosen to maximize the π^0 decay photon detection efficiency. The optimized detection efficiency was obtained using Monte Carlo simulations. The thickness of the converters was determined to be 1.8, 1.0, and 1.0 radiation lengths for the A, B, and C layer respectively.

4.4.2 Scintillators and wavelength shifters

The scintillator material used is BC-408 from Bicron [87]. Its emission spectrum peaks between 420 and 440 nm (cf. figure 4.11). Each scintillator strip in the A-layer has a trapezoidal form with basic dimensions of $21 \times 10 \times 275$ mm^3. The scintillator strips in the B and C layers have the same dimensions as the strips used for the A layer (but they are rectangular, not trapezoidal) except that they are 397 mm long and that they are bent to obtain the right stereo angle of 44.58° and -46.55° for the B and C layer, respectively. This configuration yields a polar resolution of about 8°, as can be seen in figure 4.12. The light attenuation in a scintillator strip can be seen in figure 4.13. An exponential was fit and an attenuation length of 280 mm was obtained. The influence of the bending procedure on the light attenuation properties are shown in figure 4.14. The light attenuation for the bend and not-bend scintillator bar are the same. Finally the scintillator strips are painted with reflective paint. This can be seen in figure 4.15.

On each side of a scintillator bar, wavelength shifters of type BCF-91A [88] are glued in a groove along both sides of each strip, as can be seen in figure 4.16. One end of the wavelength shifter ends in a connector (cf. figure 4.10), the other end is painted with reflective paint. The improvement of the signal caused by the reflective paint is shown in figure 4.17. It can be seen that adding the reflective paint causes an increase in gain with a factor of 2. If no wavelength shifters are used and the scintillator bar is directly read out by a PMT the gain would be 3 times higher than the configuration with painted scintillator bars with wavelength shifters. A light-attenuation measurement of the wave-length shifters is shown in figure 4.18. An attenuation length of 362.5 mm was measured. The increase in signal near the end of the fiber (x >110 mm) is caused by reflection at the mirrored fiber edge. The absorption and emission spectrum of the wave length shifters is plotted in figure 4.11. It can be seen that the absorption spectrum of the wave length shifters fit the frequency of the photons that are emitted by the scintillator very well. Although this construction yields less light than a contruction with scintillators directly read out by PMTs, it was chosen in this way because of a lack of space and the fact that the PMTs would then be very close to the magnet. This means that they would have to be shielded heavily.

A picture of the detector in construction is shown in figure 4.15 with the scintillator bars and wavelength shifters visible.

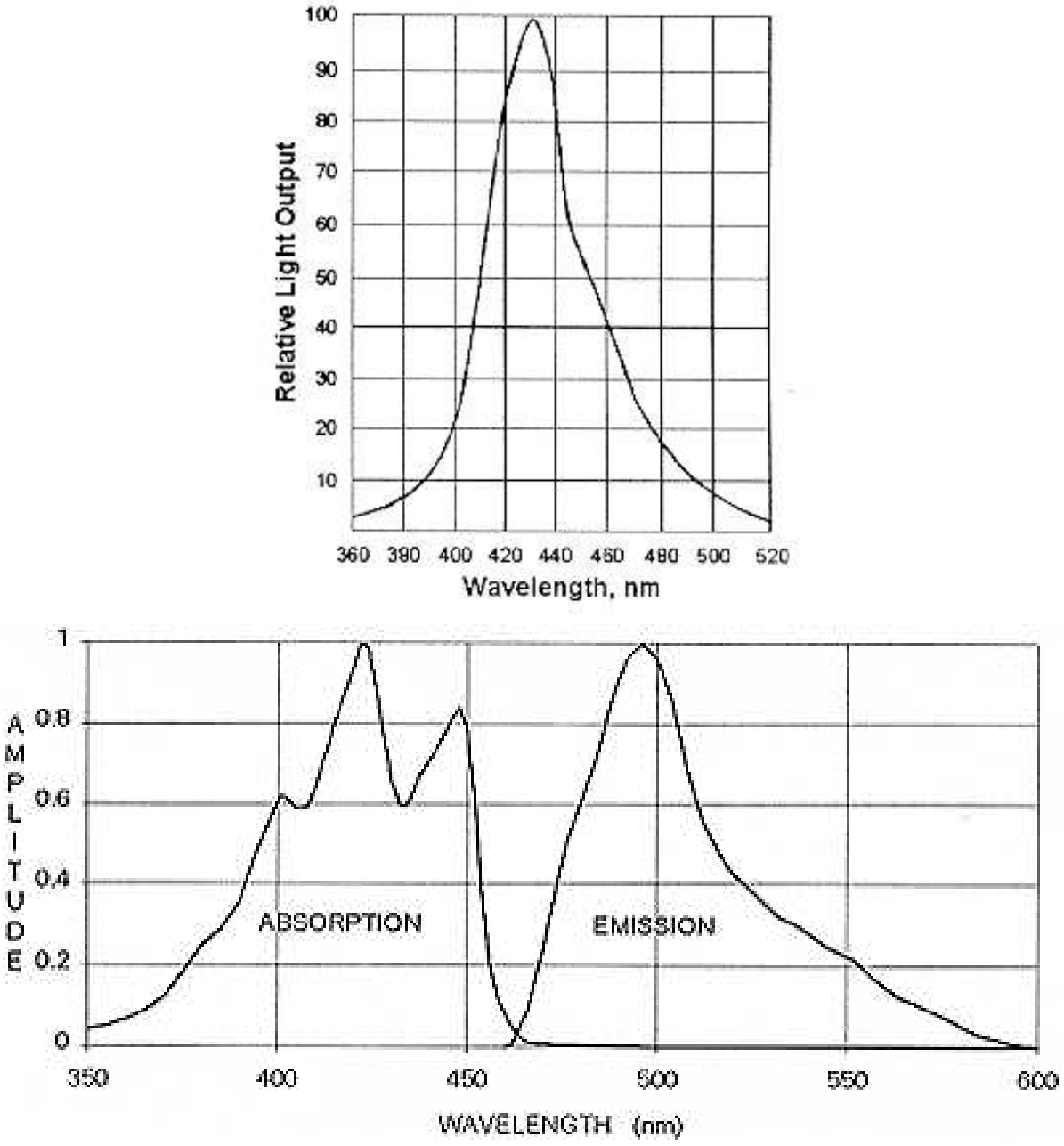

Figure 4.11: The upper plot shows the emission spectrum of the BC-408 scintillator. The lower one shows the absorption and emission spectrum of the BCF-91A wavelength shifter that is glued to the scintillator.

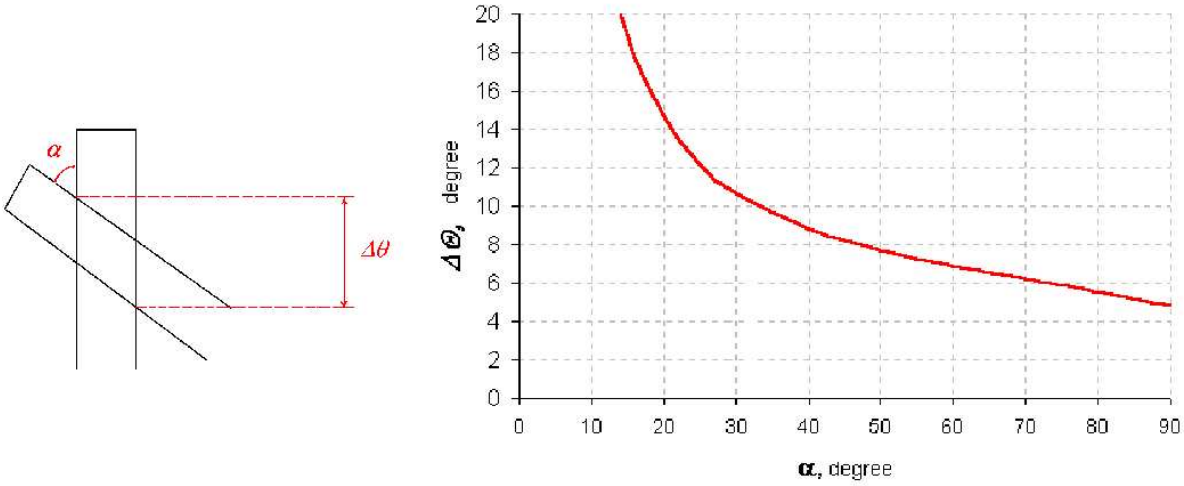

Figure 4.12: Angular resolution as a function of the angle between two strips in subsequent layers.

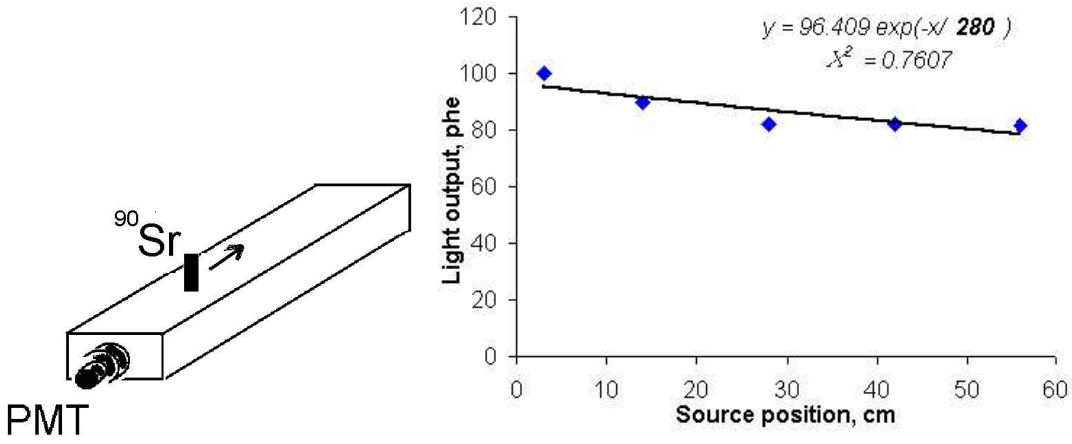

Figure 4.13: Light attenuation test of a BC-408 scintillator strip using a ^{90}Sr source.

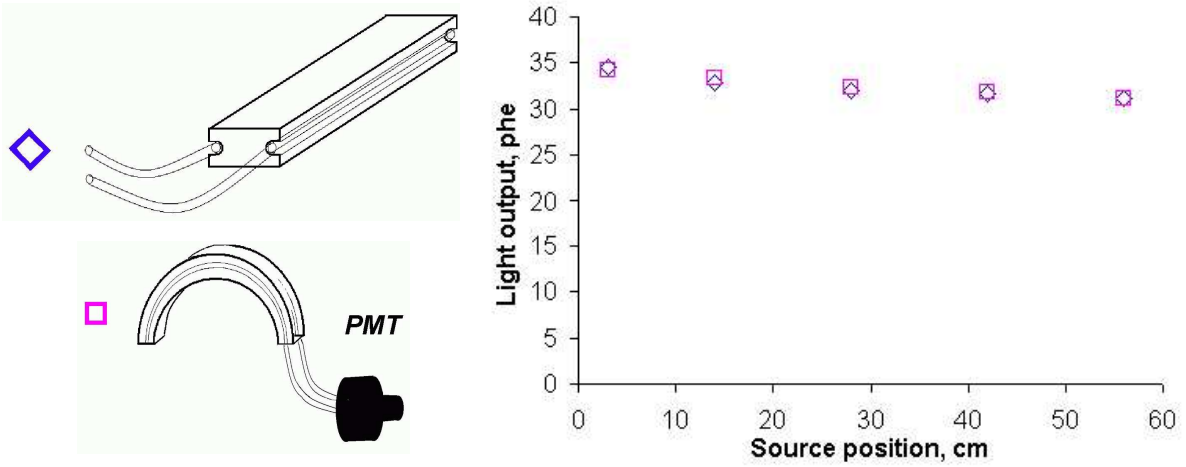

Figure 4.14: Light attenuation test using a ^{90}Sr source with bent and not bent scintillator strips with the wavelength shifting fibers attached.

4.4.3 Light-guides

The light coming out of the wavelength shifters is guided towards PMTs through 2 meter long light-guides. The light-guides are encapsulated in black plastic to protect them form outside photons. Light belonging to one connector are called a light-guide bundle. This can be seen in figure 4.10. The light-guides used are from Bicron, type BCF-98 [89]. The light-guides allow the PMTs to be placed far enough from the recoil magnet so that they can function properly (with the right magnetic shielding).

4.4.4 The PMTs

The light-guides are read out by 6 Hamamatsu H7546 PMTs [90]. The connection of the light-guides to the PMTs happens through a Poly-Oxy-Methylene (POM) matrix. A technical drawing of the connector can be found in figure 4.19. The matrix allows a maximum of 64 light-guides to be aligned on the PMT's entrance window. The alignment of this matrix on the PMT was done by performing several optical cross-talk measurements. In these measurements the optical cross-talk between neighboring pixels on the PMT was measured for different alignments of the matrix by only illuminating four pixels (in the connector) close to the corners of the matrix. The alignment with the minimum amount of cross-talk was chosen.

The PMTs have 64 anodes each. A schematic drawing can be seen in figure 4.20. Two light guides from one scintillator strip will be read out by two anodes located next to each other on the PMT. The mapping of the light-guides on the PMTs is done as follows. Only light-guides coming from the same layer go to the same PMT. Light-guides coming from the same scintillater will be put next to each other on the PMT entrance window. Light-guides coming from neightbouring scintillator strips never end up next to each other on the PMT entrance window. In this way the probability that two neighboring strips (on the PMT) fire in the same event is minimized. This makes it easier to study (and correct) for cross-talk in the

Figure 4.15: Photograph of the unfinished photon-detector. The wave-length shifters (green) and scintillator strips (white) are visible. The black fibers are light-guides for the Gain Monitoring System.

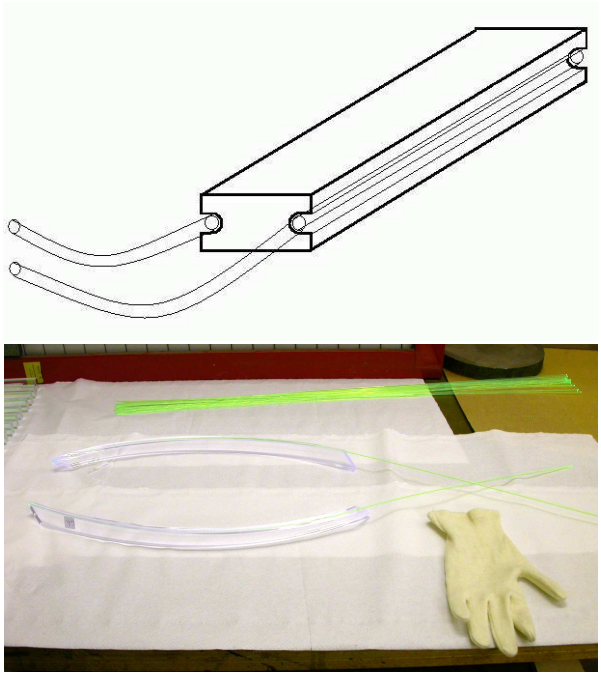

Figure 4.16: Sketch (upper) and photograph (lower) of light-guides glued to the scintillator bar. The green fibers are the wave length shifters.

PMT. The strips of one layer are connected to two PMTs, the left side of a layer is read out by a PMT that is located on the left side of the beam and the analogue is done for the right side of a layer.

4.4.5 The recoil detector PMT test stand

The same PMT type is used for both the PD and the Scintillating Fiber detector. A test stand was set up in order to test the PMTs and compare the results with the specifications provided by the supplier. The PMT test stand is described below.

Overview of the Setup

The PMT test stand was developed to determine a suitable operating voltage, to measure the cathode uniformity, and the gain linearity of the 64 channel Hamamatsu H7546 PMTs. These PMTs are delivered together with a base that divides the applied voltage over the anodes. The photon-detector uses 6 such PMTs for its readout; the SciFi Detector needs 78 tubes. The PMTs bought for the photon-detector have the standard Hamamatsu base and are of the "old" type (H7546B) that has a different anode output pinning compared to the new type bought for the SciFi Detector. The PMTs for the latter were also ordered with tighter specifications of cathode uniformity than the standard tubes and with a different base that is optimized for a better gain linearity. The "old" type was choosen for the photon-detector for budgetary reasons.

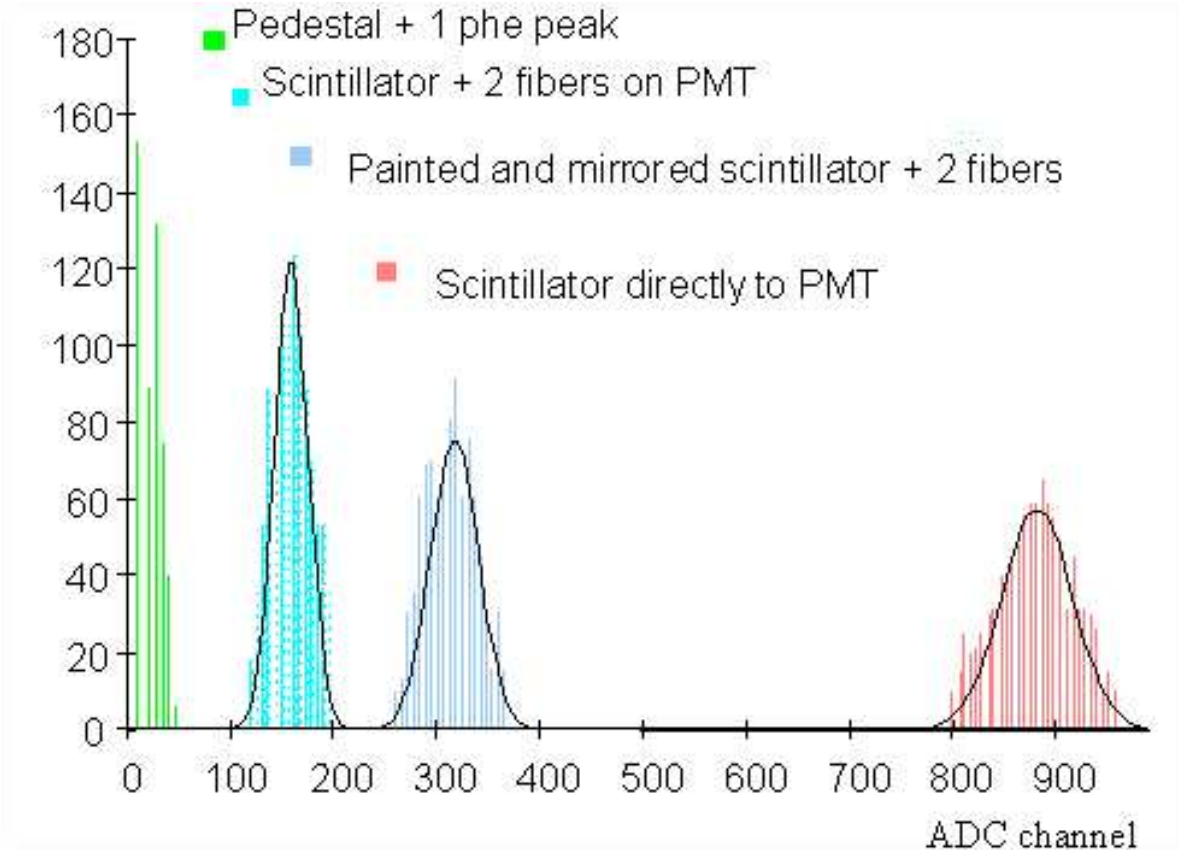

Figure 4.17: Measured light output for different configurations of the scintillator plus wavelength shifters system.

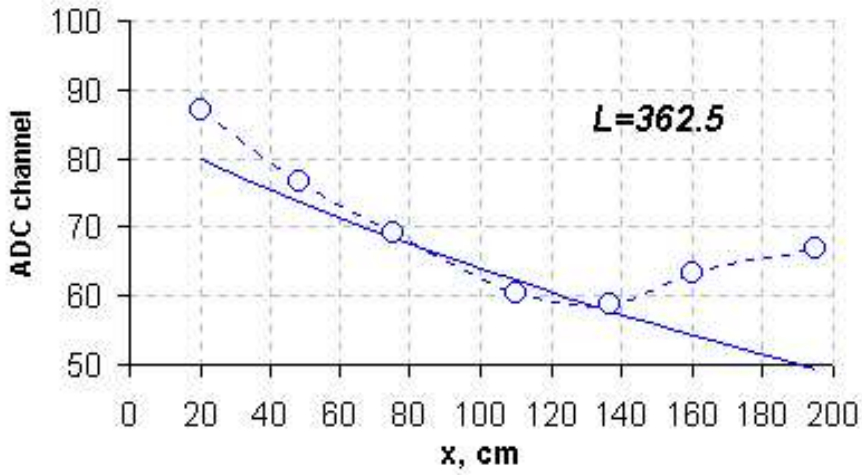

Figure 4.18: Light attenuation measurement with a blue LED of a 362.5 mm long BCF-91A wavelength shifter. The increase in the signal seen near the end of the fiber is caused by reflection at the mirrored fiber edge. The line is an exponential fit.

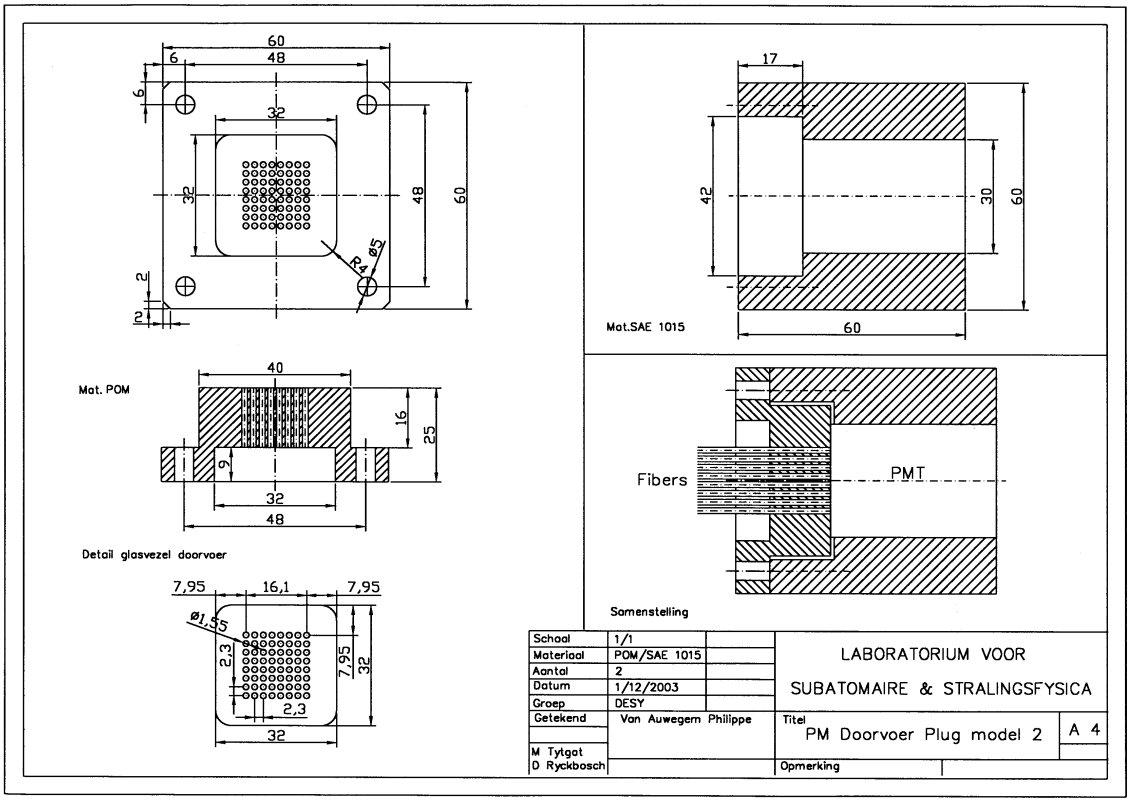

Figure 4.19: Technical drawing of the light-guide to PMT connector and the PMT case.

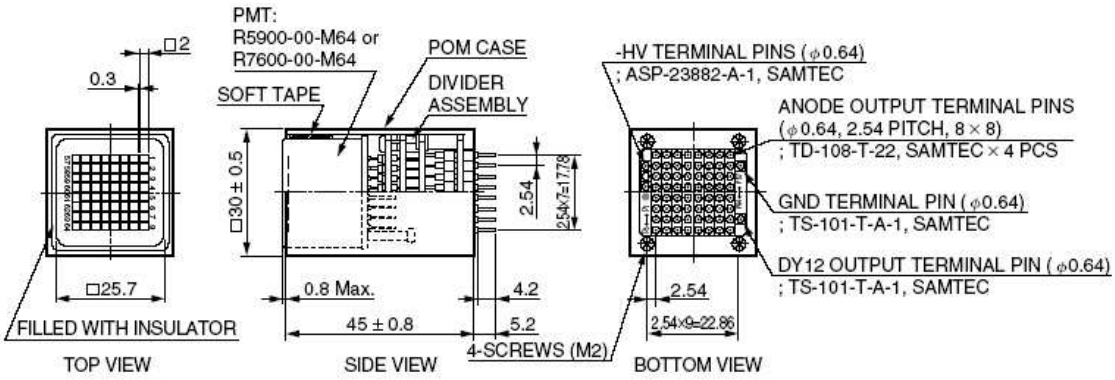

Figure 4.20: Technical drawing of the Hamamatsu H7546 PMT.

In the PMT test stand the measurements are performed inside a wooden black box with a size of $1.5\times1\times1$ m^3, which is made completely light-tight. Whithin this black box there is an aluminum box that houses three custom made printed circuit boards (PCBs) on which three PMTs are mounted (one PMT per PCB). Each PCB has one high voltage (HV) cable and two 32-channel flat cables going outside the black box to a high voltage supply and a charge sensitive ADC (QDC), respectively. The metal box is mounted on the ends of two rails that are about 1 m long. At the other end a blue LED is mounted in the center of the triangle formed by the three PMTs. In front of the blue LED is a metal filter holder mounted on a 21 cm long positioning axis (from ISEL), containing 5 optical neutral-density filters (a neutral density filter reduces light of all wavelengths equally) from Farb with a transparency of 0.39, 11, 31, 51, and 100 %. Finally, a reference PMT (with a radius of 1 cm) is mounted on top of the metal box to monitor the LED response. Figure 4.21 shows a picture of the aluminum box with the 3 PCBs and 1 PMT mounted on the PCB on top. In figure 4.22 a close up of the metal filter holder can be seen. An overview of the entire setup inside the black box is displayed in figure 4.23.

Outside the box there is the positioning axis controller (ISEL IMS-6) to steer the axis that moves the filters horizontally in front of the LED. The signal of the Hamamatsu PMTs is 10 times amplified using a LeCroy 612A amplifier. The readout of the PMT signals is done with CAEN V792 32-channel VME QDCs. A Struck SIS3610 VME I/O register is used to trigger a gate generator module for the QDC gate signal and to pulse an LED driver. The HV for the PMTs is supplied by a CAEN N470 NIM high voltage unit controlled by a VME CAENET controller. Finally, the VME SIS3100/1100 based DAQ is done via a Pentium PC running SUSE Linux 8.1, that also controls the IMS-6 controller via RS-232. Figure 4.24 shows a circuit diagram of the entire teststand.

The DAQ and hardware controlling software is written in C. Each test is performed in 7 steps. First, the PMT's are "warmed up" for 3 hours at 450 V. Then the pedestals of all channels are measured to prepare the pedestal subtraction for the next steps. Then the working voltage is determined. After that, the uniformity of the cathode across the pixels is measured at different LED intensities. The next step is to measure the gain linearity for all channels. Finally, the pedestals are remeasured to check for shifts. In a single measurement (one uniformity measurement for example) 100,000 events are triggered and recorded.

Pedestal Measurement

The pedestals are measured with the LED on and with a PMT HV of 450 V. Measuring in this way ensures that any noise, including the one induced by the LED, is included. In figure 4.25 results of a pedestal measurement of a PMT is plotted.

Every event below $\mu + 2.5\sigma$ (2.5σ cut) is considered a pedestal event, where μ is the mean value and σ the standard deviation of a Gaussian fit to the pedestal spectrum. All pedestals have a variance of about 2 to 5 channels.

At the end of each series of measurements the pedestals are determined again and fit with a Gaussian. The difference of the mean pedestal channel before and after the measurements is calculated for each channel to look for possible shifts. These differences were always within 1.5 standard deviations.

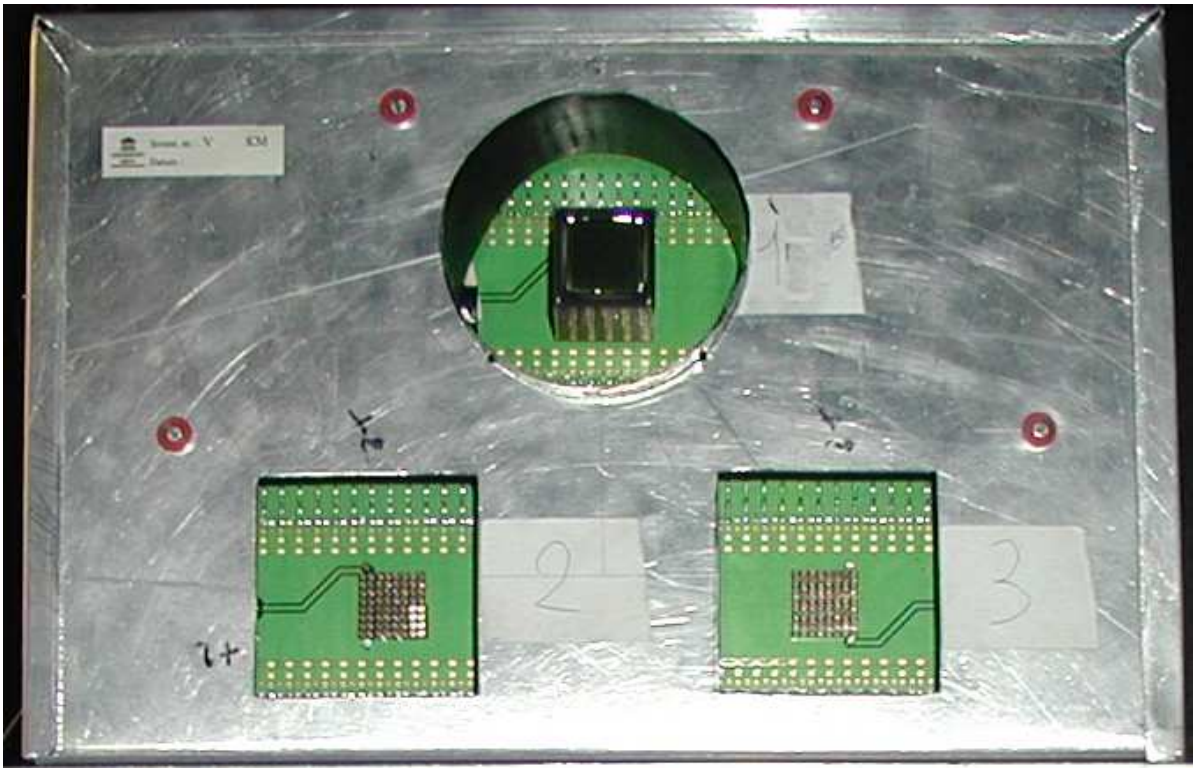

Figure 4.21: The metal box containing the three PCBs. A PMT is mounted on PCB 1.

Working Voltage & Noise

To determine a suitable working voltage for a tube the Single Photo-Electron (SPE) spectrum is measured for each pixel at 600, 700, 750, 770, 790, 800, 820, 840, 860, 880, 900, 920, 940, 960, 980, and 1000 V. According to the Hamamatsu specifications 1000 V is the maximum voltage to be applied to the PMTs. A pedestal subtraction is performed and the number of counts above the pedestal is computed as a function of the HV value. If the HV and thus the gain is high enough, the single photon-electron peak lies completely above the pedestal. From that moment on the number of counts above the pedestal in principle becomes independent of the HV value, this reveals itself as a plateau in the diagram of the number of counts versus HV value. Due to increasing noise of the tube with increasing HV, the plateau usually still has a rising slope until a certain HV where the PMT stops working. Some HV curves are shown in figure 4.26.

The start of the plateau is identified using the following function that is fit to the HV diagram:

$$f(x) = a \cdot \left(1/\left(1 + \mathrm{e}^{(b-x)}\right)\right) + (d + e \cdot (x/f)), \tag{4.1}$$

where $f(x)$ is the number of counts, x is the HV and $a,\ b,\ c,\ d,\ e$, and f are the parameters of the fit. With the results of this fit the first and second derivatives of the HV curve are calculated. Going from high to low voltage, the point where one of the two derivatives becomes larger than 0.2, is taken as starting point of the plateau. The two derivatives are taken to ensure the stability of the plateau. This value can be chosen arbitrary and is set to 0.2 to ensure that,

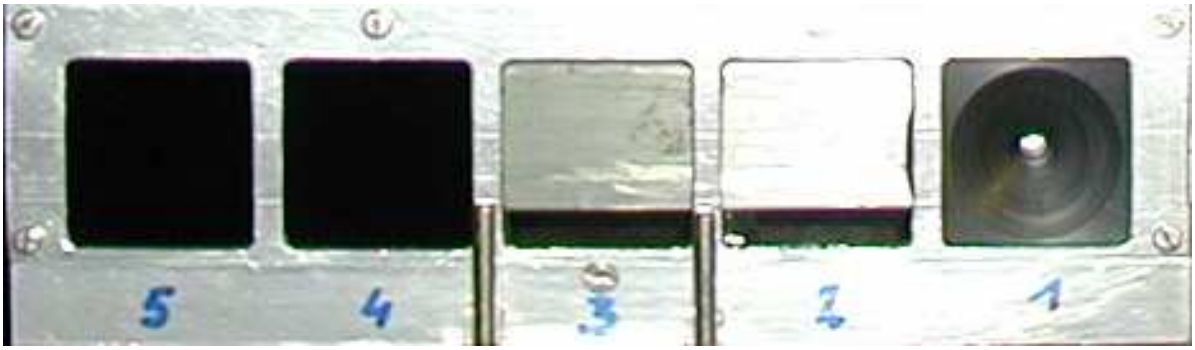

Figure 4.22: The metal filter holder with 5 filters. From left to right: 0.39, 11, 31, 51, 100% transparency. Behind filter 1 a blue LED is visible.

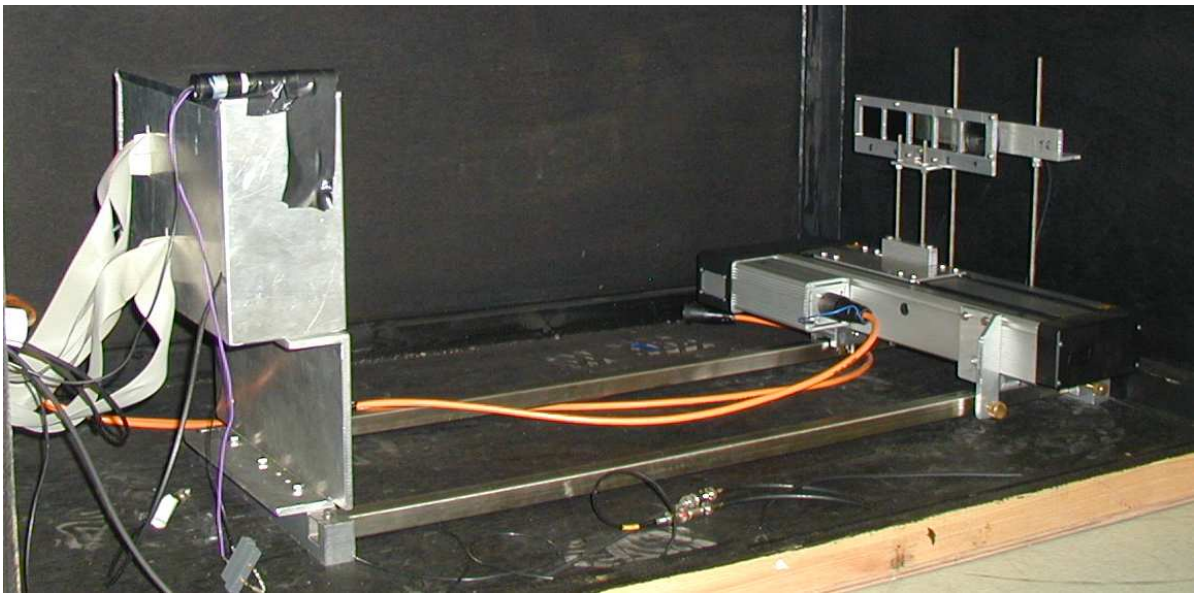

Figure 4.23: General view of the PMT teststand with the reference PMT taped on the metal box.

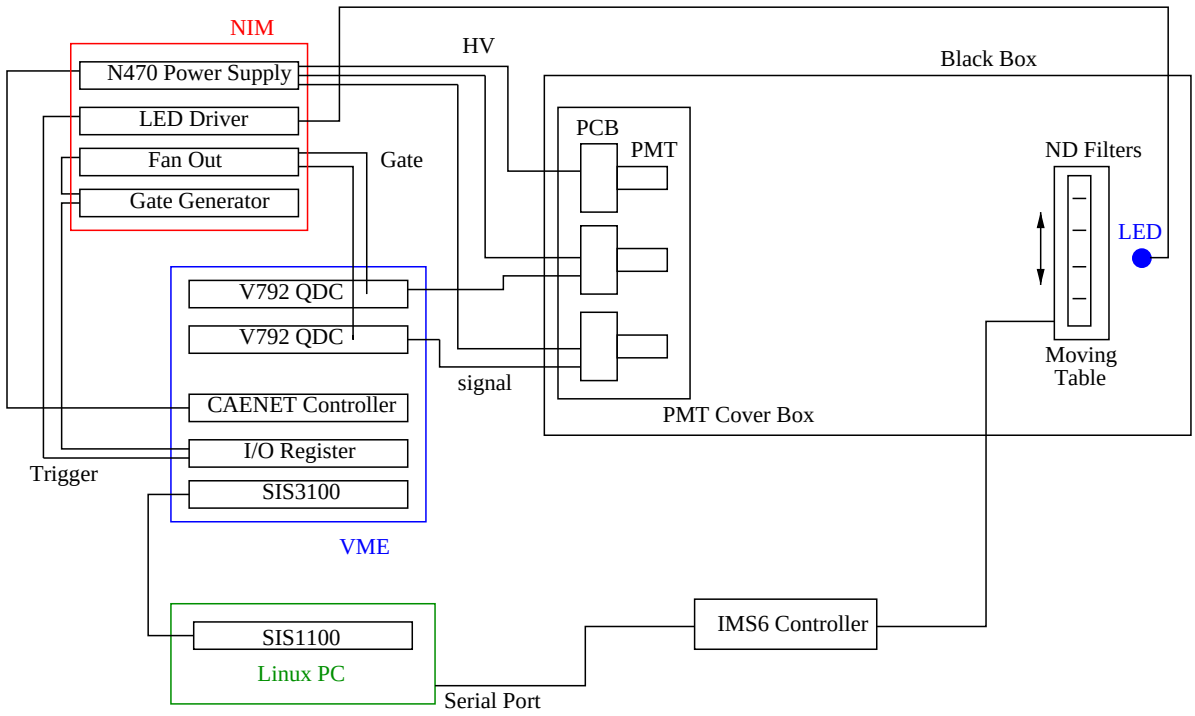

Figure 4.24: A schematic drawing of the teststand.

because the plateau starts close to the maximum voltage, one obtains a working voltage at the very beginning of the plateau. For some channels no clear plateau could be found.

For all further test measurements the HV was set to 880 V that is for more than 75% of the channels inside the plateau. The final working voltage was chosen using the final setup of the photon-detector so that the minimum ionizing particle signal was well (> 100 channels) above the pedestal.

The same measurements (except the fitting) are repeated with the LED off to see how the noise behaves as function of the HV, where the noise level is defined as the number of counts above pedestal. It appeared that this noise is negligibly small as function of HV.

QDC calibration

In order to calibrate the QDC response in number of photo-electrons the following function [91] is used to fit the spectra:

$$\begin{aligned}\frac{f(x)}{10^5} &= \mathrm{e}^{-\mu}\left(\frac{1-w}{\sigma_0\sqrt{2\pi}}\mathrm{e}^{-\frac{(x-Q_0)^2}{2\sigma_0^2}} + w\alpha\mathrm{e}^{-\alpha(x-Q_0)}\right) \\ &\quad + \sum_{n=1}^{\infty}\frac{\mu^n\mathrm{e}^{-\mu}}{n!}\left(\frac{1-w}{\sigma_1\sqrt{2\pi n}}\mathrm{e}^{-\frac{(x-Q_0-nQ_1)^2}{2n\sigma_1^2}} + w\alpha\mathrm{e}^{-\alpha(x-Q_0)}\right),\end{aligned} \tag{4.2}$$

with $f(x)$ being the QDC spectrum and x the QDC channel. The parameters of the fit are μ that corresponds to the mean number of induced photo-electrons in the tube collected by the first

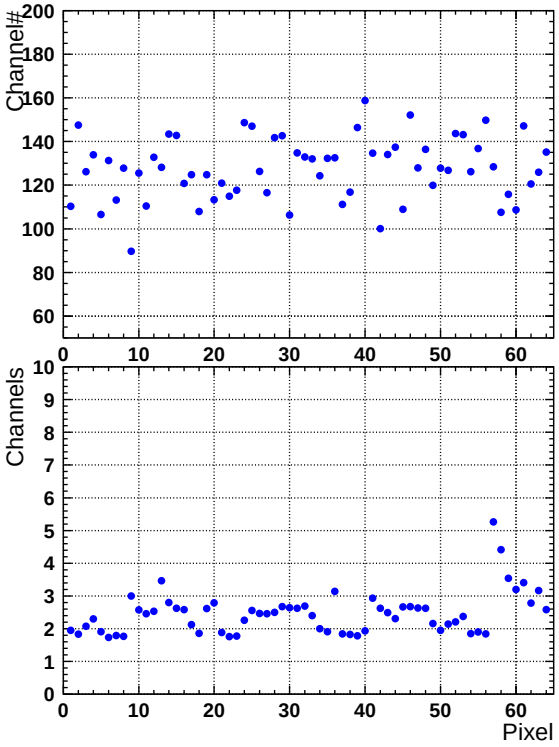

Figure 4.25: Top: mean value of fit pedestals of a PMT. Bottom: sigma value of fit pedestals of a PMT.

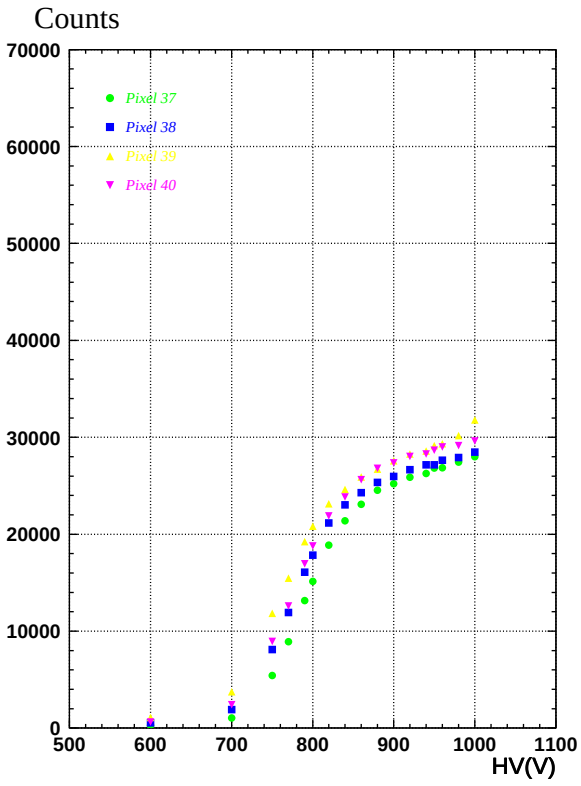

Figure 4.26: The HV plateaus of four channels belonging to the same PMT.

dynode, Q_0 being the mean pedestal channel, Q_1 being the SPE peak position relative to the pedestal in number of channels, σ_0 and σ_1 are the pedestal and SPE peak width respectively, and finally w and α characterize the noise; w is the probability that a measured signal is accompagnied by a background event (like thermo-emission) and α is the coefficient of the exponential decay of this background.

If the 0.39 % transparency filter is used μ has a value around 0.5. With such a small μ, $\frac{\mu^n e^{-\mu}}{n!}$ in Eq. 4.2 becomes rapidly very small with increasing n. When using this filter only the first 10 terms of the sum in Eq. 4.2 are taken into account. Some fitting examples can be found in figure 4.27. The Q_1 values of all pixels of a PMT are plotted in figure 4.28, the error bars represent the standard deviation of Q_1. In one channel one can see that Q_1 is not defined very well, this happens for up to 4 pixels per PMT. One also observes that Q_1 is systematically lower for the first and last 8 pixels. These pixels are located on the edge of the PMT.

When Q_0 and Q_1 are known and $\mu > 25$ the mean number of PEs can be extracted from a spectrum easily by fitting a Gaussian to it. The mean channel x_{mean} can then be used to calculate the mean number of PEs (μ):

$$\mu = \frac{x_{mean} - Q_0}{Q_1}. \tag{4.3}$$

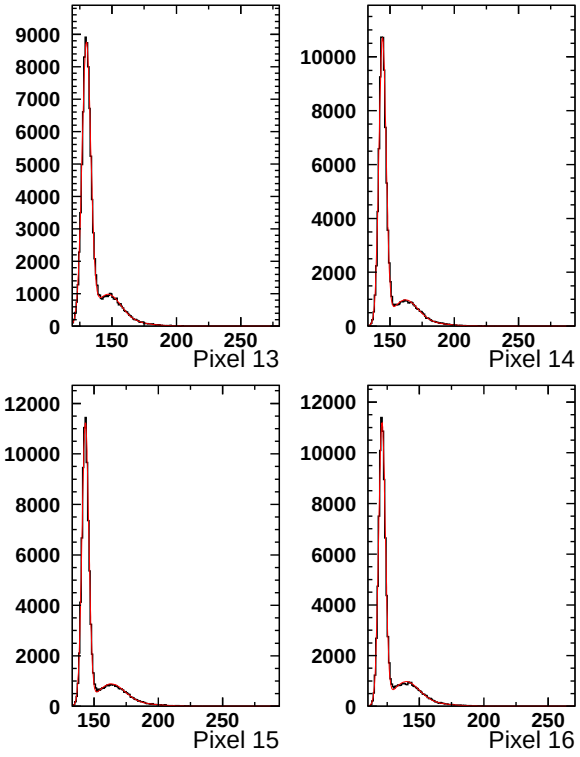

Figure 4.27: Fit SPE spectra of some channels (HV = 880 V). The number of counts in each QDC channel is plotted. The red line is a fit to the spectrum defined in Eq. 4.2.

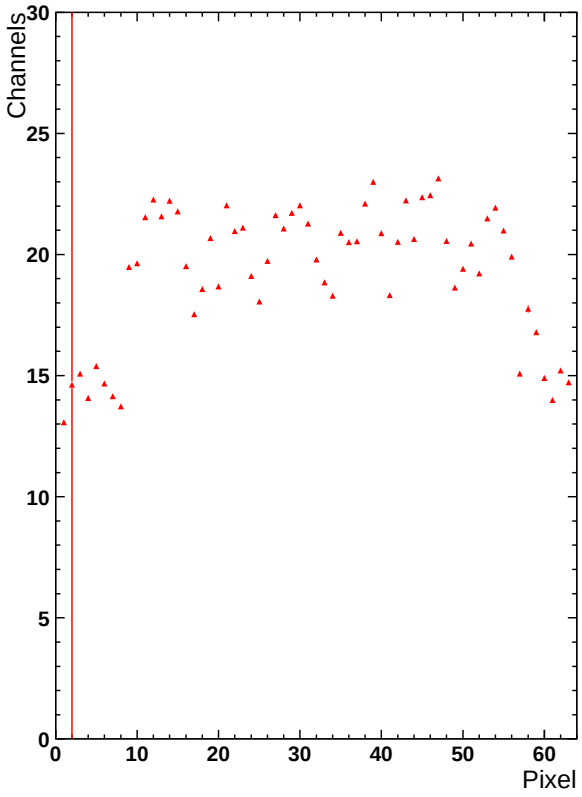

Figure 4.28: Q_1 values for all the pixels of a PMT. The error bar represents the standard deviation. One can see that for pixel number two Q_1 is undetermined and that Q_1 is systematically lower for the first and last 8 pixels. These pixels are located on the edge of the PMT.

Uniformity

To measure the cathode gain uniformity the entire PMT was illuminated by the LED. This measurement was performed using the filter with the lowest transparency. This means that the PMT was operated in SPE regime or that $\mu < 1$. This was done in order to reduce the cross-talk. The mean number of photo-electrons (μ) was calculated using Eq. 4.2 and normalized to the mean μ of all channels. The signals (in PEs) of all channels relative to the mean μ of all channels can be found for one of the PMTs in Fig. 4.29. It can be seen that although Q_1 is lower in the first and the last 8 pixels (cf. figure 4.28), the average number of PE is systematically higher in these pixels compared to the other ones (cf. figure 4.29). The measured uniformity is confirmed with a measurement done by Hamamatsu described in the next paragraph.

For 78 PMTs Hamamatsu provided the results of their uniformity measurement. These results were compared with this uniformity measurement and a good agreement was found, keeping in mind that the test methods were completely different. Hamamatsu used a Tungsten filament light operated at 2856 K as a light source and measured the output current. A com-

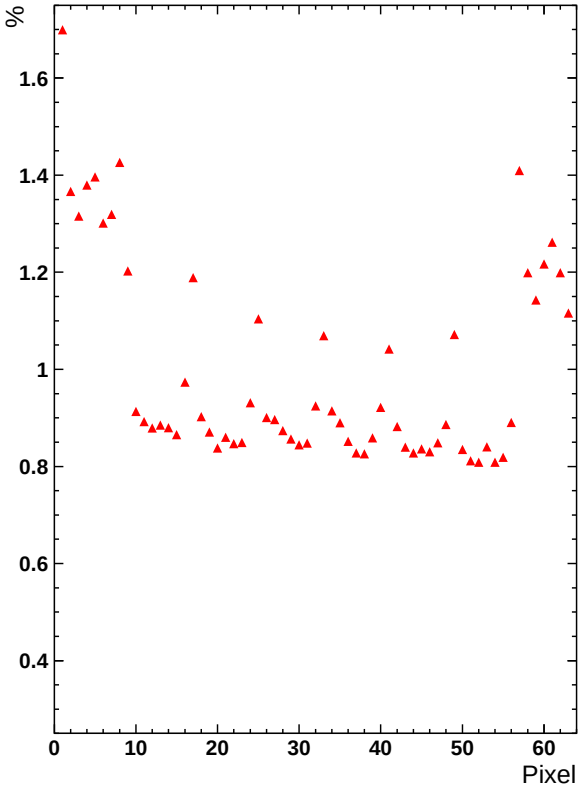

Figure 4.29: Example of the uniformity ($\frac{\mu}{\mu_{mean}}$) of a PMT, measured with the 0.39 % transparency filter.

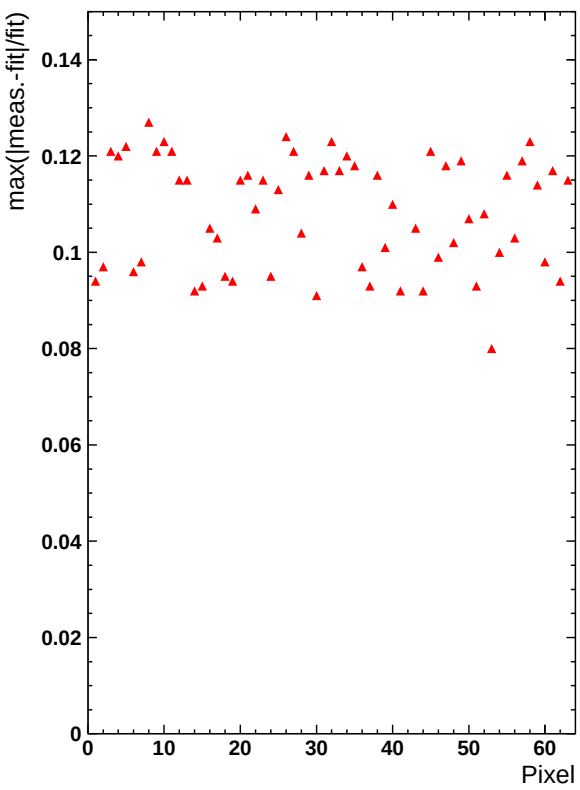

Figure 4.30: Deviation from linearity for all pixels of a PMT.

parison between this measurement and the Hamamatsu measurement is shown in figure 4.31 for two PMTs.

Gain linearity

The linearity of the PMT gain is measured using the five optical filters. The different filter transparencies correspond to a mean number of PEs in the range of 0.50 to roughly 125.

The QDC PE calibration was performed using the darkest filter (0.39 %). For the other filters the obtained Q_0 and Q_1 values were inserted into Eq. 4.3 to get the mean number of PEs.

The deviation from linearity is defined as:

$$\max\left(\frac{|\mu_{lf}(i)-\mu_m(i)|}{\mu_{lf}(i)}\right), \tag{4.4}$$

with i (1...5) runs over the different transparency filters, μ_{lf} is the μ-value from the linear fit, and μ_m is the measured μ. The deviation from linearity for a random PMT is shown in figure 4.30. The deviation is between 8 and 12 %.

The cross-talk between different pixels is not negligible because the PMT is illuminated as a whole during the measurement. Thus, when a transparency filter with a transparency larger than 0.39 % is used, a pixel response can become higher due to cross-talk with neighboring

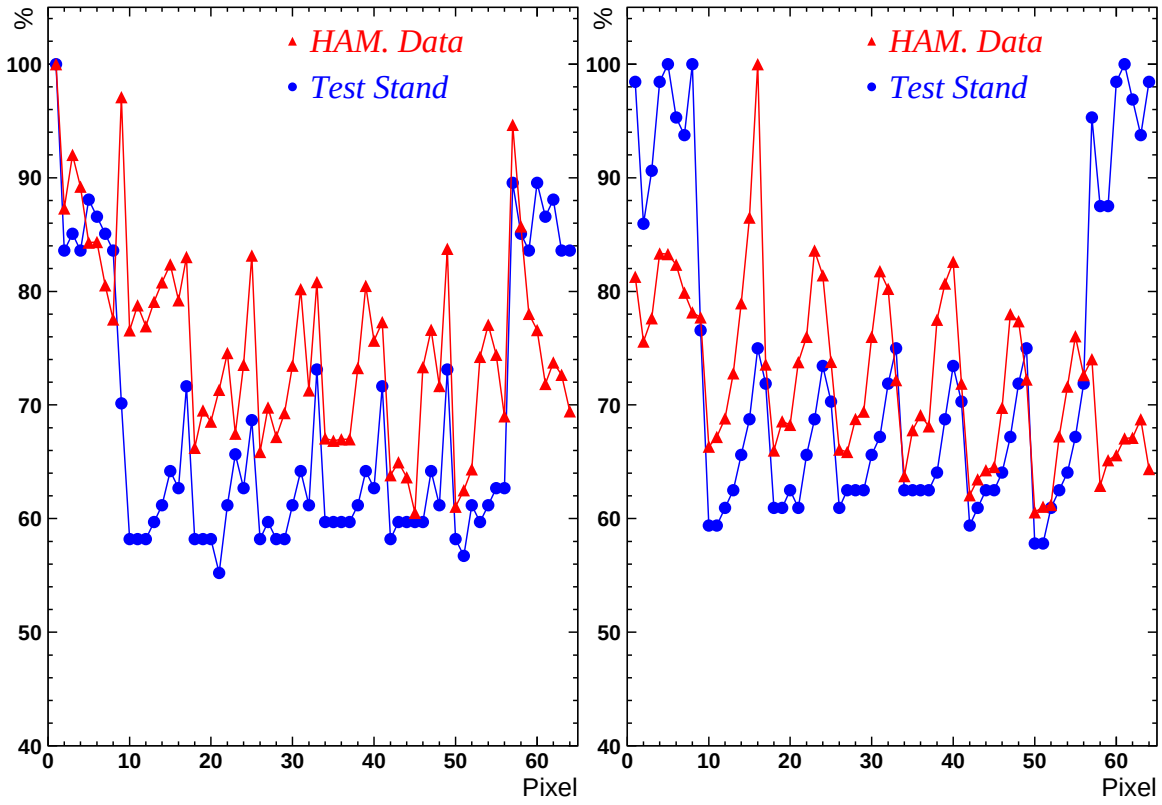

Figure 4.31: Comparison of the uniformity measured by Hamamatsu and in this work. On the left side for PMT with serial number PA1604 and the right side for PMT with serial number PA1580. The pixel with highest μ is set to 100 %.

channels. This means that in reality the deviation from linearity is expected to be a bit worse than what is seen in Fig. 4.30.

Conclusion

Almost 100 Hamamatsu H7645 PMTs were tested. All pixels except one were operational. For most pixels a HV plateau could be found. Pixels with numbers 1 to 8 and especially 56 to 64 (following the Hamamatsu numbering scheme) always show a lower gain (cf. figure 4.28) that is around 1/3 less than the gain of other pixels.

A uniformity measurement was performed and a good agreement was found between the Hamamatsu uniformity measurement taking the two different methods into account.

The linearity was also tested, but only a minimum value of the deviation of linearity could be obtained because no cross-talk correction could be made.

4.4.6 The magnetic shielding of the PMTs

The PMTs have to operate close to the recoil magnet. They are positioned where the magnetic field is still about 20 mT. Because the PMTs can only work properly in a magnetic field up to

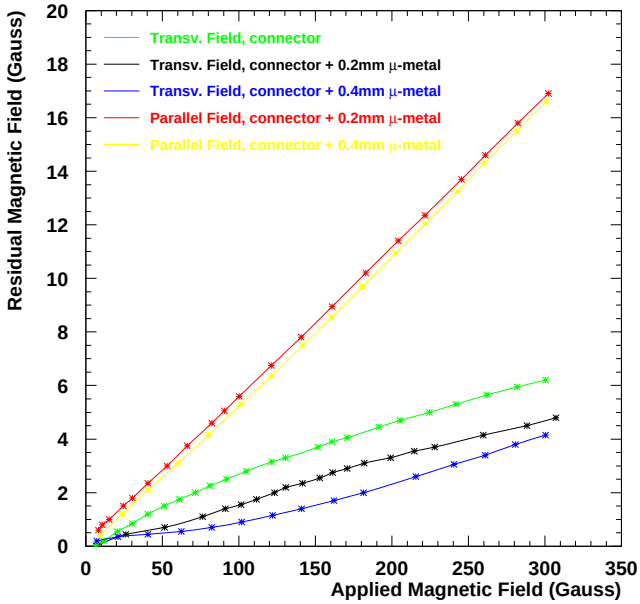

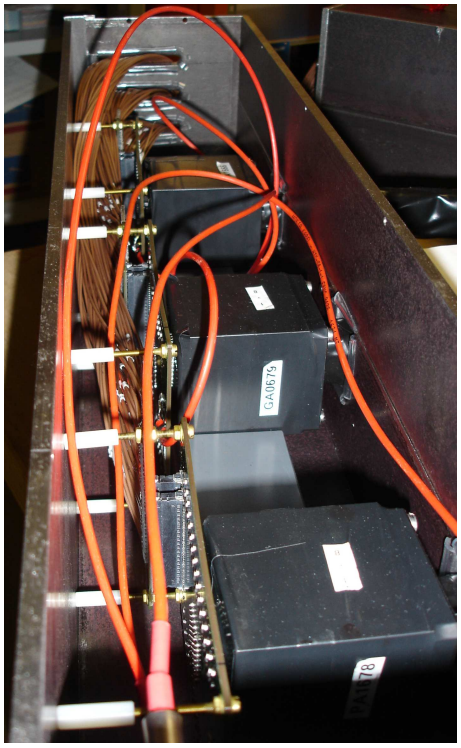

Figure 4.32: Left: the result of the magnetic shielding test. Right: a picture of 3 shielded PMTs inside a metal box.

0.5 mT, magnetic shielding is needed. The amount of shielding was determined with a magnet test using a dipole magnet at DESY. The results of this test can be seen in figure 4.32. The shielding that was chosen is an SAE1015 soft steel case (drawn in the upper right corner of figure 4.19) and 2×0.2 mm μ-metal "sheets" located between the PMT and the soft steel case. The PMTs where placed in such a way that the magnet field is transverse to their orientation inside the metal box in order to have the lowest magnetic field inside the shielding as can be seen in figure 4.32.

4.4.7 Amplification, digitization, and a cosmic trigger

The signals coming from the PMTs are fed to a fan-in/amplifier that adds the two signals coming from one strip together, amplifies it, and sends this as a differential signal (to reduce cross-talk) over 40 m of flat cable from the experimental area to the electronic trailer. There a fan-out converts the differential signal into a signal that can be read out by a QDC. The fan-out has two outputs per signal: one output transports the signal over 70 m of flat cable before being delivered to the QDCs (Caen V792). This 70 m of delay flat cable was necessary because at the design the delay between an event and the HERMES trigger was not taken into account. The other output is used to construct a cosmic trigger, using Caen V812 discriminators and Caen V976 logic units, by demanding coincidences between the top and bottom part of the detector. The fan-in/fan-out modules are custom made. A schematic overview of the whole

chain is presented in figure 4.33.

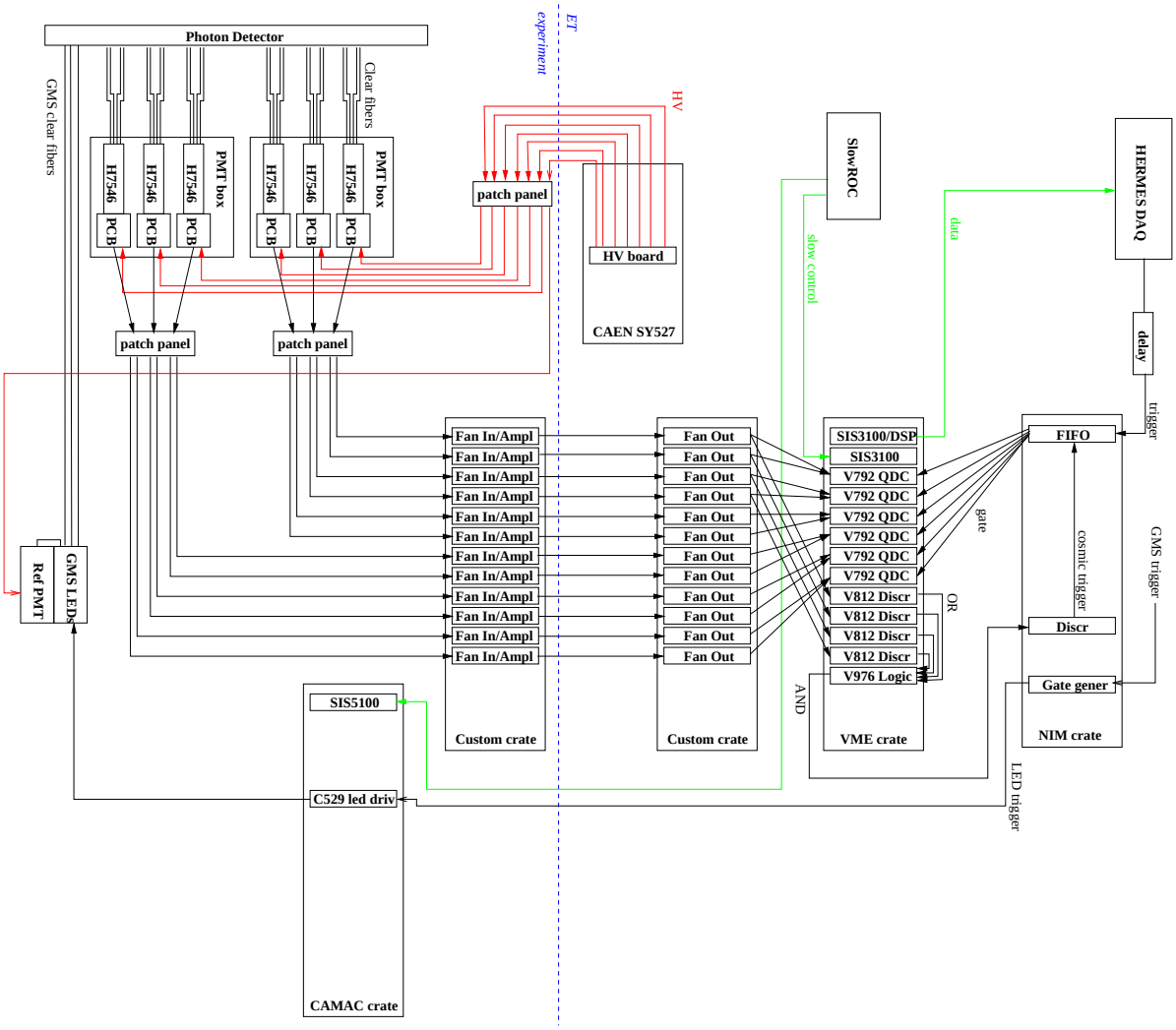

Figure 4.33: Schematic drawing of the recoil photon-detector DAQ chain.

4.4.8 The gain monitoring system

The Gain Monitoring System (GMS) consists of a light source containing 20 blue LEDs driven by an LED driver. This light is transported over 148 light-guides (one guide per strip) to all strips. The stability of the LEDs is monitored by a reference PMT that also reads out the very stable light output from an alpha-source surrounded by a crystal. A plot containing measurements of GMS-light with the PD PMTs and the reference PMT, and alpha-source light with the reference PMT is shown in figure 4.34. The range in run numbers covers a time of the order of a day. It can be seen that the signals are quiet stable: the drift of the GMS signal in the PD and the reference PMT is at most half a channel. The drift of the alpha source

signal, which is 20 times larger than the LED signal, is around 2 channels. Finally the GMS signal will be corrected for the LED stability.

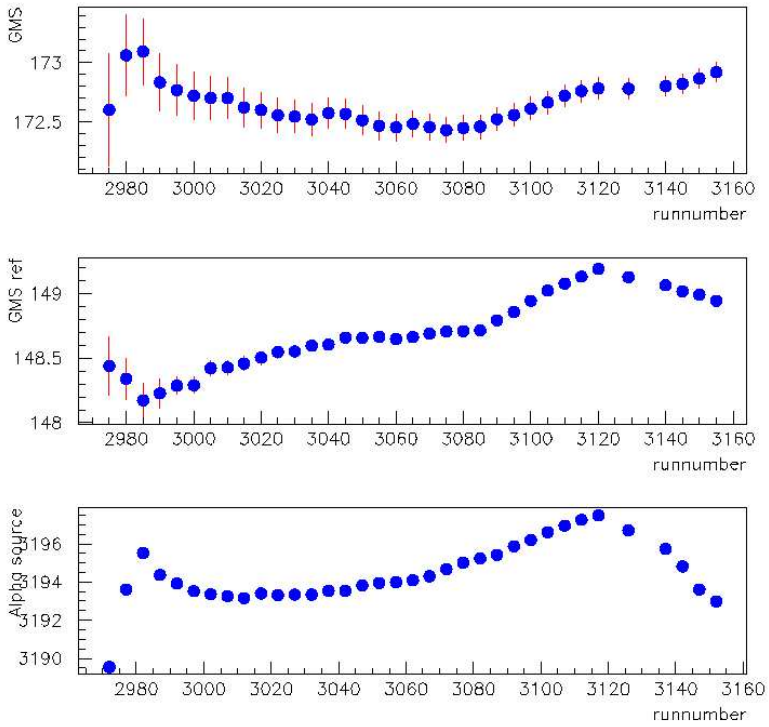

Figure 4.34: Mean of a Gaussian fit of a QDC spectra versus run number. The "error" bars represent the width of the Gaussian fit. From top to bottom: GMS light in one of the PD channels, GMS light measured by the reference PMT, and light from the alpha source surrounded by a crystal measured by the reference PMT.

4.4.9 The test-beam

At the Gesellschaft für SchwerIonenforschung (GSI) in Darmstadt a prototype of the photon-detector was tested with a mixed pion/proton beam with a momentum range of 300 - 900 MeV. This secondary beam comes from a primary ^{12}C beam on a 120 mm thick B_4C target. The photon-detector response was checked and its particle-identification capabilities investigated. The setup and results are discussed in this section.

Setup

A drawing and the scintillator bar mapping of the photon-detector prototype are illustrated in figure 4.35. It consists of three layers of preshower material and a 1 cm wide scintillator strip like the photon-detector. Instead of Tungsten the same radiation length of lead was used. Each scintillator strip has two wavelength shifters. The light is transported over 2 meters of light-guide to one H7546 PMT. The detector read-out is illustrated in figure 4.36. Scintillators

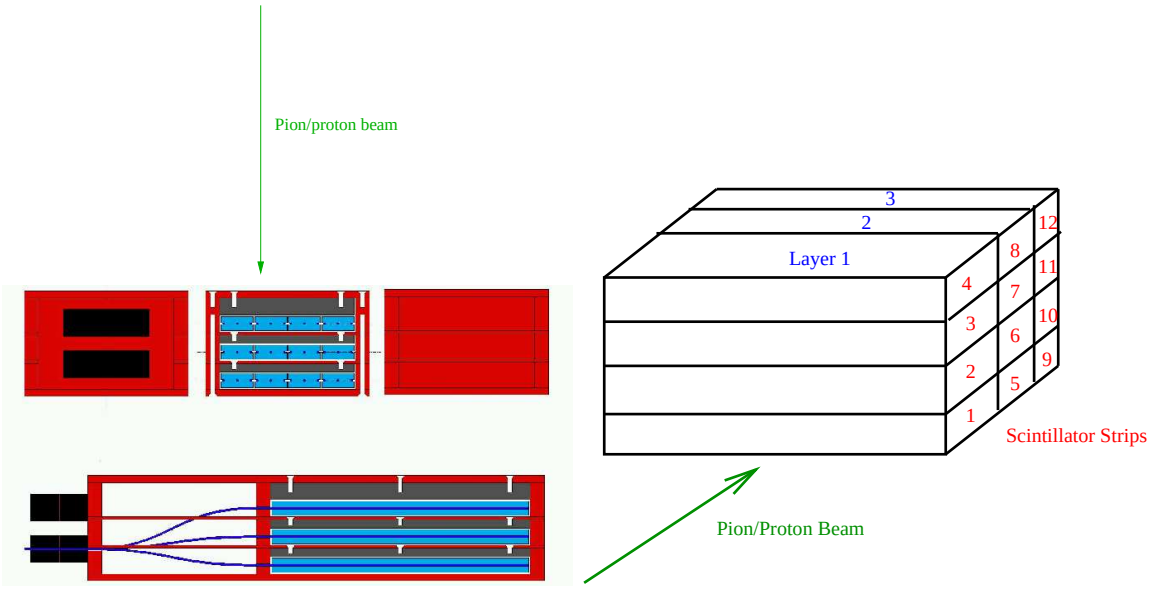

Figure 4.35: Drawings of the photon-detector prototype. On the left side in gray is the preshower converter and in blue the scintillator strips, wavelength shifters, and light-guides. On the right side the mapping of the scintillator strips is given.

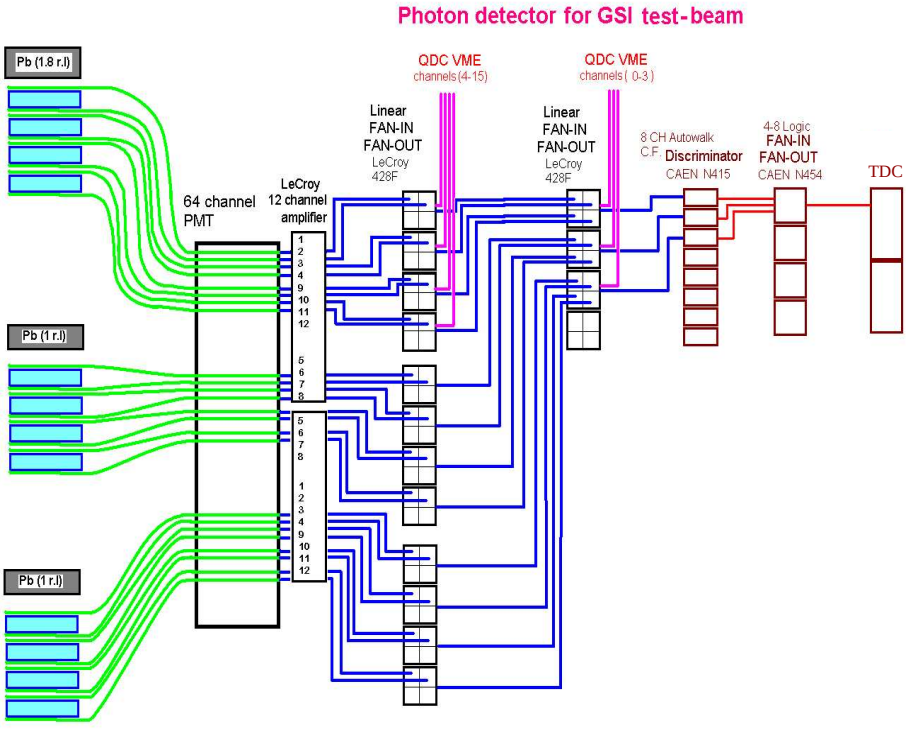

Figure 4.36: Scheme of the photon-detector prototype readout at GSI.

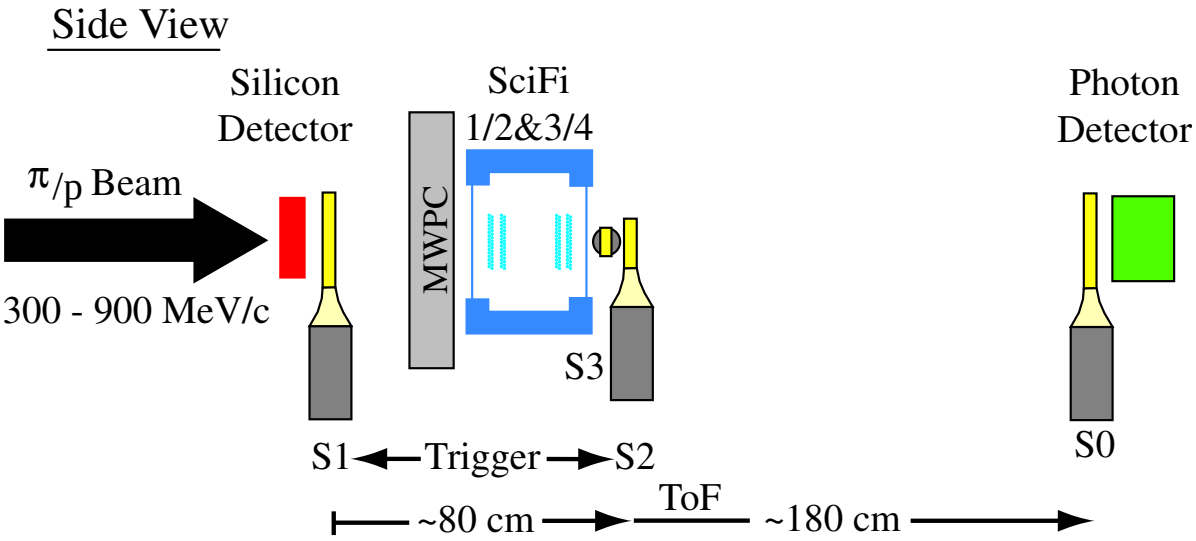

Figure 4.37: Sketch of the test setup at GSI. The scintillators S0, S1, and S2 are scintillators that are read out by a PMT. Prototypes of all three recoil detectors and a MWPC are set up.

S1 and S2 were used to generate a trigger. LeCroy fan-in/fan-out modules sum the two signals coming from the same scintillator strip. Also, all the strips per layer were summed using LeCroy fan-in/fan-out modules and read out by a QDC. The summed signal of each layer went to a dicriminator. A logic OR was applied on the outputs of the discriminator using a logic fan in/fan out. This output is delayed using a timer (CAEN N93B) and used as a stop signal by a TDC.

The setup in the experimental area at GSI is drawn in figure 4.37. S0 and S1 are used to perform a Time-of-Flight (ToF) measurement in order to separate pions from protons, as can be seen in figure 4.38 for a 600 MeV beam. The pions are well separated from the protons. The Multi-Wire Proportional Chamber (MWPC) was used to measure the beam position.

First signals and tracks

The QDC spectra of all the strips are shown in figure 4.39 (left). The spectra are numbered as in figure 4.35. Two peaks are visible. The one with the highest energy deposition comes from proton-induced showers and the peak at lower energy deposition comes from pion-induced showers. The clearest spectra can be seen in strip 2, 6, and 10. That is the place were the center of the beam was located. The photon-detector response using ToF PID summed over each layer is shown in figure 4.39 (right).

Some tracks can be seen in figure 4.40 where 18 events are displayed. An arbitrary threshold has been applied on the QDC-values (to cut away the noise peak or pedestal). Tracks are visible: one can see that strips that are positioned behind each other with respect to the pion/proton beam (cf. figure 4.35) have a hit in the same event that could point to a track of a beam particle passing through the detector, e.g., if there is a high QDC signal in strip 1 there is also one in strip 5 and strip 9.

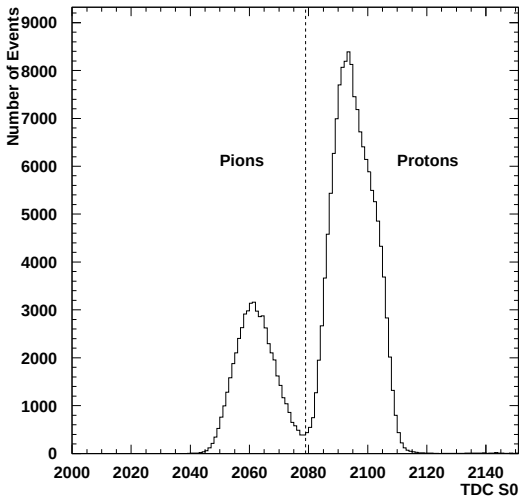

Figure 4.38: Time-of-flight measurement of a 600 MeV mixed pion/proton beam. A clear separation between pions and protons can be seen.

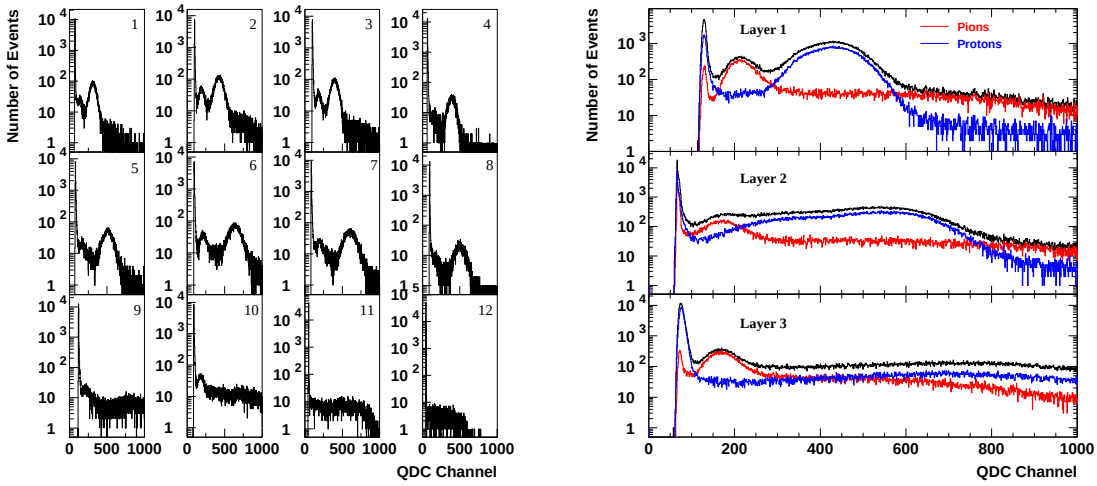

Figure 4.39: Left: QDC spectra of all the scintillator strips. The numbering of the spectra follows the mapping shown in figure 4.35. Right: the photon-detector response using ToF PID summed over each layer. All these measurements were done with a 600 MeV mixed pion/proton beam.

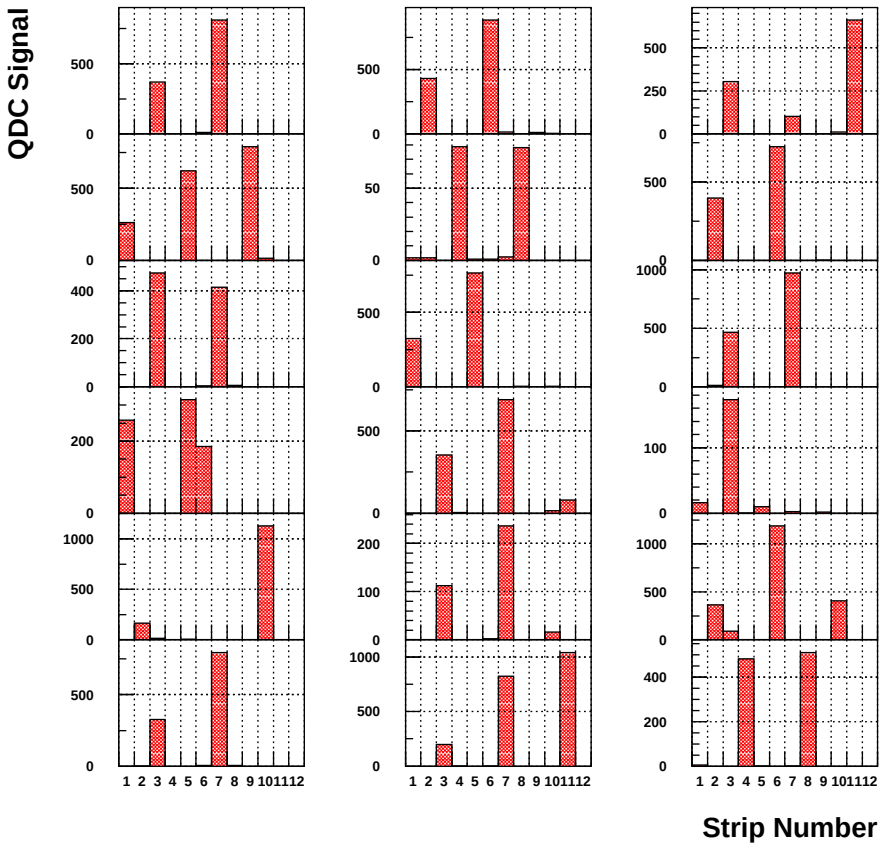

Figure 4.40: QDC signal versus strip number for 18 events measured with the 600 MeV beam. Tracks can be seen (the mapping is shown in figure 4.35), e.g., hit in strip 1, 5, and 9.

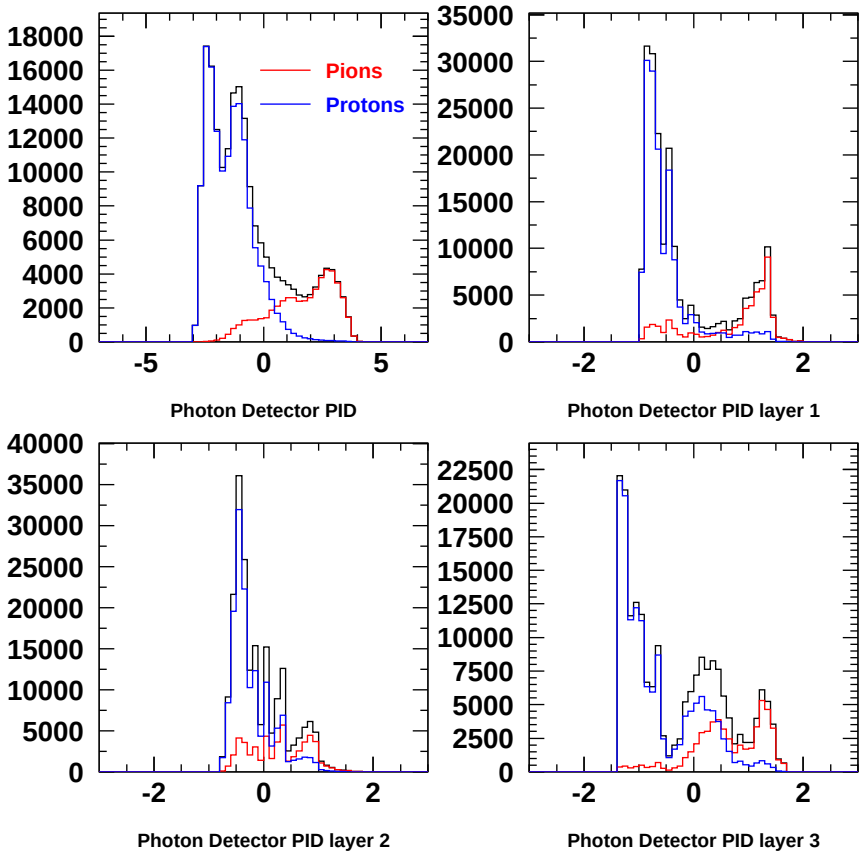

Figure 4.41: $\mathrm{PID_{PD}}$ values per layer and for all layers together. ToF PID was used to identify the particles. A 600 MeV mixed pion/proton beam was used to acquire the data. A PID value of 1 means that it is 10 times more likely that the particle is a pion than a proton.

Particle identification

Using the same PID formalism as described in section 3.5.2, a new PID value $\mathrm{PID_{PD}}$ can be defined:

$$\mathrm{PID_{PD}} = \log \frac{\mathcal{L}_\pi}{\mathcal{L}_p}, \tag{4.5}$$

where $\mathcal{L}$ is the likelihood to detect a pion or a proton. For the likelihood the normalized detector response (for a proton or pion) is taken. The $\mathrm{PID_{PD}}$ values are plotted per layer and for all layers in figure 4.41. Particle identification is possible with the photon-detector for particle momenta of 600 MeV and higher, especially when all layers are combined. Particles with lower momentum (450 MeV) were not detected because they were stopped in the silicon or scintillating fiber tracker before reaching the photon-detector.

Conclusion

The GSI test-beam proved that the photon-detector is able to detect pions and protons with a momentum higher than 600 MeV. Also indications of tracks were seen. It is also possible to use the photon-detector for particle identification for pion/proton momenta above 600 MeV.

In the final setup the normalized detector response cannot be used to calculate the likelihoods because the particle type is not known beforehand as no time of flight information is available. Instead a Monte Carlo simulation will be used to extract the likelihoods for pions and protons.

4.4.10 The cosmic run at DESY

A few months before installation in HERMES, the recoil detector was completely assembled and set up in the East Hall. There the recoil detector took cosmic data using the cosmic trigger generated by the photon-detector. It was the first data taking with the complete photon-detector. Results of this test stand are discussed in this section.

The cosmic trigger

The cosmic trigger used for this test was a logical OR between all lower strips in the A layer (with a number between 16 and 45 following the mapping of the photon-detector shown in figure 4.42).

Cosmic muons to calibrate the photon-detector

Almost all cosmic muons are Minimum Ionizing Particles (MIPs). Therefore, the energy deposition of these particles per unit of scintillator length is known to be 2 MeV/cm. An attempt was made to calibrate all the scintillator strips using cosmic muons. Cosmic muons were selected by requiring a signal (28σ above pedestal) in two opposite strips (e.g., strip 5 and 35 in the A layer). The obtained spectra are then fit with a Gaussian. The mean of the fit Gaussian minus the mean of the pedestal gives the number of QDC channels per 2 MeV, which calibrates the QDC spectra. The result of this calibration is shown in figure 4.43. The fact that some strips do not have a value is due to the distribution of the cosmic muons, which falls off proportional to $\cos^2(\phi)$ with ϕ the angle of the cosmic muon with the zenith-nadir axis. This means that it is possible to calibrate some of the strips using cosmic muons but not all of them (it is basically impossible to rotate the PD). For the HERMES data negatively charged pions will be used to calibrate the PD. With the right constraint on the momentum and charge only negative pions that are minimum ionizing particles are selected and there is virtually no contribution of other negatively charged particles in this sample.

Conclusion

The cosmic run produced the first data taken with the full recoil detector setup and allowed to test all components (e.g., the GMS (cf. figure 4.34), logic units, delays, magnet on test, etc.). Everything worked and an attempt was made to calibrate the PD using cosmic muons that was

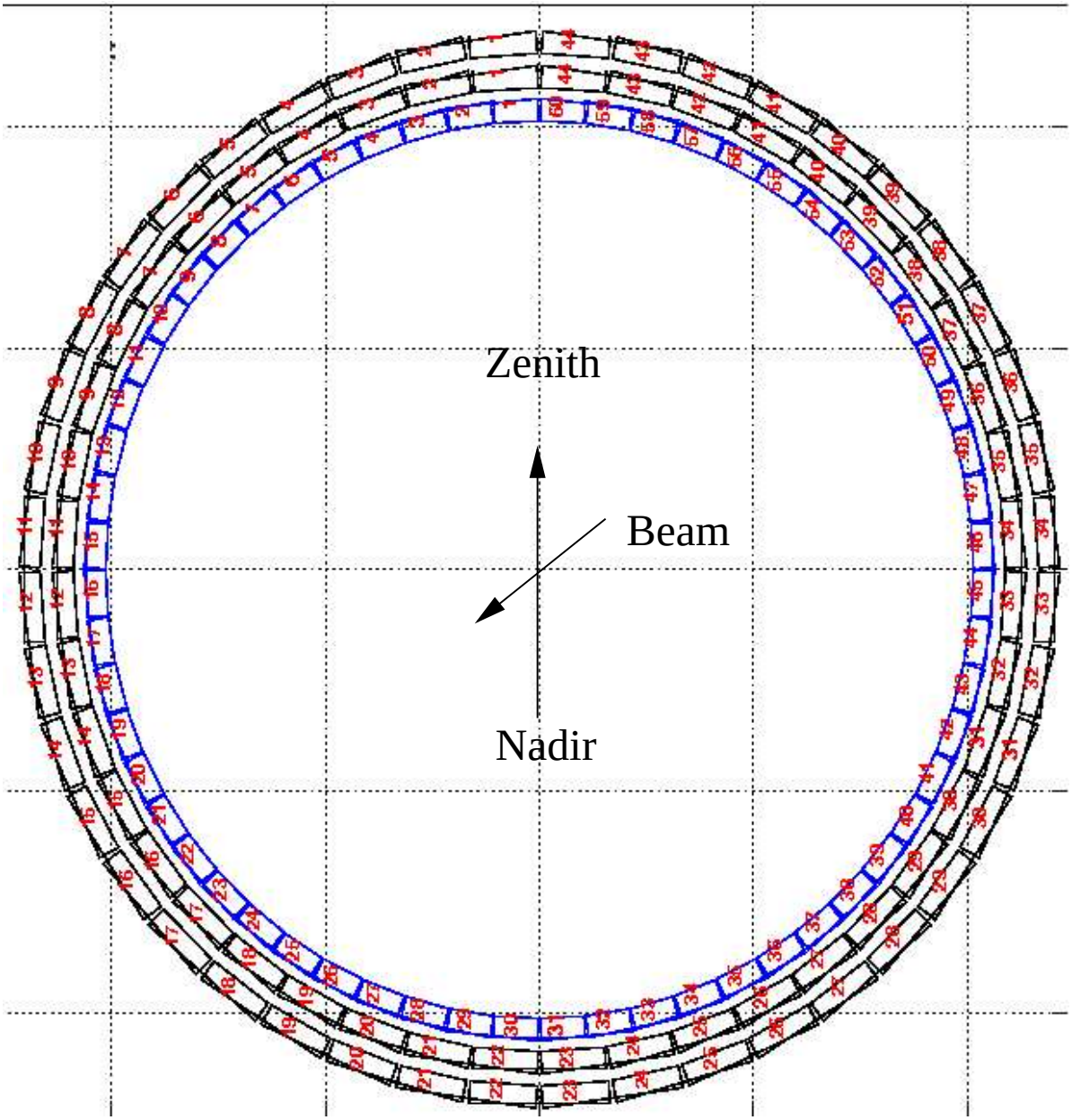

Figure 4.42: Mapping of the photon-detector strips. From the inside out: the A layer, the B layer, and the C layer.

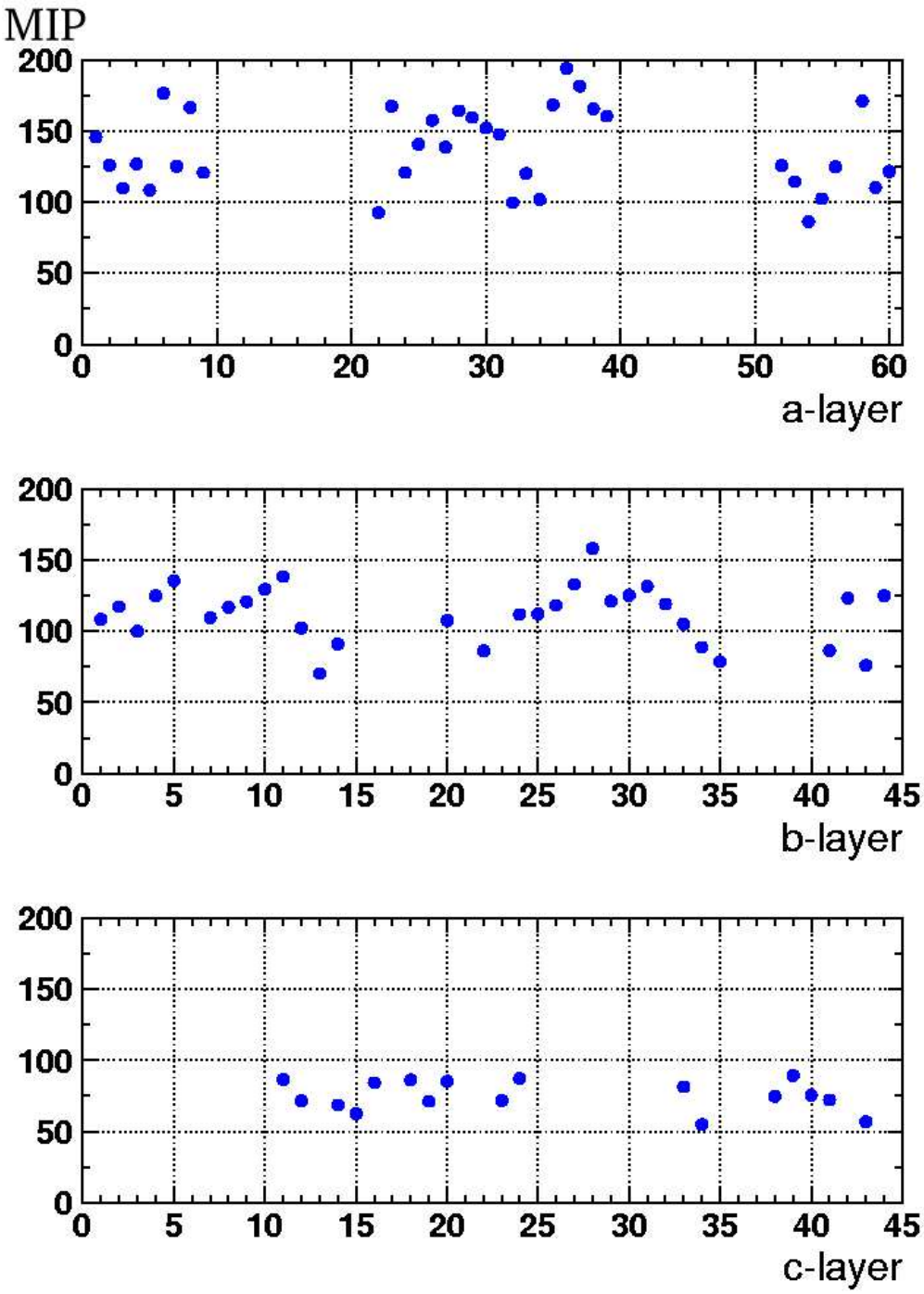

Figure 4.43: The MIP signal in QDC channels versus strip number. The gaps are due to the distribution of cosmic muons.

partially successful. Not all the scintillator strips could be calibrated due to the distribution of the cosmic radiation.

4.5 The recoil magnet

The recoil magnet is a super-conducting solenoid magnet, cooled with liquid helium, that provides a magnetic field of 1 T longitudinally with the beam direction. In this field charged particles (e.g., recoil protons) are deflected and their momentum can be determined by the bending radius and it also protects the scintillators from electrons from Bhabha and Møller scattering by deflecting them. A picture of the recoil magnet is shown in 4.44.

4.6 Recoil data taking

The HERMES recoil detector has been installed at the end of 2005 and was taking data at the moment that this thesis was written.

Figure 4.44: A picture of the recoil solenoid.

Chapter 5

Used Monte Carlo simulations

In this chapter the Monte Carlo simulations used for the p_t-broadening analysis are described starting with a section about the Vector Meson Dominance (VMD) model as it is used in some of the Monte Carlo simulations. The part of the analysis where Monte Carlo simulations are crucial is the correction for acceptance, smearing, and radiative effects described in section 6.8. For p_t-broadening, the difference between two measurements of p_t, this correction heavily depends on Monte Carlo simulations. This is illustrated in following simplified example[1]: suppose the acceptance effects are the same for every target and independent of the kinematics, then the real $\langle p_t^2 \rangle$ equals:

$$\langle p_t^2 \rangle^{real}_{D,Ne,Kr,Xe} = A \cdot \langle p_t^2 \rangle^{measured}_{D,Ne,Kr,Xe}, \tag{5.1}$$

where A is a correction factor for detector acceptance and efficiency. The real p_t-broadening then becomes:

$$\Delta\langle p_t^2 \rangle^{real}_{Ne,Kr,Xe} = \langle p_t^2 \rangle^{real}_{Ne,Kr,Xe} - \langle p_t^2 \rangle^{real}_{D} = A \cdot \Delta\langle p_t^2 \rangle^{measured}_{Ne,Kr,Xe}. \tag{5.2}$$

One has to know the acceptance effects to extract the real p_t-broadening out of the measured one. If the ratio instead of the difference was taken then the acceptance effects would cancel (in this simplified example):

$$\frac{\langle p_t^2 \rangle^{real}_{Ne,Kr,Xe}}{\langle p_t^2 \rangle^{real}_{D}} = \frac{A \cdot \langle p_t^2 \rangle^{measured}_{Ne,Kr,Xe}}{A \cdot \langle p_t^2 \rangle^{measured}_{D}} = \frac{\langle p_t^2 \rangle^{measured}_{Ne,Kr,Xe}}{\langle p_t^2 \rangle^{measured}_{D}}. \tag{5.3}$$

Monte Carlo studies were also performed to estimate the exclusive vector meson contribution in the hadron sample and also to study the nuclear dependence of the radiative corrections.

5.1 The vector meson dominance model

In deep-inelastic scattering the exchanged virtual photon interacts with a quark of the nucleon. Besides the so-called bare part of the photon, which couples to the electromagnetic charge of

[1] In reality acceptance effects can introduce a combination of multiplicative and additive factors that can depend on track position, kinematic variables, etc.

the quarks, the virtual photon can also fluctuate into a quark anti-quark pair. This pair can last long enough to induce a cloud of gluons around the quarks so that this state develops into a hadronic state that can interact with the nucleon or with the nucleus as a whole. This is called incoherent and coherent vector meson production, respectively. This interaction can be described phenomenologically only in terms of models for hadron-hadron interactions. The vector meson dominance model [104] is the most prominent model that describes the data succesfully over a wide kinematic range. Besides the hadronic part, the photon exhibits also a so-called anomalous part that can be seen as a fluctuation into a quark anti-quark pair with a larger virtuality then the mass of the vector meson (this can be seen as an excited vector meson). These states are taken into account by the generalized vector meson dominance model [105]. In the PYTHIA Monte Carlo (cf. section 5.2) and the RHOMC Monte Carlo (cf. section 5.4) both models are implemented.

5.2 The HERMES Monte Carlo chain with the PYTHIA generator

The HERMES Monte Carlo chain with the PYTHIA generator is illustrated in a flow chart in figure 5.1. This Monte Carlo was used to correct data for radiative and acceptance effects and is described in more detail in this section.

5.2.1 The PYTHIA lepton kinematics generation

As indicated in figure 5.1 the PYTHIA [92] generator generates the kinematics of the scattered lepton according to the Born $\gamma p(n)$ cross section. This cross section equals:

$$\sigma^{\gamma p(n)} = \sigma^{\gamma p(n)}_{direct} + \sigma^{\gamma p(n)}_{VMD} + \sigma^{\gamma p(n)}_{anomalous}, \tag{5.4}$$

and is calculated using a parameterization of $F_2(x, Q^2)$. The direct part is illustrated in figure 2.1 and VMD parts of the cross section in figure 5.2. The direct cross section is the direct interaction of the photon with the nucleon. The VMD and anomalous parts of the cross section are described in section 5.1. In PYTHIA the vector meson can interact in three different ways with the nucleon called elastic, single-diffractive, and double-diffractive scattering. In single-diffractive scattering the nucleon or the vector meson gives rise to a resonance and one ends up with multiple final-state particles. In double-diffractive vector meson scattering, both the nucleon and the vector meson break up. This is illustrated in figure 5.2.

The generated cross-sections implemented in PYTHIA were tuned in order to better describe the HERMES data. More information about the cross-section tuning and the used parameterizations are in [93].

5.2.2 Radiative corrections with RADGEN

The generated lepton kinematics are passed to a program called RADGEN [94]. This program decides whether or not a real photon was radiated by the incoming or outgoing lepton. This initial or final state radiation of a real photon is illustrated in figure 5.3. If a real photon was

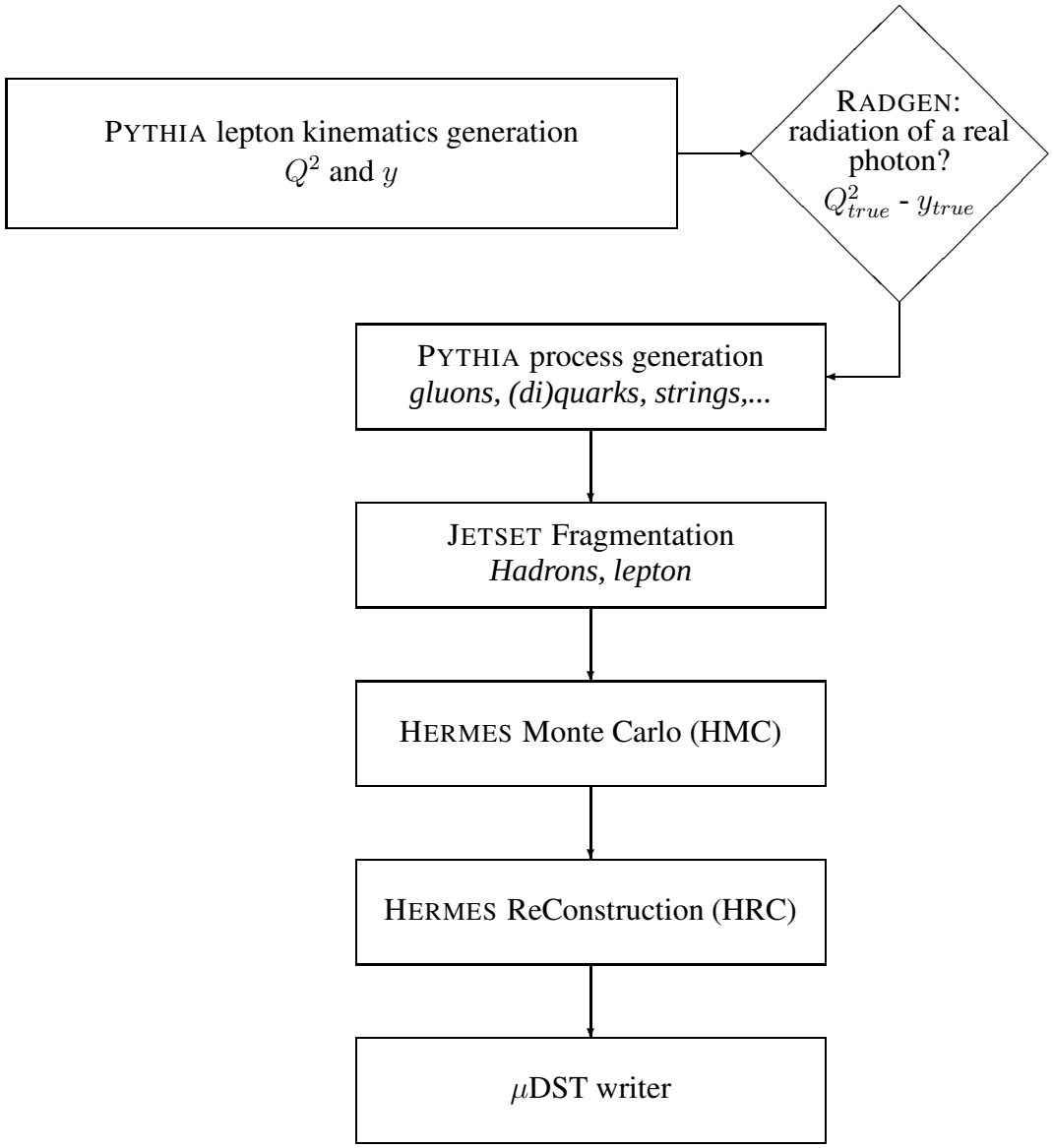

Figure 5.1: Flow chart of the HERMES Monte Carlo chain using the PYTHIA generator.

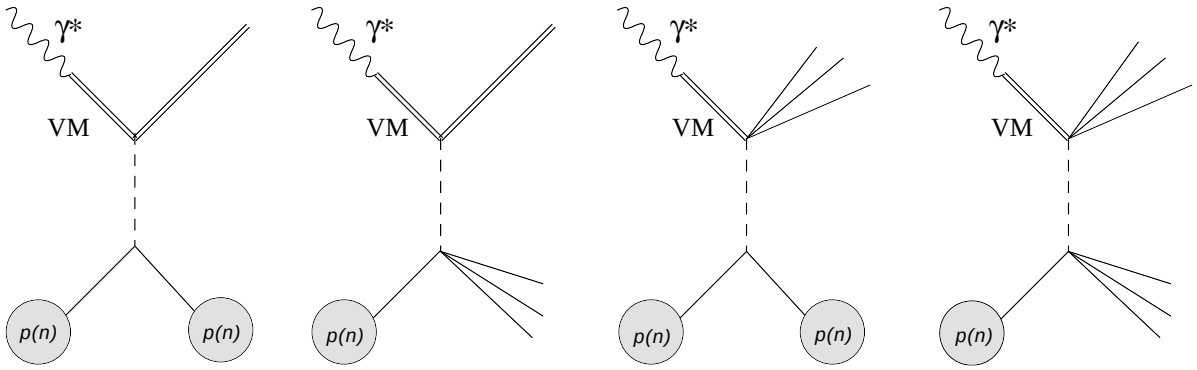

Figure 5.2: Illustration of elastic, single, and double diffractive vector meson (VM) scattering, from left to right: elastic, proton single diffractive, vector meson single diffractive, and double diffractive scattering.

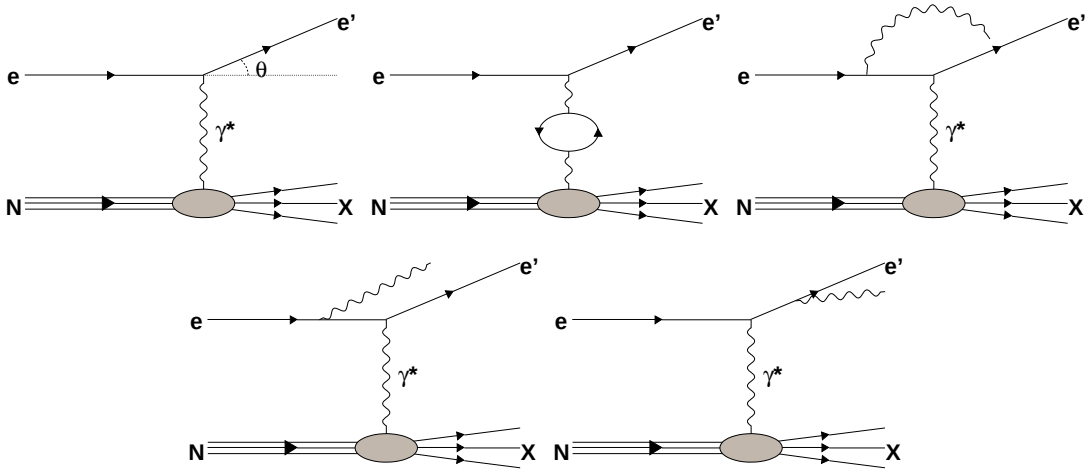

Figure 5.3: The QED Feynman diagrams taken into account by RADGEN.

radiated, the 4-momentum of this photon is stored and true values of Q^2 and y are passed to the PYTHIA generator (see next section). The stored 4-momentum of the radiated photon is enough to calculate all the true kinematics of the event because of conservation of four momentum:

$$k = k' + \gamma^* + \gamma_{\mathbf{rad}}, \tag{5.5}$$

with γ^* the 4-momentum of the virtual photon, and $\gamma_{\mathbf{rad}}$ the 4-momentum of the real radiated photon.

It is possible that the energy of the radiated photon is so large that only elastic scattering off the target is possible. This scattering has to be taken into consideration as well as loop corrections. In this analyisis only events with at least one detected hadron in the final state are selected; these hadrons cannot be produced in elastic scattering, so the elastic contribution is not applicable here.

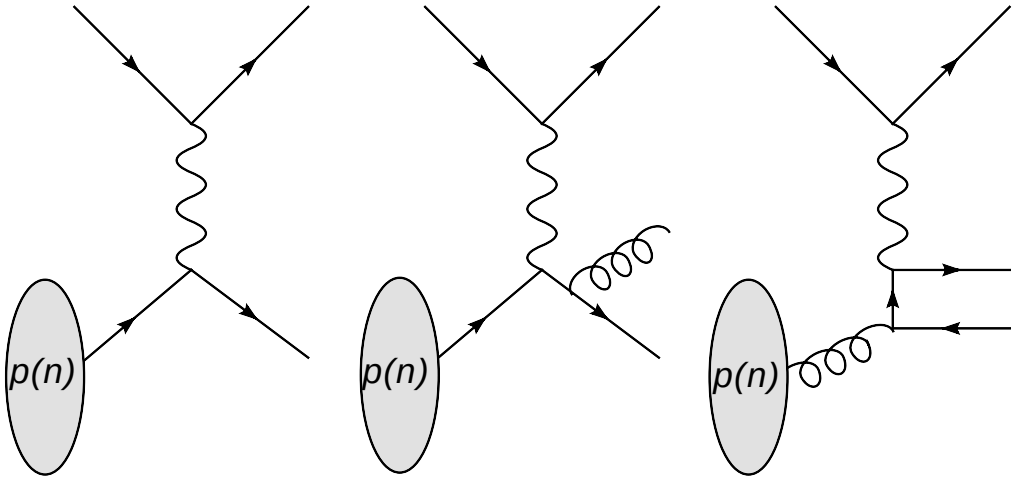

Figure 5.4: Diagrams of first and next-to-leading order QCD processes. From left to right: the Born diagram, QCD Compton, and photon-gluon fusion.

5.2.3 The PYTHIA process generation

In this step PYTHIA generates the quarks, gluons, strings, etc. according to the process that was chosen in the first step. Most important are the two highest order QCD processes. They are illustrated in figure 5.4 together with the Born diagram. The first one is QCD Compton scattering, the second one is photon-gluon fusion.

The PYTHIA generator is able to simulate scattering on a nucleon target (proton or neutron). In this analysis a D target was simulated by taking the sum of two Monte Carlo productions, one with a neutron, and another one with a proton as target. These two productions have the same number of generated events and were added with a weight equal to one[2].

5.2.4 JETSET fragmentation

JETSET [95] creates the final hadronic state using the output from PYTHIA according to the LUND string fragmentation model [32]. It is possible to tune parameters in JETSET that have an impact on the fragmentation process. These parameters were tuned to optimally describe the hadron multiplicities measured at HERMES ([13] and [15]). At this point all the events generated are at generator level.

5.2.5 The HERMES Monte Carlo

The final hadronic state is then passed to the HERMES Monte Carlo (HMC) that is a Monte Carlo simulation of the HERMES spectrometer based on the GEANT3 toolkit described in [96]. This program calculates particle acceptance and interaction effects due to the HERMES

[2]Normally productions with the same number of integrated luminosity are added. This was not done because this production was used to unfold data for all used targets (D, Ne, Kr, and Xe). A test comparing unfolded data using different MCs (including this one) is described in section 6.8.7.

spectrometer. For each particle the trajectory through the spectrometer is simulated taking into account the interaction with all the different spectrometer materials as well as the magnetic fields. The result is that for all detectors lying on a particle track their response is simulated, which is similar to the detector response recorded during real data taking. The output of HMC has the same format as the HDC output of the HERMES spectrometer.

5.2.6 HERMES ReConstruction

The HERMES ReConstruction code (HRC) uses the output of HMC to reconstruct the entire event. The HRC software is also used in the reconstruction of real data (see section 3.5.5).

5.2.7 The μDST writer

In this final step the output of HRC is rewritten into ADAMO tables in the same format as real HERMES data but with additional information relevant to the Monte Carlo. In a Monte Carlo simulation every step and every particle is known, while in the experimental data only what is detected can be known. Therefore, some extra tables are filled in μDSTs for Monte Carlo simulation data like process type (e.g, photon-gluon fusion, VMD, etc.), particle type (e.g, pion, u-quark, photon, etc.), and parent particle.

5.3 The HERMES Monte Carlo chain with the DISNG/LEPTO generator

The HERMES Monte Carlo chain that uses the DISNG/LEPTO generator is illustrated in a flow chart in figure 5.5. This Monte Carlo was used to study the influence of the nuclear dependence of the radiative corrections on the unfolding for radiative and acceptance effects described in section 6.8.7. This is possible because this Mont Carlo is able to simulate lepton scattering on nuclear targets although nuclear effects such as color transparency and nuclear attenuation are not simulated.

This chain is the same as the one using PYTHIA except that the DISNG generator generates the lepton kinematics uniformly distributed in a ν and $\log Q^2$ box and not according to a cross section as the PYTHIA generator does. Afterwards every event is weighted according to the cross section, which is calculated in a similar way as in PYTHIA but here only the direct photon process is included. At this stage RADGEN applies the radiative corrections. After that, LEPTO [97] generates the process. All the following steps are the same as described in previous section.

5.4 RHOMC

The RHOMC [98, 99] Monte Carlo only simulates exclusive production of ρ^0 vector mesons and their decay. First, the lepton kinematics are generated in a $\log Q^2$, E', and $\phi_{e'}$ box and afterwards weighted according to the cross section. Then the ρ^0 is generated and decays. After that the event is passed to HMC, HRC, and the μDSTwriter. This chain is illustrated in a flow

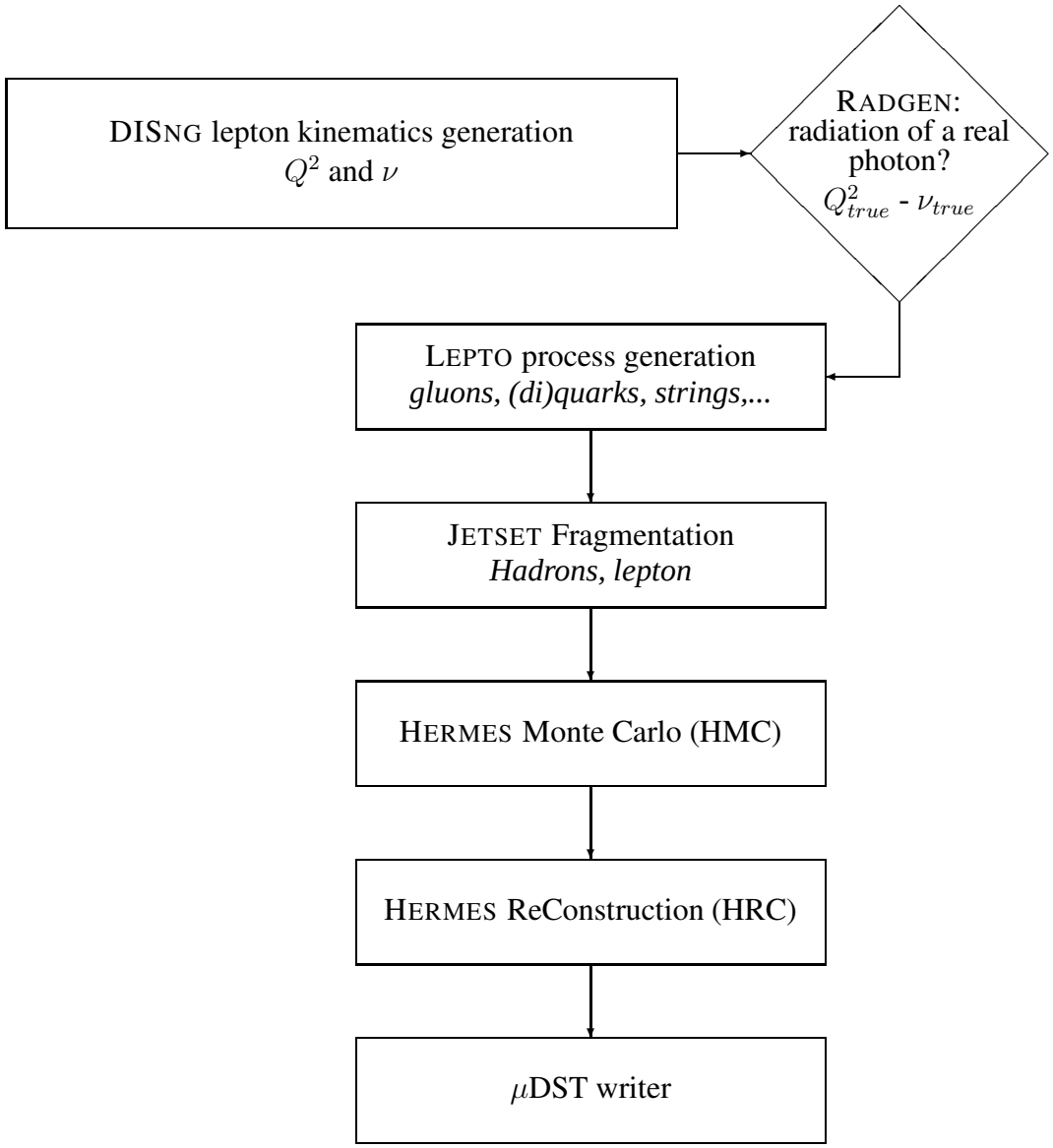

Figure 5.5: Flow chart of the HERMES Monte Carlo chain using DISNG/LEPTO as generator.

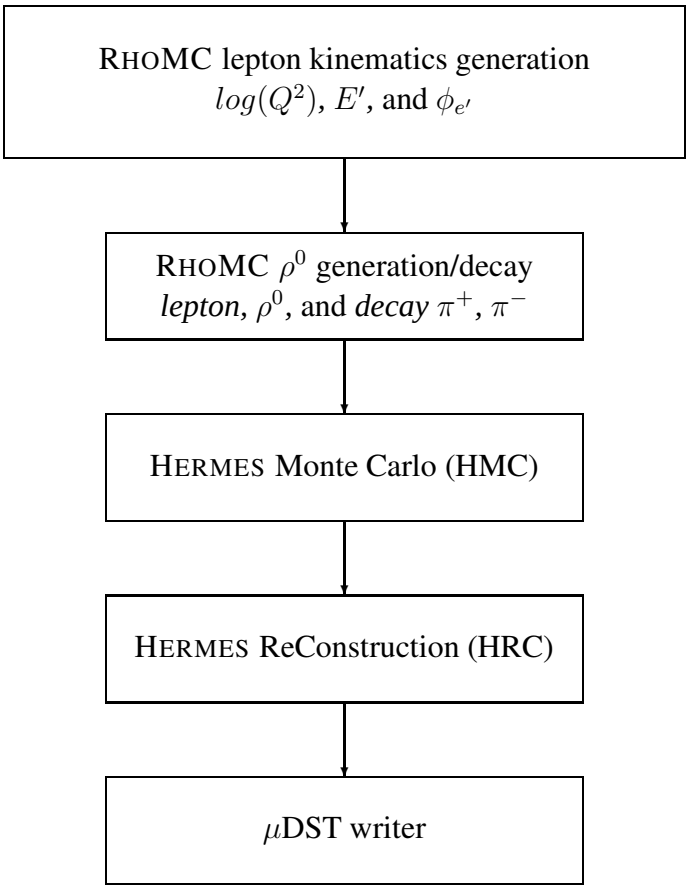

Figure 5.6: Flow chart of the HERMES Monte Carlo chain using RHOMC as generator.

chart in figure 5.6. The RHOMC Monte Carlo was used to correct data for pions coming from the decay of exclusively produced ρ^0 particles (cf. section 5.1). The advantage of RHOMC is that there are many parameters (e.g., spin density matrix elements, t'-slopes) that can be tuned in order to describe the HERMES data [99]. Also by doing this it is possible to simulate exclusive ρ^0 production on nuclear targets by changing the t'-slope parameter (see section 6.7).

Chapter 6

Analysis

The data used for this analysis are from the years 1999 (Kr and D target), 2000 (Ne and D target), 2004 (Kr, Xe, and D target), and 2005 (Kr, Xe, and D target). For D both data taken with a polarized target (from the 1999 and 2000) and with an unpolarized target were used. One can use the polarized target data summing over both polarization states when the obtained total luminosity is the same for both states. For the HERMES experiment this is easy to do because on average the target polarization changes in 1 to 3 minute intervals meaning that on a year basis one obtains the same statistics for both target polarizations. This section describes how the data was selected and the analysis steps to obtain p_t-broadening at Born level as a function of A, Q^2, ν, and z for different hadron types produced on Ne, Kr, and Xe targets. Here, Born level means that a correction was made for QED radiative effects, detector efficiency, and acceptance in order to be able to compare the obtained results with theoretical models. Data consistency checks were performed to check the stability of the data over several data taking years and different target gas densities. A charge-symmetric background correction was applied, followed by a correction for RICH hadron-identification in-efficiencies (called RICH unfolding). Then a correction was made for the contamination of the hadron sample originating from exclusive vector mesons. Finally, a correction for detector acceptance and QED radiative effects was applied using an unfolding method described in [108] to obtain p_t-broadening at Born level. A schematic view of these steps is shown in table 6.1.

Step#	Description	Result
1	Raw $\langle p_t^2 \rangle$ extraction from data (μDSTs)	$\langle p_t^2 \rangle^{raw}_{D,Ne,Kr,Xe}$
2	Charge-symmetric Background (CSB) correction	$\langle p_t^2 \rangle_{D,Ne,Kr,Xe}$
3	RICH unfolding	$\langle p_t^2 \rangle_{D,Ne,Kr,Xe}$
4	Exclusive vector meson correction	$\langle p_t^2 \rangle_{D,Ne,Kr,Xe}$
5	Unfolding for radiative and acceptance corrections	$\langle p_t^2 \rangle^{Born}_{D,Ne,Kr,Xe}$
6	$\langle p_t^2 \rangle^{Born}_{Ne,Kr,Xe} - \langle p_t^2 \rangle^{Born}_{D}$	$\Delta\langle p_t^2 \rangle^{Born}_{Ne,Kr,Xe}$

Table 6.1: The analysis steps taken to extract p_t-broadening

Data quality	Requirement
Dead time correction factor	$0.5 < \eta_{Dead} < 1.0$
First burst in run	do not select
Bad μDST record	do not select
No logbook data quality info	do not select
Dead calorimeter blocks	do not select
Dead paddles in the preshower	do not select
TRD bad	do not select
High voltage trips	do not select

Table 6.2: Applied data quality requirements.

6.1 Data-quality

The quality of the data is monitored during data taking, using slow control information as well as trigger and event rates. However, because the online data are uncalibrated, it is difficult to fully judge whether a given data set is suitable for analysis. Also, depending on the analysis, different requirements on the performance of the detectors, background, beam and target conditions, etc. are requested. Therefore a careful (iterative) study of the data quality is made offline by the responsible group. They analyze the data burst-wise and provide a list with criteria that are (not) fulfilled. This list is called a burst-list and is used to check for requirements needed for the specific analysis. The data quality requirements for this analysis are presented in table 6.2. The dead time correction factor constraint ensures that the DAQ system was working properly and that the calculated trigger life time has physical values. The first burst in a run is rejected because information might be lost or mixed up during initialization of the DAQ at the beginning of a run. Bad μDST records are records that are not synchronized or with missing entries. These are not selected. If there is no data-quality information written in the logbook the burst is also not selected. All the remaining constraints make sure that the drift chambers are working properly, the PID detectors are fine and that all blocks in the calorimeter and luminosity detector are working.

6.2 Geometric and kinematic constraints

In this section a description is given of all the geometric and kinematic constraints used for this analysis. A summary of the applied constraints can be found in table 6.3.

Because every track of interest has to come directly from the target, a z-vertex constraint and a transverse vertex offset constraint are applied. The z-vertex constraint guarantees that the z coordinate of the track vertex lies within the target cell and the transverse vertex offset constraint makes sure that the transverse offset of the track vertex is reasonable so that it is very likely that the track originates from a target atom. The constraint on the track position in the calorimeter (also called the calo fiducial constraint), the front and rear (field) clamp position, and the septum plate position are there to make sure that the track is well within the HERMES spectrometer acceptance. In order to separate leptons and hadrons the PID constraints de-

Constraints for all tracks	
z-vertex	$\lvert z_{vertex}\rvert < 20$ cm
Transverse vertex offset	$d_{vertex} < 0.75$ cm
Track position in calorimeter	$\lvert x_{calo}\rvert < 175$ cm, $30 < \lvert y_{calo}\rvert < 108$ cm
Track position at front field clamp	$x_{ffc} < 31$ cm
Track position at septum plate	$y_{sp} > 7$ cm
Track position at rear field clamp	$y_{rfc} < 54$ cm
Track position at rear clamp	$\lvert x_{rc}\rvert \leq 100$ cm, $\lvert y_{rc}\rvert \leq 54$ cm
Constraints to identify leptons and hadrons	
Lepton identification	$0 < PID3 + PID5 - \Phi < 100$
Scattered lepton identification	lepton with highest momentum
Hadron identification	$-100 < PID3 + PID5 - \Phi < 0$
Scattered lepton constraints	
DIS scale	$1 < Q^2 < 10$ GeV^2
Invariant mass of hadronic final state	$W^2 > 10$ GeV^2
Energy of the virtual photon	$\nu < 23$ GeV
Hadron constraints	
RICH Quality factor	rQp > 0
Hadron energy fraction	$0.2 < z < 1.0$, $z_{total} < 1.07$
Transverse momentum squared	$p_t^2 < 4$ GeV^2
Identified as a pion or kaon using RICH	$2 < p_h < 15$ GeV, RICH IRT method
Not identified hadrons	$p_h > 1$ GeV, RICH best method

Table 6.3: Table containing the geometric and kinematic constraints applied to the data

scribed in section 3.5.2 were applied. If there are more then one lepton in an event, the lepton with the highest momentum was chosen as the scattered one regardless of its charge. This allows for a charge-symmetric background correction described in section 6.5. Constraints were applied on Q^2 to select the scale of the deep-inelastic process ($Q^2 > 1$ GeV^2 means parton scale), on W^2 so that the invariant mass of the hadronic final state is above the highest resonant nucleon state (W^2 = 10 GeV^2), and on ν to avoid the region ($\nu > 23$ GeV) where radiative corrections and their associated uncertainties become too large. The Q^2, W^2, and ν constraint imply that $\nu > 5.39$ GeV, $0.0404 < \theta_{lepton} < 0.2827$ rad, $0.1955 < y < 0.8342$, and $0.0232 < x < 0.9887$. For hadrons the RICH quality factor (rQp, described in section 3.5.2) constraint is there to select only identified hadrons. The constraint on z wa applied to select mostly leading hadrons and to reject target remnants. The total reconstructed z (z_{total}) cannot be larger then 1 (in an ideal world) but to account for detector smearing and resolution this constraint was set to 1.07. When dealing with an identified hadron sample (pions or kaons) the hadron-momentum constraint was chosen in order to be able to do RICH unfolding, which is a correction method for RICH inefficiencies described in section 6.6. For un-identified hadrons the momentum constraint does not have to be so strict, the ν and z constraint imply that the hadron momentum (p_h), depending on the hadron type, has to be larger then $\sim$1 GeV. There

are two methods that use RICH detector data for identifying hadrons, one is called the Indirect Ray Tracing (IRT) method and the other one is called the Direct Ray Tracing (DRT) method and they are described in [101]. For an identified-hadron sample one has to apply RICH unfolding to correct for RICH inefficiencies (cf. section 6.6). This unfolding only works for hadrons identified using the IRT method. When an unidentified-hadron sample was selected, the best of the two methods was chosen (this depends on the kinematics of the hadron), this method is called the RICH best method. The hadron identification is only used to calculate z, which requires the mass of the hadron.

The number of obtained SIDIS events, after applying the constraints mentioned above and correcting for the charge-symmetric Background (cf. section 6.5), are shown in table 6.4.

6.3 Binning

The binning used for Q^2, ν, z, and p_t^2 can be found in table 6.5. The bins in Q^2, ν, and z are chosen in a way that the statistical error bars are as small as possible and that there are enough bins left to observe trends. The binning in p_t^2 is a bit more delicate. In the data the p_t^2 value per hadron is available, so to calculate average p_t^2 the following formula can be used:

$$\langle p_t^2 \rangle = \frac{\sum_i^{\#hadrons} (p_t^2)_i}{\#hadrons}. \tag{6.1}$$

After the unfolding described in section 6.8 the information of the p_t^2 value per event is lost. Only the number of hadrons per bin is known. In this case the average is calculated using:

$$\langle p_t^2 \rangle = \sum_i^{bins} \left[\frac{h(i)}{\sum_j^{bins} h(j)} \langle p_t^2 \rangle_{data}(i) \right] = \frac{\sum_i^{bins} h(i) \langle p_t^2 \rangle_{data}(i)}{\#hadrons}, \tag{6.2}$$

where $h(i)$ is the number of hadrons in bin i, $\langle p_t^2 \rangle_{data}(i)$ is the average p_t^2 in bin i, extracted from raw data. The binning in p_t^2 was chosen to have the minimum amount of bins with a minimal discrepancy between average p_t^2 calculated using 6.1 and 6.2 (without unfolding).

6.4 Data consistency

The HERMES spectrometer changed over time due to the installation of new detectors, removal of old detectors, repairs, etc. To check if these changes have an effect on the measured p_t-broadening, a comparison of the measured p_t-broadening on a krypton target for several data-taking years (1999, 2004, and 2005) was made. By doing this one also checks automatically for differences coming from low-/high-density target gas data-taking, caused by, e.g., a lower chamber efficiency when using high-density target gas. In 1999 only low-density target gas was used while in 2004 and 2005 mainly high-density target gas were used. Results of this check can be seen in figure 6.1 where ratios of p_t-broadening over three years of data taking are shown (1999 was taken as the reference year) versus Q^2, z, and ν. It is clear that p_t-broadening is consistent. Therefore summation of all years is possible.

	$h^+ \times 10^3$	$h^- \times 10^3$	$\pi^+ \times 10^3$	$\pi^- \times 10^3$	$K^+ \times 10^3$
$\frac{Kr}{D}$(99c0)	$\frac{124.563}{269.272}$	$\frac{76.447}{177.806}$	$\frac{82.269}{188.878}$	$\frac{64.978}{150.983}$	$\frac{19.857}{39.746}$
$\frac{Ne}{D}$(00c1)	$\frac{557.572}{1047.000}$	$\frac{351.371}{689.960}$	$\frac{382.101}{735.240}$	$\frac{299.495}{585.617}$	$\frac{84.668}{153.516}$
$\frac{Kr}{D}$(04b0)	$\frac{158.491}{403.659}$	$\frac{98.079}{269.387}$	$\frac{105.783}{284.302}$	$\frac{083.584}{229.197}$	$\frac{25.062}{59.066}$
$\frac{Xe}{D}$(04b0)	$\frac{103.021}{403.659}$	$\frac{63.139}{269.387}$	$\frac{67.640}{284.302}$	$\frac{53.914}{229.197}$	$\frac{16.755}{59.066}$
$\frac{Kr}{D}$(05b1)	$\frac{204.956}{822.767}$	$\frac{126.755}{542.306}$	$\frac{136.193}{580.035}$	$\frac{107.773}{460.669}$	$\frac{31.951}{119.159}$
$\frac{Xe}{D}$(05b1)	$\frac{196.891}{822.767}$	$\frac{120.027}{542.306}$	$\frac{128.681}{580.035}$	$\frac{102.069}{460.996}$	$\frac{31.414}{119.159}$
D	2542.698	1679.459	1788.455	1426.466	371.487
Ne	557.572	351.371	382.101	299.495	84.668
Kr	488.010	301.281	324.245	256.335	76.870
Xe	299.912	183.166	196.321	155.983	48.169

Table 6.4: SIDIS accumulated statistics.

Kinematic variable	bins (limits)
Q^2	1-2-3-10 GeV^2
ν	5-11-15-17-23 GeV
z	0.2-0.4-0.6-0.8-1.0
p_t^2	0.0-0.1-0.2-0.3-0.5-0.7-1.0-4.0 GeV^2

Table 6.5: Binning used for this analysis.

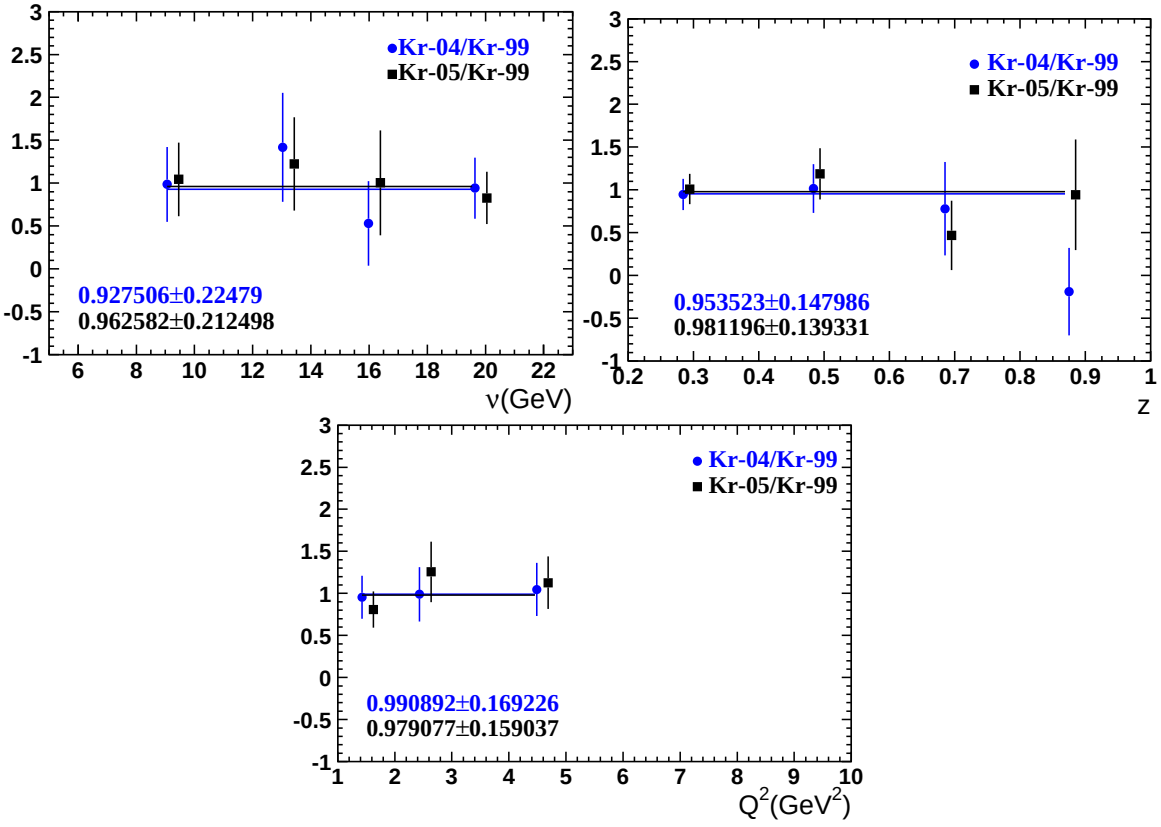

Figure 6.1: The ratio of p_t-broadening for negatively charged pions measured on a krypton target is shown versus ν, Q^2, and z. Data taking year 1999 was taken as reference year. The shown values are results of fitting a constant.

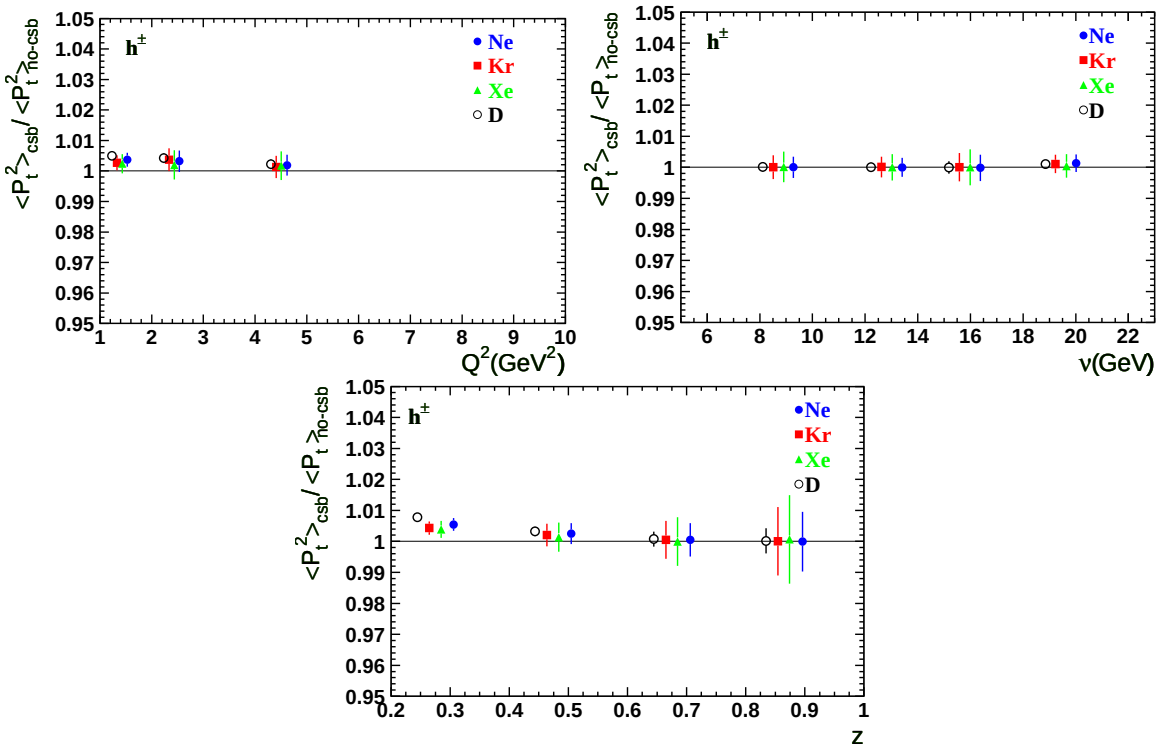

Figure 6.2: The ratio of $\langle p_t^2 \rangle$ with charge-symmetric background (csb) and without charge-symmetric background (no-csb) versus Q^2, ν, and z.

6.5 Charge-symmetric background correction

If there is more then one detected lepton in an event, the lepton with the highest momentum is chosen as the scattered beam lepton, neglecting its charge. If this lepton has a charge that is not equal to the beam charge, the event is considered as background and is taken into account with a weight equal to -1. In this way the event is subtracted twice (if the weight is set to 0 it is subtracted once). This was done to correct for the same background but where the lepton had the same charge as the beam. By doing this one assumes that this background is charge-symmetric. The impact of this correction on $\langle p_t^2 \rangle$ in function of Q^2, ν, and z can be seen in figure 6.2. In order to make an interpretation of these plots easier figure 6.3 is shown. This plot shows the effect of the charge-symmetric background correction on hadron spectra versus a two-dimensional binning. The effect of the correction is largest when it introduces a slope in a bin in ν, z, or Q^2, e.g., in the first bin in z. It is clear that the Charge-Symmetric Background (CSB) correction does not change the p_t-broadening results as can be seen in figure 6.4.

6.5.1 Error calculation

When running over data, all the events with a positive weight and events with a negative weight are added separately in a way described in table 6.6: N_p is defined as the sum of the absolute weight values of all selected hadrons with a positive event weight. N_n is the same as N_p but

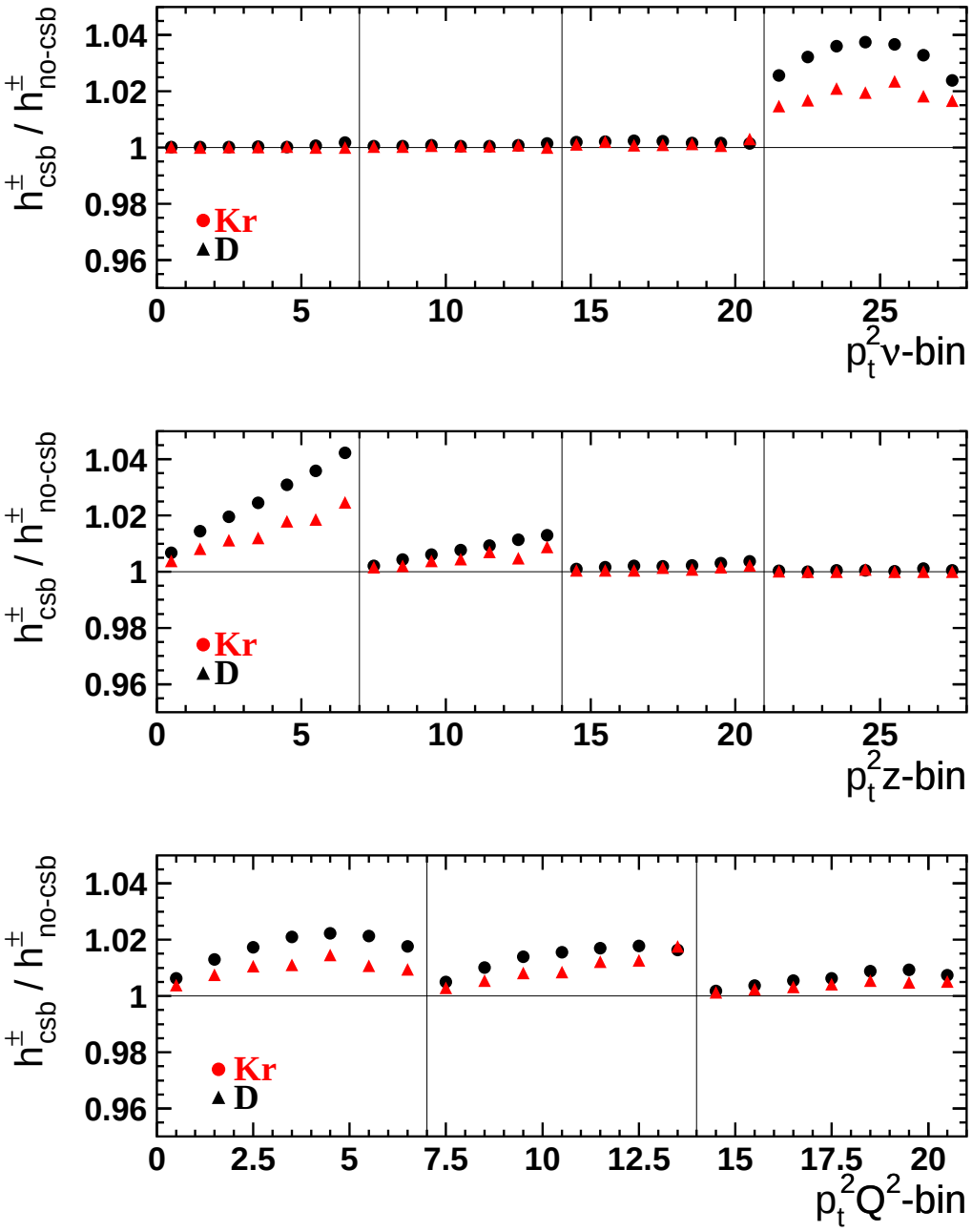

Figure 6.3: Ratios of hadron counts (with and without charge-symmetric background) versus a two dimensional binning. The number shown on the x-axis equals p_t^2-bin# + $(7-1)$ $z, Q^2,$ *or* ν-bin#.

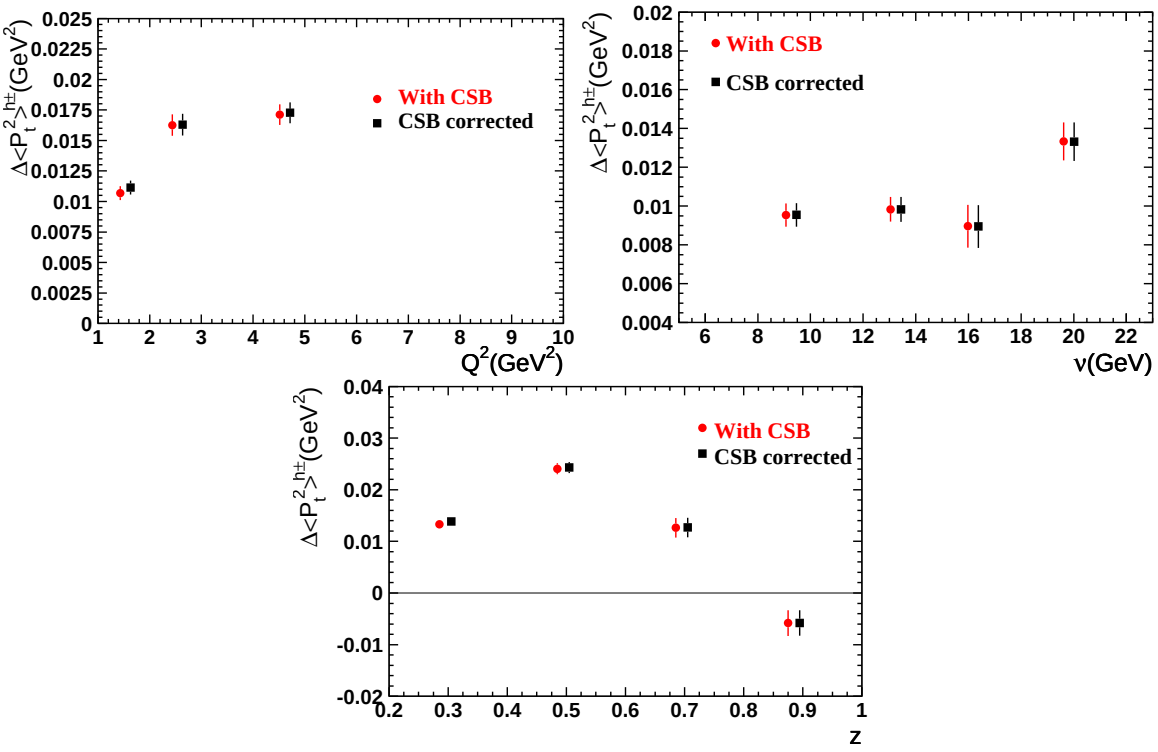

Figure 6.4: Influence of the charge-symmetric background correction on the p_t-broadening.

now the weight has to be negative, and $N = N_p - N_n$. The error on $\langle p_t^2 \rangle$ (= $\frac{\sum p_t^2}{N}$) is (see also table 6.6):

$$\sqrt{\frac{1}{N-1}\left[\left(\frac{\sum p_t^4}{N}\right) - \left(\frac{\sum p_t^2}{N}\right)^2\right]}. \tag{6.3}$$

This formula is used to calculate errors on $\langle p_t^2 \rangle$ bin per bin.

6.6 RICH Unfolding

When extracting p_t-broadening for a certain hadron type the RICH detector is used to identify hadrons. Every detector has its limitations; also the RICH detector will sometimes misidentify hadrons. One can try to correct for these misidentifications using a parameterization of the RICH performance. To do this a Monte Carlo simulation of the RICH detector was used. This simulation was tuned using data of particles coming from decays like a $\Phi \rightarrow K^+K^-$. In this way one can reconstruct the Φ meson by assigning the kaon mass to both detected hadrons and investigate the RICH efficiency. Decay particles were used because in this way the particle type is known beforehand and can be compared with the identification coming from the RICH detector.

The RICH performance is parameterized in P-matrices [101]. These matrices relate the vector of identified particles ($\vec{I}$) to the vector of true particles ($\vec{N}$):

Variable	Definition	weight (w_i)
N_p	$\sum_i^{events} \lvert w_i \rvert$	> 0
N_n	$\sum_i^{events} \lvert w_i \rvert$	< 0
N	$N_p - N_n$	-
$(\sum p_t^2)_p$	$\sum_i^{events} \lvert w_i \rvert \cdot (p_t^2)_i$	> 0
$(\sum p_t^2)_n$	$\sum_i^{events} \lvert w_i \rvert \cdot (p_t^2)_i$	< 0
$\sum p_t^2$	$(\sum p_t^2)_p - (\sum p_t^2)_n$	-
$(\sum p_t^4)_p$	$\sum_i^{events} \lvert w_i \rvert \cdot (p_t^4)_i$	> 0
$(\sum p_t^4)_n$	$\sum_i^{events} \lvert w_i \rvert \cdot (p_t^4)_i$	< 0
$\sum p_t^4$	$(\sum p_t^4)_p - (\sum p_t^4)_n$	-

Table 6.6: Variables used for the error calculation in formula (6.3).

$$\begin{pmatrix} I_\pi \\ I_K \\ I_P \\ I_X \end{pmatrix} = \begin{pmatrix} P_\pi^\pi & P_\pi^K & P_\pi^P \\ P_K^\pi & P_K^K & P_K^P \\ P_P^\pi & P_P^K & P_P^P \\ P_X^\pi & P_X^K & P_X^P \end{pmatrix} \cdot \begin{pmatrix} N_\pi \\ N_K \\ N_P \end{pmatrix}, \tag{6.4}$$

where X stands for unidentified hadrons and P_j^i is the probability that a hadron of type i is identified as a hadron of type j. After removing the last row of the P-matrix and the last element of $\vec{I}$ one obtains P_{trunc} and $\vec{I}_{trunc}$, respectively. If P_{trunc} is invertible then the following equation is obtained:

$$\vec{N} = P_{trunc}^{-1} \cdot \vec{I}_{trunc}. \tag{6.5}$$

This can be used to extract the vector of true hadrons from the observed hadron fluxes. In practice this is done by using the elements of P_{trunc}^{-1} as a weight for the selected hadron. For example, if only pions are selected and the RICH detector identifies a hadron as a kaon, then the hadron gets weight $(P^{-1})_\pi^K$. If also the charge-symmetric background correction is applied then this weight (coming from the RICH unfolding) is multiplied by the weight coming from the charge-symmetric background correction.

The P-matrices were always calculated as a function of momentum and track multiplicity per detector half. Three sets of P-matrices were calculated using three different Monte Carlo simulation tunes. The e-tune is a tune using data from decayed Φ particles [102]. The h-tune uses data from decayed K_s, Φ, and Λ ($\overline{\Lambda}$) particles [103]. The main variable that was tuned in the Monte Carlo was the mirror roughness. The average between the mirror roughness used for the e-tune and the h-tune was taken as a center tune. The P-matrices calculated using the center tune were used to do the RICH unfolding. A set of P-matrices for track multiplicity one per detector half is shown in figure 6.5.

In table 6.7 a comparison in statistics is made between applied and not-applied RICH unfolding. One can observe differences on the few-percent level.

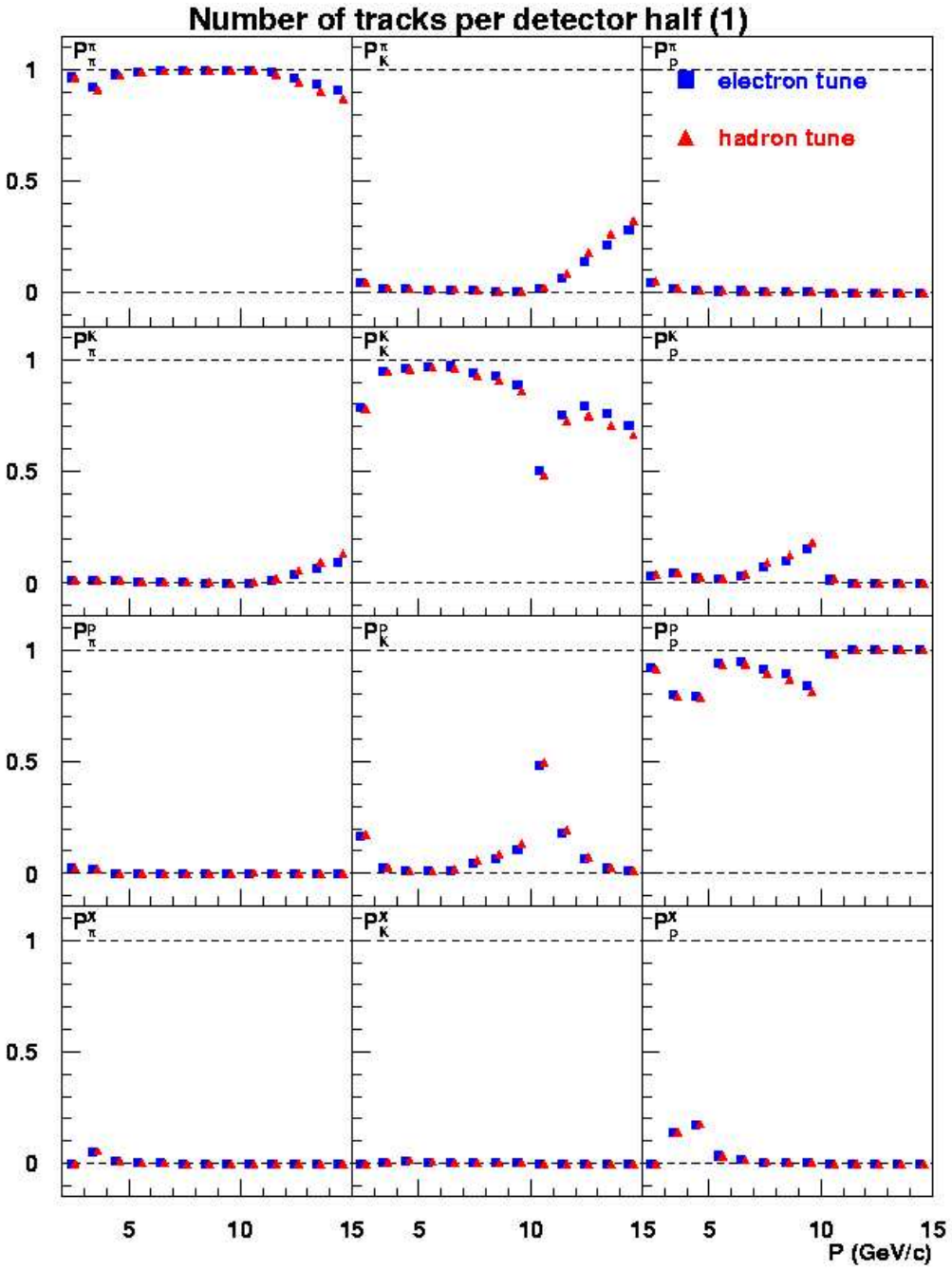

Figure 6.5: The elements of the P-matrices are shown in function of hadron momentum (here denoted as P) for a track multiplicity of 1 in a detector half using the e-tune and the h-tune.

	$\pi^+ \times 10^3$	$\pi^- \times 10^3$	$K^+ \times 10^3$
D	$\frac{1788.455}{1781.202}$	$\frac{1426.466}{1445.966}$	$\frac{371.487}{355.705}$
Ne	$\frac{382.101}{379.544}$	$\frac{299.495}{303.492}$	$\frac{84.668}{81.615}$
Kr	$\frac{324.245}{320.814}$	$\frac{256.335}{259.919}$	$\frac{76.870}{72.394}$
Xe	$\frac{196.321}{194.192}$	$\frac{155.983}{158.289}$	$\frac{48.169}{44.615}$

Table 6.7: Table containing the accumulated SIDIS statistics: $\frac{without\ RICH\ unfolding}{with\ RICH\ unfolding}$.

6.6.1 Systematic uncertainty

To estimate the systematic uncertainty of the RICH unfolding the maximal difference between the extracted p_t-broadening values between the center tune and the e/h - tunes were taken. The typical systematic error is around the 1 % level, except at high z bins because there the value of the p_t-broadening becomes smaller and the difference between the tunes becomes typically 10 % larger. Some numerical values are given in table 6.8.

6.7 Contamination from exclusive and diffractive processes

The detected hadron sample in semi-inclusive deep-inelastic scattering events contains a contribution of decay particles coming from exclusive vector mesons. This background cannot easily be cut away with a constraint on the invariant mass because it can happen that one of the two decay-pions is out of the acceptance of the HERMES spectrometer. The p_t-broadening of these particles is modified because they are coming from a decaying exclusive produced ρ^0. Therefore these particles are considered as background. A correction for this was made using the RhoMC Monte Carlo described in section 5.4.

First, the kinematics of ρ^0 decay pions was studied on a D target using the PYTHIA Monte Carlo generator together with HMC and HRC. Then the RhoMC Monte Carlo (also together with HMC and HRC) was used to simulate exclusive and diffractive processes on nuclear targets in order to correct the data for these processes.

6.7.1 Studying exclusive processes using a Monte Carlo simulation

A Monte Carlo study was made in order to have an idea of the magnitude of the exclusive vector meson decay contamination. The PYTHIA Monte Carlo was used to simulate phys-

Ne (π^+)	bin# 1	bin# 2	bin# 3	bin# 4
ν	$\frac{4.3\cdot10^{-5}\ GeV^2}{1.0\cdot10^{-2}\ GeV^2}$	$\frac{4.5\cdot10^{-5}\ GeV^2}{4.0\cdot10^{-3}\ GeV^2}$	$\frac{6.0\cdot10^{-5}\ GeV^2}{4.0\cdot10^{-4}\ GeV^2}$	$\frac{1.1\cdot10^{-4}\ GeV^2}{1.8\cdot10^{-3}\ GeV^2}$
z	$\frac{2.1\cdot10^{-5}\ GeV^2}{8.9\cdot10^{-3}\ GeV^2}$	$\frac{4.4\cdot10^{-5}\ GeV^2}{1.1\cdot10^{-2}\ GeV^2}$	$\frac{3.5\cdot10^{-4}\ GeV^2}{-1.4\cdot10^{-2}\ GeV^2}$	$\frac{4.4\cdot10^{-5}\ GeV^2}{-2.1\cdot10^{-2}\ GeV^2}$
Q^2	$\frac{6.9\cdot10^{-5}\ GeV^2}{4.5\cdot10^{-4}\ GeV^2}$	$\frac{4.9\cdot10^{-5}\ GeV^2}{9.2\cdot10^{-3}\ GeV^2}$	$\frac{6.8\cdot10^{-5}\ GeV^2}{1.0\cdot10^{-2}\ GeV^2}$	
Kr (π^-)	bin# 1	bin# 2	bin# 3	bin# 4
ν	$\frac{3.9\cdot10^{-5}\ GeV^2}{1.9\cdot10^{-2}\ GeV^2}$	$\frac{1.5\cdot10^{-5}\ GeV^2}{2.2\cdot10^{-2}\ GeV^2}$	$\frac{1.0\cdot10^{-4}\ GeV^2}{1.5\cdot10^{-2}\ GeV^2}$	$\frac{6.5\cdot10^{-5}\ GeV^2}{2.1\cdot10^{-2}\ GeV^2}$
z	$\frac{1.6\cdot10^{-5}\ GeV^2}{2.6\cdot10^{-2}\ GeV^2}$	$\frac{5.9\cdot10^{-6}\ GeV^2}{3.6\cdot10^{-2}\ GeV^2}$	$\frac{9.0\cdot10^{-6}\ GeV^2}{2.0\cdot10^{-2}\ GeV^2}$	$\frac{1.3\cdot10^{-4}\ GeV^2}{-8.8\cdot10^{-3}\ GeV^2}$
Q^2	$\frac{3.9\cdot10^{-5}\ GeV^2}{1.9\cdot10^{-2}\ GeV^2}$	$\frac{6.2\cdot10^{-5}\ GeV^2}{3.0\cdot10^{-2}\ GeV^2}$	$\frac{1.1\cdot10^{-5}\ GeV^2}{3.0\cdot10^{-2}\ GeV^2}$	
Xe (K^+)	bin# 1	bin# 2	bin# 3	bin# 4
ν	$\frac{4.3\cdot10^{-4}\ GeV^2}{6.0\cdot10^{-2}\ GeV^2}$	$\frac{3.8\cdot10^{-4}\ GeV^2}{4.7\cdot10^{-2}\ GeV^2}$	$\frac{4.4\cdot10^{-4}\ GeV^2}{5.4\cdot10^{-2}\ GeV^2}$	$\frac{3.9\cdot10^{-4}\ GeV^2}{5.3\cdot10^{-2}\ GeV^2}$
z	$\frac{1.7\cdot10^{-4}\ GeV^2}{6.5\cdot10^{-2}\ GeV^2}$	$\frac{7.5\cdot10^{-4}\ GeV^2}{7.8\cdot10^{-2}\ GeV^2}$	$\frac{1.1\cdot10^{-3}\ GeV^2}{1.1\cdot10^{-1}\ GeV^2}$	$\frac{3.9\cdot10^{-2}\ GeV^2}{2.5\cdot10^{-1}\ GeV^2}$
Q^2	$\frac{5.8\cdot10^{-4}\ GeV^2}{6.1\cdot10^{-2}\ GeV^2}$	$\frac{2.6\cdot10^{-4}\ GeV^2}{5.8\cdot10^{-2}\ GeV^2}$	$\frac{3.8\cdot10^{-4}\ GeV^2}{6.4\cdot10^{-2}\ GeV^2}$	

Table 6.8: Table containing the systematic uncertainties ($\frac{\delta_{sys}}{\Delta\langle p_t^2\rangle}$) due to the RICH unfolding.

Reconstructed invariant mass of hadrons with opposite charge	$0.6 < M_{h^+h^-} < 1.0$ GeV
Hadron multiplicity	$N_h = 2$
Transverse momentum transfer to hadronic vertex	$t' >$ -0.4 GeV^2
Exclusivity variable ΔE	$\Delta E < 0.6$ GeV

Table 6.9: Additional constraints applied in order to reconstruct exclusive produced ρ^0 particles and to select their decay pions.

ical processes because it is a generator that includes a lot of processes including exclusive and diffractive meson production and it has the possibility to switch processes on and off. This generator is used together with a Monte Carlo describing the HERMES spectrometer (HMC+HRC) to produce events on a D target. A comparison was made between two PYTHIA Monte Carlo productions: one with only the semi-inclusive process switched on and one with all processes switched on. Results of this study can be seen in figure 6.6. There is only a significant vector meson decay contribution in the pion sample at high z as seen in figure 6.6. More extensive studies showed that the vector meson decay contribution in the pion sample showed up at high z and low p_t and that the contribution of other exclusive processes is negligible. Therefore, there is a correction applied only for pions coming from exclusive ρ^0 decays only.

Reconstructed exclusive ρ^0s

To correct the data sample for exclusive produced ρ^0 decay pions one has to deal with the fact that there is no Monte Carlo simulation available that can generate both coherent and incoherent ρ^0 particles produced on nuclear targets. Instead one can make two Monte Carlo productions (using RhoMC), one that has only incoherent ρ^0 production and one that simulates coherent ρ^0 production. This is possible because the coherent part can be simulated by changing the t'-slope parameter in the Monte Carlo, t' is the transverse momentum transfer to the hadronic vertex. The t'-slope is the negative slope of a t'-spectrum when plotted logarithmically on the vertical axis. The incoherent ρ^0 production has a typical t'-slope of 6.7 GeV^{-2}, while the coherent ρ^0 production has a t'-slope that depends on the atomic number but that is always higher then 6.7 GeV^{-2}. The t'-slopes are extracted using data. In order to extract a t'-spectrum from exclusive produced ρ^0 the same constraints that are described in table 6.3 are applied plus additional constraints described in table 6.9.

The mass of a ρ^0 particle is 770 MeV, the reconstructed mass constraint was taken between 600 and 1000 MeV. To select only exclusive and/or diffractive events the t' and ΔE constraint are applied, with ΔE:

$$\Delta E = \nu - E_{\rho^0} + \frac{t}{2M_p}, \tag{6.6}$$

with E_{ρ^0} the energy of the reconstructed ρ^0, M_p is the mass of the proton, and t is the momentum transfer to the hadronic vertex.

The reconstructed mass spectrum of ρ^0s produced on several targets can be seen in figure 6.7, the hadron momentum constraint used is the same as the one for an unidentified hadron

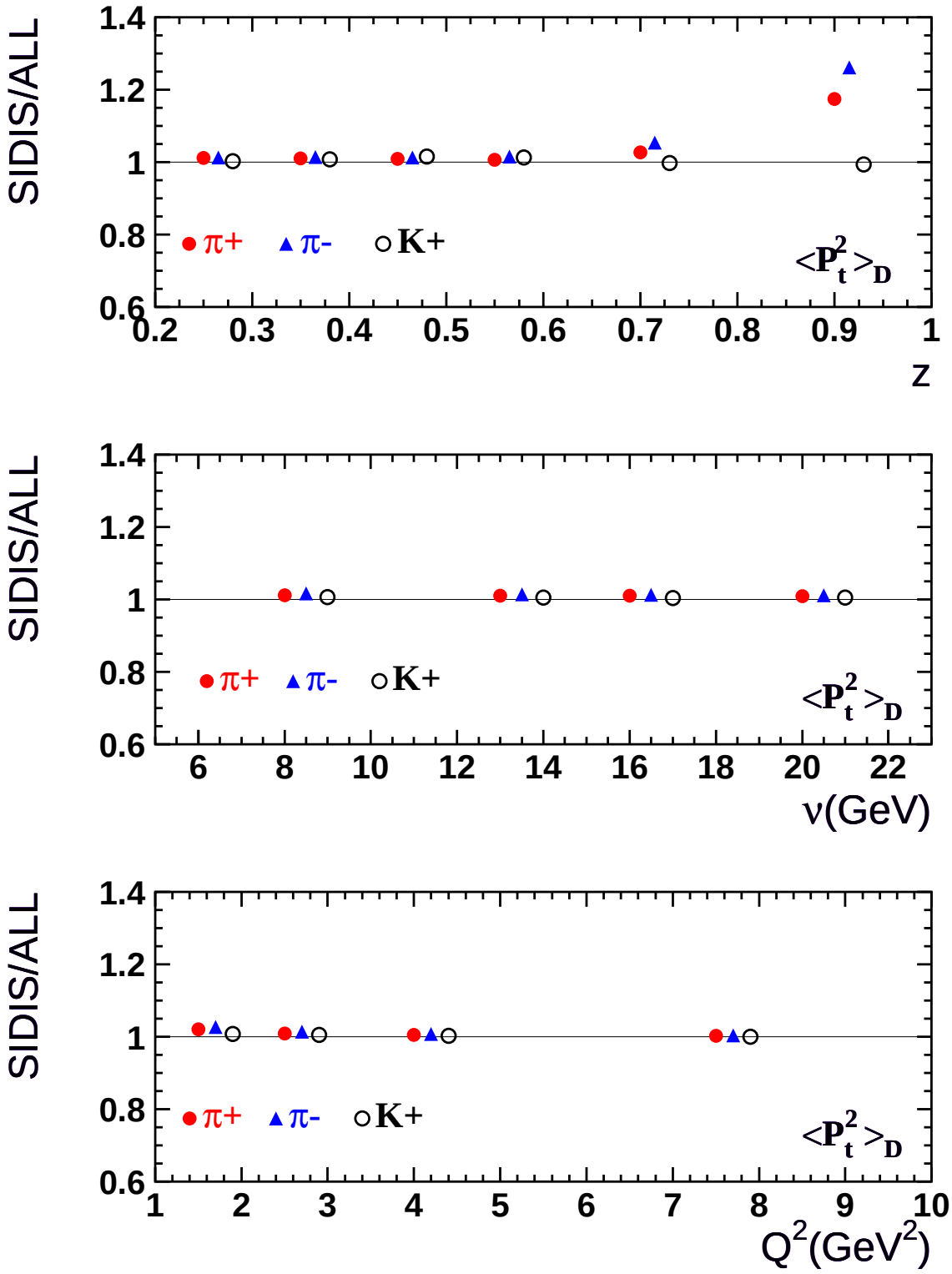

Figure 6.6: Ratios of average p_t^2 of formed hadrons obtained using the PYTHIA Monte Carlo, once with only the semi-inclusive process switched on and once with all processes switched on. This is shown for various hadron types versus z, Q^2, and ν.

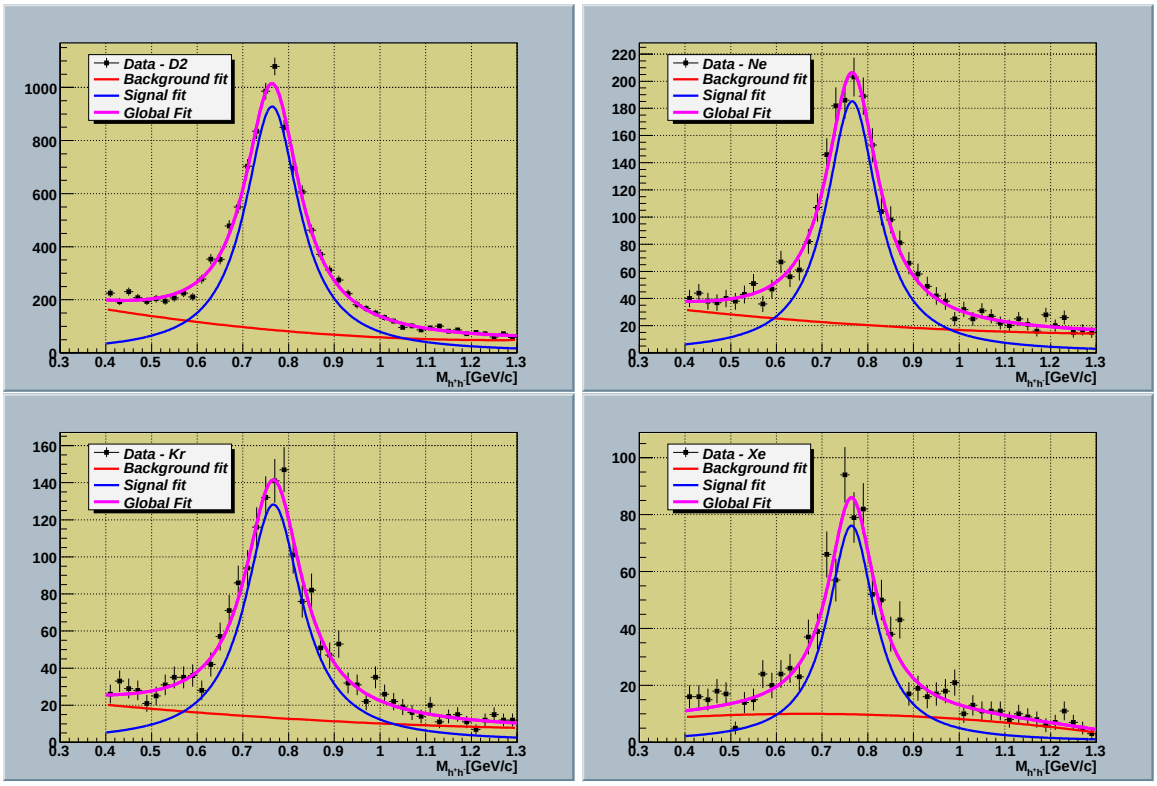

Figure 6.7: The reconstructed invariant mass spectrum of ρ^0 particles produced on several targets. Also the fits to obtain the signal and the background is shown.

sample ($p_h > 1$ GeV). The reconstructed mass spectrum where the identified hadron momentum constraint was $2 < p_h < 15$ GeV is not shown but the result was a difference of 5% in the number of reconstructed ρ^0s.

The number of reconstructed ρ^0s is used to normalize the RhoMC Monte Carlo simulation to the data. Because this Monte Carlo simulation does not provide a perfect description of the data over a large kinematic range this normalization is made dependent on the kinematic area in which the semi-inclusive deep-inelastic scattering events are selected. In practice this means that two renormalizations are needed: one for the unidentified-hadron sample and one for the identified one. The difference between the two normalizations is the hadron-momentum constraint due to the requirement for RICH unfolding (described in section 6.6).

The coherent slope of the t'-spectra is a parameter that has to be set to produce a RhoMC Monte Carlo production that describes the data. To obtain this parameter the t'-spectrum of the reconstructed ρ^0 are fit with [106]:

$$f(t') = a_n(b_{incoh}e^{b_{incoh}t'} + a_0 b_{coh}.e^{b_{coh}t'}), \tag{6.7}$$

with b_{incoh}, b_{coh}, a_n, and a_0 parameters of the fit, b_{incoh} is the incoherent slope and is the same for all targets, b_{coh} is the coherent slope and is different for all nuclear targets, and a_0 is the relative weight of the coherent ρ^0 production to the incoherent one. In practice it turned out that the obtained coherent slopes are in agreement within statistical errors with

the slopes obtained in another analysis [107] using the same fit function. Therefore, this parameter was fixed in the fit, in order to use already existing RhoMC productions. Before fitting this function, the t'-spectra were corrected for background by fitting the reconstructed mass (cf. figure 6.7) with the sum of a Breit-Wigner function (to describe the signal) and a second order polynomial (to describe the background). Events with $M_{h^+h^-}$ between 0.4 and 0.6 GeV and between 1.0 and 1.2 GeV were selected. The resulting t'-spectrum (of these events) was then renormalized with a factor equal to the ratio of the number of background events in the signal peak (which is provided by the $M_{h^+h^-}$ fit) and the total number of events in the (background) t' spectra. Then this renormalized (background) t'-spectrum is subtracted from the obtained t'-spectrum. Results of the fits can be found in table 6.10, both for the identified hadron momentum constraint ($2 < p_h < 15$ GeV) as for the unidentified hadron momentum constraint ($p_h > 1$ GeV). The t'-spectrum of hydrogen was fit as a check, but then the slope parameter was not fixed. One can see that the results of the fit are independent of the hadron momentum constraint. Therefore the same fit results are used for both normalizations.

$p_h >$ **1 GeV**	H	D	Ne	Kr	Xe
$b_{coh}[GeV^{-2}]$	6.7	-	83	154	186
a_0	-	≈ 0	0.465 ± 0.045	0.335 ± 0.034	0.193 ± 0.040
2 $< p_h <$ **10 GeV**	H	D	Ne	Kr	Xe
$b_{coh}[GeV^{-2}]$	6.7	-	83	154	186
a_0	-	≈ 0	0.478 ± 0.048	0.335 ± 0.027	0.193 ± 0.040

Table 6.10: This table shows the coherent slope (b_{coh}) together with the coherent to incoherent ratio (a_0) for different targets for both un- and identified hadron momentum constraint. Note that b_{coh} was fixed.

6.7.2 Contribution from $\Phi \rightarrow K^+ + K^-$ decay

It might happen that K^+-K^- decay pairs coming from exclusive Φ decays might be seen as a ρ^0 because it is not required that the two hadrons are identified pions when the ρ^0 is reconstructed. The mass of the Φ particle is 1020 MeV. The mass of $K^{\pm}$ is 493.7 MeV. One can use a frame where the momentum of the produced Φ is zero (center-of-mass frame). This means that the decay-kaon has a momentum of $\sqrt{(\frac{1020}{2})^2 - (493.7)^2} = 127.9$ MeV. In the frame used they both get the same amount of momentum in opposite directions (127.9 MeV). After detecting these kaons, they are treated as pions (which have a mass of 139.6 MeV). This means that the energy part of their four vector has to be equal to $\sqrt{139.6^2 + 127.9^2}$ = 189.3 MeV. The reconstructed mass of the ρ^0 then equals $\sqrt{(2 \cdot 189.3)^2}$ = 378.7 MeV. This is well below the lowest limit on the reconstructed mass of 500 MeV to become a significant contribution. This result changes under boost into the lab-frame. In this frame the invariant mass assuming the pion-mass for the kaons is always lower then the one calculated in the center-of-mass frame.

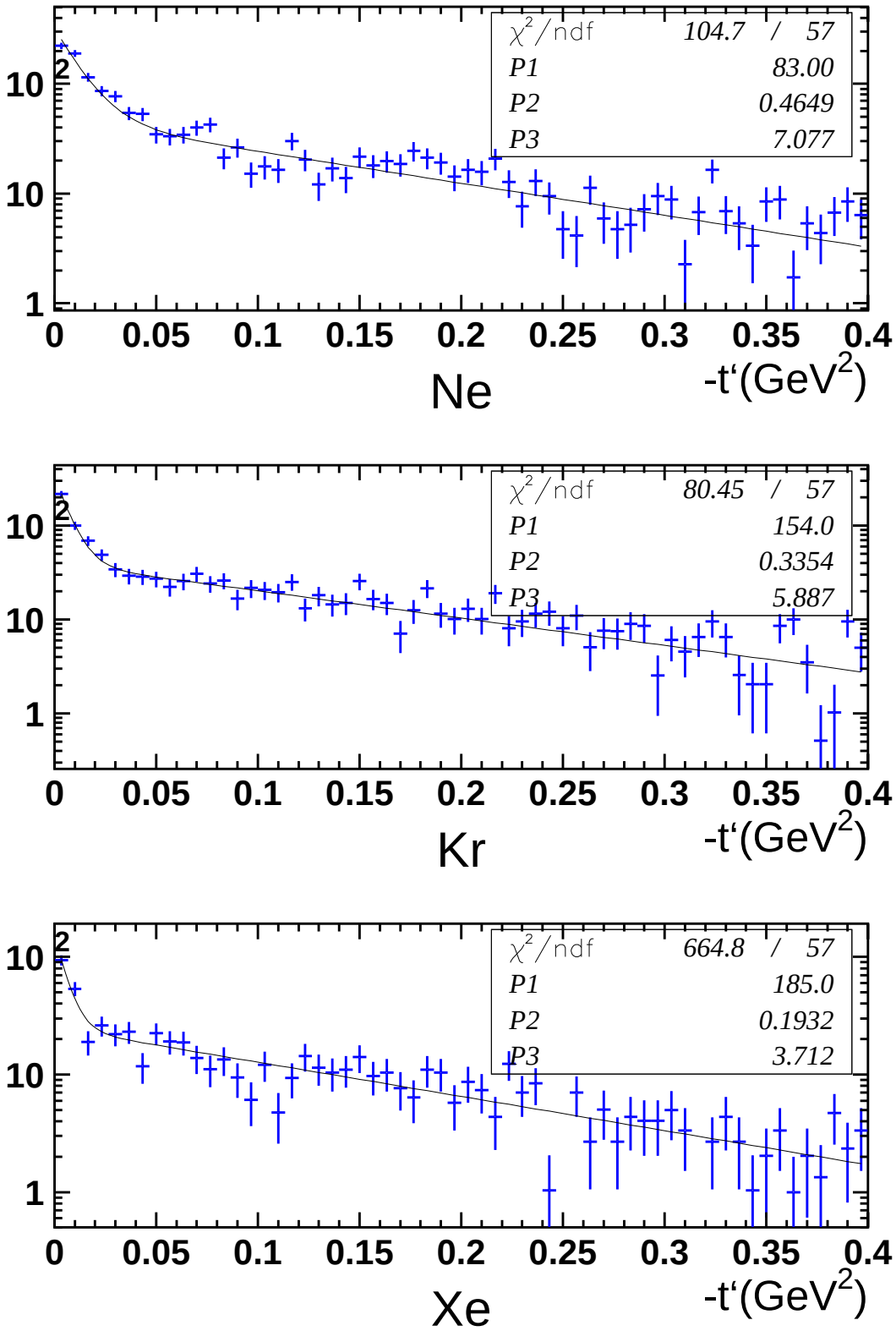

Figure 6.8: The figure shows fit t' spectra of ρ^0s produced on Ne, Kr, and Xe targets using 1 GeV $< p_h$. Fit parameter P1 represents the coherent slope, P2 equals a_0, and P3 is a_n (as in formula 6.7).

6.7.3 Simulated exclusive ρ^0s using RhoMC

There is no Monte Carlo simulation available that can generate both coherent and incoherent ρ^0 particles produced on nuclear targets. Instead one can make two Monte Carlo productions (using RhoMC), one that has only incoherent ρ^0 production and one that simulates coherent ρ^0 production. This is possible because the coherent part can be simulated by changing the t'-slope parameter in the Monte Carlo simulation. The incoherent ρ^0 production has a typical t'-slope of 6.7 GeV^{-2}, while the coherent ρ^0 production has a t'-slope that depends on the atomic number but that is always higher than 6.7 GeV^{-2}. The t'-slopes are extracted from data. In order to extract a t'-spectrum of exclusive ρ^0s in a Monte Carlo production the same procedure as for data was applied.

For every target two Monte Carlo productions were made: one with the incoherent slope and one with the coherent slope parameter set. Then both Monte Carlo productions were normalized to each other using the total number of reconstructed ρ^0s. This normalization was made dependent on the hadron momentum constraint. These two (normalized) Monte Carlo productions were added together and the Monte Carlo production with the coherent slope parameter gets a_0 (obtained from the t' spectra fit using data) as additional weight. The new Monte Carlo production is able to estimate the ρ^0-decay pion contribution in the data depending on the hadron-momentum constraint.

6.7.4 Correction for ρ^0-decay pions

A ρ^0 correction is applied only if the selected hadron sample contains pions, e.g., if only kaons are selected no correction is applied. The correction will be explained by using an example. Suppose only negatively charged pions are selected. First the total number of reconstructed ρ^0s is extracted from the data using the constraints mentioned above. Then the new produced Monte Carlo is renormalized to this number. Afterwards the number of negative pions per kinematic bin is counted in the reconstructed Monte Carlo. Because this Monte Carlo is normalized to the data it is possible to directly subtract this number from the number of negatively charged pions present in the corresponding kinematic bin of the data. This happens in an analogue way if all hadrons or positively charged pions are selected. When unfolding for acceptance and QED radiative effects (see section 6.8) is applied after this correction then all exclusive and single/double diffractive processes are switched off in the Monte Carlo used for this unfolding (process codes 91, 92, 93, and 94 in the PYTHIA Monte Carlo simulation). This method only works when the newly constructed Monte Carlo production describes the data well enough. A comparison of spectra from Monte Carlo and data can be seen in figure 6.9. If one takes the data as a model to test the Monte Carlo against, one obtains a χ^2 of 0.98, 2.58, and 2.73 for Ne, Kr, and Xe targets, respectively. The largest uncertainty is coming from the coherent slope (first 4-5 data points) where a slope has to be fit on less than 6 data points. Therefore, the a_0 parameter was varied to estimate the systematic uncertainty described in the next section, which has only an effect in this low t' region. This correction only has a significant impact at high z where the p_t-broadening moves towards zero as can be seen in figure 6.10.

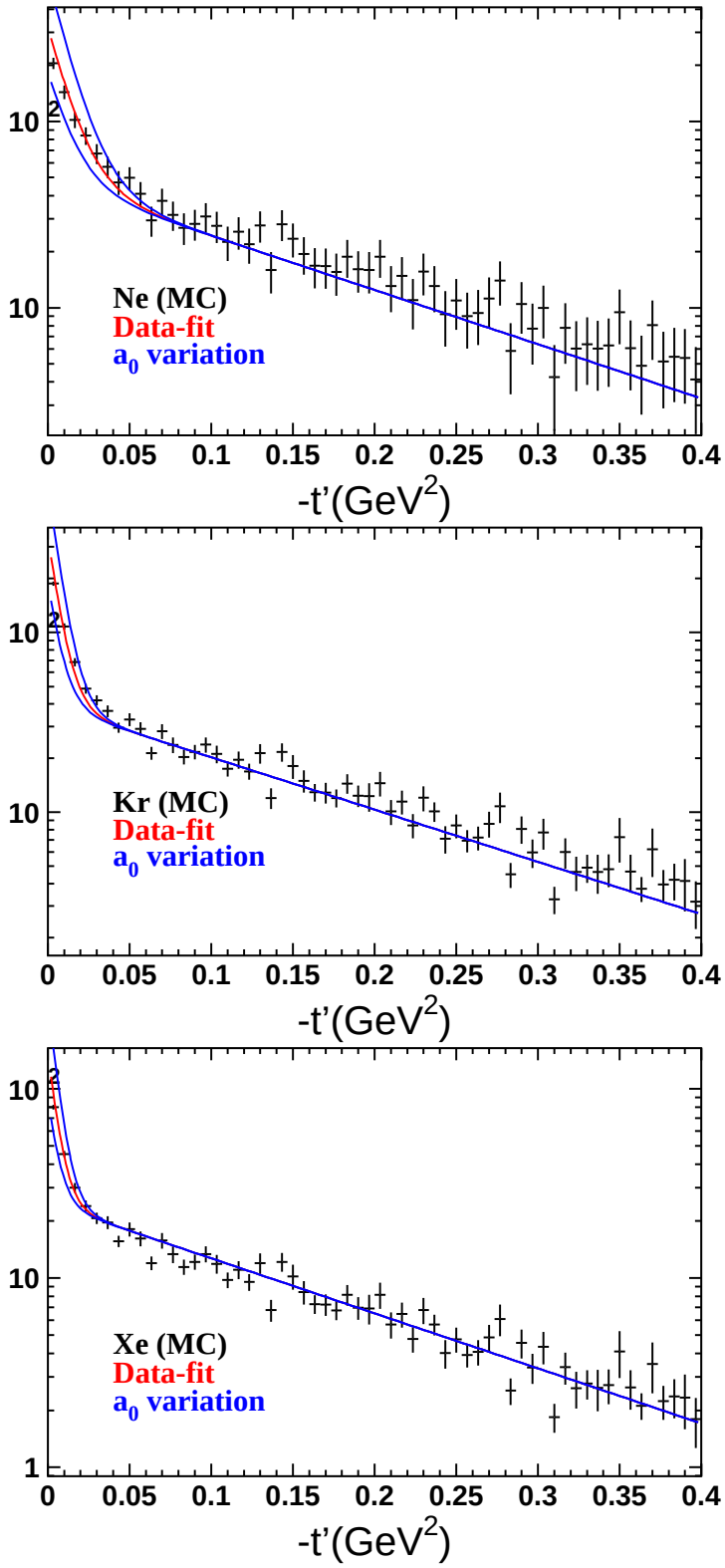

Figure 6.9: Comparison of the t'-spectra of reconstructed Monte Carlo (see section 6.7.3) and data. The black points are Monte Carlo data points, the red line is the fit result of fitting the data, the blue lines are the same functions but with varied a_0.

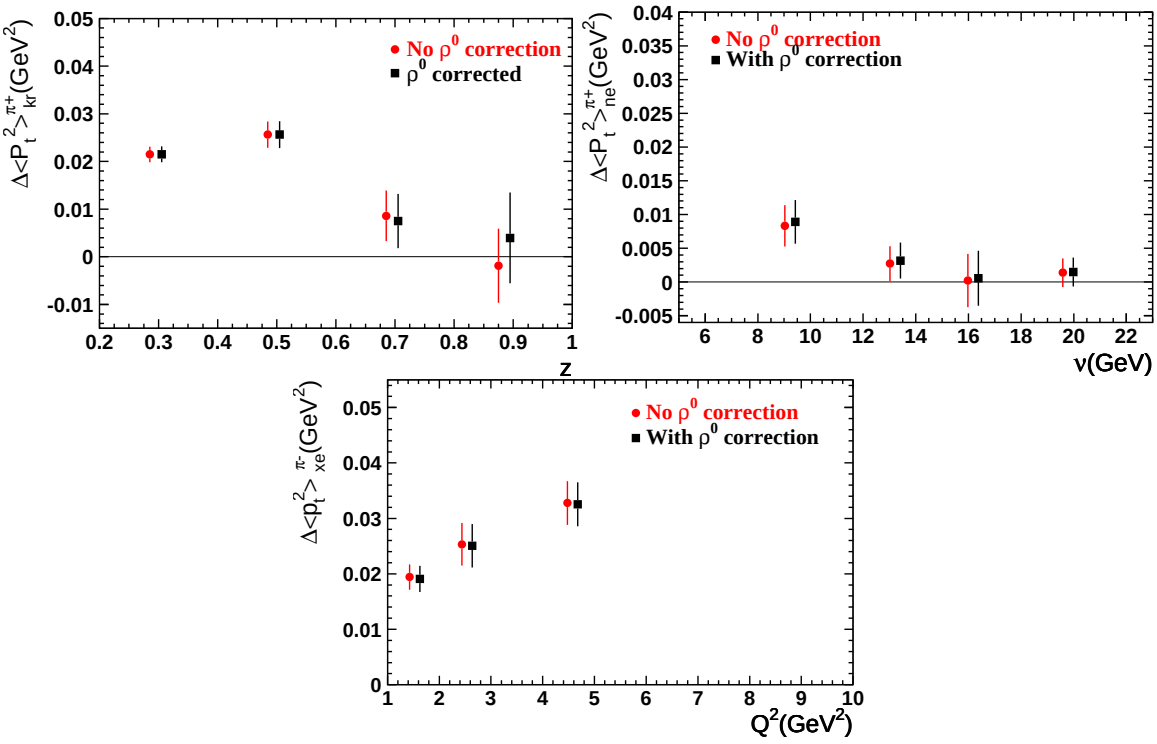

Figure 6.10: The effect of the ρ^0 correction on p_t-broadening versus z, ν, and Q^2.

6.7.5 Systematic uncertainty

The systematic uncertainty of the ρ^0 correction was estimated by redoing the ρ^0 correction using a_0 from the fit described in section 6.7.1 once multiplied by 2 and once divided by 2. The result of this variation on the function fit can be seen in figure 6.9. The maximal difference between the so-obtained p_t-broadening and the originally obtained one was taken as systematic uncertainty. Some numerical values are given in table 6.11. The systematic uncertainty is of the order of a few percent except in the highest z bin where it is a factor of 10 larger.

6.8 Unfolding for acceptance, smearing, and QED radiative effects

The HERMES spectrometer has a limited kinematic and geometric acceptance. To compare the obtained results with theoretical predictions a correction for the acceptance is needed. In lepton scattering it is possible that the incoming and/or the outgoing lepton radiates a real photon that is not detected. If this happens the calculated kinematics of the event are wrong. Limited detector resolution causes events that should have been in a certain kinematic bin to move to another (neighboring) one. This is called smearing. An unfolding method described in [108] was used to correct for both acceptance, smearing, and QED radiative effects simultaneously. This method is described briefly in the following section.

Ne (π^+)	bin# 1	bin# 2	bin# 3	bin# 4
ν	$\frac{4.7\cdot10^{-4}\ GeV^2}{1.2\cdot10^{-2}\ GeV^2}$	$\frac{6.6\cdot10^{-4}\ GeV^2}{5.1\cdot10^{-3}\ GeV^2}$	$\frac{6.0\cdot10^{-4}\ GeV^2}{1.4\cdot10^{-3}\ GeV^2}$	$\frac{2.7\cdot10^{-4}\ GeV^2}{2.2\cdot10^{-3}\ GeV^2}$
z	$\frac{3.6\cdot10^{-5}\ GeV^2}{9.0\cdot10^{-3}\ GeV^2}$	$\frac{2.4\cdot10^{-4}\ GeV^2}{1.1\cdot10^{-2}\ GeV^2}$	$\frac{1.4\cdot10^{-3}\ GeV^2}{-1.3\cdot10^{-2}\ GeV^2}$	$\frac{8.9\cdot10^{-3}\ GeV^2}{-6.8\cdot10^{-3}\ GeV^2}$
Q^2	$\frac{6.6\cdot10^{-4}\ GeV^2}{1.4\cdot10^{-3}\ GeV^2}$	$\frac{3.8\cdot10^{-4}\ GeV^2}{9.9\cdot10^{-3}\ GeV^2}$	$\frac{1.9\cdot10^{-4}\ GeV^2}{1.1\cdot10^{-2}\ GeV^2}$	
Kr (π^-)	bin# 1	bin# 2	bin# 3	bin# 4
ν	$\frac{5.5\cdot10^{-4}\ GeV^2}{2.0\cdot10^{-2}\ GeV^2}$	$\frac{6.4\cdot10^{-4}\ GeV^2}{2.3\cdot10^{-2}\ GeV^2}$	$\frac{6.0\cdot10^{-4}\ GeV^2}{1.6\cdot10^{-2}\ GeV^2}$	$\frac{2.3\cdot10^{-4}\ GeV^2}{2.1\cdot10^{-2}\ GeV^2}$
z	$\frac{7.0\cdot10^{-6}\ GeV^2}{2.5\cdot10^{-2}\ GeV^2}$	$\frac{2.3\cdot10^{-4}\ GeV^2}{3.5\cdot10^{-2}\ GeV^2}$	$\frac{2.0\cdot10^{-3}\ GeV^2}{1.9\cdot10^{-2}\ GeV^2}$	$\frac{1.1\cdot10^{-2}\ GeV^2}{1.5\cdot10^{-3}\ GeV^2}$
Q^2	$\frac{6.6\cdot10^{-4}\ GeV^2}{1.9\cdot10^{-2}\ GeV^2}$	$\frac{3.4\cdot10^{-4}\ GeV^2}{3.1\cdot10^{-2}\ GeV^2}$	$\frac{1.7\cdot10^{-4}\ GeV^2}{3.0\cdot10^{-2}\ GeV^2}$	
Xe (π^-)	bin# 1	bin# 2	bin# 3	bin# 4
ν	$\frac{4.8\cdot10^{-4}\ GeV^2}{2.6\cdot10^{-2}\ GeV^2}$	$\frac{5.7\cdot10^{-4}\ GeV^2}{3.0\cdot10^{-2}\ GeV^2}$	$\frac{5.1\cdot10^{-4}\ GeV^2}{2.8\cdot10^{-2}\ GeV^2}$	$\frac{1.9\cdot10^{-4}\ GeV^2}{2.8\cdot10^{-2}\ GeV^2}$
z	$\frac{7.0\cdot10^{-6}\ GeV^2}{3.5\cdot10^{-2}\ GeV^2}$	$\frac{1.8\cdot10^{-4}\ GeV^2}{4.5\cdot10^{-2}\ GeV^2}$	$\frac{1.9\cdot10^{-3}\ GeV^2}{2.6\cdot10^{-2}\ GeV^2}$	$\frac{9.5\cdot10^{-3}\ GeV^2}{1.8\cdot10^{-3}\ GeV^2}$
Q^2	$\frac{5.9\cdot10^{-4}\ GeV^2}{2.6\cdot10^{-2}\ GeV^2}$	$\frac{3.0\cdot10^{-4}\ GeV^2}{3.6\cdot10^{-2}\ GeV^2}$	$\frac{1.5\cdot10^{-4}\ GeV^2}{4.4\cdot10^{-2}\ GeV^2}$	

Table 6.11: The systematic uncertainties ($\frac{\delta_{sys}}{\Delta\langle p_t^2\rangle}$) in p_t-broadening due to the ρ^0 correction.

6.8.1 The unfolding formalism

The equation describing unfolding using smearing matrices $S(i,j)$ is:

$$X_{1(2)}(i) = L_{1(2)}k(i)\sum_{j=0}^{n_B} S_{1(2)}(i,j)B_{1(2)}(j), \qquad i = 1...n_X \tag{6.8}$$

Where:

- i: the experimental bin ($i = 1...n_X$)
- j: the Born level bin ($j = 0...n_B$)
- $X_p(i)$: the experimental yield in bin i for process p.
- L_p: the overall luminosity.
- $k(i)$: the common integrated luminosity for both experiment and Monte Carlo.
- $S_p(i,j)$: the smearing matrix for process p in the used binning, defined as:

$$S(i,j) \equiv \frac{\partial\sigma^X(i)}{\partial\sigma^B(j)} = \frac{n(i,j)}{n^B(j)}, \qquad i = 1...n_X,\ j = 0...n_B \tag{6.9}$$

  with $n^B(j)$ the original Born distribution and $n(i,j)$ is a matrix of dimension $n_X \cdot (n_B+1)$. Each element $n(i,j)$ holds the number of hadrons where the Born level kinematics fall in bin j, and the experimental kinematics fall in bin i. These quantities have to be extracted from Monte Carlo. The extra column $j = 0$ are events for which the original Born level kinematics fall outside the acceptance of the HERMES detector and the kinematic constraints that are applied but still get smeared into an experimental bin i by some QED radiative or instrumental effect.

- $B_p(j)$[1]: the original Born distributions, obtained by the unfolding process. This quantity will eventually be the objective of the unfolding.

6.8.2 Application on this analysis

The two processes that were chosen in this analysis are both hadron production. The first process is hadron production binned in p_t^2 and the second process is hadron production that is not binned in p_t^2. The goal is to obtain $\langle p_t^2\rangle$ at Born level. This will be explained using an example.

Suppose the unfolding happens only in p_t^2 and there are 11 bins in p_t^2. Process 1 would then be hadron production is those 11 bins, process 2 would be hadron production in one bin that has exactly the range of the 11 bins of process 1. Using formula (6.8) one can write:

$$X_1(i) = L_1k(i)\sum_{j=0}^{11} S_1(i,j)B_1(j), \qquad i = 1...11 \tag{6.10}$$

[1]Note the difference between $n^B(j)$ and $B_p(j)$ mainly is that the first one is obtained with Monte Carlo and the other one is obtained after unfolding the data.

$$X_2 = L_2 k \sum_{j=0}^{1} S_2(1,j) B_2(j), \quad (i=1) \tag{6.11}$$

Because the experimental luminosity has to be the same, $L_1 = L_2 = L$.

The unknown vector $k(i)$ is a vector of arbitrary normalization constants incorporating integrated experimental and Monte Carlo luminosities, as well as not simulated inefficiencies. These are unknown. However, it is assumed that they are constant over the kinematic range used in this analysis. This means that one can write $k(i) = k$ and solve equation (6.11) for k:

$$k = \frac{X_2}{L \sum_{j=0}^{1} S_2(1,j) B_2(j)}, \tag{6.12}$$

and write for the experimental hadron yield in bin i:

$$X_1(i) = \frac{X_2 \sum_{j=0}^{11} S_1(i,j) B_1(j)}{\sum_{j=0}^{1} S_2(i,j) B_2(j)}, \tag{6.13}$$

or

$$\frac{X_1(i)}{X_2} = \frac{\sum_{j=1}^{11} S_1'(i,j) B_1(j) + S_1(i,0) B_1(0)}{\sum_{j=0}^{1} S_2(i,j) B_2(j)}, \tag{6.14}$$

where $S_1'(i,j)$ is $S_1(i,j)$ with row $j=0$ removed. The denominator of equation (6.14) equals the experimental number of hadrons of process 2 from the Monte Carlo, n_2^X. Equation (6.14) can be written as:

$$\sum_{j=1}^{11} S_1'(i,j) B_1(j) = \frac{X_1(i)}{X_2} . n_2^X - S_1(i,0) B_1(0). \tag{6.15}$$

If S_1' has an inverse, one can write:

$$B_1(j) = \sum_{j=1}^{n_X} [S_1']^{-1}(j,i) . [\frac{X_1(i)}{X_2} . n_2^X - S_1(i,0) B_1(0)], \quad j = 1...11 \tag{6.16}$$

which provides the number of hadrons per bin at Born level. The average p_t^2 at Born level becomes:

$$\langle p_t^2 \rangle = \sum_{j=1}^{11} [\frac{B_1(j)}{\sum_{i=1}^{11} B_1(i)} \langle p_t^2 \rangle_{data}(j)], \tag{6.17}$$

where the average transverse momentum squared of the bin originates from the data.

6.8.3 Problems with filling the vectors and matrices

When filling the smearing matrices $S(i,j)$ some problems are encountered if the same Monte Carlo sample is used for the calculation of both $n^X(i,j)$ and $n^B(j)$. For $n^X(i,j)$ there is no problem at all, the value of the true kinematic variables are taken and $n(i,j)$ can be constructed. However, when the original number of events in Born bin j has to be filled from a Monte Carlo production problems show up. This is because the lepton kinematics were generated in a box and therefore it can happen that the true kinematics, which are reconstructed

by RADGEN (RADGEN is the part in the Monte Carlo that generates QED radiative effects, see section 5.2.2), fall outside the box in which the Monte Carlo was generated. In this way the normalization is not correct. The only solution to this problem is to use a totally separate Monte Carlo production with QED radiative effects switched off (or without RADGEN), which is produced in 4π. In this Monte Carlo production without RADGEN the true kinematics simply are those calculated in the Monte Carlo before any reconstruction.

6.8.4 Renormalization of Monte Carlo productions

Because two separate Monte Carlo productions are used to construct the smearing matrix, they have to be (re-)normalized to each other. To do this the luminosity was used, this means that $n(i,j)$ and $n^B(j)$ are divided by the total luminosity of the Monte Carlo production of origin.

6.8.5 Used Monte Carlo simulation(s)

To fill the smearing matrices and the Born vectors the PYTHIA generator was used in combination with JETSET, which describes hadronization on a D target.

Tests were also performed with the DISNG generator and JETSET with D and Xe as a target to test the influence of the nuclear dependence of radiative corrections and to make an estimation of the model dependence of the unfolding.

Some effort was put into using a Monte Carlo that describes nuclear effects: the BUU Monte Carlo using the ($Hermes$-tuned) PYTHIA generator together with a transport model based on the Boltzmann-Uehling-Uhlenbeck (BUU) equation [100]. This project was abandoned because there is no support available concerning this Monte Carlo and its source code is not open.

The PYTHIA generator only allows nucleon targets (proton or neutron). In order to simulate a D target the sum of two productions was made: one with a proton target and one with a neutron target. Both productions were added with a weight equal to one. The DISNG generator has the possibility to set targets with more than one nucleon, although nuclear effects like attenuation and nuclear transparency are not simulated.

More information concerning the used Monte Carlo simulations can be found in chapter 5.

6.8.6 Unfolding consistency test

The consistency of the unfolding code is tested by unfolding the reconstructed part of the Monte Carlo production that is also used to perform the unfolding itself (i.e., to construct the smearing matrices). If the unfolding is implemented in a consistent way, the unfolded Monte Carlo production has to be (exactly) the same as the Born level Monte Carlo production. The results of this test was that the ratio of the Born level Monte Carlo and the unfolded Monte Carlo was 1 within 0.00001, this means that the implementation of the unfolding passed this test.

6.8.7 Nuclear dependence of QED radiative effects

The Monte Carlo productions used to construct the smearing matrices and Born vectors have D as a target. Because the unfolding also includes QED radiative effects and these effects depend on the atomic number of the target, an investigation was done using a Monte Carlo production with DISNG and JETSET, which allows the use of nuclear targets and has QED radiative effects included. There are no large effects expected due to the fact that only semi-inclusive events are selected. By doing so elastic contributions are excluded. A comparison is made of p_t-broadening on a Xe target where in one case Xe was unfolded using a DISNG production on a Xe target and in the other case using a PYTHIA production on a D target. D was in both cases unfolded using PYTHIA. Results of this study can be seen in figure 6.11. It is clear that more Monte Carlo statistics are needed in order to draw conclusions. If PYTHIA and DISNG productions are used together (or compared), two additional constraints were applied on the PYTHIA events: $W^2_{true} > 4$ GeV^2 and $Q^2_{true} > 0.5$ GeV^2 because in the DISNG production used in this section, the LEPTO generator does not generate events below these constraints.

The differences are not included into the systematic uncertainty because also two different generators are compared here (see also section 6.8.8). In order to assigns a reasonable systematic uncertainty one would need DISNG Monte Carlo productions with a D and a Xe target and then redo the previously discussed comparison. At the moment this thesis is written such productions were not available.

6.8.8 Unfolding in one or more dimensions

To obtain p_t-broadening versus atomic number A, a one-dimensional unfolding was done in p_t^2. In order to obtain p_t-broadening versus z a two-dimensional unfolding was done using a combined binning in p_t^2 and z; p_t-broadening versus Q^2 and ν was obtained using an analogous two-dimensional unfolding.

The semi-inclusive deep-inelastic cross-section depends on five kinematic variables (e.g., ν, Q^2, p_t^2, z, and ϕ). When one does an unfolding in these 5-dimensions then a result is expected that is independent of the physical model used in the Monte Carlo, if the unfolding is done within the HERMES acceptance and the radiative corrections are not taken into account. If the unfolding covers regions outside the acceptance (this is the case in this analysis) it happens that events are outside the HERMES acceptance at Born level but inside the acceptance at the reconstructed level. This contribution sits in the background bin ($j = 0$ in formula (6.9)) and depends on the model included in the Monte Carlo used to do the unfolding regardless of a 1-dimensional or 5-dimensional unfolding.

In order to reduce the model dependence of the unfolding as much as possible a five dimensional unfolding was investigated but it turned out that it is not possible to fill certain elements in the smearing matrix[2], e.g., elements that are at low z and at high p_t^2. In this case the smearing matrix is not invertible and the unfolding fails. One could of course remove these empty bins but it is unclear how to handle them when one integrates over a kinematic range where

[2] A Monte Carlo production was made with more than 100 million generated events and even then certain diagonal elements of the smearing matrix could not be filled. In this case the smearing matrix is not invertible and the unfolding cannot function.

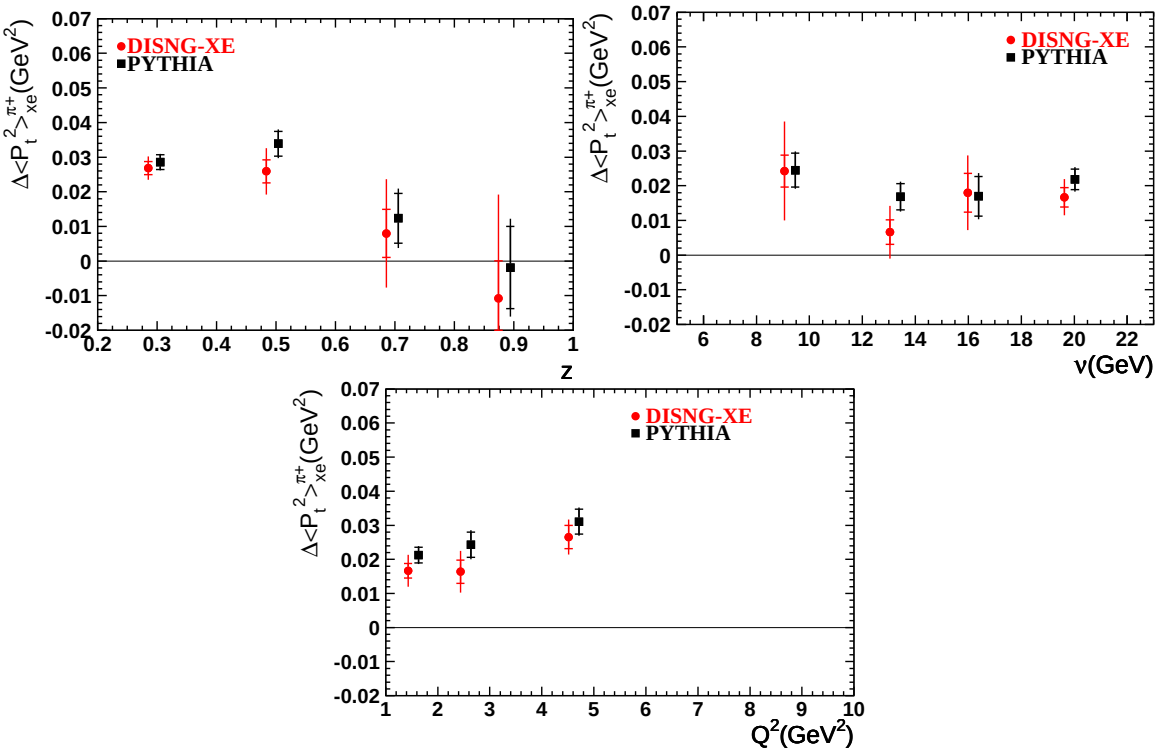

Figure 6.11: Unfolded p_t-broadening using the PYTHIA and DISNG Monte Carlo's (to unfold the data) is shown. The inner error bars are statistical error bars and the outer ones the quadratic sum of the statistical and the systematic uncertainties caused by Monte Carlo statistics. The data taken with a Xe target was unfolded with the PYTHIA Monte Carlo (using D as target) and with the DISNG Monte Carlo (using Xe as target). To unfold the D data the PYTHIA Monte Carlo (using D as target) was used.

certain bins are missing. Instead the unfolding is done in one or two dimensions as mentioned before. The unfolding using the PYTHIA Monte Carlo was compared with an unfolding done using the DISNG Monte Carlo in order to estimate the systematic uncertainty caused by the Monte Carlo generator. One can see in figure 6.12 a comparison between unfolded values obtained by unfolding using a PYTHIA Monte Carlo production where $Q^2_{true} > 0.5$ GeV^2 and $W^2_{true} > 4$ GeV^2, or $Q^2_{true} > 1.0$ GeV^2 and $W^2_{true} > 10$ GeV^2 constraints are applied. Unfolded data using the PYTHIA Monte Carlo simulation without any additional constraints is also shown. This Monte Carlo simulation was used to obtain the final results. The other Monte Carlo production was DISNG where the LEPTO generator does not produce events with W^2_{true} below 10 GeV^2 or Q^2 below 1 GeV^2. As can be seen in figure 6.12 the W^2_{true} and Q^2_{true} constraint in the LEPTO generator changes the unfolded result that is probably due to the fact that these constraints cut away a part of the events generated outside the kinematic constraints that smear inside the applied kinematic constraints on reconstructed level. The difference between the unfolded values using the DISNG production and the ones unfolded with the PYTHIA production with no constraints on W^2_{true} and Q^2_{true} is quadratically added to the systematic uncertainty and can be interpreted as an estimate of the generator dependence of the unfolding. This systematic uncertainty is a dominant one that reaches up to 5 % in the lowest z, Q^2, and ν bins.

6.8.9 Impact of the unfolding

What the unfolding does to $\langle p_t^2 \rangle$ as a function of z, Q^2, and ν for a Xe target can be seen in figure 6.13. The effect of the unfolding ranges from basically 0 up to 60 % in the lowest ν bin.

The impact of the unfolding on normalized p_t-spectra in 1- and 2-dimensional binning can be seen in figure 6.14. The unfolding tends to push the p_t^2-spectra to higher p_t^2 values. In the 2-dimensional binning the p_t-spectra are normalized for each bin in Q^2, ν, or z. One can see that in the highest ν-bin there is a suppression in the lowest p_t^2-bin that is restored to a "normal" p_t^2-spectrum after the unfolding.

6.8.10 Error calculation

The statistical error calculation is based on the dilution matrix ($D(i,j)$) described in [108]:

$$D(i,j) = [S'_1]^{-1}(j,i) \cdot n_2^X. \tag{6.18}$$

This leads to a statistical error on $B_1(j)$ equal to:

$$\delta B_1(j) = \sqrt{\sum_{i=1}^{n_X} D^2(j,i) \cdot \delta^2(X_1(i))}, \tag{6.19}$$

where $\delta(X_1(i))$ is the statistical error on $X_1(i)$ (the experimental yield in bin i for process 1). For more details see [108].

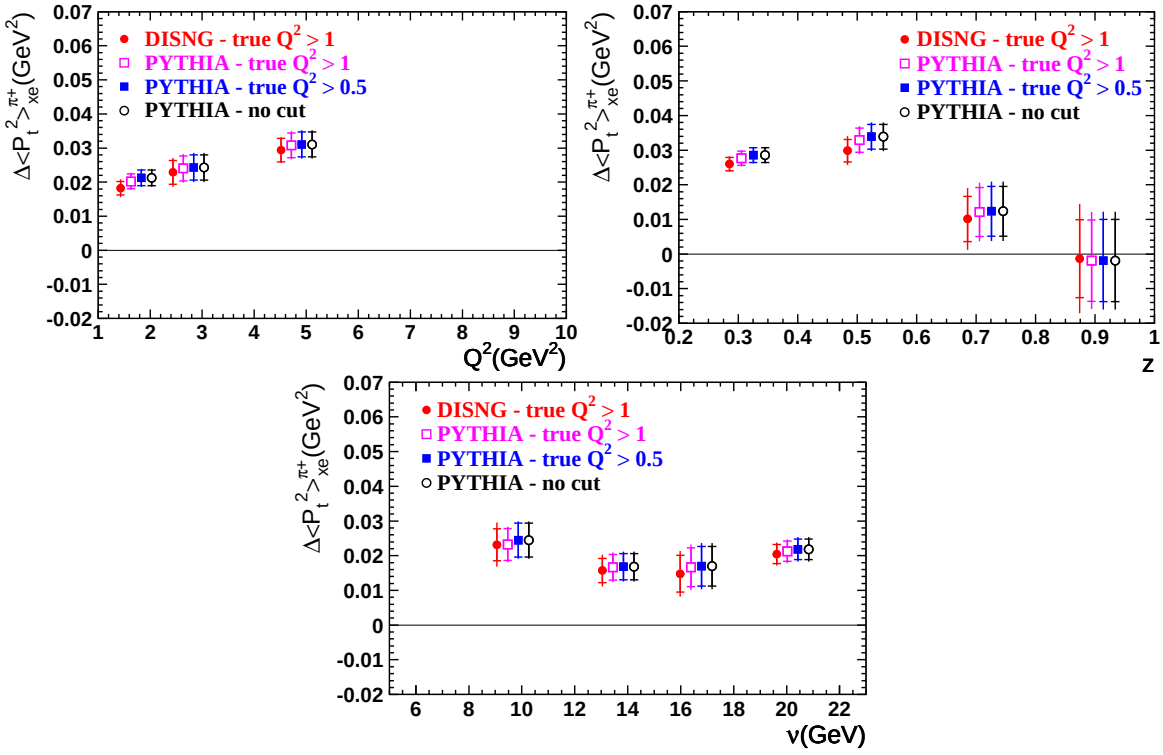

Figure 6.12: Unfolded p_t-broadening using two different Monte Carlo productions is shown versus Q^2, z, and ν. For more detail see section 6.8.8. The inner error bars are statistical error bars and the outer ones the quadratic sum of the statistical and the systematic uncertainties caused by finite Monte Carlo statistics. The systematic uncertainty is the error caused by Monte Carlo statistics.

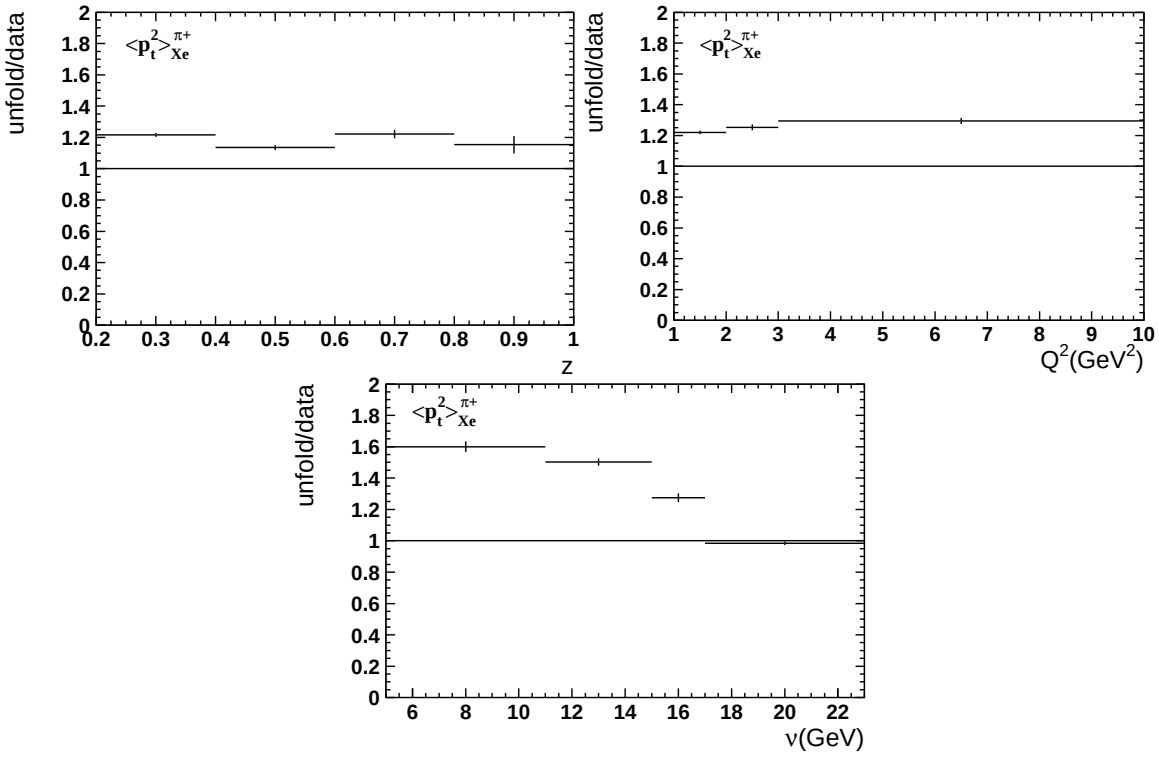

Figure 6.13: The plot shows the ratio between unfolded $\langle p_t^2 \rangle$ and not unfolded $\langle p_t^2 \rangle$ versus z, Q^2, and ν.

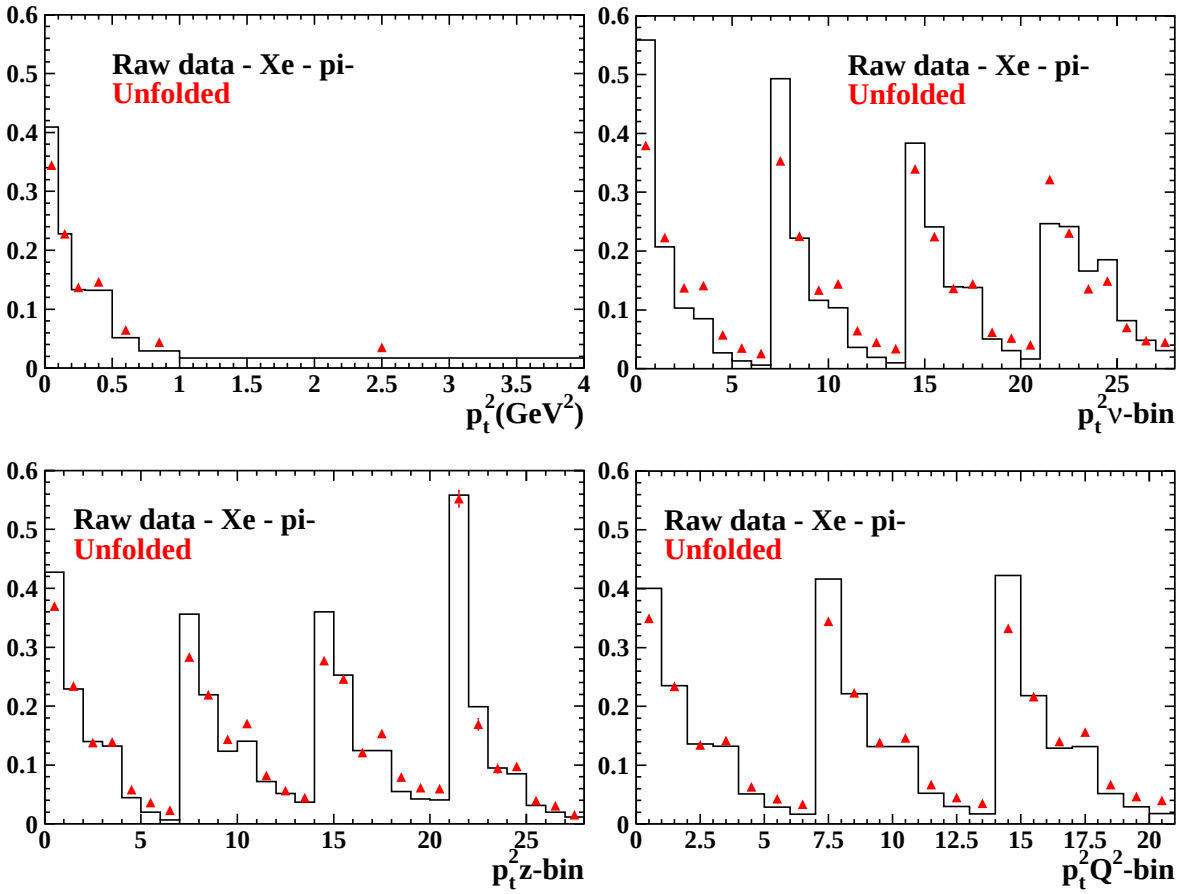

Figure 6.14: These plots show the impact on the unfolding on normalized p_t^2-spectra that are binned in 1 or 2 dimensions. The plots with the 2 dimensional binning in the x-axis (upper-right and lower plots) have a number in the x-axis equal to p_t^2-bin# $+ (7-1)\cdot z$, Q^2, or ν-bin#. The p_t-spectra in these plots are normalized for each bin in z, Q^2, or ν.

6.8.11 Systematic uncertainty calculation

There is a systematic uncertainty in the unfolding procedure caused by limited statistics of the Monte Carlo production used to build the smearing matrices and Born vectors. To calculate these errors a brute-force method was used. Many smearing matrices were generated using a random generator that generates for each element a number according to a Gaussian with the value of the original element as its central value and as the width the statistical error on that element. The generated smearing matrices are then used to redo the unfolding. The standard deviation on the unfolded values is then taken as the systematic uncertainty of the unfolding. This systematic uncertainty is a dominant one with values around 5% except in the highest z-bin; there the p_t-broadening reaches values close to 0 and the statistics in both the Monte Carlo simulation and the data decreases.

Chapter 7

Results on p_t-broadening

In this section p_t-broadening results are shown for versus ν, z, Q^2, and $A^{1/3}$. All these results are corrected for charge-symmetric background, exclusive ρ^0 decay pions (if applicable), RICH-unfolding (if applicable), and unfolding for QED radiative effects, detector acceptance and smearing. The systematic uncertainty consists of the systematic uncertainty of the RICH unfolding (if applicable), the unfolding for acceptance, smearing, and QED radiative effects (from limited Monte Carlo statistics and from the generator dependence of the unfolded results), and the ρ^0-correction (if applicable). These errors were added quadratically. The results can be seen in figures 7.1-7.4 [109] and will be discussed in the following sections. Please note that although theorists like A. Accardi, B. Kopeliovich, J. Nemchik, H.J. Pirner, and X.N. Wang [110] expressed there profound interest in p_t-broadening no theoretical comparisons with the HERMES data are available at the moment this thesis was written. The interpretations given are qualitative/naive ones and some are based on the model described in [30]. The number of models available to describe nuclear effects is high. This analysis might confirm/reject some of them.

7.1 A dependence

The A-dependence of p_t-broadening is shown in figure 7.1. The p_t-broadening has an amplitude around 0.02 GeV^2 (depending on A). The average p_t^2 is around 0.22 GeV^2 meaning that p_t-broadening is a 10 % effect, which is substantial. A linear dependence on $A^{1/3}$ is observed. This indicates that the p_t-broadening is linear with the radius of the nucleus. The average z of these measurements is around 0.39 (see table A.2). One can see in figure 7.2 that p_t-broadening reaches a maximum around this z-value. This indicates that the production time is long and this could explain why p_t-broadening depends on the radius of the nucleus.

The p_t-broadening of π^+ and π^- is consistent within the error bars, this is probably due the fact that all targets are almost isoscalar. Xe has the largest deviation of isoscalarity ($\langle$protons/neutrons$\rangle$ = 0.70). Isoscalar targets mean that there is no reason why a produced π^+ should behave differently as a produced π^- because they contain most probably one valence quark from a nucleon and one light sea-quark. The p_t-broadening of the K^+ is higher compared to the p_t-broadening of pions. The only difference is that a kaon contains a strange anti-quark from the quark-sea. This might indicate that the transverse momentum of

the strange sea quarks is larger in a nucleon inside a nucleus then in a bare nucleon. The larger statistical error bars for kaons is due to the fact that they contain strangeness and strangeness production is suppressed at the HERMES kinematics by $\sim$30 %.

7.2 The z-dependence of p_t-broadening

The z-dependence of p_t-broadening is shown in figure 7.2. In general one can see that the p_t-broadening goes up with increasing z and reaches a maximum for a z around 0.5 and then decreases towards zero for $z \to 1$. A low $z = \frac{E_h}{\nu}$ points towards low hadron energy as E_h defines the maximal transverse momentum possible for the final-state hadron. A competing process is that the number of interactions is expected to rise for decreasing z because more energy was lost. An increasing number of interactions means an increase of $\langle p_t^2 \rangle$ (similar to a "random walk") and an increase in p_t-broadening.

At a low hadron momentum (low z) there is not so much freedom for an increase in transverse momentum (low E_h). At increasing z the number of reinteractions is expected to decrease but the upper limit for transverse momentum increases; transverse momentum broadening becomes more "free". This might explain the rise in p_t-broadening versus z at low z.

A correlation between z and ν can be seen in table A.4. In the plotted z range $\langle \nu \rangle$ varies from 11 to 15 GeV. The p_t-broadening versus ν behavior in this range (cf. figure 7.3) can not explain the z behavior at all.

A difference between pions and kaons and a dependence on atomic number A is also observed, for more details on this see section 7.1.

At high z, p_t-broadening goes down to reach 0 for $z \to 1$. This is in agreement with the gluon bremsstrahlung model described in section 2.1.8 and can be explained by conservation of energy. When z equals 1 then the detected hadron carries all the energy of the virtual photon. This means that no interaction could have happened because if so z would be lower then 1. No interactions means that the pre-hadron had to be formed immediately and that the production time is zero.

7.3 The ν-dependence of p_t-broadening

The ν dependence of p_t-broadening can be seen in figure 7.3. One could conclude that p_t-broadening versus ν is constant although there is a hint that p_t-broadening decreases with increasing ν. An increase in p_t-broadening versus ν can be expected because of time-dilation (increase of the production time), but this is not seen in figure 7.3. Because $\nu = \frac{E_h}{z}$ a correlation between ν and z is expected and can be seen in table A.10; $\langle z \rangle$ indeed decreases for increasing ν and in this low-z region p_t-broadening goes up slightly. However, for high ν the p_t-broadening values are too low to be explained by a ν-z correlation.

A difference between pions and kaons and a dependence on atomic number A is also observed in figure 7.2, for more details on this see section 7.1.

The constant ν behavior would mean that color neutralization happens outside the nucleus. This is in favor of parton-energy-loss models without absorption (cf. section 2.1.8).

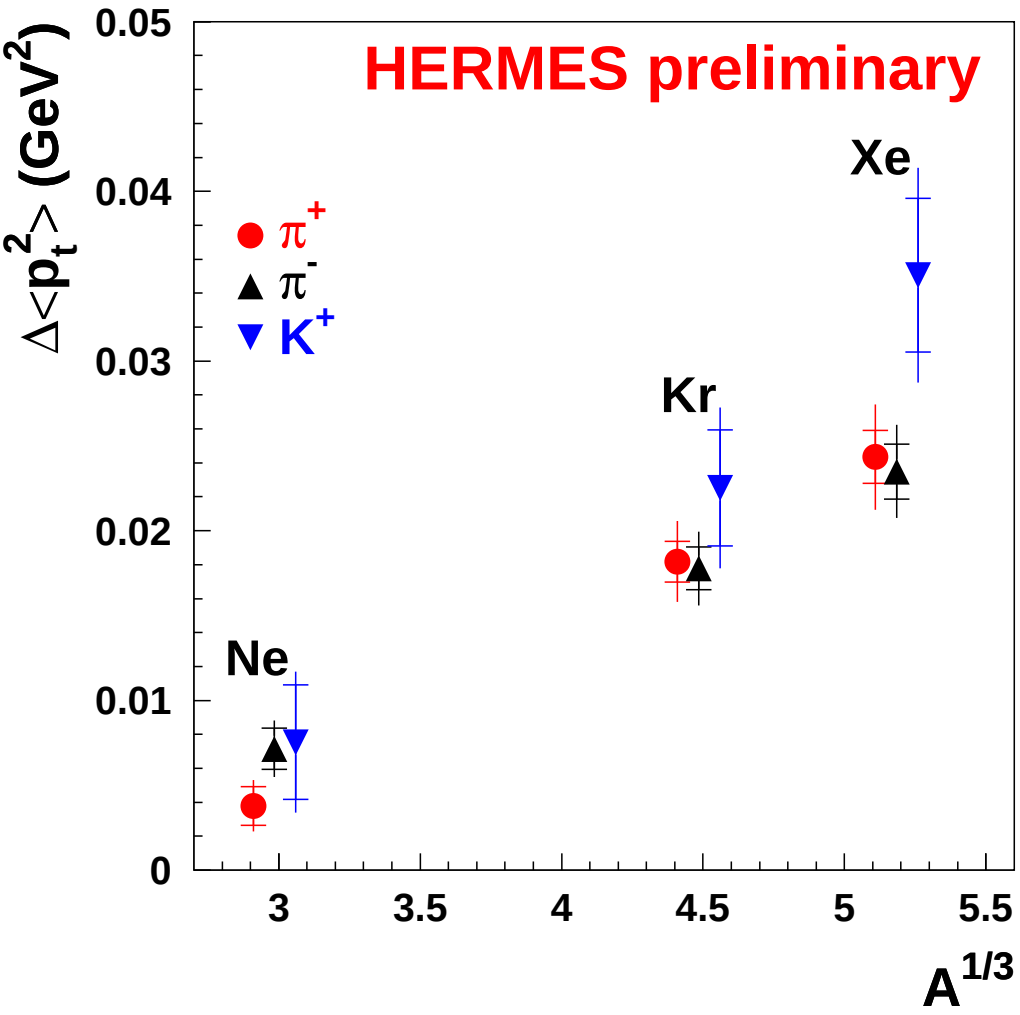

Figure 7.1: The dependence of p_t-broadening on the atomic number $A^{1/3}$ is shown for several hadron types. A difference is observed between pions and kaons. The inner error bars represent the statistical error and the outer ones the quadratic sum of the statistical and systematic uncertainties.

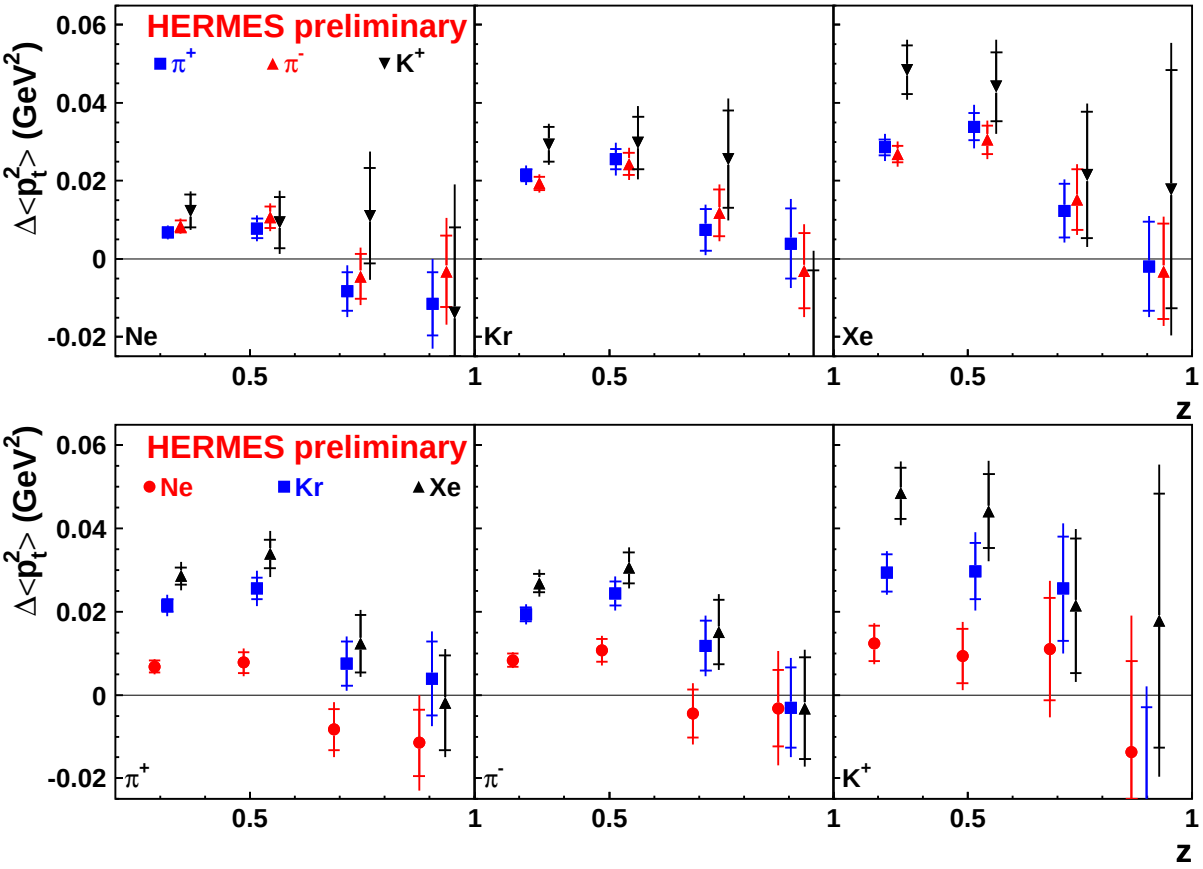

Figure 7.2: The z-dependence of p_t-broadening for different hadron types produced on several targets. The inner error bars represent the statistical error and the outer ones the quadratic sum of the statistical and systematic uncertainties.

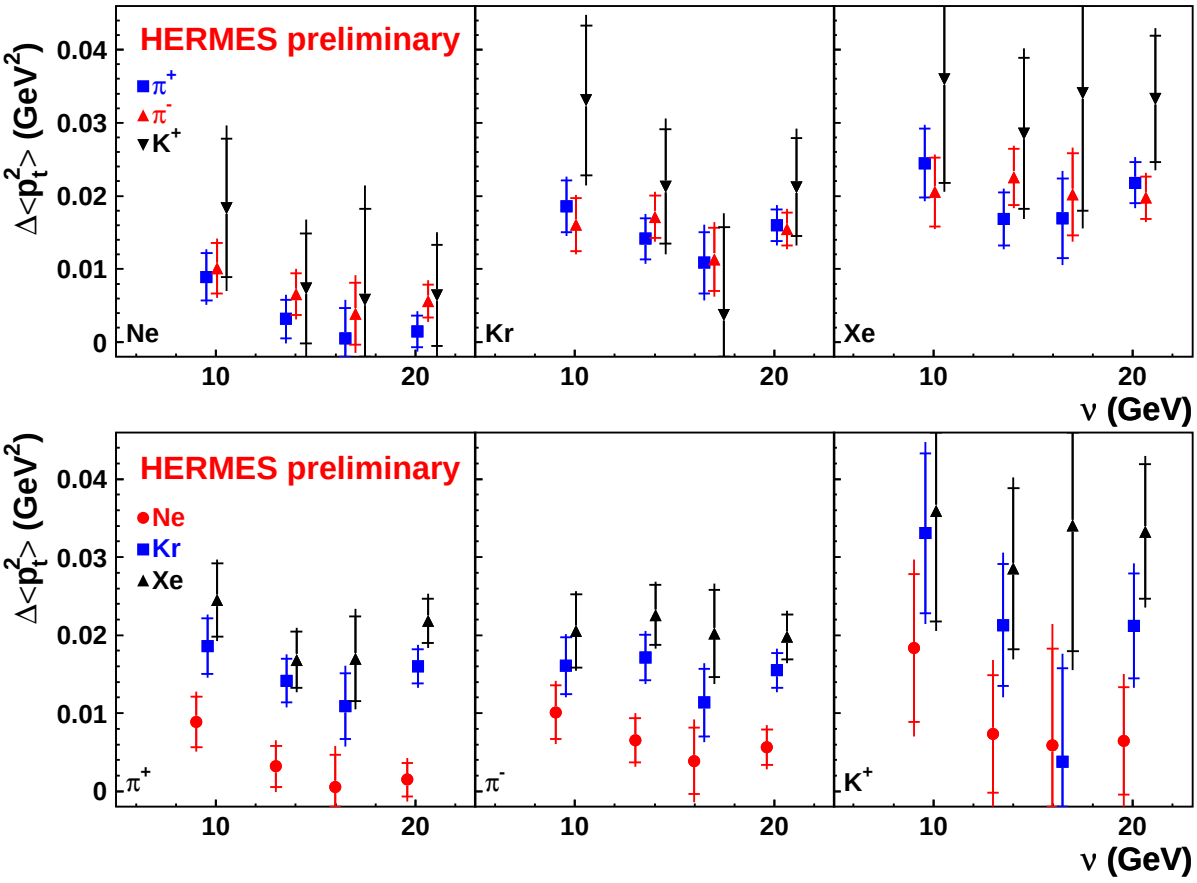

Figure 7.3: The ν-dependence of p_t-broadening for different hadron types produced on several targets. The inner error bars represent the statistical error and the outer ones the quadratic sum of the statistical and systematic uncertainties.

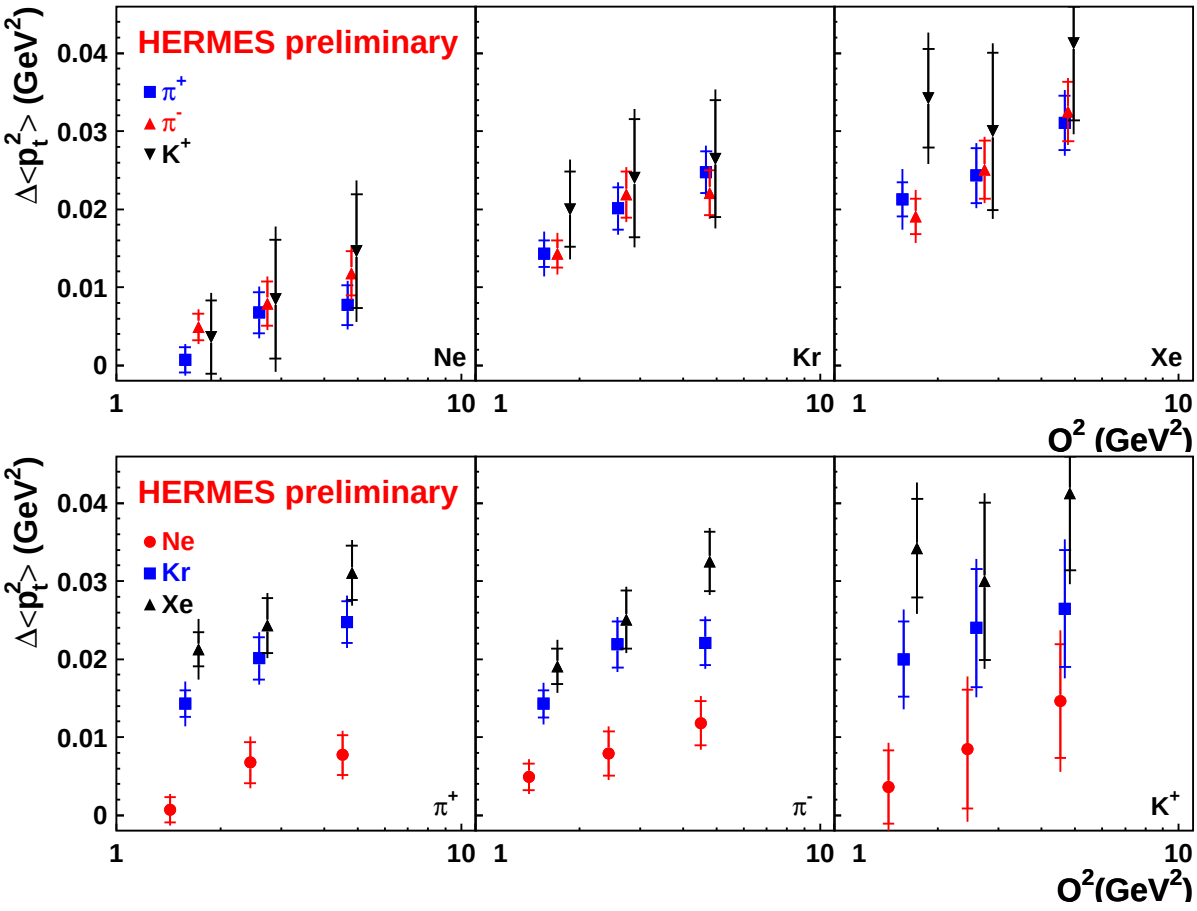

Figure 7.4: The Q^2-dependence of p_t-broadening for different hadron types produced on several targets. The inner error bars represent the statistical error and the outer ones the quadratic sum of the statistical and systematic uncertainties.

7.4 The Q^2 dependence of p_t-broadening

In figure 7.4 the Q^2 dependence of p_t-broadening can be seen. There is a clear increase in p_t-broadening for increasing Q^2. It is not clear how to explain this behavior.

No strong correlations between Q^2 and other kinematic variables in table A.16 can be observed.

A difference between pions and kaons and a dependence on atomic number A is also observed, for more details on this see section 7.1.

The Q^2 behavior observed is opposite to the behavior that is expected in the gluon bremsstrahlung model (cf. section 2.1.8). In the model a decrease of p_t-broadening is expected for increasing Q^2. The opposite is observed. This might be caused by the fact that the average z is lower than 0.5 in this plot ($\langle z \rangle$ is around 0.40) and the model only claims to work for leading hadrons with a z above 0.5.

7.5 Conclusion

The p_t-broadening results using HERMES data versus $A^{1/3}$, z, ν, and Q^2 are obtained for π^+, π^-, and K^+ produced on Ne, Kr, and Xe targets. Although some (naive) interpretations can be made about the p_t-broadening behavior, one needs a model containing several effects in order to make a more thorough interpretation. There is a prediction concerning the p_t-broadening behavior in the gluon bremsstrahlung model. It predicts the z behavior correctly, but fails to predict the Q^2 dependence. This might be due to the fact that $\langle z \rangle$ is not above 0.5 as required but around 0.4 in the p_t-broadening versus Q^2 and ν plots. At the moment several models are available and this analysis might confirm and/or reject some of them once they publish their "predictions".

Together with the HERMES analysis of nuclear attenuation [19] and p_t-ratios [107] this experiment provides the most complete and precise data set concerning the space-time evolution of hadronization.

Chapter 8

Summary

The point is reached to provide a summary of what was done in this thesis. This work was performed at the HERa MEasurement of Spin (HERMES) experiment located in Hamburg, Germany. Accelerated leptons (electrons and positrons) are scattered off a "fixed" gaseous target at the HERMES experiment. These leptons are accelerated using the Hadron Elektron Ring Anlage (HERA), a storage ring for hadrons and leptons. Various targets can be used, from H to Xe. The scattered lepton and other produced particles are detected by a forward acceptance spectrometer.

The first part of this work consists of hardware research and development done in order to construct and test a photon-detector as one of the three detectors of the HERMES recoil detector. The HERMES recoil detector was built in order to improve the detection of recoil particles, which will improve the identification of deeply virtual Compton scattering (DVCS) events. In deeply virtual Compton scattering, a lepton scatters of a quark, the quark emits a real photon and the nucleon stays intact. This process provides access to the Generalized Parton Distribution functions (GPDs) that contain information on the structure of the nucleon. Ji's sum rule is a relation between the total angular momentum of quarks in the nucleon and the GPDs. At HERMES the total spin of the quarks in the nucleon was measured, allowing access, via Ji's sum rule, to the orbital momentum of quarks.

In previous studies of DVCS at HERMES only the scattered lepton and the produced photon could be detected. The missing mass technique was then used to determine that target nucleon stays intact. Due to background processes, the constraint needed on the missing mass was severe and the data sample was greatly reduced. The main background processes that cause this are semi-inclusive deep-inelastic scattering and the associated Bethe-Heitler process. In semi-inclusive deep-inelastic scattering (here) a lepton scatters of a nucleon (that does not stay intact) and the scattered lepton and one photon are detected. In the associated Bethe-Heitler process the incoming or outgoing lepton emits a photon that is detected and the target nucleon is excited and decays. These processes have the same final state as the DVCS process and are the main reason for HERMES to install a new detector to detect the recoil particles.

The HERMES recoil detector consists of a target cell, a silicon-detector, a scintillating fiber tracker, and a photon-detector. All are inside a super-conducting magnet. The silicon detector uses energy deposition to determine the momentum of the particle because in its energy range the energy deposition is an unambiguous function of the momentum of the particle. The low momentum cut-off is determined by the amount of material between the interaction point

and the detector. That is the reason why this detector is placed inside the beam-vacuum. The scintillating fiber tracker is located outside the beam-vacuum and is surrounded by the photon-detector. It consists of two barrels with layers of scintillating fibers. It detects particles by converting their energy deposition into light. It measures two space points of a charged particle and from the bending of the assigned track (in the magnetic field provided by the super-conducting magnet) a momentum measurement can be derived. The photon-detector is located between the scintillating fiber tracker and the magnet. It consists (from the inside out) of three layers of tungsten showering material followed by scintillating strips. The showering material is needed to detect photons that have a high probability to induce a particle shower in tungsten. This particle shower is detected by the scintillating strips. The scintillating strips are read out by 64-channel photo-multiplier tubes (PMTs). These tubes are identical to the ones used to read out the scintillating fibers of the scintillating fiber tracker. A test stand was built to test all these PMTs for noise, gain, uniformity, and linearity. A blue light emitting diode (LED) was used to light the PMT. The gain was tested by determining the voltage where the single-photo-electron signal is above the noise. The single-photon-electron signal is the signal one gets when the photocathode of the PMT emits 1 electron, which is multiplied by the dynodes. It appeared that the working voltage was close to the maximum voltage specified by the supplier of the PMTs. To test the uniformity, the PMT was lighted uniformly by the LED and the output signals per pixel were compared to each other. The pixels on the edges of the PMT appeared to have a higher response than the other pixels. The linearity was measured by plotting the PMT response versus light intensity. The deviation from linearity was determined by a linear fit and taking a normalized difference between the fit and the measurement. The deviation of linearity was around 10 %. This measurement was not corrected for cross-talk, so real linearity is expected to be somewhat worse.

The first test of a prototype of the photon-detector was performed at the Gesellschaft für SchwerIonenforschung (GSI) Darmstadt. A mixed proton/pion beam was available with different momenta. It was found that particles can be detected and that pion/proton particle identification is possible for momenta higher than 600 MeV. The photon-detector as a whole was tested for the first time in Hamburg using cosmic muons. It was also possible to calibrate most of the strips using cosmics that enter the strips perpendicularly. Some strips could not be calibrated due to the angular distribution of cosmics (it is unlikely to have cosmic muons that travel horizontally).

The second part of this work is an analysis performed concerning the transverse momentum broadening of hadrons produced in deep-inelastic scattering on a nuclear target compared to a D target. In deep-inelastic scattering a lepton is scattered off a nucleon (that can be inside a nucleus). The energy of the lepton is high enough to resolve the inner structure of the nucleon and a quark is struck. This quark hadronizes and is detected. Hadronization is a consequence of confinement. Confinement is the observation that quarks are always in a bound state. This process of forming a hadron out of quarks is not yet understood. By looking at hadronization in a nuclear environment one can measure effects that contain information about this process. One can split the hadronization process into three parts: first the struck quark emits gluons until it picks up an antiquark and forms a color-neutral pre-hadron. The time between the interaction and the formation of the pre-hadron is called the *production time*. This pre-hadron can be interpreted as a quark anti-quark pair that is not a final hadron yet. This prehadron can undergo elastic and inelastic interactions. After a time, called the *formation* time, the

final-state hadron is formed. This object can also interact with the nuclear medium and this cross section is very well known. There are many models available that describe hadronization. They can be divided in three classes: one that has only partonic effects, that only happen before the pre-hadron is formed, included. Other models have only hadronic effects, that take place after the pre-hadron is formed, included. There are also models that combine partonic and hadronic effects.

Measuring p_t-broadening is probing the production time. This is because inelastic scattering of the pre-hadron is suppressed if the detected hadron carries a large energy fraction of the struck quark and the elastic cross section of the pre-hadron is smaller than the elastic cross section of a hadron. The mean free path of a hadron is much longer than the diameter of the nuclear targets used in this analysis.

A linear dependence of p_t-broadening versus atomic number $A^{1/3}$ was found. This means that the broadening increases with the radius of the nucleus and points to a "long" production time. The p_t-broadening is constant as a function of the energy of the struck quark. One could expect that the broadening rises as a function of ν because of time dilation. The velocities of these particles are relativistic so one expects relativistic effects. This constant behavior means that the pre-hadron is formed outside the nucleus and favors models with only partonic effects. The broadening behavior versus the fraction of the momentum of the struck quark carried by the final-state hadron (z) is constant and goes to 0 if the fraction reaches 1. Broadening is a measurement of the production time; a non-zero production time means the quark had time to lose energy, thus, due to energy conservation, forcing z to be less than 1. Broadening clearly increases versus transferred 4-momentum (from the lepton to the quark). This behavior is not straightforward and is interesting. This analysis can hopefully distinguish between several models. At the time this thesis was written most models did not have a "prediction" of p_t-broadening published.

Chapter 9

Nederlandse samenvatting

Het werk dat hier gepresenteerd wordt, kadert in het HERMES experiment dat zich in het Deutsche Elektronen SYnchrotron (DESY) in Hamburg, Duitsland bevindt. HERMES is een acroniem voor "Hera MEasurement of Spin" en maakt gebruik van versnelde leptonen (elektronen en positronen) met een impuls van 27.6 GeV die opgeslagen zijn in de "Hadron Elektron Ring Anlage" (HERA). In HERMES laat men de versnelde leptonen botsen met nucleonen of atoomkernen die niet versneld zijn. Deze worden in gasvorm geïnjecteerd in een target cel. Het verstrooide elektron en eventueel andere deeltjes die geproduceerd worden na de interactie van het lepton met de target worden gedetecteerd door een voorwaartse spectrometer. Deeltjes die verstrooid worden onder grote hoeken, een terugstoot proton bijvoorbeeld, worden niet gedetecteerd. Als de 4-impuls (Q^2) overdracht van het lepton naar de target groot genoeg is kan men door middel van het gedetecteerde lepton meer te weten komen over de interne structuur van het nucleon. Indien Q^2 groter is dan 1 GeV^2 spreekt men van diep inelastische verstrooiing en is men in staat de interne structuur van het nucleon te detecteren. Het is gebleken dat een nucleon geen elementair deeltje is maar bestaat uit kleinere deeltjes. Deze deeltjes werden eerst partonen genoemd. Later werden partonen geïdentificeerd met quarks en gluonen. Zo bestaat een proton uit drie valentie quarks (een up, een up en een down quark) en zijn de gluonen de dragers van de sterke kracht. Ze zorgen ook voor confinement: het fenomeen dat een quark zich niet zelfstandig manifesteert maar enkel in een gebonden toestand met andere quarks voorkomt.

Deze thesis bestaat uit twee aparte delen. Enerzijds was er de constructie en tests voor de HERMES recoil detector, meer specifiek voor de foton-detector, en een test die was uitgevoerd voor de "scintillating fiber tracker". Anderzijds was er een analyse van gegevens, genomen met de HERMES spectrometer, in verband met transversaal impuls verbreding van hadronen geproduceerd aan atoomkernen vergeleken met hadronen geproduceerd aan vrije nucleonen.

In 2001 heeft de HERMES collaboratie beslist om een recoil detector rond de gas cel te bouwen om trage recoil deeltjes te detecteren. Het proces waar men het meest in geïnteresseerd is, is diep virtuele Compton verstrooiing. In dit proces wordt een lepton verstrooid aan een proton target. Het lepton zendt een virtueel foton uit dat wordt geabsorbeerd door een quark in de target. Dit quark zendt op zijn beurt een reëel foton uit en het proton blijft intact. Dit proces is gevoelig aan de zogenaamde Veralgemeende Parton Distributie functies (GPD). Deze functies bevatten informatie over the structuur van het nucleon. Er is een relatie tussen 2 van deze functies en het totaal impulsmoment van de quarks aanwezig in het nucleon. Deze relatie

wordt Ji's somregel genoemd. Het totaal impulsmoment van de quarks in het nucleon is gelijk aan de som van de quark spin en het quark orbitaal impulsmoment. De quark spin contributie is reeds gemeten door onder andere het HERMES experiment en blijkt ongeveer 30 % van de totale nucleon spin te zijn. Dit wetende kan, gebruik makende van Ji's sum rule, het aandeel van het orbitaal impulsmoment van de quarks berekend worden.

De HERMES voorwaartse spectrometer is in staat om het verstrooide elektron en het geproduceerde foton te detecteren. Het foton wordt gedetecteerd in de calorimeter. Het grootste probleem bij het meten van diep virtuele Compton verstrooiing is dat het terugstoot proton niet gedetecteerd wordt. Om zich ervan te vergewissen dat het proton trefdeeltje intact gebeleven is, wordt gebruik gemaakt van de ontbrekende-massa methode. Hierbij wordt de ontbrekende 4-impuls berekend aan de hand van de reeds gedetecteerde deeltjes. Uit deze 4-impuls wordt dan de massa van het ontbrekende deeltje berekend. Deze massa moet gelijk zijn aan de zeer goed gekende massa van het proton. Vermits elke detector een zekere resolutie heeft, wordt er een piek verwacht met als centrale waarde de massa van het proton. Het zo gevormde spectrum van onbrekende massa wordt gebruikt om de diep virtuele Compton verstrooiing evenementen te selecteren. Er is een proces dat geassocieerde Bethe Heitler verstrooiing genoemd wordt. In dit proces wordt een reëel foton uitgezonden door het inkomende of uitgaande lepton en het proton wordt hierbij aangeslagen. Dit proces is achtergrond tesamen met diep inelastische verstrooing waarbij een bijkomstig foton gedetecteerd wordt. De onbrekende massa in deze evenementen is breed uitgesmeerd rond de massa van het proton. Deze processen verplichten een zeer conservatieve ontbrekende massa snede om zeker te zijn dat deze achtergrond minimaal bijdraagt. Deze snede zorgt er ook voor dat vele "echte" diep virtuele Compton verstrooings evenementen weggesneden worden. Om dit in de toekomst te vermijden heeft de HERMES collaboratie besloten om een recoil detector te bouwen om het recoil proton te detecteren.

De HERMES recoil detector bestaat in feite uit drie detectoren, een targetcel en een supergeleidende magneet. De targetcel bestaat uit zeer dun aluminium (om het materiaal waar verstrooide deeltjes door gaan te beperken) waar de targets in gastoestand in gepompt worden. Rond de targetcel (in het vacuum van de bundel) bevindt zich een silicium strip detector, ontworpen om de laagst energetische terugstoot protonen te detecteren. De laagste detecteerbare impuls wordt bepaald door de hoeveelheid materiaal er zich tussen de interactie en de detector bevindt. Daarom werd de silicium detector in het vacuum geplaatst. De silicium detector gebruikt de energie afzetting van het proton ter bepaling van de impuls vermits er een eenduidige relatie bestaat tussen beide (de zogenaamd Bethe-Bloch functie) in het energiegebied waar deze detector operationeel is. Rond de silicium detector, buiten het vacuum van de bundel, bevindt zich de zogenaamde "scintillating fiber" detector. Deze detector is ontworpen ter detectie van terugstoot protonen met een hogere impuls en gebruikt de afbuiging van geladen deeltjes in het magneetveld, geproduceerd door de supergeleidende magneet, om de impuls te bepalen. Het meten van afbuigingen vereist spoorbepaling van geladen deeltjes en om dit te kunnen doen bestaat deze detector uit twee cilinders. Elke cilinder bestaat op zich uit twee lagen dikke scintillerende vezels die een diameter van 1 mm hebben. De binnenste laag heeft de vezels evenwijdig geörienteerd met de bundel. In de buitenste laag maken de vezels een hoek van 10° met de binnenste laag. Op deze manier kan de detector twee ruimtepunten per spoor bepalen en een spoor kan gefit worden (ook de silicium detector heeft de mogelijkheid om twee ruimtepunten per spoor te bepalen wat de spoorbepaling vergemakkelijkt). De scintillerende vezels worden uitgelezen door ongeveer 80 64-kanaals

Photomultiplier Tubes of PMTs. Deze werden alle getest in dit werk. Rond de "scintillating fiber" tracker is de foton-detector geplaatst. Deze detector moet fotonen detecteren afkomstig van het verval van aangeslagen protonen. Dit om enerzijds deze evenementen weg te snijden vermits ze achtergrond zijn voor de diep virtuele Compton scattering, anderzijds om deze evenementen te identificeren en eventueel te analyseren. In deze thesis is er werk verricht in de constructie en test van deze detector.

De foton-detector bestaat uit drie lagen. Elke laag bestaat uit een laag wolfram (aan de binnenkant) gevolgd door scintillerende strips. In wolfram is de kans groot dat het foton een lawine van secundaire geladen deeltjes induceert, de zogenaamde "showers". Deze geladen deeltjes worden dan gedetecteerd in de scintillerende strips. In de binnenste laag zijn de strips evenwijdig georienteerd aan de bundel. In de twee buitenste lagen maken de scintillerende strips een hoek van respectievelijk -45° en +45° met de binnenste laag. Elke strip heeft aan beide zijden een groef waar een golflengte verlengende vezel in gelijmd is. Deze vezels absorberen het licht komende van de scintillerende strips en zenden licht uit met een langere golflengte. In dit geval zenden de scintillerende strips licht uit in het blauwe deel van het spectrum, de vezels absorberen het blauwe licht en zenden licht uit in het groene deel van het spectrum. Deze vezels voeren het groene licht naar de connectoren aan de rand van de foton-detector. Aan deze connectoren worden lichtgeleiders (optische vezels) aangesloten. Deze vezels voeren het licht ver genoeg van het magnetisch veld naar PMTs om uitgelezen te worden. De PMTs die gebruikt worden zijn dezelfde 64-kanaals PMTs die gebruikt worden voor de "scintillating fiber" detector. Een connector was ontworpen om 64 optische vezels te connecteren en te positioneren op het ingangsvenster van de PMT. De positionering van de vezels ten opzichte van elkaar op een connector is zo gekozen dat naburige strips een kleine kans hebben om een signaal te genereren in hetzelfde evenement. Dit opent de mogelijkheid om achteraf te corrigeren voor "cross-talk" ("cross-talk" is het induceren van een signaal in kanalen in de buurt van het oorspronkelijke signaal). De vezels werden dan in een connector gelijmd en een "cross-talk" meting werd gebruikt om deze op de PMT te positioneren. Verschillende "cross-talk" metingen werden uitgevoerd voor verschillende positioneringen. De positionering met de laagste cross-talk werd uiteindelijk gebruikt. Hoewel de PMTs ongeveer 2 m van de magneet verwijderd zijn, moeten ze toch nog afgeschermd worden van het magnetisch veld. Dit gebeurt met een kombinatie van "SAE1015" of zacht metaal en μ-metaal. Een afschermingstest in een magneet werd uitgevoerd om de dikte en de optimale kombinatie van de afscherming te bepalen. De PMTs die gebruikt worden voor de foton-detector en diegene die gebruikt worden voor de scintillating fiber tracker werden getest. Voor deze test werd een donkere doos gebouwd waarin plaats is voor 3 PMTs, een 1 kanaals referentie-PMT, een blauwe LED op 1 m afstand van de PMTs en 5 lichtfilters geplaatst op een programmeerbare positioneer-as die de filters voor de LED kan plaatsen. Deze filters attenueren het licht uitgezonden door de LED. Verscheidene tests werden uitgevoerd met deze opstelling. Eerst werd er een ruistest uitgevoerd waarbij geen licht werd geïnjecteerd in de PMT en waar de ruis bestudeerd werd. De ruis bleek stabiel en verwaarloosbaar klein te zijn. Een andere test was het bepalen van een werkplateau, hierbij werd een zeer kleine lichtpuls gegenereerd zodat de PMT in het 1 foto-elektron regime werkt. In dit regime wordt de lichtpuls zo klein gekozen dat ze door de photokathode omgezet wordt in 1 elektron en dit elektron wordt dan door de dynodes versterkt. Dit is het kleinst mogelijk signaal. De positie van dit signaal ten opzichte van de ruis wordt geplot in functie van de aangelegde hoogspanning op de PMT. De aangelegde

hoogspanning waarbij het signaal volledig boven de ruis komt wordt werkspanning genoemd. De bedoeling van deze test is om deze te bepalen. Het bleek dat deze werkspanning vrij dicht ligt bij de maximale spanning die gespecifieerd wordt door de fabrikant. Een andere test was het testen van de uniformiteit van de PMT respons. Hierbij wordt de PMT uniform belicht door de LED. De respons van alle pixels wordt dan vergeleken. Het bleek dat de pixels die zich aan de randen bevinden consistent een hogere respons hebben. Een andere test was het bepalen van de lineariteit van de versterking van de PMT. Hiervoor werden lichtpulsen met verschillende intensiteiten in de PMT geïnjecteerd. De PMT respons werd bestudeerd in functie van de amplitude van de lichtpuls. Het bleek dat er een afwijking van lineariteit was voor de hoogste signalen. De laatste test was de tijdsafhankelijkheid van de ruis. Er werd binnen de fout geen afhankelijkheid waargenomen.

De eerste test met een prototype van de fotondetector gebeurde in het Geselschaft für Schwer-Ionenforschung (GSI), Damstadt. Hierbij werd gebruik gemaakt van een bundel die bestond uit protonen en pionen met dezelfde impuls. Het uitleesprincipe werd succesvol getest en deeltjesidentificatie bleek mogelijk voor impulsen hoger dan 600 MeV. De volledige fotondetector met finale elektronische uitleesketen werd voor het eerst getest in DESY, gebruik makende van kosmische straling (die hoofdzakelijk bestaat uit muonen). Dit was succesvol en een gedeelte van de fotondetector kon geijkt worden met deze kosmische straling. Een ander deel niet, vermits kosmische straling vooral in vertikale richting voorkomt en enkel kosmische straling die loodrecht door de scintillator strips gaat, gebruikt kan worden voor de ijking.

Het tweede deel van deze thesis handelt over de analyse van HERMES gegevens in verband met de transversale impuls verbreding van verschillende hadron types (geladen pionen en kaonen) geproduceerd in semi-exclusieve diep-inelastische verstrooiing van leptonen aan atoomkernen vergeleken met hadronen geproduceerd aan nucleonen. Dit effect wordt p_t-verbreding genoemd. In diep-inelastische verstrooiing van leptonen heeft het lepton een voldoende hoge energie om te verstrooien aan de (quark-gluon) structuur van het nucleon. Het lepton zendt een virtueel foton uit dat geabsorbeerd wordt aan een parton (bijv. een quark). Dit quark wordt uit het nucleon gestoten en zal uiteindelijk hadronizeren in een hadron. Hoe hadronizatie precies werkt, is tot op heden niet begrepen. Om hadronizatie te bestuderen worden atoomkernen gebruikt omdat zij het hadronizatie proces "verstoren": er treden effecten op, die informatie verschaffen over verschillende stadia van het hadronizatie proces.

Er zijn diverse theoretische modellen beschikbaar die pogen de ruimte-tijd evolutie van hadronizatie te beschrijven. Deze modellen worden hier getest aan de hand van voorspellingen die zij maken van nucleaire effecten. Tot op heden is geen enkel model in staat om een accurate voorspelling te maken voor alle gegevens die beschikbaar zijn. In het algemeen wordt het hadronizatie proces opgesplitst in drie delen: in het eerste deel zendt het verstrooide quark gluonen uit, al of niet in een geïnduceerd sterk veld van aanwezige nucleonen. Het quark verliest hierbij energie en na een bepaalde tijd, *productietijd* genaamd, "bindt" het quark zich met een anti-quark en vormt het een kleur-neutraal *pre-hadron*. Een pre-hadron is een quark-antiquark paar dat nog niet de eigenschappen bezit van een hadron. Nucleaire effecten die plaatshebben gedurende de productietijd worden partonische effecten genoemd. Na de vorming van het pre-hadron kan dit object nog elastische en inelastische interacties ondergaan met het medium. Na een tijd die *vormingstijd* genoemd wordt, wordt het finale hadron gevormd. Dit hadron kan ook nog interacties met het medium ondergaan. Effecten die plaatsvinden na de vormimg van het pre-hadron worden hadronische effecten genoemd. Modellen beschrijven

enkel partonische, enkel hadronische, of een combinatie van beide effecten.

De analyse van p_t-verbreding is eigenlijk een meting van de productietijd omdat na de vorming van het pre-hadron de inelastische interacties onderdrukt worden, als men hadronen selecteert die een hoge fractie bezitten van de originele energie van het verstrooide quark. De elastische werkzame doorsnede van het pre-hadron wordt kleiner geschat dan de elastische werkzame doorsnede van het hadron. De gemiddelde vrije weglengte van het hadron is veel langer dan de diameter van de atoomkernen gebruikt in deze analyse.

In de analyse van de p_t-verbreding zijn er verschillende correcties toegepast. De gegevens werden gekorrigeerd voor ladingssymmetrische achtergrond. Deze achtergrond is afkomstig van elektron-positron paarvorming door interacties van deeltjes met materiaal van de spectrometer. Het kan dus gebeuren dat het "verkeerde" lepton geselecteerd wordt zijnde het verstrooide lepton. Om hiervoor te corrigeren werd het lepton met de hoogste impuls geselecteerd als het verstrooide lepton. Als dit lepton niet dezelfde lading bezit als de leptonen van de bundel, wordt dit evenement aangerekend met gewicht -1. Dit omdat dit evenement zeker een achtergrond evenement is, en er ook gecorrigeerd dient te worden voor hetzelfde evenement maar waarbij het gedetecteerde lepton dezelfde lading als de bundel bezit. Er dient ook gecorrigeerd te worden voor misidentificaties van hadron types. De detector die gebruikt wordt om hadronen te identificeren is de zogenaamde *ring imaging Čerenkov* (RICH) detector. Deze detector meet de openingshoek van de lichtkegel uitgezonden door deeltjes die zich sneller dan de lichtsnelheid in een materiaal voortbewegen (maar trager dan de lichtsnelheid in vacuum). Uit deze hoek wordt de snelheid van het deeltje berekend. De impuls van een geladen deeltje is bekend uit de gemeten afbuiging in het magneetveld. Deze informatie in combinatie met de snelheid is voldoende om het hadron te identificeren. Deze identificatie is echter niet perfect en er dient gecorrigeerd te worden voor misidentificaties. Deze correctie gebeurd met een unfolding methode waar een goede simulatie van de detector in kwestie onontbeerlijk is. De twee voorgaande correcties hebben geen noemenswaardig effect op de p_t-verbreding.

Het kan voorkomen dat het virtueel foton vooraleer het verstrooit aan een parton fluctueert in een hadron met dezelfde kwantumgetallen als het virtueel foton. Dit hadron (een ρ^0 is het meest waarschijnlijk in de HERMES kinematica) kan verstrooid worden aan de atoomkern als geheel of aan een nucleon aanwezig in de atoomkern. Het eerste geval wordt coherente verstrooiing genoemd, het tweede geval incoherente verstrooiing. Dit ρ^0 deeltje kan dan vervallen in pionen en deze kunnen gedetecteerd worden. Er dient gecorrigeerd te worden voor dit proces vermits deze pionen niet afkomstig zijn van een hadronizatie proces in de atoomkern. Deze correctie werd uitgevoerd met behulp van een simulatie van dit proces genormeerd op gereconstrueerde ρ^0 deeltjes. Deze correctie had enkel een noemenswaardige invloed in het kinematische regime waar de energie van het finale hadron bijna even groot was als de energie van het verstrooide quark. De laatste correctie was een correctie voor de begrensde acceptantie en resolutie van de spectrometer, samen met stralingseffecten. Stralingseffecten zijn effecten afkomstig van het feit dat ingaande en uitgaande leptonen fotonen kunnen uitzenden die niet gedetecteerd worden. In dit geval is de berekende kinematica van het virtuele foton niet correct omdat er gebruik gemaakt wordt van behoud van 4-impuls en de 4-impuls van het niet-gedetecteerde foton niet in rekening kan worden gebracht. Deze correctie werd uitgevoerd door een unfolding methode die gebruik maakt van een simulatie van de eigenlijke evenementen, een simulatie van stralingseffecten, en een simulatie van de spectrometer (met

acceptantie en resoluties). Deze correctie had de grootste invloed op het eindresultaat.

De p_t-verbreding is lineair ten opzichte van het atoomnummer $A^{\frac{1}{3}}$. Dit betekent dat de verbreding recht evenredig is met de straal van de atoomkern, wat op een lange productietijd wijst. De verbreding versus energiefractie van de verstrooide quark gedragen door het hadron is constant en voor fracties gaande naar 1 gaat de verbreding naar 0. Dit is een indicatie dat de productietijd naar 0 gaat voor fracties dicht bij 1 en is het gevolg van energiebehoud: als de productietijd groter is dan 0 dan heeft het verstrooide quark tijd om energie te verliezen en kan de fractie nooit meer 1 zijn. De p_t-verbreding is constant in functie van de energie van het virtuele foton. De p_t-verbreding zou normaal gezien moeten stijgen voor een stijgende energie van het virtuele foton door tijddilatatie. In deze evenementen hebben deeltjes relativistische snelheden wat betekent dat een hogere energie zorgt voor een tijdrek ten opzichte van de waarnemer die zich niet beweegt. Dit p_t-verbredingsgedrag kan erop wijzen dat het pre-hadron altijd buiten de atoomkern gevormd wordt en zodoende modellen met enkel partonische effecten bevoordeelt. De p_t-verbreding in functie van de 4-impuls van het virtueel foton stijgt voor een stijgende 4-impuls. Dit gedrag kan niet eenduiding verklaard worden. Deze observaties kunnen leiden tot het uitsluiten van bepaalde modellen die hadronizatie trachten te verklaren.

Bibliography

[1] M. Anselmino, A. Efremov, and E. Leader, Phys. Rept. **261** (1995) 1

[2] M. Breidenbach *et al.*, Phys. Rev. Lett. **23** (1969) 935

[3] J. Callan, C.G., and D.J. Gross, Phys. Rev. Lett. **22** (1969) 156

[4] B. Povh, K. Rith, C. Scholz, F. Zetsche, Particles and Nuclei, Springer Akademischer Verlag, Heidelberg 1996

[5] Particle Data Group, J. Phys. G: Nucl. Part. Phys. **33** (2006) 1

[6] S. Chekanov et al., Phys. Rev. D **67** (2003) 012007

[7] R. Voss, T. Sloan, G. Smadje, Phys. Rept. **162** (1988) 45

[8] ZEUS *public plots* , found on www-zeus.desy.de/public_results/functiondb.php?id=ZEUS-prel-03-032

[9] V.N. Gribov and L.N. Lipanov, Sov. J. Nucl. Phys. **15** (1972) 438

[10] L.N. Lipanov, Sov. J. Nucl. Phys. **20** (1975) 94

[11] G. Altarelli and G. Parisi, Nucl. Phys. B **168** (1980) 409

[12] Y.L. Dokshitzer, Sov. Phys. JETP **46** (1977) 641

[13] B. Maiheu, Hadronization in electron - proton scattering at HERMES, PhD thesis, University of Gent, 2006

[14] J.C. Collins, D.E. Soper, and G. Sterman, High Energy Phys. **5** (1988) 1

[15] A. Hillenbrand, Measurement and simulation of the fragmentation process at HERMES, PhD thesis, University of Erlangen, DESY-THESIS-2005-035

[16] R. Baier, D. Schiff, and B.G. Zakharov, Ann. Rev. Nucl. Part. Sci. **50** (2000) 37

[17] A. Accardi, arXiv:0706.34227

[18] M. Arneodo *et al.*, Phys. Lett. B **211** (1988) 493

[19] A. Airapetion *et al.*, Phys. Lett. B. (2007) 1

[20] A. Bialas, Acta Phys. Polon. B **11** (1980) 475

[21] M. Gyulassy and M. Plŭmer, Nucl. Phys. B **346** (1989) 1

[22] J. Czyzewski and P. Sawicki, Z. Phys. C **56** (1992) 493

[23] N.Z. Akopov, G.M. Elbakian, L.A. Grigorian, hep-ph/0205123

[24] T. Falter *et al.*, Nucl. Phys. B **594** (2004) 61

[25] J. Dias De Deus, Phys. Lett. B **166** (1986) 98

[26] A. Accardi, V. Muccifora, H.J. Pirner, Nucl. Phys. A **720** (2003) 131

[27] F. Arleo, JHEP **0211** (2002) 044

[28] F. Arleo, Phys. Lett. B **532** (2002) 231

[29] X.N. Wang and X. Guo, Nucl. Phys. A **696** (2001) 788

[30] B.Z. Kopeliovic, J. Nemchik, E. Predazzi, and A. Hayashigaki, Nucl. Phys. A **740** (2003) 211

[31] M.B. Johnson *et al.*, Phys. Rev. C **65** (2002) 025203

[32] B. Anderson *et al.*, Phys. Rept. **97** (1983) 31

[33] B. Nilsson-Almqvist and E. Stenlund, Commut.Phys.Commun. **43** (1987) 387

[34] T. Falter, Nuclear reactions of high energy protons, photons, and leptons, PhD thesis, University of Giessen, 2004

[35] O. Nachtmann and H. J. Pirner, Z. Phys. C **21** (1984) 277

[36] R.L. Jaffe, F. E. Close, R.G. Roberts, and G.G. Ross, Phys.Lett.B **134** (1984) 449; Phys. Rev. D **31** (1985) 1004

[37] O. Nactmann and H.J. Pirner, Annalen Phys. **44** (1987) 13

[38] A. Bialas and M. Gyulassy, Nucl. Phys. B **291** (1987) 793

[39] A. Bialas and T. Chmaj, Phys. Lett. B **133** (1983) 241

[40] B.Z. Kopeliovic, J. Nemchik, and I. Schmidt, Nucl. Phys. A **782** (2007) 224

[41] B. Kopeliovich, J. Nemchik, and E. Predazzi, hep-ph/9511214

[42] R. Baier *et al.*, Nucl. Phys. B **484** (1997) 265

[43] picture found on http://www.particleadventure.org/frameless/quark_confinement.html

[44] The HERMES Collaboration, *HERMES internal note*, The HERMES recoil detector, technical design report

[45] A.V. Belitsky *et al.*, Nucl. Phys. B **574** (2000) 347

[46] M. Burkardt, Phys. Rev. D **62** (2000) 071503

[47] J.P. Ralston and B. Pire, Phys. Rev. D **66** (2002) 111501

[48] S.J. Brodsky *et al.*, Nucl. Phys. B **596** (2001) 99
M. Diehl *et al.*, Nucl.Phys.B **596** (2001) 33 [Erratum-ibid. B **605** (2001) 647]

[49] X. Ji, Phys. Rev. Lett. **78** (1997) 610

[50] J.C. Collins *et al.*, Phys. Rev. D **56** (1997) 2982

[51] J.C. Collins and A. Freund, Phys. Rev. D **59** (1999) 074009

[52] X. Ji and J. Osborne, Phys. Rev. D **58** (1998) 094018

[53] A.V. Radyushkin, Phys. Rev. D **58** (1998) 114008

[54] M. Diehl *et al.*, Phys. Lett. B **411** (1997) 193

[55] A.V. Belitsky *et al.*, Nuc. Phys. B **629** (2002) 323

[56] B. Krauss, Deeply Virtual Compton Scattering and the HERMES-Recoil Detector, PhD thesis, Physikalisches Institut II, FAU Erlangen-Nürnberg, 2005

[57] A.A. Solokov and I. M. Ternov, Phys. Dokl. **8** (1964) 1203

[58] D. P. Barber *et al.*, Nucl. Instrum. Meth. A **329** (1993) 79

[59] M. Beckmann *et al.*, Nucl. Instrum. Meth. A **479** (1993) 334

[60] C. Baumgarten *et al.*, Nucl. Instrum. Meth. A **496** (2003) 277

[61] D. R. Swenson and L. W. Anderson, Nucl. Instrum. Meth. B **29** (1988) 627

[62] A. Nass *et al.*, Nucl. Instrum. Meth. A **505** (2003) 633

[63] C. Baumgarten *et al.*, Nucl. Instrum. Meth. A **508** 268

[64] C. Baumgarten *et al.*, Nucl. Instrum. Meth. A **482** 606

[65] T. Benich *et al.*, Nucl. Instrum. Meth. A **471** (2001) 314

[66] K. Ackerstaff *et al.*, Nucl. Instrum. Meth. A **417** (1998) 230

[67] M. G. Van Beuzekom *et al.*, Nucl. Instrum. Meth. A **409** (1998) 255

[68] J. T. Brack *et al.*, Nucl. Instrum. Meth. A **469** (2001) 47

[69] A. Andreev *et al.*, Nucl. Instrum. Meth. A **465** (2001) 482

[70] S. Bernreuther *et al.*, Nucl. Instrum. Meth. A **367** (1995) 96

[71] S. Bernreuther *et al.*, Nucl. Instrum. Meth. A **416** (1998) 45

[72] W. Wander, Reconstruction of High Energy Scattering Events in the HERMES Experiment, PhD. thesis, Physikalisches Institut II, FAU Erlangen-Nürnberg, HERMES-97-031

[73] N. Akopov *et al.*, Nucl. Instrum. Meth. A **479** (2002) 511

[74] E.C. Aschenauer *et al.*, Nucl. Instrum. Meth. A **440** (2000) 338

[75] R. Kaiser, D. Deschepper, and E. Cisbani, *HERMES internal note*, Particle Identification with the HERMES RICH detector: Description of the different approaches.

[76] A. Maas, *HERMES internal note*, The RICH PID scheduler

[77] S.F. Pate, *HERMES internal note*, Test of the H0 Forward Trigger Scintillators for HERMES.

[78] B. Maiheu and U. Elschenbroich, *HERMES internal*, The HERMES Trigger Hodoscope (H1) and preshower detector (H2): experimenters guide.

[79] X. Artru, G.B. Yodh, and Mennessier, Phys. Rev. D **12** (1975) 1289

[80] H. Avakian *et al.*, Nucl. Instrum. Meth. A **417** (1998) 69

[81] M. Kobayashi *et al.*, KEK Internal Report (1993) 93

[82] R. Kaiser (for the HERMES PID Group), *HERMES internal note*, Particle Identification at HERMES

[83] F. Menden, Determination of the Gluon Polarization in the Nucleon, PhD thesis, Albert-Ludwigs-University Freiburg, DESY-THESIS-2001-060

[84] CERN Programming Techniques Group, ADAMO-Entity-Relationship Programming System, *User Guide* (1993) Version 3.3

[85] The HERMES collaboration, DESY-PRC 02-01

[86] M. Reinecke *et al.*, *HERMES internal*, A silicon strip recoil detector for momentum measurement and tracking at HERMES

[87] *BC-408 data sheet*, found on www.detectors.saint-gobain.com

[88] *BCF-91A data sheet*, found on www.detectors.saint-gobain.com

[89] *BCF-98 data sheet*, found on www.detectors.saint-gobain.com

[90] *H7546 data sheet*, found on http://sales.hamamatsu.com/index.php?id=13199677&language=2&#

[91] E.H. Bellamy *et al.*, NIM A **339** (1994) 469

[92] T. Sjostrand, L. Lonnblad, S. Mrenna, and P. Skanks, FERMILAB-PUB-03-457

[93] P. Liebing, Can the Gluon Polarization in the Nucleon be extracted from HERMES Data on single high-pt Hadrons?, PhD thesis, University Hamburg, DESY-THESIS-2004-036

[94] I. Akushevich, H. Böttcher, and D. Ryckbosch, hep-ph/9906408

[95] T. Sjöstrand, Comput. Phys. Commun. **82** (1994) 74

[96] R. Brun, R. Hagelberg, M. Hansroul, and J.C. Lasalle, CER-DD-78-2-REV

[97] G. Ingelman, A. Edin, and J. Rathsman, Comput. Phys. Commun. **101** (1997) 108

[98] M. Hartig, *HERMES internal note*, Notes on RHOMC

[99] A. Rostomyan *HERMES talk(s)*, http://www-hermes.desy.de/groups/mgmtgrp/COLLABMEETINGS/VM_NOV06/rhomc*.pdf (closed)

[100] T. Falter, K. Gallmeister, and U. Mosel, Phys.Rev.C **67** (2003) 054606

[101] B. Hommez, H. Jackson, R. Kaiser, Y. Miyashi, *HERMES internal note*, Using the RICH detector for Physics Analysis, http://www-hermes.desy.de/groups/richgrp/rich/richanalysis/analysis.ps

[102] B. Hommez, *HERMES internal note*, Tuning the RICH paramters in the Monte Carlo

[103] T. Hasegawa, Y. Miyachi *HERMES internal note*, Estimation of RICH particle identification accuracy using decaying particles

[104] J.J. Sakurai, Phys. Rev. Lett. **22** (1969) 981

[105] J.J. Sakurai and D. Schildknaap, Phys. Lett. B **40** (1972) 121

[106] HERMES Collaboration, K. Ackerstaff *et al.*, Phys. Rev. Lett. **82** (1999) 3025

[107] A. Jgoun and Y. Van Haarlem, *HERMES internal note*, Nuclear medium effects on the transverse momentum of the produced hadrons in sidis

[108] A. Miller, *HERMES internal note*, Applying radiative Corrections to Ratios of Cross Sections for Deep Inelastic Scattering, http://www.triumf.ca/people/miller/hermes/Uradcorr.ps.gz

[109] Y. Van Haarlem, A. Jgoun, P. Di Nezza for the HERMES collaboration, arXiv: 0704.3712

[110] A. Accardi, B. Kopeliovich, H.J. Pirner, and X.N. Wang, *private communication*

Appendix A

Data tables for the p_t-broadening results

A.1 p_t-broadenig versus A$^{1/3}$

$\Delta\langle p_t^2\rangle^{\pi^+}$(GeV^2)	Value	Stat. error	Sys. uncertainty
Ne	0.0038	0.0011	0.00099
Kr	0.0182	0.0012	0.0021
Xe	0.0243	0.0016	0.0027
$\Delta\langle p_t^2\rangle^{\pi^-}$(GeV^2)			
Ne	0.0072	0.0012	0.0011
Kr	0.0178	0.0013	0.0022
Xe	0.0235	0.0016	0.0022
$\Delta\langle p_t^2\rangle^{K^-}$(GeV^2)			
Ne	0.0075	0.0034	0.0024
Kr	0.0225	0.0034	0.0033
Xe	0.0351	0.0045	0.0044

Table A.1: Table containing numerical values for the p_t-broadening versus $A^{1/3}$ plot.

$\Delta\langle p_t^2\rangle^{\pi^+}$	$\langle Q^2\rangle$(GeV^2)	$\langle\nu\rangle$(GeV)	$\langle z\rangle$	$\langle z^2\rangle$
Ne	2.4043±0.0024	14.4790±0.0068	0.39987±0.00028	0.19014±0.00029
Kr	2.4160±0.0026	14.7017±0.0074	0.39207±0.00030	0.18227±0.00030
Xe	2.4141±0.0033	14.7843±0.0095	0.38994±0.00038	0.18019±0.00038
$\Delta\langle p_t^2\rangle^{\pi^-}$				
Ne	2.3406±0.0026	14.6154±0.0077	0.39325±0.00031	0.18429±0.00032
Kr	2.3553±0.0028	14.7633±0.0082	0.38601±0.00033	0.17702±0.00033
Xe	2.3556±0.0035	14.816±0.010	0.38412±0.00042	0.17516±0.00042
$\Delta\langle p_t^2\rangle^{K^+}$				
Ne	2.4802±0.0052	14.271±0.014	0.41410±0.00059	0.20028±0.00060
Kr	2.4855±0.0055	14.498±0.015	0.40783±0.00062	0.19415±0.00062
Xe	2.4798±0.0070	14.670±0.020	0.40625±0.00078	0.19219±0.00077

Table A.2: Average values of Q^2, ν, z, and z^2 per hadron type per bin for the p_t-broadening versus $A^{1/3}$ plot. These numbers are extracted from data without applying corrections.

A.2 p_t-broadening versus z

$\Delta\langle p_t^2\rangle^{\pi^+}_{Ne}$(GeV^2)	Value	Stat. error	Sys. uncertainty
z-bin# 1	0.0068	0.0014	0.0011
z-bin# 2	0.0078	0.0025	0.0021
z-bin# 3	-0.0083	0.0050	0.0044
z-bin# 4	-0.0115	0.0080	0.0083
$\Delta\langle p_t^2\rangle^{\pi^+}_{Kr}$(GeV^2)			
z-bin# 1	0.0215	0.0015	0.0020
z-bin# 2	0.0256	0.0026	0.0033
z-bin# 3	0.0075	0.0053	0.0037
z-bin# 4	0.0040	0.0089	0.0071
$\Delta\langle p_t^2\rangle^{\pi^+}_{Xe}$(GeV^2)			
z-bin# 1	0.0286	0.0021	0.0027
z-bin# 2	0.0339	0.0034	0.0043
z-bin# 3	0.0123	0.0069	0.0042
z-bin# 4	-0.0019	0.0011	0.0062

Table A.3: Table containing numerical values for the p_t-broadening versus z plot for positive charged pions.

$\Delta\langle p_t^2\rangle_{Ne}^{\pi^+}$	$\langle Q^2\rangle$(GeV^2)	$\langle\nu\rangle$(GeV)	$\langle z\rangle$	$\langle z^2\rangle$
z-bin# 1	2.4374±0.0031	15.1592±0.0085	0.28642±0.00012	0.085189±0.000069
z-bin# 2	2.3919±0.0048	13.842±0.014	0.48542±0.00019	0.23886±0.00019
z-bin# 3	2.3190±0.0071	13.106±0.019	0.68635±0.00028	0.47427±0.00039
z-bin# 4	2.192±0.011	11.457±0.025	0.87610±0.00043	0.77026±0.00076
$\Delta\langle p_t^2\rangle_{Kr}^{\pi^+}$				
z-bin# 1	2.4465±0.0033	15.3289±0.0091	0.28537±0.00012	0.084585±0.000074
z-bin# 2	2.4035±0.0052	14.061±0.015	0.48458±0.00020	0.23803±0.00020
z-bin# 3	2.3277±0.0080	13.317±0.022	0.68519±0.00032	0.47266±0.00044
z-bin# 4	2.191±0.013	11.575±0.029	0.87486±0.00049	0.76802±0.00088
$\Delta\langle p_t^2\rangle_{Xe}^{\pi^+}$				
z-bin# 1	2.4387±0.0042	15.413±0.012	0.28526±0.00016	0.084527±0.000094
z-bin# 2	2.4080±0.0067	14.133±0.020	0.48398±0.00026	0.23747±0.00026
z-bin# 3	2.328±0.010	13.307±0.029	0.68559±0.00041	0.47323±0.00057
z-bin# 4	2.230±0.017	11.624±0.038	0.87391±0.00066	0.7664±0.0012

Table A.4: Average values of Q^2, ν, z, and z^2 per hadron type per bin for the p_t-broadening versus z plots for positive charged pions. These numbers are extracted from data without applying any correction.

$\Delta\langle p_t^2\rangle_{Ne}^{\pi^-}$(GeV^2)	Value	Stat. error	Sys. uncertainty
z-bin# 1	0.0084	0.0016	0.0011
z-bin# 2	0.0107	0.0028	0.0023
z-bin# 3	-0.0045	0.0057	0.0046
z-bin# 4	-0.0032	0.0092	0.010
$\Delta\langle p_t^2\rangle_{Kr}^{\pi^-}$(GeV^2)			
z-bin# 1	0.0194	0.0016	0.0017
z-bin# 2	0.0244	0.0029	0.0029
z-bin# 3	0.0118	0.0060	0.0042
z-bin# 4	-0.0030	0.0096	0.0070
$\Delta\langle p_t^2\rangle_{Xe}^{\pi^-}$(GeV^2)			
z-bin# 1	0.0296	0.0022	0.0024
z-bin# 2	0.0306	0.0037	0.0032
z-bin# 3	0.0152	0.0078	0.0047
z-bin# 4	-0.003	0.012	0.0066

Table A.5: Table containing numerical values for the p_t-broadening versus z plot for negative charged pions.

$\Delta\langle p_t^2\rangle^{\pi^-}_{Ne}$	$\langle Q^2\rangle$(GeV^2)	$\langle\nu\rangle$(GeV)	$\langle z\rangle$	$\langle z^2\rangle$
z-bin# 1	2.3847±0.0033	15.3071±0.0094	0.28494±0.00013	0.084324±0.000076
z-bin# 2	2.3290±0.0052	13.885±0.016	0.48412±0.00021	0.23757±0.00021
z-bin# 3	2.1957±0.0076	13.084±0.023	0.68624±0.00033	0.47412±0.00046
z-bin# 4	2.050±0.011	11.583±0.028	0.87697±0.00049	0.77178±0.00087
$\Delta\langle p_t^2\rangle^{\pi^-}_{Kr}$				
z-bin# 1	2.3956±0.0035	15.384±0.010	0.28430±0.00014	0.083955±0.000080
z-bin# 2	2.3399±0.0057	14.033±0.017	0.48394±0.00023	0.23740±0.00023
z-bin# 3	2.2144±0.0087	13.310±0.026	0.68521±0.00037	0.47271±0.00051
z-bin# 4	2.060±0.013	11.655±0.033	0.87482±0.00056	0.7680±0.0010
$\Delta\langle p_t^2\rangle^{\pi^-}_{Xe}$				
z-bin# 1	2.4005±0.0045	15.447±0.013	0.28380±0.00017	0.08365±0.00010
z-bin# 2	2.3310±0.0073	14.060±0.022	0.48400±0.00030	0.23744±0.00029
z-bin# 3	2.191±0.011	13.272±0.033	0.68412±0.00047	0.47120±0.00066
z-bin# 4	2.077±0.017	11.670±0.042	0.87627±0.00073	0.7705±0.00129

Table A.6: Average values of Q^2, ν, z, and z^2 per hadron type per bin for the p_t-broadening versus z plots for negative charged pions. These numbers are extracted from data without applying any correction.

$\Delta\langle p_t^2\rangle^{K^+}_{Ne}$(GeV^2)	Value	Stat. error	Sys. uncertainty
z-bin# 1	0.0123	0.0043	0.0025
z-bin# 2	0.0094	0.0065	0.0048
z-bin# 3	0.011	0.012	0.011
z-bin# 4	-0.014	0.022	0.025
$\Delta\langle p_t^2\rangle^{K^+}_{Kr}$(GeV^2)			
z-bin# 1	0.0485	0.0062	0.0045
z-bin# 2	0.0298	0.0067	0.0066
z-bin# 3	0.026	0.013	0.0094
z-bin# 4	-0.025	0.022	0.016
$\Delta\langle p_t^2\rangle^{K^+}_{Xe}$(GeV^2)			
z-bin# 1	0.0485	0.0062	0.0045
z-bin# 2	0.0442	0.0089	0.0082
z-bin# 3	0.022	0.016	0.0087
z-bin# 4	0.018	0.031	0.022

Table A.7: Table containing numerical values for the p_t-broadening versus z for positive charged kaons.

$\Delta\langle p_t^2\rangle_{Ne}^{K^+}$	$\langle Q^2\rangle$(GeV^2)	$\langle\nu\rangle$(GeV)	$\langle z\rangle$	$\langle z^2\rangle$
z-bin# 1	2.4581±0.0068	14.684±0.019	0.29175±0.00027	0.08838±0.00016
z-bin# 2	2.4737±0.0098	14.063±0.029	0.48830±0.00038	0.24169±0.00037
z-bin# 3	2.580±0.016	13.549±0.039	0.68279±0.00056	0.46932±0.00077
z-bin# 4	2.537±0.030	11.687±0.054	0.86537±0.00091	0.7510±0.0016
$\Delta\langle p_t^2\rangle_{Kr}^{K^+}$				
z-bin# 1	2.4575±0.0072	14.970±0.020	0.29005±0.00028	0.08733±0.00017
z-bin# 2	2.503±0.011	14.187±0.030	0.48733±0.00040	0.24072±0.00039
z-bin# 3	2.560±0.017	13.620±0.043	0.68273±0.00061	0.46925±0.00085
z-bin# 4	2.573±0.032	11.699±0.062	0.8685±0.0011	0.7566±0.0019
$\Delta\langle p_t^2\rangle_{Xe}^{K^+}$				
z-bin# 1	2.4595±0.0091	15.153±0.025	0.29036±0.00036	0.08755±0.00021
z-bin# 2	2.485±0.013	14.380±0.038	0.48705±0.00051	0.24045±0.00050
z-bin# 3	2.559±0.022	13.644±0.055	0.68098±0.00077	0.4667±0.0011
z-bin# 4	2.525±0.043	11.765±0.082	0.8667±0.0015	0.7537±0.0026

Table A.8: Average values of Q^2, ν, z, and z^2 per hadron type per bin for the p_t-broadening versus z plots for positive charged kaons. These numbers are extracted from data without applying any correction.

A.3 p_t-broadening versus ν

$\Delta\langle p_t^2\rangle^{\pi^+}_{Ne}$(GeV^2)	Value	Stat. error	Sys. uncertainty
ν-bin# 1	0.0089	0.0032	0.0021
ν-bin# 2	0.0032	0.0027	0.0020
ν-bin# 3	0.0006	0.0041	0.0032
ν-bin# 4	0.0015	0.0022	0.0017
$\Delta\langle p_t^2\rangle^{\pi^+}_{Kr}$(GeV^2)			
ν-bin# 1	0.0186	0.0036	0.0019
ν-bin# 2	0.0142	0.0028	0.0019
ν-bin# 3	0.0109	0.0042	0.0030
ν-bin# 4	0.0160	0.0022	0.0017
$\Delta\langle p_t^2\rangle^{\pi^+}_{Xe}$(GeV^2)			
ν-bin# 1	0.0245	0.0047	0.0022
ν-bin# 2	0.0168	0.0036	0.0020
ν-bin# 3	0.0170	0.0055	0.0034
ν-bin# 4	0.0218	0.0028	0.0020

Table A.9: Table containing numerical values for the p_t-broadening versus ν plot for positive charged pions.

$\Delta\langle p_t^2\rangle^{\pi^+}_{Ne}$	$\langle Q^2\rangle$(GeV^2)	$\langle\nu\rangle$(GeV)	$\langle z\rangle$	$\langle z^2\rangle$
ν-bin# 1	2.1387±0.0039	9.0260±0.0045	0.45957±0.00064	0.24748±0.00070
ν-bin# 2	2.5010±0.0045	13.0159±0.0033	0.41137±0.00053	0.20245±0.00054
ν-bin# 3	2.6039±0.0069	15.9793±0.0024	0.38487±0.00070	0.17580±0.00069
ν-bin# 4	2.4124±0.0042	19.5881±0.0050	0.34797±0.00040	0.13897±0.00035
$\Delta\langle p_t^2\rangle^{\pi^+}_{Kr}$				
ν-bin# 1	2.1486±0.0044	9.0723±0.0050	0.45154±0.00070	0.23863±0.00076
ν-bin# 2	2.5008±0.0049	13.0381±0.0036	0.40309±0.00056	0.19402±0.00058
ν-bin# 3	2.6234±0.0075	15.9832±0.0026	0.38138±0.00075	0.17220±0.00073
ν-bin# 4	2.4206±0.0044	19.6180±0.0053	0.34520±0.00041	0.13656±0.00036
$\Delta\langle p_t^2\rangle^{\pi^+}_{Xe}$				
ν-bin# 1	2.1469±0.0057	9.0643±0.0066	0.44998±0.00092	0.23716±0.00099
ν-bin# 2	2.5053±0.0064	13.0411±0.0047	0.40249±0.00072	0.19320±0.00074
ν-bin# 3	2.6280±0.0095	15.9851±0.0034	0.37866±0.00094	0.16952±0.00092
ν-bin# 4	2.4023±0.0056	19.6282±0.0067	0.34393±0.00052	0.13550±0.00045

Table A.10: Average values of Q^2, ν, z, and z^2 per hadron type per ν-bin for the p_t-broadening versus ν plots for positive charged pions. These numbers are extracted from data without applying any correction.

$\Delta\langle p_t^2\rangle^{\pi^-}_{Ne}$(GeV^2)	Value	Stat. error	Sys. uncertainty
ν-bin# 1	0.0101	0.0035	0.0021
ν-bin# 2	0.0066	0.0028	0.0020
ν-bin# 3	0.0039	0.0043	0.0032
ν-bin# 4	0.0057	0.0022	0.0018
$\Delta\langle p_t^2\rangle^{\pi^-}_{Kr}$(GeV^2)			
ν-bin# 1	0.0161	0.0036	0.0018
ν-bin# 2	0.0171	0.0029	0.0018
ν-bin# 3	0.0113	0.0043	0.0027
ν-bin# 4	0.0155	0.0023	0.0017
$\Delta\langle p_t^2\rangle^{\pi^-}_{Xe}$(GeV^2)			
ν-bin# 1	0.0205	0.0047	0.0019
ν-bin# 2	0.0226	0.0038	0.0019
ν-bin# 3	0.0202	0.0056	0.0032
ν-bin# 4	0.0198	0.0029	0.0017

Table A.11: Table containing numerical values for the p_t-broadening versus ν plot for negative charged pions.

$\Delta\langle p_t^2\rangle^{\pi^-}_{Ne}$	$\langle Q^2\rangle$(GeV^2)	$\langle\nu\rangle$(GeV)	$\langle z\rangle$	$\langle z^2\rangle$
ν-bin# 1	2.0976±0.0043	9.0423±0.0051	0.45584±0.00072	0.24383±0.00079
ν-bin# 2	2.4232±0.0049	13.0179±0.0037	0.40614±0.00059	0.19779±0.00061
ν-bin# 3	2.5301±0.0075	15.9867±0.0027	0.37919±0.00077	0.17098±0.00076
ν-bin# 4	2.3451±0.0045	19.6333±0.0055	0.34129±0.00043	0.13361±0.00037
$\Delta\langle p_t^2\rangle^{\pi^-}_{Kr}$				
ν-bin# 1	2.1170±0.0048	9.0582±0.0057	0.44639±0.00078	0.23347±0.00085
ν-bin# 2	2.4354±0.0054	13.0304±0.0041	0.39771±0.00062	0.18930±0.00064
ν-bin# 3	2.5372±0.0080	15.9848±0.0029	0.37574±0.00082	0.16764±0.00080
ν-bin# 4	2.3528±0.0047	19.6440±0.0058	0.33945±0.00045	0.13212±0.00039
$\Delta\langle p_t^2\rangle^{\pi^-}_{Xe}$				
ν-bin# 1	2.1207±0.0063	9.0680±0.0073	0.4463±0.0010	0.2333±0.0011
ν-bin# 2	2.4244±0.0068	13.0341±0.0052	0.39702±0.00080	0.18842±0.00082
ν-bin# 3	2.528±0.010	15.9896±0.0037	0.3734±0.0010	0.1653±0.0010
ν-bin# 4	2.3635±0.0060	19.6499±0.0074	0.3368±0.00056	0.12972±0.00048

Table A.12: Average values of Q^2, ν, z, and z^2 per hadron type per ν-bin for the p_t-broadening versus ν plots for negative charged pions. These numbers are extracted from data without applying any correction.

$\Delta\langle p_t^2\rangle^{K^+}_{Ne}$(GeV^2)	Value	Stat. error	Sys. uncertainty
ν-bin# 1	0.0183	0.0095	0.0062
ν-bin# 2	0.0074	0.0075	0.0057
ν-bin# 3	0.006	0.012	0.0094
ν-bin# 4	0.0064	0.0069	0.0051
$\Delta\langle p_t^2\rangle^{K^+}_{Kr}$(GeV^2)			
ν-bin# 1	0.033	0.010	0.0055
ν-bin# 2	0.0213	0.0078	0.0051
ν-bin# 3	0.004	0.012	0.0071
ν-bin# 4	0.0212	0.0067	0.0043
$\Delta\langle p_t^2\rangle^{K^+}_{Xe}$(GeV^2)			
ν-bin# 1	0.036	0.014	0.0059
ν-bin# 2	0.029	0.010	0.0054
ν-bin# 3	0.034	0.016	0.0092
ν-bin# 4	0.0333	0.0086	0.0045

Table A.13: Table containing numerical values for the p_t-broadening versus ν plot for positive charged kaons.

$\Delta\langle p_t^2\rangle_{Ne}^{K^+}$	$\langle Q^2\rangle$(GeV^2)	$\langle\nu\rangle$(GeV)	$\langle z\rangle$	$\langle z^2\rangle$
ν-bin# 1	2.1813±0.0083	9.0339±0.0096	0.4554±0.0012	0.2379±0.0013
ν-bin# 2	2.5737±0.0096	12.9916±0.0069	0.4129±0.0011	0.2033±0.0011
ν-bin# 3	2.695±0.015	15.9804±0.0053	0.4083±0.0015	0.1947±0.0015
ν-bin# 4	2.5162±0.0098	19.554±0.011	0.38217±0.00095	0.16638±0.00084
$\Delta\langle p_t^2\rangle_{Kr}^{K^+}$				
ν-bin# 1	2.1751±0.0093	9.0910±0.011	0.4555±0.0014	0.2379±0.0015
ν-bin# 2	2.570±0.010	13.0004±0.0073	0.4072±0.0011	0.1970±0.0011
ν-bin# 3	2.723±0.016	15.9692±0.0056	0.4019±0.0016	0.1890±0.0016
ν-bin# 4	2.505±0.0098	19.561±0.012	0.37536±0.00096	0.16035±0.00084
$\Delta\langle p_t^2\rangle_{Xe}^{K^+}$				
ν-bin# 1	2.176±0.012	9.125±0.014	0.4543±0.0018	0.2361±0.0019
ν-bin# 2	2.557±0.013	13.0152±0.0095	0.4084±0.0014	0.1976±0.0015
ν-bin# 3	2.680±0.020	15.9889±0.0070	0.4007±0.0020	0.1871±0.0019
ν-bin# 4	2.509±0.012	19.6135±0.014	0.3736±0.0012	0.1587±0.0010

Table A.14: Average values of Q^2, ν, z, and z^2 per hadron type per ν-bin for the p_t-broadening versus ν plots for positive charged kaons. These numbers are extracted from data without applying any correction.

A.4 p_t-broadening versus Q^2

$\Delta\langle p_t^2\rangle^{\pi^+}_{Ne}$(GeV^2)	Value	Stat. error	Sys. uncertainty
Q^2-bin# 1	0.0007	0.0016	0.0012
Q^2-bin# 2	0.0068	0.0026	0.0020
Q^2-bin# 3	0.0077	0.0025	0.0019
$\Delta\langle p_t^2\rangle^{\pi^+}_{Kr}$(GeV^2)			
Q^2-bin# 1	0.0143	0.0017	0.0023
Q^2-bin# 2	0.0201	0.0027	0.0020
Q^2-bin# 3	0.0248	0.0027	0.0021
$\Delta\langle p_t^2\rangle^{\pi^+}_{Xe}$(GeV^2)			
Q^2-bin# 1	0.0212	0.0022	0.0032
Q^2-bin# 2	0.0243	0.0036	0.0022
Q^2-bin# 3	0.0311	0.0035	0.0023

Table A.15: Table containing numerical values for the p_t-broadening versus Q^2 plot for positive charged pions.

$\Delta\langle p_t^2\rangle^{\pi^+}_{Ne}$	$\langle Q^2\rangle$(GeV^2)	$\langle\nu\rangle$(GeV)	$\langle z\rangle$	$\langle z^2\rangle$
Q^2-bin# 1	1.42912±0.00063	14.2591±0.0097	0.40610±0.00040	0.19667±0.00041
Q^2-bin# 2	2.43837±0.00097	14.514±0.014	0.39678±0.00058	0.18675±0.00059
Q^2-bin# 3	4.52431±0.00463	14.931±0.012	0.38906±0.00055	0.17897±0.00055
$\Delta\langle p_t^2\rangle^{\pi^+}_{Kr}$				
Q^2-bin# 1	1.43044±0.00069	14.494±0.011	0.39814±0.00042	0.18852±0.00043
Q^2-bin# 2	2.4386±0.0010	14.738±0.016	0.38968±0.00062	0.17981±0.00062
Q^2-bin# 3	4.5140±0.0050	15.113±0.013	0.38129±0.00057	0.17116±0.00056
$\Delta\langle p_t^2\rangle^{\pi^+}_{Xe}$				
Q^2-bin# 1	1.42950±0.00089	14.608±0.014	0.39482±0.00054	0.18531±0.00054
Q^2-bin# 2	2.4357±0.0013	14.773±0.020	0.38794±0.00078	0.17803±0.00078
Q^2-bin# 3	4.5141±0.0064	15.174±0.017	0.38130±0.00074	0.17122±0.00073

Table A.16: Average values of Q^2, ν, z, and z^2 per hadron type per Q^2-bin for the p_t-broadening versus Q^2 plots for positive charged pions. These numbers are extracted from data without applying any correction.

$\Delta\langle p_t^2\rangle^{\pi^-}_{Ne}$(GeV^2)	Value	Stat. error	Sys. uncertainty
Q^2-bin# 1	0.0049	0.0017	0.0014
Q^2-bin# 2	0.0079	0.0028	0.0020
Q^2-bin# 3	0.0118	0.0028	0.0020
$\Delta\langle p_t^2\rangle^{\pi^-}_{Kr}$(GeV^2)			
Q^2-bin# 1	0.0143	0.0017	0.0020
Q^2-bin# 2	0.0219	0.0029	0.0020
Q^2-bin# 3	0.0221	0.0029	0.0017
$\Delta\langle p_t^2\rangle^{\pi^-}_{Xe}$(GeV^2)			
Q^2-bin# 1	0.0191	0.0023	0.0026
Q^2-bin# 2	0.0250	0.0037	0.0021
Q^2-bin# 3	0.0325	0.0038	0.0020

Table A.17: Table containing numerical values for the p_t-broadening versus Q^2 plot for negative charged pions.

$\Delta\langle p_t^2\rangle^{\pi^-}_{Ne}$	$\langle Q^2\rangle$(GeV^2)	$\langle\nu\rangle$(GeV)	$\langle z\rangle$	$\langle z^2\rangle$
Q^2-bin# 1	1.42589±0.00069	14.418±0.011	0.40199±0.00044	0.19336±0.00045
Q^2-bin# 2	2.4345±0.0011	14.669±0.016	0.38853±0.00064	0.17934±0.00065
Q^2-bin# 3	4.4944±0.0053	15.048±0.014	0.37654±0.00061	0.16703±0.00060
$\Delta\langle p_t^2\rangle^{\pi^-}_{Kr}$				
Q^2-bin# 1	1.42574±0.00075	14.572±0.012	0.39440±0.00046	0.18573±0.00047
Q^2-bin# 2	2.4349±0.0012	14.848±0.018	0.38058±0.00067	0.17126±0.00066
Q^2-bin# 3	4.4859±0.0056	15.134±0.015	0.37146±0.00064	0.16203±0.00062
$\Delta\langle p_t^2\rangle^{\pi^-}_{Xe}$				
Q^2-bin# 1	1.42522±0.00096	14.634±0.015	0.39197±0.00059	0.18321±0.00059
Q^2-bin# 2	2.4354±0.0015	14.856±0.022	0.38024±0.00086	0.17106±0.00085
Q^2-bin# 3	4.4754±0.0071	15.207±0.020	0.36942±0.00081	0.16022±0.00078

Table A.18: Average values of Q^2, ν, z, and z^2 per hadron type per Q^2-bin for the p_t-broadening versus Q^2 plots for negative charged pions. These numbers are extracted from data without applying any correction.

$\Delta\langle p_t^2\rangle^{K^+}_{Ne}$(GeV^2)	Value	Stat. error	Sys. uncertainty
Q^2-bin# 1	0.0036	0.0047	0.0032
Q^2-bin# 2	0.0085	0.0076	0.0054
Q^2-bin# 3	0.0146	0.0073	0.0054
$\Delta\langle p_t^2\rangle^{K^+}_{Kr}$(GeV^2)			
Q^2-bin# 1	0.0200	0.0048	0.0042
Q^2-bin# 2	0.0240	0.0076	0.0046
Q^2-bin# 3	0.0265	0.0075	0.0048
$\Delta\langle p_t^2\rangle^{K^+}_{Xe}$(GeV^2)			
Q^2-bin# 1	0.0342	0.0063	0.0056
Q^2-bin# 2	0.029	0.010	0.0051
Q^2-bin# 3	0.0413	0.0099	0.0062

Table A.19: Table containing numerical values for the p_t-broadening versus Q^2 plot for positive charged kaons.

$\Delta\langle p_t^2\rangle_{Ne}^{K^+}$	$\langle Q^2\rangle$(GeV^2)	$\langle\nu\rangle$(GeV)	$\langle z\rangle$	$\langle z^2\rangle$
Q^2-bin# 1	1.4372±0.0014	13.983±0.021	0.41065±0.00083	0.19710±0.00083
Q^2-bin# 2	2.4386±0.0020	14.277±0.030	0.4166±0.0012	0.2025±0.0012
Q^2-bin# 3	4.5372±0.0096	14.825±0.025	0.4185±0.0012	0.2044±0.0012
$\Delta\langle p_t^2\rangle_{Kr}^{K^+}$				
Q^2-bin# 1	1.4413±0.0015	14.211±0.022	0.40465±0.00086	0.19078±0.00086
Q^2-bin# 2	2.4397±0.0022	14.546±0.032	0.4086±0.0013	0.1957±0.0013
Q^2-bin# 3	4.525±0.010	15.000±0.026	0.4132±0.0012	0.1992±0.0012
$\Delta\langle p_t^2\rangle_{Xe}^{K^+}$				
Q^2-bin# 1	1.4412±0.0019	14.407± 0.029	0.4038±0.0011	0.1897±0.0011
Q^2-bin# 2	2.4378±0.0028	14.716±0.040	0.4070±0.0016	0.1932±0.0016
Q^2-bin# 3	4.539±0.013	15.137±0.034	0.4103±0.0015	0.1960±0.0015

Table A.20: Average values of Q^2, ν, z, and z^2 per hadron type per Q^2-bin for the p_t-broadening versus Q^2 plots for positive charged kaons. These numbers are extracted from data without applying any correction.

Acknowledgements

Ten eerste zou ik mijn promotor Dirk Ryckbosch ten zeerste willen bedanken voor de kans die ik van hem gekregen heb om te doctoreren. Door me naar Hamburg in Duitsland te zenden is er een nieuwe wereld voor me open gegaan, dit had ik niet verwacht! In Hamburg heb ik geleerd zelfstandig te werken binnen een collaboratie. Dit was uiteraard niet mogelijk geweest zonder de financiele steun van het Fonds voor Wetenschappelijk Onderzoek (FWO) Vlaanderen.

Verder wens ik de mensen die zorgden voor de aangename werksfeer binnen het Instituut voor Nucleaire Wetenschappen (INW) in Gent te bedanken waar ik vooral het eerste jaar van mijn doctoraat vertoefd heb: Arne, Arne, Bino, Brecht, Luc, Freya, Michael, Peter, Robert (op dinsdagmorgend) en Tiko (de tweedehands BMW zal voor een andere keer zijn).

Most of the time during my PhD I spent in Hamburg in the Argonne-Gent office together with Uli with whom I did the first cross check of my preliminary analysis and who almost taught me how to ski. Later Charlotte joined and we had a lot of short discussions outside. Thanks for the great time!

Concerning the hardware part of my PhD I would like to thank Bino Mahieu who introduced me to the fascinating world of the HERMES Hodoscopes, Elke Aschenauer and Michael Tytgat for advice concerning the PMT test stand, and Yorck Holler who I could ask really everything concerning hardware.

For the analysis part of this work I would like to acknowledge Pasquale Di Nezza who advised me during the whole analysis and the two releases. Thank you for all the discussions in Frascati and Hamburg. Also special thanks to Anton Jgoun, who taught me, with a lot of drawings, the ins and outs of the unfolding for acceptance and radiative effects procedure. I would also like to acknowledge Elke for her advise concerning Monte Carlo simulations and general support, Delia and Naomi for very useful discussions.

Thanks to Rebecca, Homer, Charlotte, and Gunar for proofreading this work.

Physics was just a part of my life in Hamburg. I would like to thank Riccardo, Alex, Frank, Caro, Beni, Larry, Rebecca, Charlotte, Markus, Achim, ... for the great evenings off we had in Hamburg.

I would like to thank especially Tatjana for the great sunday afternoons, Tania for always inviting me to great happenings in Hamburg, Minze for not speaking English with me (Minze danke, daß Du nicht Englisch mit mir geredet hast) and Lisa for the nice evenings in Familien Eck.

Verder zou ik Frederik willen bedanken voor de talrijke bezoeken, reisjes en discussies.

Deze thesis was niet tot stand gekomen indien mijn ouders er niet geweest waren, bedankt. Speciale dank aan mijn grootouders die het studeren van hun kleinkinderen altijd gestimuleerd hebben en mijn zus voor haar niet aflatende steun.